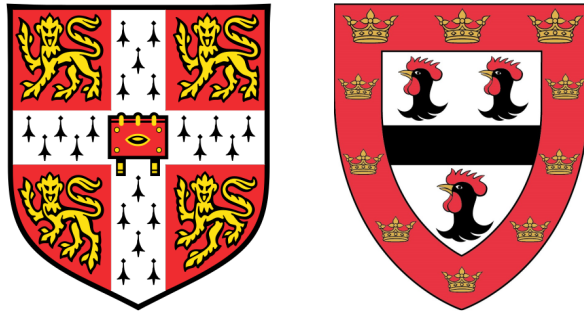


The Atmospheric Fingerprints of Volcanism

Simulating volcanic outgassing and secondary atmospheres on rocky planets



Philippa Kate Liggins

Department of Earth Sciences
University of Cambridge

This dissertation is submitted for the degree of
Doctor of Philosophy

Jesus College

July 2022

Declaration

I hereby declare that except where specific reference is made to the work of others, the contents of this dissertation are original and have not been submitted in whole or in part for consideration for any other degree or qualification in this, or any other university. This dissertation is my own work and contains nothing which is the outcome of work done in collaboration with others, except as specified in the text and Preface. This dissertation contains fewer than 225 pages including appendices, bibliography, footnotes, tables and equations, as stipulated by the Degree Committee of Earth Sciences.

Chapters 3 and 4 in this thesis represent published manuscripts, so have received inputs from coauthors and reviewers. Chapter 5 is about to be submitted, and has received input from coauthors. In all cases except those laid out below, I wrote and ran all the relevant models, the manuscript and the supplementary information, made all the figures and responded to reviewer comments.

Chapter 5, looking at the rate of thermochemical re-equilibration in volcanic atmospheres, represents a collaborative effort with Sean Jordan (a PhD student at the Institute of Astronomy in Cambridge). While writing what would become the published manuscript in Chapter 4, it became apparent that timescales to equilibrium for volcanic atmospheres would be required to justify assuming thermochemical equilibrium in lower temperature scenarios. This research eventually developed into a paper of its own, Chapter 5. Sean ran the atmospheric compositions I produced through the kinetics network described in Chapter 5, performed the analysis to find the rate limiting step and produced Figs. 5.4 and 5.5. Sean also wrote an initial version of the supplementary information presented in Appendix C, which I have edited down for addition in this thesis.

Philippa Kate Liggins
July 2022

The Atmospheric Fingerprints of Volcanism

Philippa Kate Liggins

The study of the atmospheric composition and evolution of rocky planet atmospheres is key to understanding both the conditions required to develop a habitable planet, and to analyse the link between the deep interior and atmosphere of rocky bodies. This thesis uses volcanism as a chemical link between the mantle of a planet and its atmosphere, with the aim of analysing how a volcanically derived or supplemented atmosphere may appear, both under the end-member case where volcanism is the only factor affecting the atmosphere, and when changing surface temperatures and atmospheric escape is considered. Chapter 2 describes a newly developed model of volcanic degassing for COHSN elements, designed with the broad range of exoplanet geochemistry in mind. It also describes a model for simulating the evolution of a volcanic atmosphere through time, based on the initial volatile content of a planetary mantle, the surface temperature and a stipulation for the escape of hydrogen. Chapter 3 demonstrates that volcanic activity can sustain a fraction of hydrogen in planetary atmospheres undergoing hydrogen escape, which may have contributed to a cold, wet early Mars, and expands the liquid water habitable zone for exoplanets. Chapter 4 shows that on planets with Venus-like atmospheric temperatures, the mantle fO_2 of a planet can be inferred from the chemistry and composition of a volcanic atmosphere as three distinct classes (defined by the presence/absence of certain indicator species) are formed. Specifically, Chapter 4 presents a set of volcanic atmospheres as an important base case for future research, exploring the effects of other processes on volcanic secondary atmospheres as produced by a range of geological conditions. Chapter 5 utilises chemical kinetics models to show that volcanic atmospheres must be at temperatures of 700 K and above in order to be accurately modelled as in thermochemical equilibrium, with the reactions of key species (NH_3 , CO and CH_4) being quenched over geological time below this point. Chapter 6 returns to the effect of hydrogen escape on volcanic atmospheres, exploring how escape modifies the atmospheric classes discussed in Chapter 4 and reduces or removes all indicators of mantle fO_2 from the atmosphere. This thesis presents a new volcanic degassing model and a number of use-cases, demonstrating the wide range of chemical speciations which volcanically generated atmospheres can form.

This thesis is dedicated to my late Grandpa Liggins.

I haven't quite explored everything we discussed which might be out in the Universe, but I
have covered one small part. I hope you'd be proud.

“Somewhere, something incredible is waiting to be known.”

– Carl Sagan

Acknowledgements

Firstly I have to thank my supervisor, Oli Shorttle, for being an endless source of ideas and encouragement to go above and beyond what I thought was possible (and sometimes even sensible), during the course of my PhD research. Your faith in my coding ability has been far greater than my own, and I'm incredibly grateful for all the skills that faith has helped me develop. My co-authors (Paul Rimmer and Sean Jordan), and collaborators outside the Cambridge bubble (Stanley Yip and Ery Hughes) also deserve special mentions. Your different viewpoints always pushed me to think harder about my assumptions, which has invariably improved the quality of my science. Thanks also go to my academic friends Marie Edmonds and David Al-Attar, for words of encouragement and advice, and my examiners, Clive Oppenheimer and Tamsin Mather, for their generous flexibility in allowing my viva to go ahead despite the Queen's funeral unexpectedly upstaging events. Clive's singing crab impression will live long in my memory! I also have to thank the wonderful, anonymous, people of the website StackOverflow, without whose advice most this thesis could never have been written. This research has been made possible by funding from the Embiricos Trust Scholarship of Jesus College Cambridge, and additional funds from the Department of Earth Sciences, for which I am extremely grateful.

Throughout my PhD I have been blessed with the support of many wonderful friends and family. To my office-mates, Craig, Christina, Penny, Hassan and Jack, thanks for the years of sage advice and keeping me sane as I whinged about the latest bug in my code. Thanks also go to a host of department friends (Kathryn, Ayesha, Nick, Hannah, Luke and others – you know who you are), for help, support and much needed breaks for tea, lunch and ice cream. Also, my parents for always providing a listening ear, chocolate in the post and a last minute read-through (sorry Mum, Dad – I've done it again...).

Particular thanks must go to Tom for graciously allowing me to ‘temporarily’ move in during the first COVID-19 lockdown; my years in Ferry House have lead to many memories I will treasure forever. Finally to my partner, Ben. As well as the dinners you have treated me to when we needed a break, and the enthusiastic advice on all things maths, Python and IDE-related, your unwavering belief that I can, in fact, do science has kept me going when nothing else did.

“It is the small everyday deeds of ordinary folk that keep the darkness at bay... small acts of kindness and love.”

– J. R. R. Tolkien, *The Lord of the Rings*

Publications

Publications arising from this thesis:

1. **Liggins, P.**, Shorttle, O. and Rimmer, P.B., 2020. Can Volcanism Build Hydrogen-Rich Early Atmospheres? *Earth and Planetary Science Letters*, 550, 116546. doi.org/10.1016/j.epsl.2020.116546 - **Chapter 3**
2. **Liggins, P.**, Jordan, S., Rimmer, P.B., and Shorttle, O., 2022. Growth and Evolution of Secondary Volcanic Atmospheres I: Identifying the Geological Character of Hot Rocky Planets. *Journal of Geophysical Research: Planets*, 127, e2021JE007123. doi.org/10.1029/2021JE007123 - **Chapter 4**
3. **Liggins, P.**, Jordan, S., Rimmer, P.B., and Shorttle, O. Growth and Evolution of Secondary Volcanic Atmospheres II: The Importance of Kinetics. In Press, *Journal of Geophysical Research: Planets*. - **Chapter 5**
4. **Liggins, P.**, Jordan, S., Rimmer, P.B., and Shorttle, O. Growth and Evolution of Secondary Volcanic Atmospheres III: Hot Atmospheres Undergoing Escape. In prep. - **Chapter 6**

Other publications produced during my time as a PhD student:

5. Yip, S., Biggs, J., Edmonds, M., **Liggins, P.**, and Shorttle, O., 2022. Contrasting Volcanic Deformation in Arc and Ocean Island Settings due to Exsolution of Magmatic Water. *Geochemistry, Geophysics, Geosystems*, 23, e2022GC010387. <https://doi.org/10.1029/2022GC010387>
6. Hughes, E.C., Saper, L., **Liggins, P.**, O'Neill, H.S.C and Stolper, E.M., 2022. The sulfur solubility minimum and maximum in silicate melt. *Journal of the Geological Society*, jgs2021-125, <https://doi.org/10.1144/jgs2021-125>
7. Hughes, E.C., **Liggins, P.**, Saper, L., and Stolper, E.M. The Effects of Oxygen Fugacity and Sulfur on the Pressure of Vapor-saturation of Magma. In Review, *American Mineralogist*.
8. Yip, S., Edmonds, M., **Liggins, P.**, and Biggs, J. The Role of Pre-Eruptive Exsolved Volatile Segregation on Volcanic Deformation and Degassing. Submitted to *Earth and Planetary Science Letters*.

Supplementary Data

The two models described and used in this thesis are freely available on GitHub at <https://github.com/pipliggins/EVo> for EVo, and <https://github.com/pipliggins/EVolve> for EVolve. Each model has a `readme.txt` file provided alongside, containing instructions on how to install the models and run a simulation. The specific model version, and data used to produce figures for Chapters 4 and 5 are also available in Zenodo repositories (Liggins, 2022b), (Liggins et al., 2022a) and (Liggins et al., 2022b), respectively.

Table of Contents

List of Figures	xix
List of Tables	xxiii
List of Symbols	xxv
1 Introduction	1
1.1 Motivation	1
1.2 Introducing rocky planets	2
1.2.1 Planetary atmospheres	5
1.3 Modelling exoplanet volcanism	7
1.4 Volcanic outgassing controls and processes	8
1.4.1 Oxygen fugacity ($f\text{O}_2$) and redox changes during degassing	9
1.4.2 Approaches to redox buffering of degassing melts in literature	11
1.5 Overview of Thesis	12
2 Models and Methods	15
2.1 EVo	16
2.1.1 Overview of the chemical model	17
2.1.2 Run types, set-up options and input parameters	31
2.1.3 Benchmarking	35
2.2 EVolve	40
2.2.1 Part 1: mantle melting	41
2.2.2 Part 2: EVo, volcanic outgassing	44
2.2.3 Part 3: atmospheric processing	45
3 Can Volcanism Build Hydrogen–Rich Early Atmospheres?	49
3.1 Introduction	49
3.2 Controls on a volcanic hydrogen atmospheres	50
3.2.1 Magma degassing	50
3.2.2 Hydrogen escape mechanisms	51
3.3 Modelling volcanic outgassing	52
3.3.1 Thermodynamics	52

Table of Contents

3.3.2	Volcanic outgassing	53
3.4	Relating outgassing to atmospheric H ₂ mixing ratios	55
3.5	$f_T(H_2)$ systematics with fO_2 and pressure	56
3.6	Achieving volcanically-sustained H ₂ atmospheres	58
3.6.1	Changing the volcanic flux	58
3.6.2	Changing the H ₂ escape rate	60
3.7	H ₂ on the early Earth	61
3.7.1	Likely escape rates on the early Earth	61
3.7.2	Hydrogen mixing ratios on the Archean Earth	64
3.7.3	Alternative H ₂ sources on the early Earth	65
3.8	Atmospheric warming of early Mars	67
3.9	Conclusions	71
4	Secondary Volcanic Atmospheres: Growth and Evolution on Hot Rocky Planets	73
4.1	Introduction	73
4.2	Methods	78
4.3	Results	79
4.3.1	Volcanic atmospheres in thermochemical equilibrium	79
4.3.2	Atmospheric classes on warm planets	82
4.3.3	Effect of the bulk silicate H/C ratio	86
4.3.4	Long-term atmospheric evolution	87
4.4	Discussion	90
4.5	Conclusions	90
5	Secondary Volcanic Atmospheres: The Importance of Kinetics	93
5.1	Introduction	94
5.2	Methods	96
5.2.1	Evolving volcanic atmospheres	96
5.2.2	Calculating chemical timescales	97
5.3	Results	99
5.3.1	Timescales to thermochemical equilibrium	101
5.3.2	Rate-limiting reactions	103
5.4	Discussion	107
5.4.1	Can volcanic atmospheres produce biosignature false positives? . . .	109
5.4.2	Model Limitations	110
5.5	Conclusions	113

Table of Contents

6 Secondary Volcanic Atmospheres: Hot Atmospheres Undergoing Escape	115
6.1 Introduction	115
6.2 Methods	117
6.2.1 Evolving volcanic atmospheres	118
6.2.2 Formulating H ₂ escape within EVolve	118
6.2.3 Validation of atmospheric escape formalism	120
6.3 Results	123
6.4 Discussion	127
6.5 Conclusions	128
7 Summary and Future Directions	131
7.1 Further Work	134
References	137
Appendix A Solubility laws as implemented in EVo	157
A.1 Laws taken from Burgasser et al. (2015)	157
A.2 CH ₄ : Ardia et al. (2013)	158
A.3 CO: Armstrong et al. (2015)	158
A.4 CO ₂ : Dixon et al. (1997)	158
A.5 CO ₂ : Dixon et al. (1997) (VC)	159
A.6 CO ₂ : Eguchi and Dasgupta, (2018)	159
A.7 H ₂ : Gaillard et al. (2003)	160
A.8 H ₂ O: Dixon et al. (1997)	161
A.9 N ₂ : Libourel, (2003)	162
A.10 Sulfide capacity laws	162
A.10.1 O'Neill and Mavrogenes, (2002)	162
A.10.2 O'Neill, (2020)	162
A.11 S ⁶⁺ : Nash et al. (2019)	163
Appendix B Appendices for Chapter 3	165
B.1 Effect of pressure and fO ₂ on volcanic gases and f _T ^V (H ₂)	165
B.2 Outgassing parameterisation	169
Appendix C Full description of the identified rate-limiting reactions	173
C.1 Atmospheric evolution	173
C.2 CO ⇌ CH ₄ system	174
C.3 N ₂ ⇌ NH ₃ system	178

List of Figures

1.1	Mass-radius diagram for detected exoplanets with equilibrium temperature.	2
1.2	Schematic of a transiting exoplanet.	4
1.3	Schematic of primordial, primary and secondary atmospheres	5
1.4	Log oxygen fugacity of various rock buffers with temperature.	9
2.1	EVo model overview.	16
2.2	A simple diagram of the C-O system in silicate melts.	28
2.3	Behaviour of sulfur in silicate melts.	29
2.4	Speciation of an OH gas with $f\text{O}_2$	34
2.5	Difference between EVo and DCompress equilibrium constants.	36
2.6	Comparing initial conditions between DCompress and EVo.	37
2.7	Demonstrating the differences in sulfur solubility between EVo and DCompress.	38
2.8	Comparing degassing paths between EVo, DCompress, SolEx and Chosetto. .	39
2.9	EVolve model overview.	41
3.1	Total hydrogen mixing ratio sustained in the troposphere according to magma $f\text{O}_2$	57
3.2	Flux effect on atmospheric hydrogen content.	59
3.3	Diffusion loss efficiency effect on atmospheric hydrogen content.	60
3.4	Comparing diffusion limited to energy limited hydrogen loss fluxes.	63
3.5	Most frequent hydrogen mixing ratios for Earth.	64
3.6	H ₂ sources on the early Earth.	66
3.7	Comparing diffusion limited to energy limited escape on Mars.	68
3.8	Most frequent hydrogen mixing ratios for Mars.	70
4.1	The effect of changing atmospheric temperature in a 0D atmosphere on surface pressure, scale height, mean molecular mass and the chemical speciation.	80
4.2	Atmospheric classes based on mantle $f\text{O}_2$	82
4.3	Sensitivity tests of atmospheric classes to changing mantle temperature and local melt fraction.	84
4.4	Atmospheric classes with $f\text{O}_2$ when the temperature is varied.	84
4.5	Equilibrium temperature of planets according to stellar luminosity and orbital distance, with atmospheric classes overlaid.	85

List of Figures

4.6	Atmospheric classes and scale heights according to mantle fO_2 and initial H/C ratio.	86
4.7	Long-term evolution of atmospheres on planets with reduced, intermediate and oxidised mantles.	88
4.8	Dominant atmospheric constituent according to the time since the onset of volcanism, mantle fO_2 and initial H/C ratio.	89
5.1	Chemical speciations of three volcanic atmospheres varying with ambient temperature.	100
5.2	Chemical timescales to equilibrium with temperature assuming instantaneous cooling from 1473 K for CO, CH ₄ and NH ₃	101
5.3	Chemical timescales to equilibrium for CO, CH ₄ and NH ₃ at four atmospheric temperatures, varying with the planet's mantle fO_2	102
5.4	Network of important reactions linking CO to CH ₄ in the chemical-kinetics network.	104
5.5	Network of important reactions linking N ₂ to NH ₃ in our chemical-kinetics network.	106
5.6	Regions in stellar luminosity - orbital distance space where volcanic gasses injected into atmospheres may reach either full, partial or minimal thermochemical equilibrium at a given atmospheric temperature.	108
5.7	Minimum chemical timescales for an S-H bond to be broken, starting the conversion of CO to CH ₄ , as a function of temperature.	113
6.1	Comparing results of two formalisms for calculating hydrogen escape.	121
6.2	Hydrogen mixing ratio for a volcanic atmosphere undergoing dry stratosphere escape.	123
6.3	Surface pressure, scale height and atmospheric speciation for atmospheres undergoing wet and dry stratosphere escape.	124
6.4	Atmospheric speciation for a high and low mantle H/C ratio, for both wet and dry stratosphere escape.	126
B.1	Effect of pressure of volcanic gases.	166
B.2	Effect of variable magmatic C content on volcanic gases.	167
B.3	H ₂ content of volcanic gases with magma fO_2	168
B.4	Stoichiometric effects on $f_T(H_2)$	170
B.5	Stoichiometric effects of $f_T(H_2)$ for Earth.	171
B.6	Stoichiometric effects of $f_T(H_2)$ for Mars (hydrous).	172
B.7	Stoichiometric effects of $f_T(H_2)$ for Mars (anhydrous).	172

List of Figures

C.1	A time-series of the volcanic atmosphere composition relaxing to ambient temperatures.	174
C.2	$\text{CO} \rightleftharpoons \text{CH}_4$ reaction rates as a function of $f\text{O}_2$ over a range of temperatures.	177
C.3	$\text{N}_2 \rightleftharpoons \text{NH}_3$ reaction rates as a function of $f\text{O}_2$ over a range of temperatures.	182

List of Tables

2.1	The solubility laws implemented in EVo.	21
2.2	EVo input options when P_{start} is known.	32
2.3	Partition coefficients for bulk melting equation used in EVolve	42
4.1	Process which can modify the composition and speciation of an atmosphere. . .	77
6.1	Binary diffusion coefficients calculated at 300 and 800 K within EVolve. . . .	119
A.1	Parameters used in solubility laws taken from Burguisser et al. (2015).	158
A.2	Coefficients for the CO ₂ solubility model of Eguchi and Dasgupta, (2018). . .	160

List of Symbols

Roman Symbols

- a Fraction of the gas phase removed during open-system degassing
- b Binary diffusion coefficient
- D Partition coefficient
- E_a Activation energy, kJ/mol
- F Molar fraction of FeO/Fe₂O₃
- $f(x)$ Atmospheric mixing ratio of species x
- f_x Fugacity of species x , bar
- F_{melt} Local melt fraction
- G Gravitationl constant, $6.6743 \times 10^{-11} \text{ m}^3 \text{ kg}^{-1} \text{ s}^{-2}$
- g Acceleration due to gravity, 9.81 m s^{-2}
- K Equilibrium constant
- k Rate constant, $\text{cm}^3 \text{ s}^{-1}$
- M Molar mass
- m Mass
- m_{XUV} Energy-limited mass loss rate
- n Number density
- N_A Avogadro's constant, $6.022\,140\,76 \times 10^{23} \text{ mol}^{-1}$
- P Total pressure
- P_{sat} Volatile saturation pressure
- R Universal gas constant, $8.3144 \text{ J mol}^{-1} \text{ K}$

List of Symbols

r	Radius
r_{ei}	Extrusive:intrusive ratio, the fraction of melt produced in the mantle which reaches the surface
T	Temperature, K
V	Molecule velocity when calculating rate constants, cm s^{-1}
v	Volume fraction of the gas phase
W	Weight fraction of an atomic element
w	Weight fraction
W_{gT}	Total weight fraction of the gas phase
X	Mole fraction

Greek Symbols

α	Escape efficiency factor, bounded between 0 -1
β	Outgassing flux factor
γ	Fugacity coefficient
μ	Mean molecular mass
ϕ	Flux, molecules $\text{cm}^{-2} \text{ s}^{-1}$
π	Pi, 3.14...
ρ	Density
σ	collisional cross-section of a molecule, cm^2

Superscripts

m	Indicates melt phase
v	Indicates volatile, or gas phase

Subscripts

i, j	subscript index
--------	-----------------

Other Symbols

\mathcal{F}_{XUV} XUV flux at the top of the atmosphere

$\Delta_f G^\circ$ Gibbs free energy of formation

$\Delta_r G^\circ$ Gibbs free energy of reaction

\mathcal{H} Pressure scale height

1

Introduction

1.1 Motivation

The detection of planets orbiting stars other than our own ('exoplanets', Mayor and Queloz, 1995) has expanded the study of planetary processes beyond our solar system. In the two decades since the discovery of the first rocky exoplanet (Queloz et al., 2009), our catalogue has expanded to include thousands of other worlds. Many of these planets are in short-period orbits around small stars, making them ideal candidates for atmospheric characterisation; rocky exoplanets already marked for investigation during the first year of the James Webb Space Telescope's (*JWST*) mission include the rocky Earth and super-Earth sized planets GJ 1214b, LHS 1140b, the Trappist-1 planets, LTT 1445 Ab, L 98-59b and K2-19b (STScI, 2022). This places us on the cusp of a second revolution in exoplanetary science, where for the first time we can investigate the atmospheres of rocky planets outside the solar system.

The study of the atmospheric composition and evolution of rocky planet atmospheres is key for understanding both the conditions required to develop a habitable planet, and to analyse the link between the deep interior and atmosphere of rocky bodies. Ahead of the upcoming influx of atmospheric measurements from missions such as *JWST*, there is a need to develop and link models of fundamental geophysical processes to those of planetary atmospheres, in order to constrain the geology, and ultimately the habitability, of rocky exoplanets we will observe.

This thesis focusses on volcanism, a universal planetary process which can form and perturb atmospheres. **The main aims of the study are to analyse how a volcanically derived or supplemented atmosphere may appear, both under the end-member case where volcanism is the only factor affecting the atmosphere, and when changing surface temperatures and atmospheric escape is considered.**

Introduction

1.2 Introducing rocky planets

Since the discovery of the first exoplanet in orbit around a sun-like star in 1995 (51 Pegasi-b Mayor and Queloz, 1995), more than 5000 exoplanets (planets in orbit around a star other than the Sun) have been discovered. These planets span a range of sizes, with radii from $3\times$ that of Jupiter, down to Earth-sized and smaller (Fig. 1.1). Of these confirmed exoplanets, nearly 1800 are classed as either ‘terrestrial’ (silicate planets with iron cores and of a similar size to Earth) or ‘Super-Earths’ (NASA, 2019), with radii between $1.25R_{\oplus} < R_p \leq 2R_{\oplus}$ (where subscript \oplus denotes Earth, Fulton et al., 2017) and masses up to $10\times$ Earth. Another ~ 350 candidate planets with radii $\leq 2R_{\oplus}$ detected by TESS (NASA’s Transiting Exoplanet Survey Satellite) are awaiting confirmation. Figure 1.1a shows every confirmed exoplanet to date, for which mass and radius are known (964 of the 5000+ confirmed exoplanets). Where data is available, the points are coloured according to the theoretical temperature of the planet if it were a black body being heated only by its star; the ‘equilibrium temperature’.

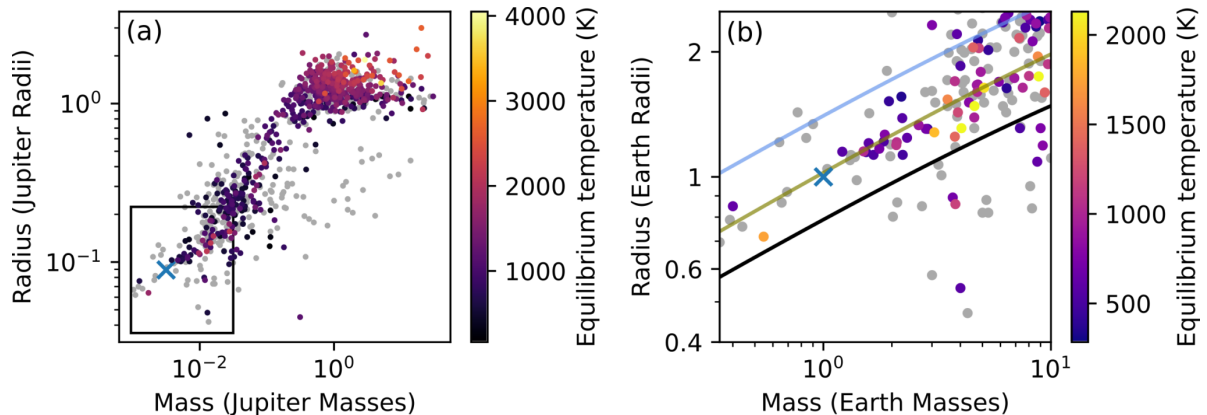


Fig. 1.1 (a) The mass and radius of all confirmed exoplanets where such data are available. Where possible, points are coloured according to the planet’s equilibrium temperature, otherwise they are plotted in grey. The box in (a) shows the limits of (b), note the change in scales. Earth is marked as a blue cross in both panels. (b) Shows only planets in the terrestrial and super-Earth categories. Lines, from bottom to top in black, green and blue, are the mass-radius relations for a body made purely from iron, enstatite ($MgSiO_3$), and water respectively (Seager et al., 2007). Data taken from the NASA Exoplanet Archive, accurate as of May 2022.

As shown in Fig. 1.1b, not all Super Earth-sized exoplanets bear much similarity to Earth; those with densities close to that of a 100% H_2O body are likely to be closer in composition and structure to a Neptune-like planet, with a significant gas envelope and very little silicate material. Instead, low-radius planets with densities high enough that they must contain a significant silicate fraction are grouped and generally referred to as the ‘rocky’ planets. In Fig. 1.1b, these planets

1.2 Introducing rocky planets

lie around and below the 100% enstatite line similarly to Earth. It should be noted that the errors on mass/radius data for exoplanets are often large, which explains the presence of some planets in Fig. 1.1b which appear to be pure iron/denser than iron.

It is interesting to note the range in equilibrium temperatures shown in both Figs. 1.1a and 1.1b. Both panels show that the majority of currently detected exoplanets have equilibrium temperatures well above the maximum seen in the solar system (Mercury's 450 K). This reflects one of a number of detection biases within the exoplanet catalogue; it is easier to detect planets that are closer to their stars, which inherently have higher equilibrium temperatures.

There are 4 common methods of exoplanet detection: radial velocity (RV), transit, direct imaging and gravitational microlensing. Of these, the transit method is by far the most prolific. In this case, a planet is detected by monitoring the brightness of a star. When a planet passes directly between the star and its observer, the observed brightness dims by an amount proportional to the area of the stellar face being obstructed. The larger and/or closer a planet is to the star, the greater the area of the stellar face that is covered during transit and the easier it is to detect due to the transit depth δ increasing, calculated as

$$\delta = \frac{r_{\text{planet}}^2}{r_{\text{star}}^2}, \quad (1.1)$$

where r_{planet} and r_{star} are the radii of the planet and star, respectively. Hence, there is a bias in the exoplanet catalogue towards large, close in planets with high equilibrium temperatures.

Planets close to their star in short-period orbits are also easier to detect, due to the greater frequency with which they pass between the star and observer. For example, most of the observing done by TESS is in 28-day chunks; as a planet must transit twice to be confirmed during that observational time period, most of the planets found by TESS have orbital periods of less than 14 days (Burt et al., 2021).

Although the transit method has these well known biases, identifying transiting exoplanets comes with a huge opportunity for further characterisation of the planet's atmosphere. The configuration of a transiting exoplanet is such that once every orbit, it will pass directly in front of, and then directly behind the parent star from the point of view of the observer (Fig. 1.2). During transit, some of the light from the parent star will pass directly through the planetary atmosphere (depicted as the blue ring in Fig. 1.2), whereupon a combination of absorption and scattering takes place which is wavelength-dependent according to the molecules present in the atmosphere. This results in modification of the transmitted light, dependent on the atmospheric composition. A planetary transmission spectrum can be obtained by dividing the planet+star transmission spectrum by that of the star alone, taken either before or after transit. In a similar procedure, when a planet is in secondary eclipse behind its star, the observer sees the starlight

Introduction

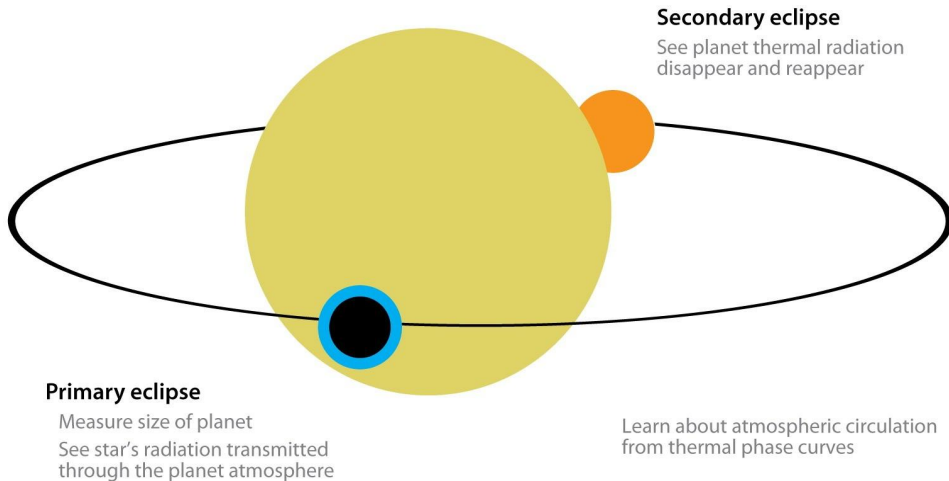


Fig. 1.2 Schematic illustration from Seager and Deming (2010) of a transiting exoplanet with primary and secondary eclipse, and their potential follow-up measurements. Note that primary eclipse is also called a transit.

alone, while shortly before and after the combined star + planet light will be seen. At near and mid-infrared wavelengths, secondary eclipse can reveal the thermal radiation from the planet, and the emission spectrum.

Both transmission and emission spectroscopy have been shown to be successful for characterising the atmospheres of gas giant exoplanets (e.g., Charbonneau et al., 2002; Deming et al., 2005; Swain et al., 2008; Hoeijmakers et al., 2019). However as with detection, spectroscopy becomes more difficult when considering smaller, rocky planets. The size of any spectral features in a transmission spectrum are approximately proportional to the atmospheric scale height (The change in altitude over which the atmospheric pressure drops by a factor of e). Smaller scale heights produce smaller transmission features, which are harder to detect with sufficient statistical significance from the background noise (Miller-Ricci et al., 2008). Ideal candidates for transmission spectroscopy have high equilibrium temperatures, small host stars, low surface gravity and a low mean molecular weight atmosphere (H_2 dominated). Even in ideal cases, the amplitude of spectral features is around 0.1 %. An Earth-like planet would be expected to have features 2-3 orders of magnitude smaller again (Kreidberg, 2017).

The theoretical difficulty of transmission spectroscopy has been borne out in recent attempts to characterise the atmospheres of rocky exoplanets. For example, recent attempts to characterise the transmission spectrum of rocky exoplanet GJ 1132b have resulted in contradictory results: Swain et al. (2021) claim to have detected a H_2 dominated (99 %) atmosphere containing HCN and CH_4 , while Mugnai et al. (2021) and Libby-Roberts et al. (2021) both find a featureless spectrum when using the same observations. A featureless

transmission spectrum has so far been the most common outcome when characterising the atmospheres of super-Earth and sub-Neptune planets, which can be indicative of either a high molecular weight atmosphere, a high-altitude aerosol layer/clouds, or essentially no atmosphere at all (e.g., Kreidberg et al., 2014; de Wit et al., 2016; Libby-Roberts et al., 2021; Garcia et al., 2022). Observations with new high-resolution, high-sensitivity telescopes such as *JWST* and *ELT*, along with future facilities such as *LUVOIR* (Hylan et al., 2019) and *HabEx* (Gaudi et al., 2020), should be able to resolve molecular species within high molecular weight atmospheres on planets orbiting low-mass stars (Morley et al., 2017; Snellen et al., 2017; Batalha et al., 2018)

1.2.1 Planetary atmospheres

The atmospheres of planets can be sorted into three categories, according to the origin of the gases from which they are formed (Fig. 1.3). Primordial atmospheres are comprised almost entirely of hydrogen gas, accreted directly from the protoplanetary disk as the planet grows. These atmospheres are characteristic of gas giant planets such as Jupiter. Primary atmospheres (Fig. 1.3b) may also contain significant fractions of H₂, but will typically also contain other reduced species such as methane, along with water and CO₂. These atmospheres can be derived from early, syn-accretionary gas release from planetesimal accretion during planet formation, and/or outgassing from an early magma ocean phase. Primary atmospheres tend to be the starting point for most smaller rocky planets; while they may accrete some gas directly from the disk, their gravitational strength is not sufficient to do this in significant quantities. For example, there is no evidence that either Earth or Venus started with a significant, H₂ dominated primordial atmosphere (Dauphas and Morbidelli, 2014).

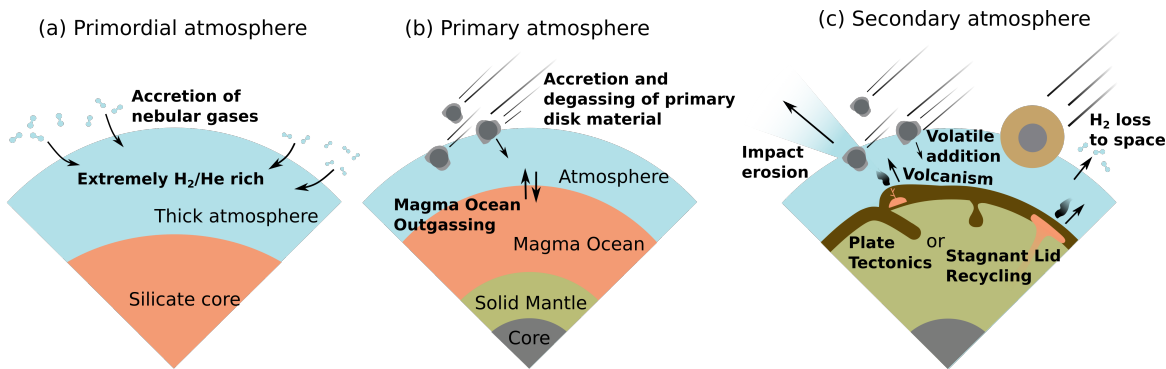


Fig. 1.3 Each of the three origins of planetary atmospheres. Rocky planets evolve through each stage, while gas giants keep their primordial atmospheres. Adapted from Sakuraba et al. (2021).

Introduction

Secondary atmospheres (Fig. 1.3c) represent the final stage of atmospheric evolution for most rocky planets. These atmospheres are heavily modified from their primary origin, with gases derived from long-term release from the interior through processes such as volcanism. Other modifying processes such as reactions with the surface (e.g., through the carbonate-silicate cycle Walker et al., 1981; Lehmer et al., 2020), loss of light gases to space (Hunten, 1973; Lammer et al., 2014), and erosion/transformation/addition of atmospheric mass through impact events (Kasting, 1990; Itcovitz et al., 2022) may also occur (Fig. 1.3c, see Chapter 4 and Table 4.1 for a more extensive list of processes).

Planets with secondary atmospheres are of significant interest to the planetary and exoplanetary community, as they represent a sub-set of exoplanets which are the most similar to Earth, and are therefore the most likely to be habitable. The co-evolution of Earth's geology and atmosphere has been a critical factor in the origin of life (Kasting, 1993; Zahnle et al., 2010; Sasselov et al., 2020). Understanding how this atmospheric evolution progressed, why Mars and Venus diverged from Earth's evolutionary path and possibly identifying exoplanets currently undergoing these processes, will revolutionise our understanding of origin-of-life chemistry and what makes a habitable planet.

Secondary atmospheres, particularly those formed containing significant volcanic gas contributions, also provide an exciting opportunity for investigating the interior of rocky exoplanets. Unlike some geophysical properties of planets, which can be inferred from their densities (Zeng and Sasselov, 2013) and the incident radiation (giving the surface temperature), the geochemistry of exoplanets is harder to interrogate remotely. Observations of planetary surfaces, from which some geochemical data may be collected (e.g., Kreidberg et al., 2021), are limited to atmosphere-free planets which are often extremely hot, thanks to a proximity to their star having ‘blown off’ the atmosphere (Kreidberg et al., 2019). This approach would severely limit the number of exoplanet geochemistries which can be investigated, despite the hints at a huge diversity in planetary geochemistry which have been seen (Putirka and Xu, 2021). On Earth, volcanic systems of silicate melt and the entrained volatiles carried to the surface provides a key link from the earth's interior to its atmosphere (discussed below in Section 1.4), through the ratio of different volatile elements and the redox state of the gases released. Similarly, on volcanically active exoplanets with low atmospheric mass, volcanism can supply volatiles to a planet's atmosphere; this couples the planet's atmospheric chemistry to its interior and provides a window into the geochemistry and composition of exoplanets which would otherwise be inaccessible. This interior-atmosphere link will be particularly strong on warm to hot planets, where low-temperature atmospheric drawdown processes (e.g., carbonate-silicate weathering) are likely to be weak or non-operational. These secondary

volcanic atmospheres, which persist over billions of years and link mantle geochemistry to observable atmospheric features, are the focus of this thesis.

1.3 Modelling exoplanet volcanism

The geochemical and geophysical range of known exoplanets, both observed (e.g., Howard et al., 2013; Angelo and Hu, 2017; Kreidberg et al., 2019; Winters et al., 2019; Lillo-Box et al., 2020; Cloutier et al., 2021; Swain et al., 2021) and theorised (Zeng et al., 2019; Madhusudhan et al., 2021), motivates a revised approach to the modelling of exoplanet geology. Critically, current tools produced for and by the Earth Sciences community for use modelling volcanic activity on Earth are very limited once applied to exoplanets. Models describing magma degassing are either restricted in their T-P range (Kress et al., 2004; Huizenga, 2005), their compositional generality (Newman and Lowenstern, 2002; Huizenga, 2005; Witham et al., 2012), or their software implementation which restricts extensibility and interfacability (Moretti et al., 2003; Kress et al., 2004; Witham et al., 2012; Burgisser et al., 2015). Others are simply unavailable to the scientific community (Gaillard and Scaillet, 2014, and Moretti et al., 2003 until 2022). Given the Earth-centric nature of these models, they also do not account for behaviour that is uncommon in terrestrial systems; for example both CO and CH₄ (along with a number of other species) have been shown to be soluble in highly reduced magmas (Ardia et al., 2013; Armstrong et al., 2015; Dalou et al., 2019). As melts this reduced are not seen on the modern Earth, available degassing models either treat these species as insoluble, or neglect them entirely. However, both Mercury and Mars are known to have magmas which are sufficiently reduced to trigger this behaviour (Wadhwa, 2008; Schmidt et al., 2013a; Zolotov et al., 2013), indicating a need to include reduced species within degassing models for wider application to planetary and exoplanetary sciences.

A number of previous studies have included an aspect of volcanism on exoplanets, explored with varying degrees of simplification. Earlier studies usually focussed purely on CO₂, or the COH system, assuming complete outgassing of any melt reaching surface pressure according to models of mantle convection (Grott et al., 2011; Noack et al., 2014; Dorn et al., 2018; Guimond et al., 2021), leaving no residual volatile in the melt. More recently (Tosi et al., 2017) and during the course of my PhD research (Ortenzi et al., 2020; Wogan et al., 2020), solubility laws developed by the volcanological community have begun to be applied to research on exoplanetary atmospheres; however, they still fall foul of many of the weaknesses discussed above. The only publicly released model from these recent papers is that of Wogan et al. (2020), which is limited in its extensibility, functionality and compositional range.

Introduction

In order to have a magma degassing model which is applicable across the diverse regimes anticipated for exoplanets, and in light of the limitations in the current suite of available models, a core component of my PhD research was to develop a state-of-the-art magma-fluid equilibrium code. The aim was to make this fully open-source and extensible, to make use of constantly updating experimental constraints, so as to be as versatile and useful as possible both for the planetary science community applying it to exoplanets, and for terrestrial volcanologists. The model I have produced to address these aims, EVo, is described in Chapter 2. In the remainder of this chapter, I briefly describe the key controls on the composition and speciation of a volcanic system during degassing, which must be addressed when selecting a modelling approach.

1.4 Volcanic outgassing controls and processes

Volcanic outgassing has contributed to the development and modification of both the atmosphere and oceans of Earth from the magma ocean period (Elkins-Tanton, 2008; Williams et al., 2021), through the Great Oxidation Event (GOE, Holland, 2002; Moussallam et al., 2019; Kadoya et al., 2020) to the present day, and in so doing has helped generate the conditions required for the emergence of life. The major components of these volcanic gases can be described using the C-O-H-S-N system, which represent around 99% of all volcanic emissions (Fischer and Chiodini, 2015).

Three key parameters regulate the composition and speciation of volcanic gases as they progress from the interior to the atmosphere: the temperature, pressure and oxidation state of the system. The current pressure, and to a lesser extent the temperature, controls the ratio of dissolved/exsolved volatiles in the magma through the solubility of each species. Volatile solubility is a measure of the maximum amount of a given species which can remain dissolved in a magma at a given pressure (see Section 2.1.1). As each volatile species has a different solubility, the composition of the gas phase will evolve with decreasing pressure, as each species in turn starts to exsolve from the melt. Reduced species such as H₂, CO and CH₄ are almost insoluble, and so start to form a separate gas phase at high pressures. They are followed by CO₂, H₂O and finally sulfur species in order of increasing solubility. In practise, although single-species solubility laws suggest that for example, there should be no water present in volcanic gases at high pressure, once a separate gas phase has formed a small amount of each volatile species present in the magma will diffuse into the gas bubbles. Therefore, volcanic gases tend to be carbon-rich (but not purely carbon species) at depth, becoming increasingly water and sulfur-rich as they rise to the surface (e.g., Fig. 3 of Gaillard and Scaillet, 2014).

1.4 Volcanic outgassing controls and processes

Simultaneously, the temperature and redox state of the system controls volatile speciation, i.e., the proportion of the volatiles present in their oxidised (H_2O , CO_2 , SO_2 ...) or reduced (H_2 , CO , H_2S ...) form. In magmatic systems, the redox state of the system is discussed in terms of oxygen fugacity, or $f\text{O}_2$, where oxidised systems such as those common on the modern Earth have a high $f\text{O}_2$, and reduced systems a low $f\text{O}_2$. Therefore, the composition and speciation of volcanic gases at the point they are erupted contains a fingerprint of the temperature, pressure and redox conditions at which they were last equilibrated. This chemical link from the atmosphere back to the mantle can be exploited to infer the mantle properties of exoplanets, based on observations of their atmospheres.

1.4.1 Oxygen fugacity ($f\text{O}_2$) and redox changes during degassing

Oxygen fugacity ($f\text{O}_2$) is a measure of the degree of oxidation of a rock, magma or mantle. It is a function of the chemical potential of oxygen, and is often also described as measuring the ‘effective partial pressure’ of oxygen in equilibrium with the material being measured. However this can be misleading, as calculating an oxygen fugacity does not necessitate the presence of a gas or fluid phase. As $f\text{O}_2$ is usually a very small value, which varies with temperature and pressure (Fig. 1.4), it is usually described relative to an equilibrium reaction within a mineral assemblage, known as a ‘rock buffer’, or ‘oxygen buffer’. These mineral assemblages provide a fixed value for $f\text{O}_2$ at a given temperature and pressure (Anenbarg and O’Neill, 2019), following defined $f\text{O}_2$ -T curves (Fig. 1.4) and allowing $f\text{O}_2$ to be discussed (somewhat) independently of T/P changes. The most commonly used rock buffers are NNO (nickel-nickel oxide), FMQ (or QFM; quartz-magnetite-fayalite) and IW (iron-wüstite). When expressed in this way, for example relative to the IW buffer, $f\text{O}_2$ can be expressed as $\Delta\text{IW} = \log_{10}(f\text{O}_2) - \log_{10}(f\text{O}_2)_{\text{IW}}$.

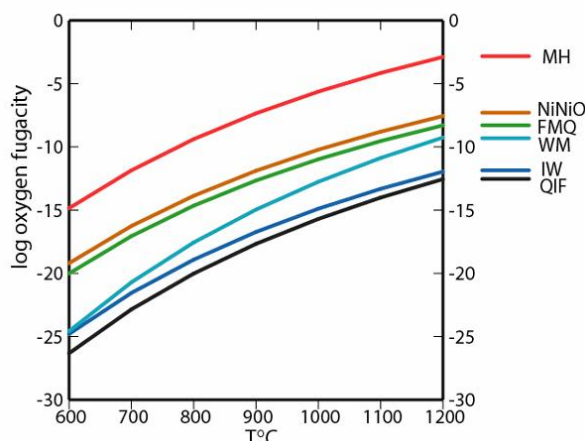


Fig. 1.4 Log oxygen fugacity - temperature diagram showing the occurrence of the buffers commonly used in Earth Sciences. Original figure from Frost (1991), coloured plot taken from Iacobino (2021).

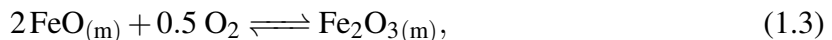
Introduction

It is important to note that although rock buffers such as the NNO buffer reaction



(with the subscript ‘s’ referring to a solid phase) show free oxygen in their reaction, these reactions do not themselves represent a controlling/influencing redox exchange occurring within a natural system (Moretti and Stefánsson, 2020). Indeed, the ‘rock buffer’ reactions rarely occur in nature (Frost, 1991); they exist purely as a convenient reference state for expressing a system’s $f\text{O}_2$ as ΔNNO i.e., with respect to the NNO reaction at equivalent P and T.

The term ‘buffer’ sometimes creates confusion, as silicate melts are often described as being buffered during processes such as degassing (Mathez, 1984; Carmichael and Ghiorso, 1986; Gaillard and Scaillet, 2014) or magmatic evolution (Christie et al., 1986; O’Neill et al., 2018). In this case, the redox buffering of a silicate magma (i.e., the application of Le Chatelier’s Principle to compensate for changes in $f\text{O}_2$) is achieved by elements which are both abundant and redox sensitive: iron and sulfur, as Fe^{II} , Fe^{III} , $\text{S}^{-\text{II}}$ and S^{VI} . While the sulfide to sulfate buffer provides a much larger electron transfer than that of Fe^{II} to Fe^{III} , the effectiveness of sulfur as a redox buffer is limited by its abundance in silicate melts, which is significantly lower than iron in most cases (Nash et al., 2019; Cicconi et al., 2020). The basic reaction controlling the redox chemistry of a silicate melt+gas system is therefore best expressed as



with the subscript ‘m’ referring to the melt phase. In the scenario of a decompressing melt with an exsolved gas phase, the $f\text{O}_2$ of the gas phase is linked to the melt through Eq. (1.3). The capacity of the melt to buffer changes in the gas phase $f\text{O}_2$ is therefore controlled by the amount of oxygen-accommodating iron present; iron-rich basaltic melts are much more effective $f\text{O}_2$ buffers than rhyolitic melts because of this (Burgisser and Scaillet, 2007; Moretti and Stefánsson, 2020).

There is a strong theoretical basis for volcanic degassing (particularly of sulfur) affecting the $f\text{O}_2$ of silicate melts (Mathez, 1984; Carmichael and Ghiorso, 1986; Carmichael, 1991; Burgisser and Scaillet, 2007; Métrich et al., 2009; Gaillard et al., 2011; Kelley and Cottrell, 2012), as evidenced by observations of melt reduction driven by sulfur degassing (Oppenheimer et al., 2011; Moussallam et al., 2014, 2016; Brounce et al., 2017; Helz et al., 2017; Longpré et al., 2017). Therefore, redox changes within degassing systems are controlled by an interplay between the effects of degassing volatiles and the iron-accommodated oxygen acting to buffer

1.4 Volcanic outgassing controls and processes

the change, while both melt and gas phase remain in thermal and chemical equilibrium. Redox evolution in magmas as they degas requires precautions to be taken when, for example, using the oxidation state of erupted basalts as a direct reflection of their mantle source.

Studies involving natural systems have noted that there is often a discrepancy between the oxidation state of erupted lavas and their co-emitted gases (e.g., Gerlach, 2004; Moussallam et al., 2014; Oppenheimer et al., 2018; Moussallam et al., 2019), with only loose correlation between observed gas compositions and those predicted by degassing models (e.g., Moussallam et al., 2016). This is attributed to a combination of factors: observed chemistries being formed as an integrated signal of gases released at multiple depths/sources and reflecting a combination of closed- and open-system degassing (gas+melt moving together, vs gas separating from a moving melt, respectively); disequilibrium degassing, where eruptive rates are too rapid for melt-gas equilibrium to be achieved (see Pichavant et al., 2013); temperature effects, where gases which have undergone adiabatic cooling appear to oxidise relative to parent melts (Oppenheimer et al., 2018; Moussallam et al., 2019); or where volcanic gases have reacted with the atmosphere, forming high-temperature reaction mixtures (Martin et al., 2007).

Iacovino (2015) has shown that with sufficient petrological data, degassing models tuned specifically to a single volcanic system (Erebus in the case of Iacovino, 2015) can explain gas emission chemistry, by mixing open- and closed-system gas emissions produced at a variety of depths from a number of different magmatic sources. However, the level of petrological data required to achieve this level of model tuning is unrealistic for most volcanic systems, and inappropriate for modelling generic, planet-wide degassing chemistry.

1.4.2 Approaches to redox buffering of degassing melts in literature

The treatment of oxygen exchange and redox buffering during degassing is controversial, and has been approached in a number of ways. Firstly, gas chemistry can be considered by ignoring oxygen exchange between iron in the melt, and the gas phase. This approach has been taken by a number of published solubility models with decompression options, notably VolatileCalc (Newman and Lowenstein, 2002) and SolEx (Witham et al., 2012). It has also been used to discuss the effect of changing volcanic gas compositions on the GOE (Moussallam et al., 2019). When the buffering capacity of iron-born oxygen within the gas-melt system is ignored, models are liable to show a greater variation in redox during decompression than is realistic in natural systems, particularly when modelling sulfur-rich magmas.

At the opposite end of the spectrum, some studies and models treat the melt+gas system as ‘open’ to oxygen, treating it as a perfectly mobile component. This is the approach taken by Kadoya et al. (2020), along with the CHOSETTO model of Moretti et al. (2003) and Moretti and Papale (2004). Moretti and Papale (2004) chose to fix the $f\text{O}_2$ of the system to either a

Introduction

rock buffer such as NNO, a constant ferric to ferrous ($\text{FeO}/\text{Fe}_2\text{O}_3$) ratio, or a constant H_2S to SO_2 fugacity ratio (suitable for rhyolitic systems).

The middle ground approach is that taken by Burgisser and Scaillet (2007), Gaillard et al. (2011) and in this work, as described in Chapter 2. In this case the gas+melt system is considered to be ‘closed’ to oxygen, conserving mass balance while allowing oxygen to be exchanged between iron in the melt, and exsolved volatiles in the gas phase, keeping both melt and gas in redox equilibrium with each-other. It has been argued that it is unrealistic to consider a magmatic system ‘closed’ to oxygen (except in a few well-defined rhyolitic cases: Moretti and Papale, 2004; Moretti and Stefánsson, 2020; Moretti, 2021) without considering any external oxygen exchange with liquid and crystals, given the lack of knowledge regarding all the relevant redox couples buffering magmatic systems. However, it is unknown whether redox reactions between solid (wall-rock or crystals) and liquid (melt or gas) phases would occur on sufficiently rapid timescales during active decompression (as opposed to a stagnant silicate mush system degassing at depth for long periods of time, which decompression models are not suited to). Regardless, since neither crystallisation nor rock-wall interactions are otherwise considered in degassing models which utilise this approach, allowing oxygen exchange without other interactions would be inconsistent.

1.5 Overview of Thesis

Chapter 1: This chapter has introduced the concept of rocky exoplanets, how they are detected and the nature of their atmospheres. Previous studies have been outlined which focus on modelling volcanic outgassing in planetary contexts, and discussed the weaknesses of currently available degassing models when applied to exoplanets. Finally, this chapter examined the key processes which control the composition and speciation of volcanic gases, discussed the concept of oxygen fugacity in the context of degassing magmas, and summarised the various methods by which $f\text{O}_2$ can be included in degassing models.

Chapter 2: The computational models applied in Chapters 3 to 6, and the chemical and mathematical methods on which they are based, are described. Benchmarking and comparisons of the volcanic outgassing model, EVo, to other similar models are also shown.

Chapter 3: The extent to which volcanism can sustain a substantial fraction of hydrogen in the atmosphere of a terrestrial planet is assessed. Outgassing of H-rich volcanic gases is balanced with escape of hydrogen to space, determining the steady-state fraction of atmospheric hydrogen which can be maintained though volcanism alone. This chapter

focusses on the early Earth and early Mars, where high hydrogen contents could have counteracted the faint young Sun and enabled both warm surface temperatures, and origin-of-life chemistry.

Chapter 4: The appearance of a purely volcanic atmosphere is assessed, along with the extent to which information about the planet's interior can be retained and read from a volcanic atmosphere. A model allowing an atmosphere to build up through sustained release of volcanic gases over time is applied, with a range of starting mantle conditions. Classes are found for planets with Venus-like atmospheric temperatures, linking atmospheric composition and speciation to mantle fO_2 even after billions of years of layered volcanic emission.

Chapter 5: The widely adopted assumption that geologically-derived atmospheres can be modelled either by a state of constant thermochemical equilibrium, or as completely quenched regardless of temperature, is challenged. Chemical kinetics models are applied to the atmospheric compositions identified in Chapter 4, determining the temperatures below which volcanically-derived atmospheres will no longer return to thermochemical equilibrium upon cooling to ambient temperatures. Planets with atmospheric temperatures below 700 K should not be modelled while assuming thermochemical equilibrium, and their atmospheres may rather reflect higher-temperature, quenched speciation.

Chapter 6: The degree to which hydrogen escape affects the redox link between mantle and volcanic atmosphere is investigated. Hydrogen escape is applied to the atmospheric compositions defined in Chapter 4. Building on work in Chapter 3, now the chemical speciation of the entire atmosphere is modelled, as H₂ escape proceeds. This chapter shows how significant rates of escape can mask a mantle fO_2 signature within the atmosphere.

2

Models and Methods

This chapter describes the thermodynamic magma degassing model known as EVo, which was developed throughout the course of my PhD and forms the backbone of all the modelling presented in this thesis. In collaboration with my supervisor, I identified a gap in the available volcanic degassing models for the use case of modelling volcanism on other planets. As discussed in Section 1.3, the few models available to the scientific community for multispecies (i.e., beyond just C-O-H) degassing are often limited with respect to the wide range of T-P and redox conditions expected to be relevant for volcanic contexts beyond Earth. EVo (derived from ‘Exoplanet Volcanism’) was developed to specifically address many of these issues. Most importantly, (1) EVo is adapted to more accurately simulate highly reduced melts, by allowing for reduced carbon species (CO and CH₄) to be present as both gas-phase species and dissolved in the melt, as well as being able to deal with both graphite under- and over-saturated conditions; (2) EVo can be initialised using the total mass of each volatile element in the system, critical for isolating the effects of large $f\text{O}_2$ changes on degassing behaviour (see Section 2.1.2 – at the time of writing, EVo is the only published model which provides this functionality); and (3) the architecture of EVo allows for the selection of the most appropriate solubility laws for the scenario being modelled, by both providing a range of pre-implemented options, and enabling the relatively easy addition of new solubility laws to the model as and when they are released. As it has been developed in Python, EVo is also available cross-platform, unlike alternative models (e.g., Moretti et al., 2003; Burgisser et al., 2015) which are often restricted to Windows, and easy to build into pre-existing frameworks.

EVo is therefore a model developed for a dual purpose; both for use during my PhD work, and as a tool for the wider community. I have endeavoured to develop a model which is freely available, easily automated and adaptable for future developments. As such, some of the

Models and Methods

functionality described in this chapter has not been utilised in this thesis, but was developed to make EVo a more rounded tool for both the volcanological and planetary science community. Also described is EVolve, the atmospheric evolution model developed for Chapters 4 to 6.

2.1 EVo

EVo is designed to model the isothermal ascent of magma during eruption, assuming that magma degassing during ascent is primarily due to the resultant pressure change. A 3-phase system is used, where the silicate melt and the gas phase coexist in constant thermochemical equilibrium, alongside a solid graphite phase under sufficiently reduced conditions. The physical-chemical separation of gas and melt is implemented as being either impossible (closed-system), or instantaneous (open system - see Section 2.1.2). The highly complex nature of volcanic systems necessitates simplifications in my approach; crystallisation kinetics and sulfide formation (see Section 2.1.1) are neglected, so in those cases where precipitation of solids during ascent is important in driving degassing, EVo may underestimate the volume and composition of gases evolved from the melt.

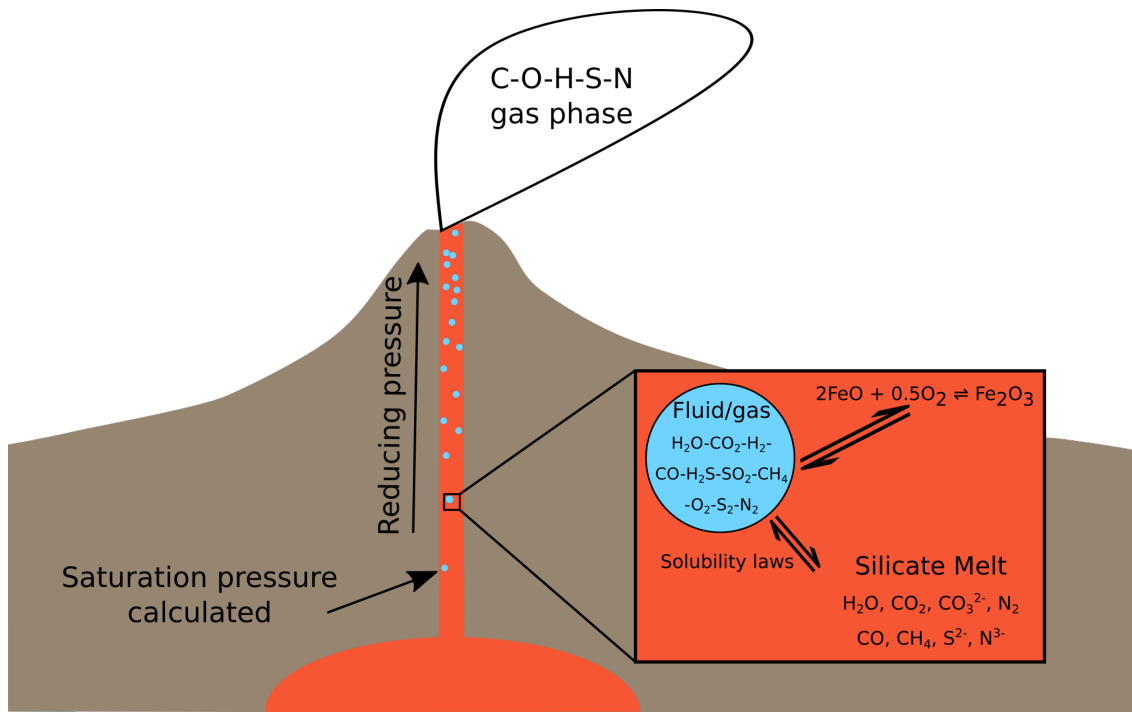


Fig. 2.1 A schematic overview of EVo, and its place in a physical system.

Figure 2.1 shows a schematic of how EVo represents a volcanic system, calculating the composition of the gas and melt phase at stages from the pressure of volatile saturation to the surface.

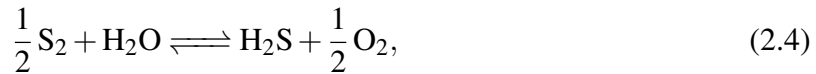
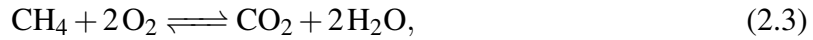
2.1.1 Overview of the chemical model

EVo computes the gas and melt volatile composition for systems of up to 5 volatile elements (C, O, H, S and N, in combinations of OH, COH, SOH, COHS and COHSN), using an ‘equilibrium constants and mass balance’ method first established by Holloway (1987) and used since by several degassing models, including Iacono-Marziano et al. (2012), Gaillard and Scaillet (2014), and Burgisser et al. (2015). As stated by Holloway (1987), this method “requires that enough equilibrium constant equations are used so that, when combined with the equation for mass balance, there are an equal number of equations and unknowns”. By combining the equilibrium constant equations which define homogenous gas-gas equilibria, and solubility laws which control heterogeneous gas-melt equilibria, at any given point the entire gas-melt system can be defined.

EVo considers 10 gas-phase species in the full COHSN system: H_2O , H_2 , O_2 , CO_2 , CO , CH_4 , S_2 , SO_2 , H_2S and N_2 . Subsets of these species are used in calculations if systems with fewer components are modelled, e.g., by definition the COH system does not include S or N-bearing species and so comprises just 6 gas-phase species. In a typical terrestrial volcanic gas, >99% (by mol) will be made up of H_2O , H_2 , CO_2 , SO_2 , H_2S and N_2 (Fischer and Chiodini, 2015), so the 10 species EVo considers are sufficient to model the bulk gas-phase chemistry, although it omits some trace species such as OCS which have been detected at various volcanoes (e.g., Mori and Notsu, 1997; Oppenheimer and Kyle, 2008; Sawyer et al., 2008). OCS in particular has been omitted due to the lack of solubility data in magmas. This reflects a limitation of this approach: even when the homogenous gas-phase equilibria are known (which for very many species they are), unless there is corresponding data for the solubility of a species in silicate liquids it cannot be included and a self-consistent solution be obtained.

Models and Methods

A set of five homogenous gas-phase equilibria, described in Eqs. (2.1) to (2.5), define the speciation of the gas phase



At thermochemical equilibrium, the abundance of each species in the gas phase are related to an equilibrium constant, K_i , one for each reaction in Eqs. (2.1) to (2.5). The general equation for these equilibria is given by



which has a general equilibrium constant reaction equation of

$$K_{2.6} = \frac{[\text{C}]^c [\text{D}]^d}{[\text{A}]^a [\text{B}]^b}, \quad (2.7)$$

where square brackets denote activity. For real gases, K_i can be calculated in terms of fugacity, f_i , so that for, e.g., Eq. (2.1)

$$K_1 = \frac{f_{\text{H}_2\text{O}}}{f_{\text{H}_2} f_{\text{O}_2}}^{0.5}. \quad (2.8)$$

The fugacity f_i of a real gas is an effective partial pressure, which replaces the mechanical partial pressure in an accurate computation of the chemical equilibrium constant. In EVo ideal mixing of real gases is assumed, so the fugacity of species i is defined as

$$f_i = \gamma_i P_i = \gamma_i X_i^v P, \quad (2.9)$$

where γ_i is the fugacity coefficient representing the deviation of the gas from ideality, so for an ideal gas $\gamma_i = 1$. P_i is the partial pressure of i , x_i^v is the mole fraction of i in the gas mixture, and P is the total pressure. x_i^v is such that when the gas phase is composed of n species, each with a mole fraction x_i^v ,

$$\sum_{i=1}^n X_i^v = 1. \quad (2.10)$$

The Lewis and Randall rule is applied to the calculation of γ_i , which states that the fugacity coefficient of species i in the gas mixture equals that of the pure species at the same pressure and temperature. The coefficients $\gamma_{\text{H}_2\text{O}}$, γ_{CO_2} and γ_{N_2} are from Holland and Powell (1991), γ_{H_2} is from Shaw and Wones (1964), and the remaining coefficients are from Shi and Saxena (1992). Coefficients taken from Shi and Saxena (1992) are only calibrated down to 1 bar. These coefficients are therefore set as $\gamma_i = 1$ for $P \leq 1$ – as gas behaviour tends to be increasingly ideal at lower pressures this is a valid assumption.

Calculating reaction constants

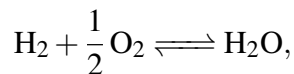
The equilibrium constants of reactions Eqs. (2.1) to (2.5) are calculated using the Gibbs free energy of the reaction as

$$\ln K = \frac{\Delta_r G^\circ}{-RT}. \quad (2.11)$$

$\Delta_r G^\circ$, the Gibbs free energy of reaction, is the difference between the Gibbs free energies of formation ($\Delta_f G^\circ$) for products and reactants *in their standard states*, thus:

$$\Delta_r G^\circ = \Delta_f G_{\text{products}}^\circ - \Delta_f G_{\text{reactants}}^\circ. \quad (2.12)$$

Therefore to calculate $\Delta_r G_1^\circ$, the Gibbs free energy of reaction Eq. (2.1):



$$\Delta_r G_1^\circ = \Delta_f G_{\text{H}_2\text{O}}^\circ - (\Delta_f G_{\text{H}_2}^\circ + 0.5\Delta_f G_{\text{O}_2}^\circ). \quad (2.13)$$

$\Delta_f G^\circ$ values are taken from the JANAF tables (Chase, 1998), with linear interpolation between temperatures using the NumPy ‘interp’ function (Harris et al., 2020). As equilibrium constants are pressure-independent, and EVo assumes decompression is isothermal, K values are only computed once, during the initial setup of a decompression calculation.

Volatile solubility and oxygen exchange

The solubility of a species is usually defined as the maximum concentration of a volatile which can remain in solution while co-existing with a pure gas phase of the same species. In a multicomponent system like that of EVo, it is assumed that the solubility of a species is related to the partial pressure/fugacity of the individual species i . Over the past 30 years a plethora of solubility laws, particularly for H_2O and CO_2 , have been developed. Different models for single species, or occasionally mixed $\text{H}_2\text{O}-\text{CO}_2$ volatiles are still being frequently introduced

Models and Methods

to the community; sometimes improvements based on new data, sometimes for a new P/T, $f\text{O}_2$, or silicate compositional regime. However, all these models are at least partially dependent on the abundance of the relevant species in the gas phase. In order to be as flexible as possible to different volcanic scenarios, and robust to future developments, EVo has been designed such that the user can select from a number of different solubility laws for various volatile species; it is also reasonably easy to add in additional solubility laws to a single file as they are released. In Table 2.1 below, the solubility laws for each species currently implemented in EVo are listed, along with the compositional, temperature, and pressure ranges they are calibrated for.

Table 2.1 The solubility laws implemented in EVo. The values listed here are strictly those used to calibrate the model – e.g., when using the Volatile-Calc spreadsheet temperatures of 600-1500 °C are allowed despite the solubility laws only being calibrated at 1200 °C. DC = D-Compress; VC-B = VolatileCalc Basalt simplification. ^a finds the sulfide capacity or dissolved sulfide/sulfate ratio in the melt, as discussed in Section 2.1.1.

Volatile	Publication	Melt Speciation	P (bar)	T (°C)	Melt Compositional range
H ₂ O	Burgisser et al. (2015) (DC)	H ₂ O _{mol}	163-3948 100-3950 250-2000	1200 825-1200 800-1000	Basalt: 48-50 wt% SiO ₂ Phonolite: 58 wt% SiO ₂ Rhyolite: 76-78 wt% SiO ₂
	Dixon (1997) (VC-B)	H ₂ O _{mol} , OH ⁻	0 - (1000-5000)	1200	Alkali Basalt: 40-49% SiO ₂
H ₂	Burgisser et al. (2015) (DC)	H ₂	220-265	700-1000	75 wt% SiO ₂
	Gaillard et al. (2003)	H ₂	220-265	800	75 wt% SiO ₂
CO ₂	Burgisser et al. (2015) (DC)	CO ₃ ²⁻	269-2059 1000-2000 500-3530	1200 850-1050 1100	Basalt: 48-50 wt% SiO ₂ Phonolite: 57 wt% SiO ₂ Rhyolite: 76-78 wt% SiO ₂
	Eguchi and Dasgupta (2018)	CO ₂ _{mol} , CO ₃ ²⁻ , graphite	500-30,000	950-1600	Foidite - Rhyolite: 39-77 wt% SiO ₂
Dixon (1997) (VC-B)	CO ₃ ²⁻	0 - (1000-5000)	1200	Alkali Basalt: 40-49 wt% SiO ₂	
	Dixon (1997)	CO ₃ ²⁻	0 - (1000-5000)	1200	Alkali Basalt: 40-49 wt% SiO ₂
CO	Armstrong et al. (2015)	C≡O complex	10-12,000	1400	46-62 wt% SiO ₂
CH ₄	Ardia et al. (2013)	CH ₄	7000-30,000	1400-1450	50-59 wt% SiO ₂
S ₂ ^a	O'Neill and Mavrogenes (2002)	S ²⁻	1	1400	40-70 wt% SiO ₂ , 1-18 wt% FeO
	O'Neill (2021)	S ²⁻	1	1200-1500	Unreported
N ₂	Libourel et al. (2003)	N ₂	1	950-1300	45-64 wt% SiO ₂ , 5-20 wt% FeO
				1400-1425	56-59 wt% SiO ₂

Models and Methods

As is also discussed in Iacobino et al. (2021) and Wieser et al. (2022) with respect to the development of VESIcal (a Python3 engine for using and comparing a range of H₂O and CO₂ solubility models), implementing the solubility laws which are published in academic papers is often problematic, particularly if the original work has not provided accompanying tools to benchmark against, given that some original manuscripts contain typos or formatting errors. Each of the solubility laws built into EVo are therefore provided in Appendix A; these laws are also found in the `solvability_laws.py` file, both for finding the abundance of a volatile in the melt based on gas phase fugacity, and for finding the reverse – the gas phase fugacity based on the concentration in the melt.

Both H and N form relatively simple binary volatile systems, present either in the gas phase, or dissolved in the silicate melt. However, C and S can both form additional phases: graphite in the case of carbon, and sulfide or anhydrite phases in the case of sulfur. In the case where graphite saturation occurs, CO₂ solubility is forced to be calculated with Eguchi and Dasgupta (2018), which can account for both graphite and fluid saturation within the same equation. Sulfur solubility, and the way EVo handles both C and S saturation is covered in Section 2.1.1.

EVo takes into account the way that iron dissolved in the melt affects the redox state of the magma by modelling the exchange of oxygen, according to



This reaction is not calculated using an equilibrium constant, but the ratio of the molar fractions of FeO and Fe₂O₃: $F = X_{\text{FeO}}/X_{\text{Fe}_2\text{O}_3}$. This can be calculated using Kress and Carmichael (1991), or in the case of iron rich magma (total Fe >15 wt%) the model of Righter et al. (2013) which is calibrated for Martian melts. This exchange of oxygen between the silicate melt and the gas phase means that redox equilibrium is always maintained in the system. The validity of this assumption has been discussed, see Sections 1.4.1 and 1.4.2.

Mass balance

As mentioned at the start of this section, the ‘mass balance and equilibrium constant’ method requires a set of mass balance equations along with the equilibrium constants already described. The total mass of each species in the magmatic system (W_{Ti}) is the sum its exsolved and dissolved components, thus

$$W_{Ti} = W_{gT} w_i^v + w_i^m. \quad (2.15)$$

W_{gT} is the total weight fraction of gas in the system, w_i^v is the weight fraction of species i in the gas phase, and w_i^m is the weight fraction of species i in the melt. w_i^m is calculated according to a

subset of the solubility laws listed in Table 2.1, and as such their dependencies differ according to the law and species in question; however, they are always dependent on the current pressure, and the fugacity of the corresponding species.

Mass conservation of volatile elements throughout the degassing process is enforced by keeping the total weight fraction of each element (W_{TH} , W_{TC} , W_{TO} , W_{TS} , W_{TN}) constant

$$\frac{W_{TO}}{M_O} = 2\frac{W_{TO_2}}{M_{O_2}} + 2\frac{W_{TH_2O}}{M_{H_2O}} + 2\frac{W_{TSO_2}}{M_{SO_2}} + 2\frac{W_{TCO_2}}{M_{CO_2}} + \frac{W_{TCO}}{M_{CO}} + \frac{W_{O(Fe)}}{M_O} \quad (2.16)$$

$$\frac{W_{TH}}{2M_H} = \frac{W_{TH_2}}{M_{H_2}} + \frac{W_{TH_2O}}{M_{H_2O}} + \frac{W_{TH_2S}}{M_{H_2S}} + 2\frac{W_{TCH_4}}{M_{CH_4}} \quad (2.17)$$

$$\frac{W_{TC}}{M_C} = \frac{W_{TCO_2}}{M_{CO_2}} + \frac{W_{TCO}}{M_{CO}} + \frac{W_{TCH_4}}{M_{CH_4}} + \frac{W_{C(graph)}}{M_C} \quad (2.18)$$

$$\frac{W_{TS}}{M_S} = \frac{W_{TH_2S}}{M_{H_2S}} + \frac{W_{TSO_2}}{M_{SO_2}} + 2\frac{W_{TS_2}}{M_{S_2}} \quad (2.19)$$

$$\frac{W_{TN}}{M_N} = 2\frac{W_{TN_2}}{M_{N_2}} \quad (2.20)$$

where W_{Ti} for each volatile species (not element) is calculated using Eq. (2.15), M_i is the molecular mass of species i , $W_{O(Fe)}$ is the weight fraction of oxygen held in iron ($\text{FeO}/\text{Fe}_2\text{O}_3$) within the melt, and $W_{C(graph)}$ is the mass of graphite in the system (see Section 2.1.1).

In order to solve for the state of the magmatic system at a given temperature and pressure, equations for chemical equilibrium (2.1) to (2.5) and (2.14), solubility laws (Table 2.1) and mass conservation (2.10) and (2.16) to (2.20) are used jointly to algebraically reduce the system down to the smallest number of equations. In the case of the COHSN system, this is 4, which requires four variables to be solved for (X_{CO} , X_{S_2} , X_{O_2} and X_{N_2}). An example of how these equations are derived and then solved is shown for the COHSN system in Section 2.1.1. It is the case that the number of equations, and therefore variables, is always $n - 1$ for n number of volatile elements involved. These reduced equations are solved simultaneously, using an iterative method from the SciPy python package (Virtanen et al., 2020), conserving the mass fraction of each volatile element to a precision of 1×10^{-5} .

Once a solution has been found for the speciation of the system at a single pressure, the volume of the gas phase (v) is calculated using

$$v = \left[1 + \frac{\mu P(1 - W_{gT})}{RT\rho_l W_{gT}} \right]^{-1}, \quad (2.21)$$

R is the universal gas constant (8.3144 J/mol K), ρ_l is the volatile-free melt density, calculated according to Lesher and Spera (2015), and μ is the mean molecular weight of the gas phase,

Models and Methods

calculated as

$$\mu = \sum_{i=1}^{10} X_i M_i. \quad (2.22)$$

Example of solving equations for the COHSN system

This section shows a worked example of how the full system of equations is algebraically reduced down to the four equations iterated to solve the system. In the COHSN system, the gas phase is made up of 10 species, in equilibrium at all times according to

$$\begin{aligned} K_1 &= \frac{f_{\text{H}_2\text{O}}}{f_{\text{H}_2} \cdot \sqrt{f_{\text{O}_2}}} & K_2 &= \frac{f_{\text{CO}_2}}{f_{\text{CO}} \cdot \sqrt{f_{\text{O}_2}}} \\ K_3 &= \frac{f_{\text{CO}_2} \cdot f_{\text{H}_2\text{O}}^2}{f_{\text{CH}_4} \cdot f_{\text{O}_2}^2} & K_4 &= \frac{f_{\text{H}_2\text{S}} \cdot \sqrt{f_{\text{O}_2}}}{f_{\text{H}_2\text{O}} \cdot \sqrt{f_{\text{S}_2}}} \\ K_5 &= \frac{f_{\text{SO}_2}}{f_{\text{O}_2} \sqrt{f_{\text{S}_2}}}, \end{aligned}$$

where f_i is calculated according to Eq. (2.9). The variables to solve for are X_{CO} , X_{S_2} , X_{O_2} and X_{N_2} , so the first aim is to calculate the mole fractions of all other species in terms of these 4 variables (written in blue, with derived species in red):

$$\begin{aligned} X_{\text{CO}_2} &= \frac{K_2 \gamma_{\text{CO}} \textcolor{blue}{X}_{\text{CO}} \sqrt{\gamma_{\text{O}_2} \textcolor{blue}{X}_{\text{O}_2} P}}{\gamma_{\text{CO}_2}} & X_{\text{SO}_2} &= \frac{K_5 \gamma_{\text{O}_2} \textcolor{blue}{X}_{\text{O}_2} \sqrt{\gamma_{\text{S}_2} \textcolor{blue}{X}_{\text{S}_2} P}}{\gamma_{\text{SO}_2}} \\ a &= \frac{\gamma_{\text{CO}_2} \textcolor{red}{X}_{\text{CO}_2} \gamma_{\text{H}_2\text{O}}^2}{K_3 \gamma_{\text{CH}_4} \sqrt{\gamma_{\text{O}_2} \textcolor{blue}{X}_{\text{O}_2}}} \\ b &= \frac{\gamma_{\text{H}_2\text{O}}}{K_1 \gamma_{\text{H}_2} \sqrt{\gamma_{\text{O}_2} \textcolor{blue}{X}_{\text{O}_2}}} + \frac{K_4 \gamma_{\text{H}_2\text{O}} \sqrt{\gamma_{\text{S}_2} \textcolor{blue}{X}_{\text{S}_2}}}{\gamma_{\text{H}_2\text{S}} \sqrt{\gamma_{\text{O}_2} \textcolor{blue}{X}_{\text{O}_2}}} + 1 \\ c &= -(1 - \textcolor{blue}{X}_{\text{CO}} - \textcolor{blue}{X}_{\text{S}_2} - \textcolor{blue}{X}_{\text{O}_2} - \textcolor{blue}{X}_{\text{N}_2} - \textcolor{red}{X}_{\text{CO}_2} - \textcolor{red}{X}_{\text{SO}_2}) \\ \textcolor{red}{X}_{\text{H}_2\text{O}} &= \frac{-b + \sqrt{b^2 - (4ac)}}{2a} \end{aligned}$$

Note that $X_{\text{H}_2\text{O}}$ is calculated by rearranging equations for K_1 , K_3 and K_4 in terms of f_{H_2} , f_{CH_4} and $f_{\text{H}_2\text{S}}$ respectively, and substituting these equations into Eq. (2.10) such that

$$X_{\text{H}_2} + X_{\text{CH}_4} + X_{\text{H}_2\text{S}} = 1 - (\textcolor{blue}{X}_{\text{O}_2} + \textcolor{blue}{X}_{\text{CO}} + \textcolor{blue}{X}_{\text{S}_2} + \textcolor{blue}{X}_{\text{N}_2} + \textcolor{red}{X}_{\text{CO}_2} + \textcolor{red}{X}_{\text{SO}_2}).$$

This is re-arranged into quadratic form for $X_{\text{H}_2\text{O}}$, and solved using the quadratic formula.

$$\begin{aligned} X_{\text{H}_2} &= \frac{\gamma_{\text{H}_2\text{O}} X_{\text{H}_2\text{O}}}{K_1 \gamma_{\text{H}_2} \sqrt{\gamma_{\text{O}_2} X_{\text{O}_2} P}} \\ X_{\text{CH}_4} &= \frac{\gamma_{\text{CO}_2} X_{\text{CO}_2} \sqrt{\gamma_{\text{H}_2\text{O}} X_{\text{H}_2\text{O}}}}{K_3 \gamma_{\text{CH}_4} (\gamma_{\text{O}_2} X_{\text{O}_2})^2} \\ X_{\text{H}_2\text{S}} &= \frac{K_4 \gamma_{\text{H}_2\text{O}} X_{\text{H}_2\text{O}} \sqrt{\gamma_{\text{S}_2} X_{\text{S}_2}}}{\gamma_{\text{H}_2\text{S}} \sqrt{\gamma_{\text{O}_2} X_{\text{O}_2}}} \end{aligned}$$

At this point, all 10 species in the gas phase can be described in terms of the 4 variables being solved for. As decompression occurs, mass conservation requires that the total amounts of each volatile element (COHSN) in the system remains constant. These mass conservation equations are set out in Eqs. (2.16) to (2.20). In order to use the molar fractions derived above in Eq. (2.15), to replace the total amounts of each species W_{Ti} in Eqs. (2.16) to (2.20), the molar fraction must be converted to weight fractions using

$$w_i = \frac{X_i M_i}{\sum_j X_j M_j}, \quad (2.23)$$

and the mass of the volatile dissolved in the melt must be calculated. Substituting Eq. (2.23) and solubility laws into Eq. (2.15) gives

$$W_{Ti} = W_{gT} \frac{X_i M_i}{\sum_j X_j M_j} + w_i^m(X_i, P, T\dots), \quad (2.24)$$

where $w_i^m(\dots)$ denotes the solubility law for species i , which is dependent on X_i , the pressure and temperature of the system, and in some cases other variables such as the $f\text{O}_2$ or silicate melt chemistry. $w_i^m(\dots)$ returns the weight fraction of the species in the melt. These functions for each of the solubility laws currently implemented in EVo are listed in Appendix A. As the gas weight fraction W_{gT} is the final unknown in the system, one of the mass conservation equations from Eqs. (2.16) to (2.20) is re-arranged in terms of $W_{gT} / \sum_j X_j M_j$, thereby reducing the number of equations to solve down to 4. In the COHSN system, the conservation equation for nitrogen (Eq. (2.20)) is chosen, re-arranged to be substituted into the remaining conservation equations as

$$\mathcal{N} = W_{gT} / \sum_j X_j M_j = \frac{W_{TN}/M_{\text{N}} - w_{\text{N}_2}^m(X_{\text{N}_2}, X_{\text{O}_2}, P)/M_{\text{N}_2}}{2 X_{\text{N}_2}}. \quad (2.25)$$

Models and Methods

The system of 4 equations to be solved simultaneously can now be derived:

$$\frac{W_{TO}}{M_O} = \mathcal{N}(2X_{O_2} + 2X_{SO_2} + X_{H_2O} + X_{CO} + 2X_{CO_2}) + \frac{w_{H_2O}^m(X_{H_2O}, P)}{M_{H_2O}} + \frac{2w_{CO_2}^m(X_{CO_2}, X_{O_2}, P, T, melt)}{M_{CO_2}} + \frac{w_{CO}^m(X_{CO}, P)}{M_{CO}} + \frac{W_{O(Fe)}}{M_O}, \quad (2.26)$$

$$\frac{W_{TH}}{2M_H} = \mathcal{N}(X_{H_2O} + X_{H_2} + X_{H_2S} + 2X_{CH_4}) + \frac{w_{H_2}^m(X_{H_2}, P)}{M_{H_2}} + w_{H_2O}^m(X_{H_2O}, P)M_{H_2O} + \frac{2w_{CH_4}^m(X_{CH_4}, P)}{M_{CH_4}}, \quad (2.27)$$

$$\frac{M_{TS}}{M_S} = \mathcal{N}(X_{SO_2} + X_{H_2S} + 2X_{S_2}) + \frac{w_{S^{2-}}^m(X_{S_2}, X_{O_2}, P, T, melt)}{M_S} + \frac{w_{S^{6+}}^m(X_{S_2}, X_{O_2}, P, T, melt)}{M_S}, \quad (2.28)$$

$$\frac{W_{TC}}{W_C} = \mathcal{N}(X_{CO} + X_{CO_2} + X_{CH_4}) + \frac{w_{CO_2}^m(X_{CO_2}, X_{O_2}, T, melt)}{M_{CO_2}} + \frac{w_{CO}^m(X_{CO}, P)}{M_{CO}} + \frac{w_{CH_4}^m(X_{CH_4}, P)}{M_{CH_4}}, \quad (2.29)$$

where *melt* is the major element composition of the silicate melt, and $W_{O(Fe)}$ is the weight fraction of oxygen tied up in FeO and Fe_2O_3 within the silicate melt. This is controlled by the fO_2 of the system, and is calculated by finding F , the ratio of FeO/ Fe_2O_3 in the melt, using either Kress and Carmichael (1991) or Righter et al. (2013), then

$$W_{O(Fe)} = M_O \frac{W_{Fe}}{M_{Fe}} \frac{1+3F}{1+2F}. \quad (2.30)$$

These four equations are solved numerically using the SciPy optimize.fsolve function, formulated as a vector equality

$$\begin{pmatrix} [W_O] \\ [W_H] \\ [W_S] \\ [W_C] \end{pmatrix} - \begin{pmatrix} [W_O]_{predicted}(X_{O_2}, X_{CO}, X_{S_2}, X_{N_2}) \\ [W_H]_{predicted}(X_{O_2}, X_{CO}, X_{S_2}, X_{N_2}) \\ [W_S]_{predicted}(X_{O_2}, X_{CO}, X_{S_2}, X_{N_2}) \\ [W_C]_{predicted}(X_{O_2}, X_{CO}, X_{S_2}, X_{N_2}) \end{pmatrix} = \begin{pmatrix} 0 \\ 0 \\ 0 \\ 0 \end{pmatrix}. \quad (2.31)$$

The `fsolve` function makes an initial guess of the value for the vector $\begin{pmatrix} X_{O_2} \\ X_{CO} \\ X_{S_2} \\ X_{N_2} \end{pmatrix}$, and then iterates, refining the guesses as appropriate until a solution is found. As the pressure is decreased in steps by EVo, the initial guess for each new pressure is the solution to the previous step. For the starting pressure, the entire system is constrained, so iteration is not required (see Section 2.1.2 for details on how this is achieved).

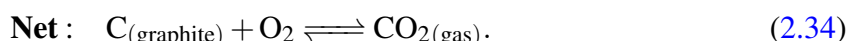
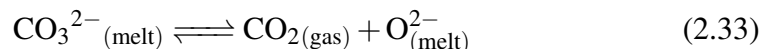
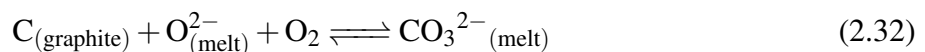
Handling additional phases: carbon and sulfur

The base degassing model described above deals with the case where there are 2 phases present: the silicate melt, containing a fraction of dissolved volatiles; and an exsolved gas phase. However, in the case of both C and S, additional phases can form outside of this 2-phase system. Here I describe how EVo handles these scenarios.

Carbon

A carbon-bearing system can become graphite saturated at low f_{O_2} (or, alternatively, diamond saturated at very high pressures Holloway et al., 1992; LaTourrette and Holloway, 1994; Frost and Wood, 1997). Figure 2.2 shows a simplified C-O magmatic system, illustrating the relationship between graphite and other phases. Note that EVo includes H which also interacts with C as CH_4 ; however this has been excluded from Fig. 2.2 to clarify the relationship between graphite and the melt/volatile phase. As is discussed further in Section 2.2.2, at highly reduced conditions C may also be soluble in the silicate melt as a range of O and H-bearing species; however, as the species and reactions involved are still highly debated these have also been left off Fig. 2.2.

In a graphite-saturated melt, the f_{CO_2} of the system is controlled by



As graphite is a pure, solid phase, it has a chemical activity of 1. The equilibrium constant equation for Eq. (2.34) is therefore written as

$$K_C = \frac{f_{CO_2}}{f_{O_2}}, \quad (2.34a)$$

Models and Methods

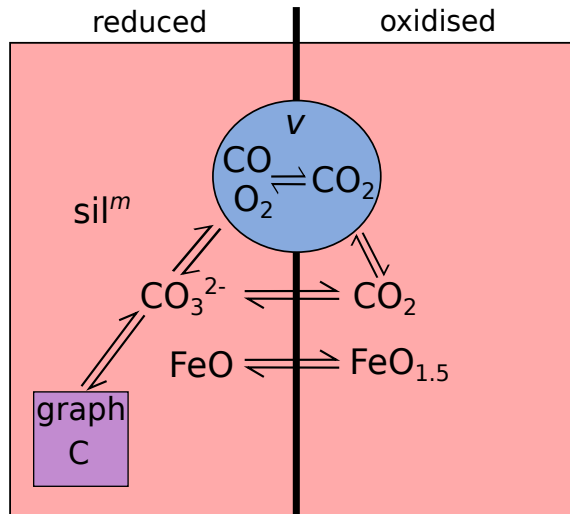


Fig. 2.2 A simple diagram of the C-O system in silicate melts. Each colour represents a different phase (gas/volatile (v), silicate melt (m) and a precipitated graphite phase). Phases and species which dominate under reducing conditions are to the left, while those which dominate under oxidising conditions are to the right. Two-way arrows indicate species that can interact within, and between different, phases.

showing that in a graphite saturated melt, f_{CO_2} is entirely controlled by the $f\text{O}_2$ of the melt (Holloway et al., 1992). K_C is calculated according to the equation of Holloway et al. (1992),

$$\log_{10} K_C = 40.07639 - 2.53932 \times 10^{-2} \cdot T + 5.27096 \times 10^{-6} \cdot T^2 + 0.0267 \cdot (P - 1)/T, \quad (2.35)$$

with T in Kelvin and P in bar.

The silicate system in EVo is checked for graphite saturation by comparing the value of f_{CO_2} as calculated using the main model as described above (which assumes no graphite saturation), to that calculated using Eq. (2.34a) ($f_{\text{CO}_2,\text{graphite}}$). If $f_{\text{CO}_2,\text{graphite}} < f_{\text{CO}_2}$, then the melt must be graphite saturated (e.g., see Fig 7b of Eguchi and Dasgupta, 2018). If graphite saturation is found, EVo then forces the use of the Eguchi and Dasgupta (2018) model for CO_2 solubility. The thermodynamics and structure of this model mean that it is applicable under both graphite and fluid saturated conditions, unlike the other option implemented in EVo, and can therefore be fed either $f_{\text{CO}_2,\text{graphite}}$ or f_{CO_2} .

Graphite saturation is only implemented in the ‘closed system’ degassing option; because in a closed system material cannot be removed, any graphite present in the melt at volatile saturation is assumed to decompress with the rest of the gas-melt system. The separate graphite phase decompresses with the gas-melt system, gradually depleting as carbon is degassed into the gas phase and the graphite phase replenishes the carbon dissolved in the melt (see Fig. 2.2). Graphite exhaustion (where the melt becomes graphite under-saturated) is detected if, to solve

for a graphite saturated system, the graphite mass in the system must be negative. The system is first checked for graphite saturation during the setup of the system, and then after every pressure step if the system is not known to already be graphite-saturated.

When solving for a graphite-saturated system, the fugacity of all 3 carbon-bearing species can be determined solely using the fO_2 and Eq. (2.34a). This removes an extra unknown from all systems containing carbon; in the example shown in Section 2.1.1, Eq. (2.29) is no longer used, and X_{CO} is no longer a variable being solved for. The mass of the carbon reservoir is calculated as the difference between the total mass of carbon in the system and the mass calculated as being present in the gas and dissolved in the silicate melt.

Sulfur

As with carbon, the sulfur system has added complexities in that additional phases can form alongside the two accounted for in EVO (the silicate melt and gas phase). However, unlike with graphite saturation, there are two additional phases which have to be considered, the abundances of which vary according to fO_2 . The simplified system is shown in Fig. 2.3a, which similarly to Fig. 2.2 shows an idealised S-O system, excluding H.

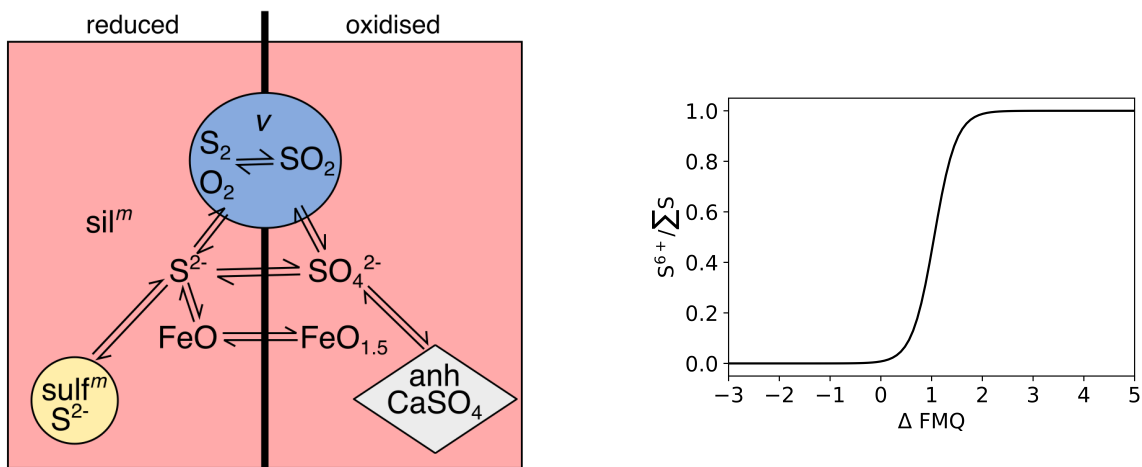
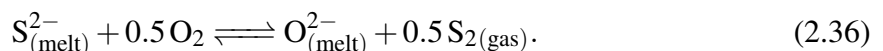


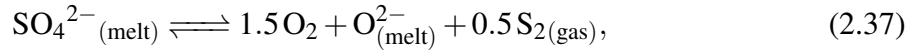
Fig. 2.3 (a) A simple diagram of the S-O system in silicate melts. Each colour represents a different phase. Phases and species which dominate under reducing conditions are to the left, while those which dominate under oxidising conditions are to the right. Two-way arrows indicate species that can interact within, and between different, phases. Taken from Hughes et al. (2021). (b) Sulfur speciation as a function of oxygen fugacity, after Jugo et al. (2010).

Under reducing conditions (approximately $<FMQ$, see Fig. 2.3b) sulfur dissolves in silicate melts as S^{2-} :



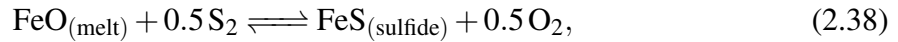
Models and Methods

By comparison, under oxidised conditions, sulfur dissolves in the melt as SO_4^{2-} through



where sulfur is instead in its S^{6+} state (Paris et al., 2001). It is well established from experimental studies that a silicate melt can contain S dissolved as one, the other, or both S^{2-} and S^{6+} across the $f\text{O}_2$ range of terrestrial magmas (Carroll and Rutherford, 1988; Nilsson and Peach, 1993; Metrich and Clocchiatti, 1996). Magma produced on other planets across the solar system is thought to have an $f\text{O}_2$ which is less than the $f\text{O}_2$ of terrestrial mid-ocean ridge basalts (MORB, e.g., Schmidt et al., 2013b; Zolotov et al., 2013), which is well within the S^{2-} stability field and is therefore expected to contain minimal S^{6+} .

When a magma becomes sulfur-saturated, the phase precipitated is $f\text{O}_2$ dependent. A melt can become sulfide (S^{2-}) saturated



or sulfate (SO_4^{2-}) saturated (usually speciated as anhydrite, CaSO_4). Silicate melts can also be multiply saturated with sulfide + sulfate \pm gas, resulting in a sulfur solubility maximum (Jugo, 2009; Hughes et al., 2021), with a corresponding solubility minimum where both S^{2-} and S^{6+} are dissolved in approximately equal concentrations (Hughes et al., 2021). Due to the complexity of the sulfur system and the fact that the additional sulfide/sulfate phases are not pure S (as is the case for graphite), EVo follows the convention of other multi-component degassing models by not simulating magmas which are sulfur-saturated, in either phase (e.g., CHOSETTO, D-Compress: Moretti et al., 2003; Burgisser et al., 2015). Instead, EVo only deals with sulfur in the gas phase (speciated as S_2 , SO_2 or H_2S), and dissolved in the melt as either S^{2-} or S^{6+} .

The dissolution of S_2 into a silicate melt has been shown experimentally to follow Eq. (2.36) (O'Neill and Mavrogenes, 2002; O'Neill, 2021). As the $\text{O}_{\text{(melt)}}^{2-}$ is viewed as a ‘structural element’ with abundances far greater than that of S^{2-} , Eq. (2.36) can define the solubility law for S_2 as

$$C_{\text{S}^{2-}} = w_{\text{S}^{2-}}^m \cdot \left(\frac{f_{\text{O}_2}}{f_{\text{S}_2}} \right)^{0.5} \quad (2.39)$$

where $C_{\text{S}^{2-}}$ is the ‘sulfide capacity’ of the melt (Fincham et al., 1954), analogous to the equilibrium constant K of Eq. (2.36). $C_{\text{S}^{2-}}$ is highly compositionally dependent and can, for given pressure and temperature conditions, be reformulated as a constant for a given melt composition. Those parameterisations for $C_{\text{S}^{2-}}$ which are implemented as options in EVo are

listed in Table 2.1. While Eq. (2.37) can similarly be re-arranged to generate a sulfate capacity $C_{S^{6+}}$ (Fincham et al., 1954)

$$C_{S^{6+}} = w_{S^{6+}}^m (f_{S_2} f_{O_2}^3)^{-0.5}, \quad (2.40)$$

at the time of writing no experimental validation (on magmatically relevant silicate compositions), nor expressions equivalent to those provided by, e.g., O'Neill (2021) for $C_{S^{2-}}$ have been published – although results mentioned in abstract (O'Neill and Mavrogenes, 2019) confirm the relationship and suggest an expression for $C_{S^{6+}}$ may be forthcoming. To determine the amount of S^{6+} in the melt, EVo instead uses Nash et al. (2019) which calculates the ratio of S^{6+}/S^{2-} as

$$\log_{10} \left(\frac{w_{S^{6+}}^m}{w_{S^{2-}}^m} \right) = 8 \log_{10} \left(\frac{w_{Fe^{3+}}^m}{w_{Fe^{2+}}^m} \right) + \frac{8.7436 \times 10^6}{T^2} - \frac{27703}{T} + 20.273, \quad (2.41)$$

for temperatures (T) of 1000 - 2000 K.

The amount of S^{2-} which can be dissolved in a silicate melt at sulfide saturation, controlled by Eq. (2.38), is referred to as the “Sulfide Content at Sulfide Saturation”, or SCSS. The SCSS has been extensively studied over the past few decades (O'Neill and Mavrogenes, 2002; Liu et al., 2007; Fortin et al., 2015; Wykes et al., 2015; Smythe et al., 2017; O'Neill, 2021), and in EVo is calculated using the model of Liu et al. (2007). EVo checks for sulfide saturation by comparing $w_{S^{2-}}^m$ as calculated using Eq. (2.39) to the SCSS. If $w_{S^{2-}}^m \geq$ SCSS, then the melt is sulfide saturated and EVo produces a warning stating that sulfide saturation has been reached, and the model is no longer valid.

2.1.2 Run types, set-up options and input parameters

Two different run types can be performed while calculating a decompression path: “Closed system” or “Open system”. Closed-system runs, the default, assume that the gas is in equilibrium with the melt and there is no physical-chemical separation between the two phases. This models a system where the gas bubbles are entrained in the melt and rise at the same speed as the magma.

In open-system degassing, a fraction of the gas released as a magma decompresses is assumed to be lost (or chemically isolated) from the melt as it is produced, mimicking a scenario where gas bubbles rise to the surface through a magma. EVo simulates this by resetting the gas fraction after every pressure step

$$W_{gT}(P - dP) = aW_{gT}, \quad (2.42)$$

Models and Methods

Table 2.2 EVo input options when P_{start} is known, dependent on the volatile system being used. (Fe) indicates that each system can be run with or without oxygen exchange with the melt, this does not affect how the run is set up. *Theoretically possible, but as yet not implemented as this is an unusual way of running a degassing model.

Run Type	Non-optional values	Optional values (only 1 column per run)	
		Gas fugacities	Melt weight fractions
OH(Fe)	T, P_{start}, W_{gT}	Either f_{H_2} OR f_{O_2}	N/A
COH(Fe)	T, P_{start} and W_{gT} and either f_{H_2} OR f_{O_2}	$f_{H_2}O$ OR f_{CO_2}	One from $w_{H_2O}^m, w_{CO_2}^m$ or $w_{graphite}^m$
SOH(Fe)	T, P_{start} and W_{gT} and either f_{H_2} OR f_{O_2}	N/A*	$w_{H_2O}^m$ OR w_S^m
COHS(Fe)	T, P_{start} and W_{gT} and either f_{H_2} OR f_{O_2}	N/A*	Two from $w_{H_2O}^m, w_{CO_2}^m$, $w_{graphite}^m$ and w_S^m
COHSN(Fe)	T, P_{start} and W_{gT} and either f_{H_2} OR f_{O_2}	N/A*	Three from $w_{H_2O}^m, w_{CO_2}^m$, $w_{graphite}^m, w_S^m$ and $w_{N_2}^m$

where dP is the pressure step (bar) and a is the fraction of the gas phase which is removed from the system after each increment (using a rather than fully removing all exsolved volatiles allows for an exploration of efficient vs inefficient open-system degassing). Once W_{gT} has been reset, the new masses of the volatile elements left in the system are calculated before the pressure is incremented. EVo tracks the evolution of the magma as a function of pressure in this scenario, and does not track the accumulated composition of the degassed volatiles, although it does provide the chemistry of the instantaneous exsolved gas phase at each pressure step.

There are three different options which can be used to set-up EVo for a decompression calculation, discussed below. These options can also be used to find the equilibrium conditions at a single pressure, either at a set pressure using option (1), or the volatile saturation pressure, found using either (2) or (3).

1) Where P_{start} and W_{gT} are known

Where the gas mass fraction is known at the pressure of interest (either for the start of a degassing run or to calculate the composition at a single point), along with the temperature, the state of the system can be found using a subset of additional parameters as described in Table 2.2.

Using these input values, all other relevant parameters for the initial conditions can be calculated. Where a melt weight fraction of a volatile is provided, the respective fugacity is calculated using the solubility laws.

Solubility models usually provide analytical expressions for the concentration of a volatile species dissolved in a magma as a function of either partial pressure, or fugacity. Analytical expression for the inverse (calculating the fugacity of a species given the concentration dissolved in the melt) are usually not provided, and in some cases cannot be found by simple re-arrangement (see Appendix A); in these cases (both the models of Dixon (1997) and Eguchi and Dasgupta (2018)) numerical methods are used to obtain the correct fugacity.

The 1-4 fugacities (depending on the number of elements considered), P, T, reactions Eqs. (2.1) to (2.5) and Eq. (2.10) are then used algebraically to find all X_i and f_i . Once all molar fractions have been calculated, the masses of each element in the system can be computed (Eqs. (2.16) to (2.20)), along with the mass of oxygen fixed by FeO* using Eq. (2.30).

2) Calculating P_{sat} , the volatile saturation pressure

In many scenarios, having to specify a starting pressure and gas fraction in order to model a decompression path is inconvenient, as these variables are often unknown. Instead, it is preferable to calculate the saturation pressure for a given system volatile content (e.g., the H₂O and CO₂ concentration of the melt prior to the onset of degassing), and start the decompression from there. EVo allows this setup option by asking for the $f\text{O}_2$ at the point of volatile saturation (usually taken to be the $f\text{O}_2$ of the magma source), and the undegassed volatile content of the melt.

When the saturation pressure of a magma with a given dissolved volatile concentration is found, the following equality holds:

$$\sum_{i=1} P_i - P = 0 \quad (2.43)$$

where P is the total pressure and P_i is the partial pressure of species i calculated according to its corresponding solubility law, for a fixed concentration in the melt. The saturation pressure is found by numerically solving Eq. (2.43) for P , where

$$P_i = \frac{f_i(w_i^m, P \dots)}{\gamma_i}, \quad (2.44)$$

using the Brent method as implemented in SciPy (Virtanen et al., 2020). This method was chosen as it allows the solution to be bracketed; this prevents the numerical solver guessing a negative pressure which is invalid within the inverted solubility laws. Once P_{sat} has been

Models and Methods

found, W_{gT} is set to 1×10^{-6} wt% (an arbitrarily small number sufficiently close to zero to not affect the results but successfully initialise the calculation), the atomic volatile masses in the system are calculated as in Eqs. (2.16) to (2.20) and decompression steps can commence.

3) Calculating P_{sat} and volatile speciation

The above two setup options work well for use-cases such as modelling the degassing path of volcanic samples, or single volcanic systems where the starting conditions (e.g., fO_2 , volatile content) are similar. However, in the work presented in this thesis a key component is comparing the gas phase/atmospheres produced when the only variable is the starting fO_2 . In set-up options 1 & 2, this poses a problem when dealing with volatile elements which exist as multiple dissolved species, particularly for H and C.

Using the simple case of the $H_2O-O_2-H_2$ system, H in the melt can be dissolved either as H_2O , or H_2 , although in oxidised to moderately reduced magmas, as seen on Earth, the H_2 component is minimal. A fixed magmatic H_2O content imposes a constant f_{H_2O} ; since the fO_2 is being lowered, f_{H_2} must increase to maintain equilibrium. A greater f_{H_2} also enforces a higher magma H₂ content; therefore, as the fO_2 of a magma is decreased with a fixed H_2O content, the dissolved H₂ must increase proportionally (Fig. 2.4).

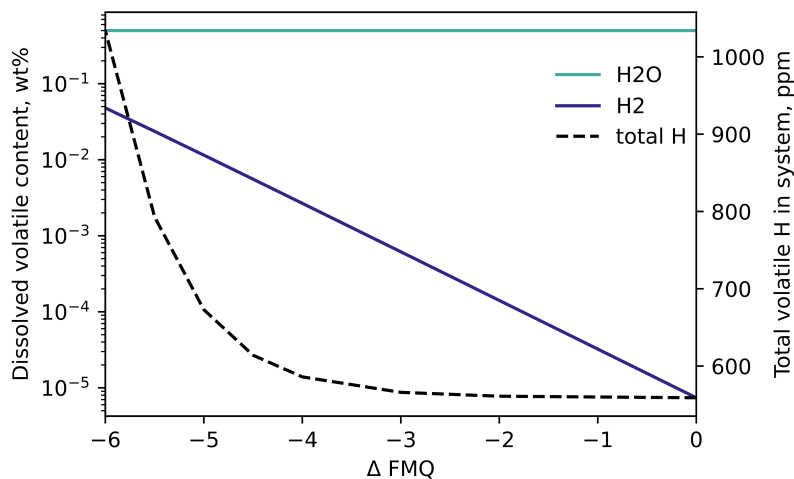


Fig. 2.4 The mass of H_2O , H_2 and total H in the silicate melt at volatile saturation, when the enforced saturation conditions are fO_2 and the dissolved H_2O content.

When comparing degassing regimes where the fO_2 is varied, Fig. 2.4 shows it is not sufficient to simply fix the magma volatile content using a single species. E.g., volcanic gases released at FMQ compared to FMQ-6 in Fig. 2.4 cannot be directly compared, as the more reduced scenario has almost double the amount of H dissolved in the melt at the point of

volatile saturation, hence the fO_2 is not the only factor being varied. Instead, for meaningful isolation of the effects of fO_2 changes alone, the *total mass of each volatile element* must be enforced, with the speciation at volatile saturation allowed to vary freely according to the fO_2 conditions.

Similarly to set-up option 2, this is solved numerically. EVo is initialised with the fO_2 at volatile saturation, and the total atomic masses of each volatile element in the system. The solver then guesses the proportion of each element which is dissolved as H_2O , CO_2 , S^{2-} and N_2 , with the remainder dissolved as other species, or in the gas phase (which is minimal at volatile saturation, but relevant in order for the system of equations to work). As in the main model, a system of 4 equations (for the COHSN system) is solved simultaneously:

$$\begin{pmatrix} [W_H]_{set} \\ [W_C]_{set} \\ [W_S]_{set} \\ [W_N]_{set} \end{pmatrix} - \begin{pmatrix} [W_H]_{predicted}(w_{H_2O}^m, w_{CO_2}^m, w_{S^{2-}}^m, w_{N_2}^m) \\ [W_C]_{predicted}(w_{H_2O}^m, w_{CO_2}^m, w_{S^{2-}}^m, w_{N_2}^m) \\ [W_S]_{predicted}(w_{H_2O}^m, w_{CO_2}^m, w_{S^{2-}}^m, w_{N_2}^m) \\ [W_N]_{predicted}(w_{H_2O}^m, w_{CO_2}^m, w_{S^{2-}}^m, w_{N_2}^m) \end{pmatrix} = \begin{pmatrix} 0 \\ 0 \\ 0 \\ 0 \end{pmatrix}. \quad (2.45)$$

This is similar in form to Eq. (2.31), but in this case the variables are the mass fractions of dissolved volatiles, rather than the molar fractions of species in the gas phase. When a guess is made for Eq. (2.45) (structured as the vector $\begin{pmatrix} w_{H_2O}^m \\ w_{CO_2}^m \\ w_{S^{2-}}^m \\ w_{N_2}^m \end{pmatrix}$), it is first passed to Eq. (2.43) to find the saturation pressure, P_{sat} , before the $[W_i]_{predicted}$ values are calculated. The key difference between this setup option and options 1 & 2 is that in this case the mass of each element in the system is known and the speciation is calculated; in the previous cases a subset of the melt or gas phase speciation is known and the solution finds the total masses of each element.

2.1.3 Benchmarking

During the development of EVo, individual elements of the model were each tested to ensure correct implementation. For example, the Kress and Carmichael (1991) relationship between fO_2 and ferric/ferrous iron was tested against the spreadsheet of Iacovino (2021), and individual solubility laws were tested either against the relevant published calculator (e.g., excel spreadsheets in the case of Newman and Lowenstern, 2002; Eguchi and Dasgupta, 2018), or against figures in the original publication where these were not provided.

EVo has also been initially tested against DCompress to ensure numerical accuracy in the thermodynamic calculation of the gas phase chemistry. In order to maximise similarity between the two models, for this comparison EVo is run using the H_2O , H_2 and CO_2 solubility laws implemented by Burgisser et al. (2015) in DCompress; to distinguish this setup from

Models and Methods

EVo under standard run conditions (with H₂ and CO₂ solubility laws from Gaillard et al. (2003) and Eguchi and Dasgupta (2018), respectively), this version is referred to as EVo(DC). The two major differences left between the two models are therefore the treatment of sulfur solubility (EVo uses the sulfide capacity, as described in Section 2.1.1, while DCompress has a solubility law for SO₂ and H₂S), and the source of the equilibrium constants. DCompress uses equations from Ohmoto and Kerrick (1977) to calculate equilibrium constants K1-K5, while EVo and EVo(DC) calculate them using more recent thermochemical data from Chase (1998) as described in Section 2.1.1. The differences between the two methods in K1-5 are shown in Fig. 2.5.

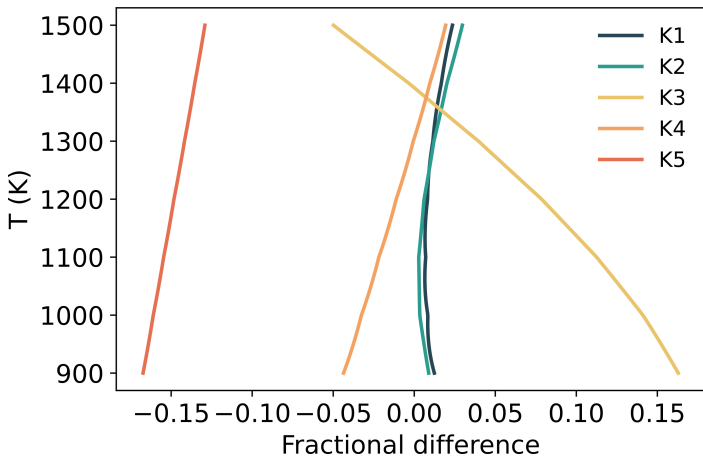


Fig. 2.5 The difference between the equilibrium constants as calculated in DCompress and EVo, expressed as K1(EVo)/K1(DC).

EVo(DC) and DCompress were run at a single pressure, using input method (1) as described in Section 2.1.2, a gas weight fraction of 0.001%, and other parameters as listed on the individual panels within Fig. 2.6 to compare the calculation of the gas phase chemistry.

In the case of the OH and COH systems, the difference between the results of the two models are $\leq 5\%$ for each species. These differences can be largely explained by differences in the value of equilibrium constants K1, K2 and K3 (Fig. 2.5). These differences in the OH/C systems can be reduced to $\leq 1\%$ by using the equilibrium constants from DCompress in EVo(DC). The particularly large difference on K5 at 1473 K is responsible for the largest difference between the two models, in the SOH and COHS setups. As the gas phase speciation is determined first using this method, and the melt S content is calculated based on the gas fugacity, the sulfur solubility law does not affect the gas phase speciation in this example; however the difference in the amount of sulfur dissolved in the melt is shown in the SOH and COHS panels of Fig. 2.6, as calculated by the different solubility laws.

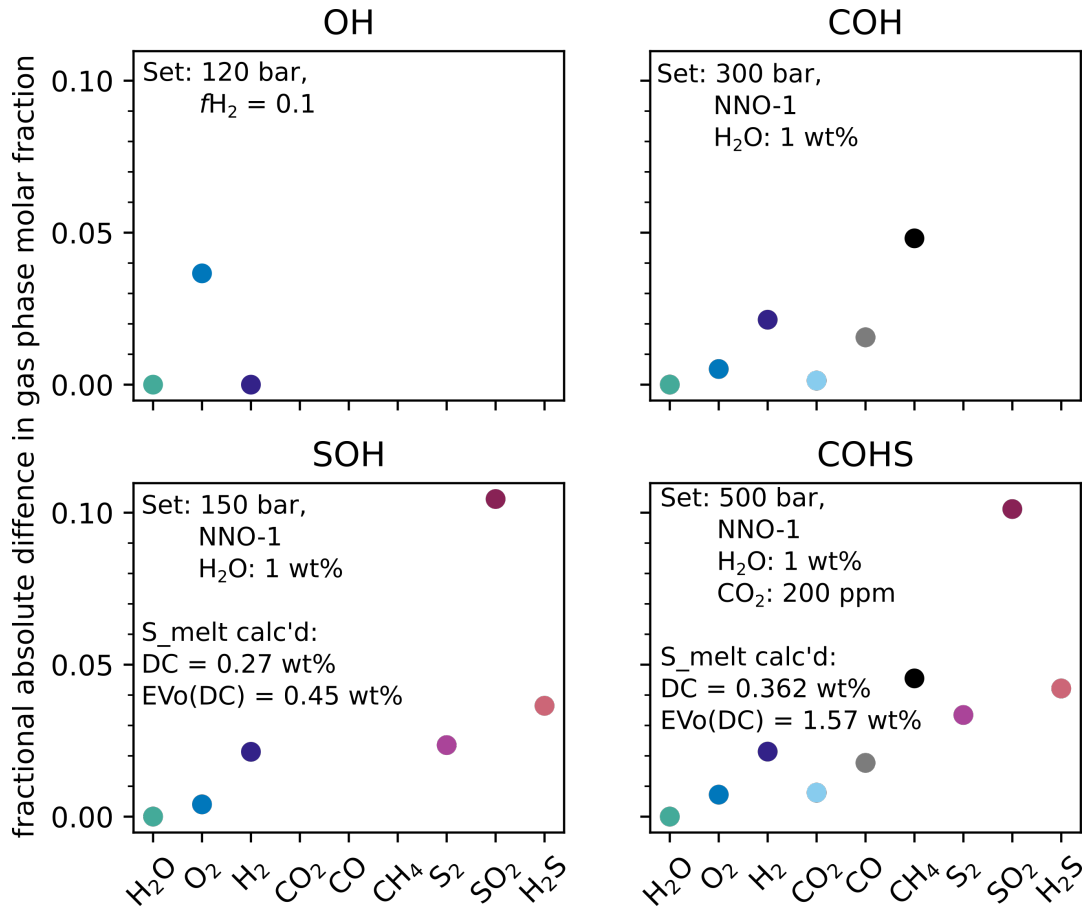


Fig. 2.6 The absolute fractional difference (calculated as $|X_{i,\text{EVo(DC)}} - X_{i,\text{DC}}|/X_{i,\text{DC}}$ where X_i is the mole fraction of each species i) between the gas phase speciation of DCompress and EVo(DC) when setup with the same input parameters. The magma composition used in the calculations is the default basalt composition for DCompress

The difference in the treatment of sulfur solubility between DCompress and EVo is demonstrated in Fig. 2.7. When given the same gas-phase fugacities for S_2 , SO_2 and H_2S across an $f\text{O}_2$ range, EVo consistently predicts a higher total dissolved S content, following an experimentally well-established trend that in reduced melts (where sulfur dissolves as S^{2-}), the solubility of sulfur increases with reducing $f\text{O}_2$ (e.g., Fincham et al., 1954; Katsura and Nagashima, 1974; Backnaes and Deubener, 2011; Lesne et al., 2015). In contrast, DCompress predicts a largely constant total sulfur content, decreasing slightly with reducing $f\text{O}_2$.

Models and Methods

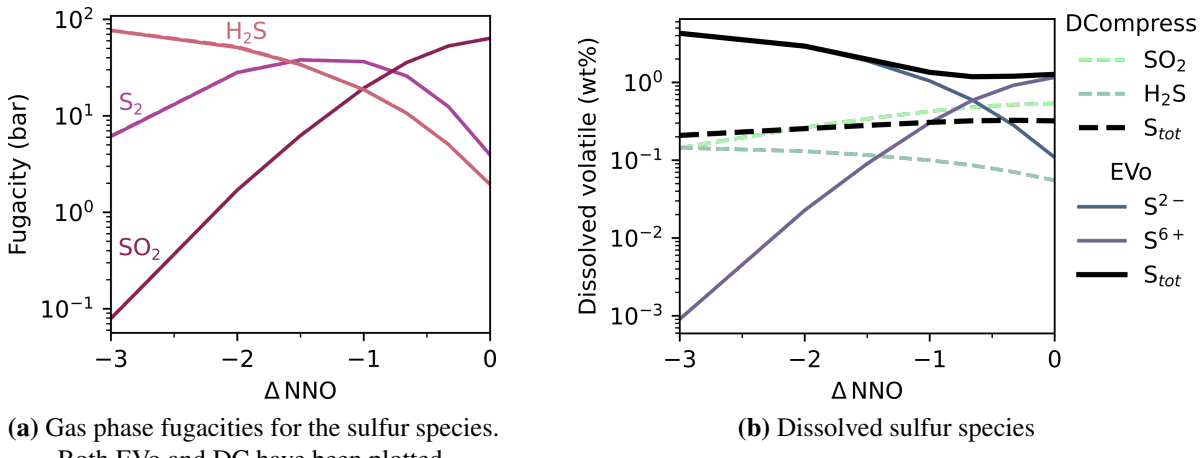


Fig. 2.7 Differences in the dissolved sulfur content for a melt at 100 bar, $f_{\text{H}_2\text{O}}=30$ bar, varying with f_{O_2} , for the S solubility laws of DCompress and EVo. For the purposes of comparing purely the effect of the different solubility laws, the results presented here for EVo were produced using the same equilibrium coefficients as are used in DCompress.

Decompression benchmarking

I now compare the results of EVo (now using it's default solubility laws) to those of 3 different models of volcanic degassing which include sulfur: DCompress (Burgisser et al., 2015), SolEx (Witham et al., 2012) and Chosetto, the newly released implementation of Moretti et al. (2003). Two decompression runs are shown in Fig. 2.8, one oxidised with an f_{O_2} of NNO+0.5, and one slightly reduced at NNO-2. SolEx is only shown in the oxidised example, as it cannot be run with an f_{O_2} lower than NNO+0.5. All 4 models were initialised with 1 wt% H_2O , 500 ppm CO_2 and 3000 ppm S. Only EVo has the option to automatically find the volatile saturation point; SolEx begins all runs at 4000 bar, while DCompress was run by adjusting the starting pressure until the total sulfur content matched the required 3000 ppm; and Chosetto's starting pressure was adjusted until it could numerically resolve.

Figure 2.8 shows (a) the volatile content of the melt, (b) the $\text{H}_2\text{O}/\text{CO}_2$ ratio in the gas phase and (c) the S/CO_2 ratio of the gas phase. All 4 models show close agreement on the dissolved volatile content as the pressure decreases, aside from the SolEx S content, which starts to rapidly decrease at a much higher pressure than other models in Fig. 2.8a. Chosetto also shows a higher CO_2 content in the melt in Fig. 2.8d. All 4 models also show similar trends in the $\text{H}_2\text{O}/\text{CO}_2$ ratio, although both SolEx and Chosetto both have systematically more CO_2 -rich gases.

The largest difference between models lies in the behaviour of sulfur during degassing. SolEx shows sulfur degassing at much higher pressures than other models, while DCompress

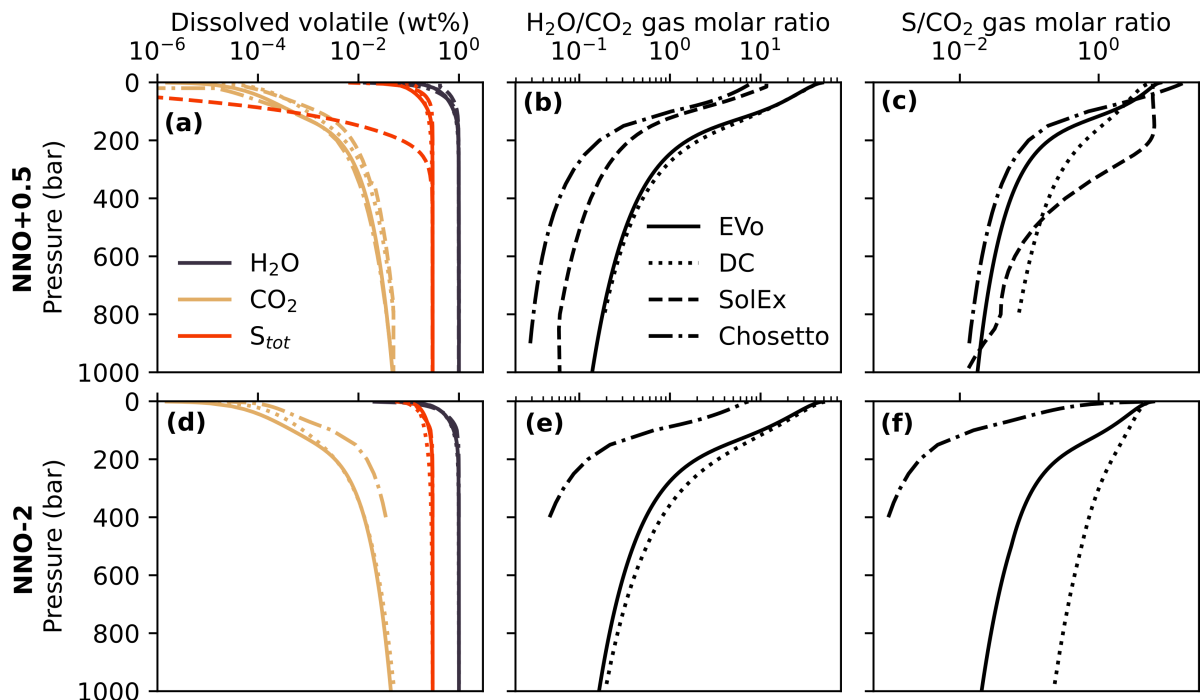


Fig. 2.8 The melt volatile content, $\text{H}_2\text{O}/\text{CO}_2$ ratio and S/CO_2 ratio in the gas phase for 4 different models during decompression. Each model was initiated with 1 wt% H_2O , 500 ppm CO_2 and 3000 ppm S . EVo is the only model which allows the saturation pressure to be found automatically; SolEx always starts at 4000 bar, P_{sat} was found manually for DCompress and Chosetto. At NNO-2, Chosetto was started at the first point it could numerically resolve.

Models and Methods

produces a more gradual release with pressure. EVo most closely resembles Chosetto under oxidised conditions, with sulfur starting to rapidly degas at 200 bar. Under reduced conditions the differences between models grow greater; the difference between Chosetto and EVo potentially being due to the presence of CO and CH₄ in the gas phase of EVo while Chosetto only considers CO₂.

The benchmarking comparisons shown in this section indicate that EVo compares well to other published models for multi-species volcanic degassing. Where models differ, for example in the COHS subplot of Fig. 2.6, the driving factors are well understood. The lack of a standard method/dataset with which to benchmark and compare such models, which often only show subsets of the common volatile species or differ in other substantive ways, is an issue across Earth Sciences; however, Fig. 2.8 shows that on a limited dataset, EVo follows similar trends to all three of the other published models which include sulfur in their parametrisations, with the exception of the sulfur/CO₂ behaviour in SolEx, which appears to be an outlier.

2.2 EVolve

EVolve is a model of volcanically-derived atmospheric evolution, which draws on the EVo model described above, and is used to produce data in Chapters 4 to 6 of this thesis. Conceptually, EVolve models the growth of a 0D atmosphere which is derived from volcanic degassing, which may or may not be undergoing hydrogen escape. This section details the equations and assumptions which are used to build EVolve; for more detail on how EVolve may relate to the natural world see Chapters 4 and 6. A schematic overview of the 3 components of EVolve, and how these components relate to processes occurring in planets are shown in Fig. 2.9.

EVolve is initialised with a mantle volatile content comprised of a H₂O, CO₂, S and N budget, regardless of the mantle *fO*₂. This H₂O and CO₂ budget is then calculated as masses of atomic H and C, and is treated as thus throughout, enabling EVo to be set-up using option (3) (see Section 2.1.2). During the initial set-up of the model, the total mass of each atomic volatile in the system (i.e., the budget in the mantle, plus any atmosphere that the model is initialised with) is recorded so that after every timestep, the mass balance of the model is checked for conservation. Mass conservation is enforced so that the difference in total system mass of each element is < 0.001 % after every timestep.

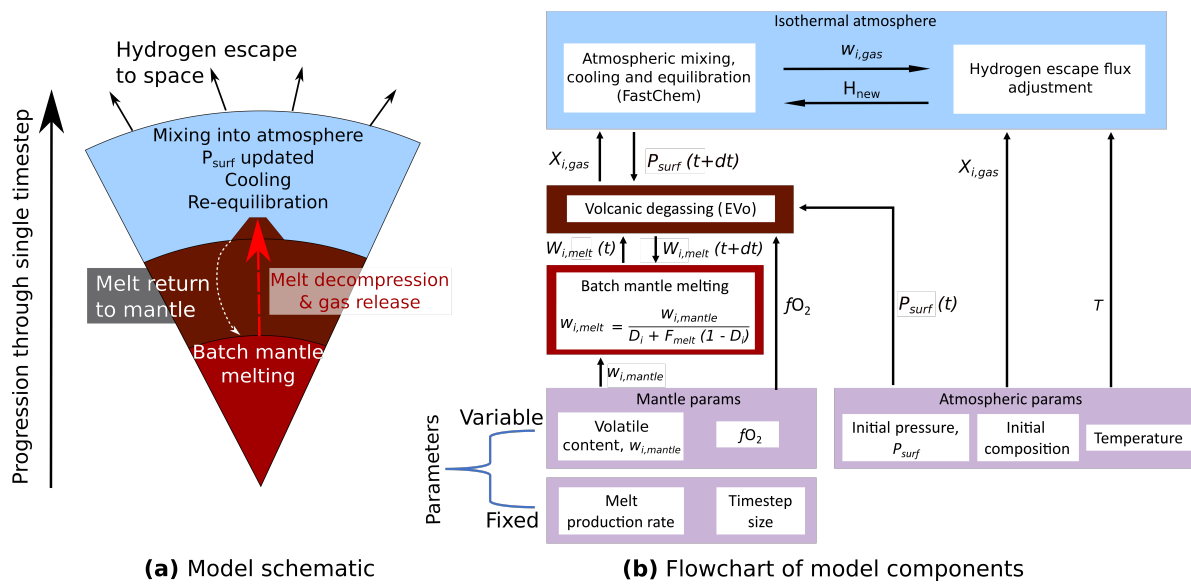


Fig. 2.9 (a) Model schematic and (b) flowchart. Arrows in (b) show direction of information flow. See text for symbols. Consideration of the escape component is left to Chapter 6.

2.2.1 Part 1: mantle melting

At the start of each time-step, a fraction of the mantle is melted. A batch mantle melting model is applied, based on the assumption that the melt will be in equilibrium with the source rock before being removed to the surface. The volatile (H, C, S and N) content of this melt is calculated using the batch melting equation

$$w_{i,melt} = \frac{w_{i,mantle}}{D_i + F_{melt}(1 - D_i)}, \quad (2.46)$$

where i indicates a single volatile species, $w_{i,melt}$ is the concentration of each volatile in the melt phase expressed as a weight fraction, $w_{i,mantle}$ is the volatile concentration in the bulk mantle, F_{melt} is the local melt fraction (which is fixed at 0.1 for the results presented in this thesis; the sensitivity of EVolve to varying the melt fraction is explored in Chapter 4 and Fig. 4.3) and D_i is the partition coefficient of the volatile (the concentration ratio of a volatile between mantle and melt at equilibrium, see Table 2.3). The volatile elements considered here all have partition coefficients less than 1 (C in graphite-saturated melts being the exception, discussed below), and therefore partition preferentially into the melt phase, generating a melt that is volatile element enriched in comparison to the bulk mantle.

Models and Methods

Table 2.3 Partition coefficients for bulk melting equation used in EVolve

Species	D _i	Reference
H	0.01	(Aubaud et al., 2004)
C (graphite undersaturated)	5.5×10^{-4}	(Rosenthal et al., 2015)
S	0.01	(Callegaro et al., 2020)
N	5.53×10^{-3} at IW, 6×10^{-4} at NNO	(Li et al., 2013)

Behaviour of carbon during mantle melting

The behaviour of carbon during partial melting of the mantle is $f\text{O}_2$ -dependent, so a single partition coefficient does not capture its behaviour during melting. When the mantle is sufficiently oxidised so that graphite is unstable, carbon behaves as a highly incompatible element. Under these conditions, the C content of a magma after batch melting can be calculated using the partition coefficient of Rosenthal et al. (2015) (Table 2.3). If the mantle is graphite saturated, as it will be at lower $f\text{O}_2$ conditions, the amount of carbon present in the melt is controlled directly by redox equilibrium between graphite and CO_3^{2-} in the silicate melt (Holloway et al., 1992).

Recent models of planetary degassing (Ortenzi et al., 2020; Guimond et al., 2021) have applied the model of Holloway et al. (1992) to claim that at low $f\text{O}_2$, the volcanic gases feeding the atmosphere should be carbon-poor compared to more oxidised conditions, as the bulk of the planet's carbon budget remains in the mantle as graphite. However, there is a growing body of evidence which suggests that at low $f\text{O}_2$, carbon can dissolve into silicate melts in forms other than CO_3^{2-} (e.g., Ardia et al., 2013; Stanley et al., 2014; Armstrong et al., 2015; Dalou et al., 2019). The model of Li et al. (2017) has therefore been chosen for use under graphite saturated conditions, which calculates the total dissolved C content without speciation:

$$\text{IW} + 1.7 \geq \log f\text{O}_2 \geq \text{IW} - 1 :$$

$$\begin{aligned} \log(\text{C, ppm}) = & -3702/T - 194P/T - 0.0034 \log(X_{\text{H}_2\text{O}}) \\ & + 0.61 \text{NBO}/T + 0.55\Delta\text{IW} + 3.5, \end{aligned} \quad (2.47)$$

$$\text{IW} - 5.3 \leq \log f\text{O}_2 \leq \text{IW} - 1 :$$

$$\log(\text{C, ppm}) = 0.96 \log(X_{\text{H}_2\text{O}}) - 0.25\Delta\text{IW} + 2.83, \quad (2.48)$$

in which T is temperature in K, P is pressure in GPa, $X_{\text{H}_2\text{O}}$ is the mole fraction of water in the silicate melt, ΔIW is the oxygen fugacity relative to the IW buffer, and $\text{NBO}/T = 2 \text{ O/T} - 4$ where $T = \text{Si} + \text{Ti} + \text{Al} + \text{Cr} + \text{P}$, the mole fractions of elements in the silicate melt (Li et al., 2017). All the results presented in this thesis assume a mantle temperature of 2000 K (e.g., Ortenzi et al., 2020) and pressure at the point of mantle melting of 2 GPa (the effect of varying the pressure of melting is explored in Chapter 4 and Fig. 4.3). The mantle is assumed to no longer be graphite-saturated if the C content of the melt calculated using Eq. (2.47) is higher than that calculated using the graphite-free partition coefficient of Rosenthal et al. (2015). If Eqs. (2.47) and (2.48) do not intersect at precisely IW-1, EVolve continues to use Eq. (2.47) (which assumes C is dissolving as CO_3^{2-}) until the intersection is reached, this occurs within a few tenths of a log unit.

Similarly to carbon, nitrogen partitioning into a melt is also $f\text{O}_2$ -dependent, although it is less well studied. Two partition coefficients are provided by Li et al. (2013), one for the IW buffer, and one for the oxidised NNO (approx IW+4) buffer (Table 2.3). I linearly interpolate between these two values to calculate $f\text{O}_2$ -appropriate partition coefficients using

$$D_N = -0.00118 \Delta\text{IW} + 0.00553. \quad (2.49)$$

It is well understood that of the total mass of magma produced in the mantle, only a fraction will be erupted to the surface as extrusive lava; the rest of the magma will remain in the lithosphere as intrusive emplacements. Accordingly, EVolve accounts for this with an extrusive:intrusive ratio (r_{ei}), to calculate the amount of melt which will reach the surface and degas to contribute to the atmosphere. This ratio can be set by the user, but in this thesis a value of 10% (Crisp, 1984) is used, following previous approaches (e.g., Dorn et al., 2018; Ortenzi et al., 2020). In nature, the total amount of volcanic outgassing is a sum of both the gases released by extrusive lavas (modelled in EVolve), and gases released from deep magmatic emplacements (passive degassing from intrusive magma). EVolve does not currently account for the passive degassing fraction, although this would be a focus for future work (see Section 7.1).

The mass of the extrusive melt which will be erupted to the surface (m_{ext} , kg) is calculated as

$$m_{\text{ext}} = r_{ei} dt m_{\text{melt}}, \quad (2.50)$$

where $r_{ei} = 0.1$, the fraction of melt by mass that reaches the surface, m_{melt} (kg yr⁻¹) is the rate of melt production in the mantle and dt (years) is the size of the timestep. Once the extrusive melt has been erupted and outgassed, as calculated in Part 2 of the model (Section 2.2.2), the extrusive melt and any residual volatiles that did not get released into the atmosphere are mixed

Models and Methods

back into the mantle reservoir, along with the intrusive melt. The new volatile content of the mantle after each outgassing time-step is calculated by recombining the three reservoirs, by simple mass balance

$$X_{i,mantle}(t + dt) = \frac{X_{i,ext}(t) m_{ext}(t) + X_{i,int}(t) m_{int}(t) + X_{i,mantle}(t) m_{mantle}(t)}{m_{ext}(t) + m_{int}(t) + m_{mantle}(t)}. \quad (2.51)$$

where m is the mass of each reservoir, and the subscripts *int* and *ext* refer to the intrusive and extrusive magmas, respectively so that at time (t),

$$m_{melt}(t) = m_{ext}(t) + m_{int}(t). \quad (2.52)$$

The lithospheric mass remains constant over time, as all the silicate melt is returned to the mantle after each time-step. This approach is conceptually consistent with a planet operating in a stagnant-lid regime, equivalent to assuming a slow return of crustal material and it's embedded volatiles to the convecting mantle via delamination or lithospheric ‘drip’ (Stern et al., 2018). Atmosphere-interior volatile cycling is assumed to be inefficient, i.e., volatiles remain in the atmosphere once outgassed (Tosi et al., 2017). This is appropriate for the hot planets considered in Chapters 4 to 6, on which low temperature, aqueous drawdown processes, such as the carbonate-silicate cycle, do not operate (including those suggested by Foley, 2019; Höning et al., 2019, for stagnant lid planets).

2.2.2 Part 2: EVo, volcanic outgassing

To calculate the gas composition input to an atmosphere from a magmatic source, the EVo model described above is used. The solubility laws selected are: Burgisser et al. (2015) for H₂O and H₂, Eguchi and Dasgupta (2018) for CO₂, Armstrong et al. (2015) for CO, Ardia et al. (2013) for CH₄ (both CO and CH₄ are set to insoluble if the starting fO_2 is above IW+1) and Libourel et al. (2003) for N₂. As described above, sulfur solubility is dictated by the sulfide capacity law of O’Neill (2021) which calculates S₂⁻ solubility as is appropriate for sulfur in reduced melts.

In EVolve, EVo is initialised using the setup described in Section 2.1.2, finding both P_{sat} and the volatile speciation. As there is no model for how the mantle fO_2 may change between the point at which batch melting begins and the pressure of volatile saturation, the fO_2 of the system is set to the mantle fO_2 at the point of volatile saturation as any change in fO_2 prior to degassing is likely to be limited (Stolper et al., 2020). This allows calculation of the mass of

atomic O in the system by fixing the $f\text{O}_2$, H, C, S and N atomic masses and allowing EVo to calculate the appropriate volatile saturation pressure.

From this point, the state of the system only needs to be calculated at the surface pressure, as a closed-system degassing scenario makes the final state path-independent. However, since the state of the system at the start of the degassing path (the saturation point) has already been found, the intermediate steps between volatile saturation and the surface pressure are calculated for convenience; the Newton-Raphson method used to solve the system of equations requires a sufficiently accurate initial guess in order to converge. The simplest way of doing this once the high pressure composition has been found, is by finding the state of the system through incremental pressure steps.

At the end of the EVo run, the state of the volcanic system at the current surface pressure is known. This data is then passed into the third, atmospheric, component of the model.

2.2.3 Part 3: atmospheric processing

Atmospheric processing in EVolve is calculated using FastChem 2.0 (Stock et al., 2018, Stock et.al., in prep). FastChem is an ultra-fast gas phase chemical equilibrium model (this is a homogenous model which can only be used for the gas phase, i.e., can only come into use when the melt phase is no longer relevant), which uses a semi-analytical approach as described in Stock et al. (2018). For a purely COHSN system, as used in EVolve, FastChem calculates the equilibrium composition of a gas phase across 85 species.

FastChem takes as an input the elemental composition of an atmosphere in a manner commonly used within the astronomical community, a scale of logarithmic abundances relative to the hydrogen content and where the hydrogen abundance is defined to be $\log \epsilon_H = 12.00$, i.e.,

$$\log_{10} \epsilon_X = \log_{10}(N_X/N_H) + 12, \quad (2.53)$$

where N_X and N_H are the number densities of element X and hydrogen, respectively.

Prior to input into FastChem, the elemental number densities for the new, mixed atmosphere (pre-existing atmosphere plus the volcanic gases erupted in the current timestep) are calculated. EVo provides the mass and speciation of the erupted gas phase as a weight fraction of the system (W_{gT}), and the composition of the gas as either mole (X_i) or weight (w_i) fractions; this composition is first converted into the absolute masses of each element (e.g., m_{TO}) erupted in

Models and Methods

the current timestep using

$$m_{TO} = M_O m_{\text{ext}} \left(\frac{W_{gT}}{\sum_j X_j M_j} (X_{\text{H}_2\text{O}} + 2X_{\text{O}_2} + 2X_{\text{CO}_2} + X_{\text{CO}} + 2X_{\text{SO}_2}) \right) \quad (2.54\text{a})$$

$$m_{TH} = 2M_H m_{\text{ext}} \left(\frac{W_{gT}}{\sum_j X_j M_j} (X_{\text{H}_2\text{O}} + X_{\text{H}_2} + 2X_{\text{CH}_4} + X_{\text{H}_2\text{S}}) \right) \quad (2.54\text{b})$$

$$m_{TC} = M_C m_{\text{ext}} \left(\frac{W_{gT}}{\sum_j X_j M_j} (X_{\text{CO}} + X_{\text{CO}_2} + X_{\text{CH}_4}) \right) \quad (2.54\text{c})$$

$$m_{TS} = M_S m_{\text{ext}} \left(\frac{W_{gT}}{\sum_j X_j M_j} (2X_{\text{S}_2} + X_{\text{H}_2\text{S}} + X_{\text{SO}_2}) \right) \quad (2.54\text{d})$$

$$m_{TN} = M_N m_{\text{ext}} \left(\frac{W_{gT}}{\sum_j X_j M_j} (2X_{\text{N}_2}) \right); \quad (2.54\text{e})$$

note the similarity in form to the equations discussed for EVo earlier. These masses are then added to those currently in the atmosphere from previous timesteps to give the new elemental composition of the atmosphere. The surface pressure is also updated according to

$$P_{\text{surf}}(t + dt) = P_{\text{surf}}(t) + \frac{m_{\text{ext}} W_{gT} g}{4\pi R_p^2}, \quad (2.55)$$

where $P_{\text{surf}}(t + dt)$ (Pa) is the surface pressure after the release of volcanic gases, $P_{\text{surf}}(t)$ is the surface pressure produced by the pre-existing atmosphere from the previous time-step (the pressure at which the volcanic gas is erupted at), W_{gT} is the weight fraction of exsolved gas in the volcanic system, g (m s^{-2}) is the surface gravity and R_p (m) is the radius of the planet.

To convert the elemental composition of the atmosphere into units acceptable by FastChem, the composition currently stored as absolute masses (m_{TO} etc.) is converted to atomic mole fractions using

$$X_i = \frac{W_{Ti}}{M_i} \cdot \frac{1}{\sum_j \frac{W_{Tj}}{M_j}}, \text{ where } W_{Ti} = \frac{m_{Ti}}{\sum_j m_{Tj}}. \quad (2.56)$$

Since a number density ratio (e.g., n_X/n_{H}) is equivalent to a mole fraction ratio (X_i/X_{H}), as both are dimensionless numbers counting the relative number of molecules present, the mole fraction ratio is substituted into Eq. (2.53) to find the elemental abundances in the mixed atmosphere for input to FastChem. The final atmospheric speciation, in thermochemical equilibrium at the pre-defined atmospheric temperature, is calculated at the new surface pressure $P_{\text{surf}}(t + dt)$. For simplicity, and due to a lack of representative P-T profiles for the atmosphere as it evolves, the atmospheric speciation is only calculated at surface pressure; i.e., EVolve models a 0D atmosphere.

Along with the atmospheric composition, provided as mole fractions, and the new surface pressure, EVolve calculates the pressure scale height (\mathcal{H}) of the atmosphere after each timestep as

$$\mathcal{H} = \frac{RT}{\mu g}, \quad (2.57)$$

where R is the universal gas constant ($8.3144598 \text{ J mol}^{-1} \text{ K}^{-1}$), T is the surface temperature (K), μ is mean molecular mass of the atmosphere (g/mol) and g is surface gravity ($\text{m}^{-2} \text{ s}^{-1}$).

If hydrogen escape is not being utilised in a model run, this marks the end of a timestep. Conservation of mass is checked, and the process loops to start the next batch of mantle melting. However, if hydrogen escape is being accounted for, further calculations within the atmospheric component are carried out to calculate the amount of hydrogen which will be lost, and the new atmospheric composition. The treatment of hydrogen escape within EVolve is described in Chapter 6, as it is not used more generally within this thesis.

3

Can Volcanism Build Hydrogen–Rich Early Atmospheres?

3.1 Introduction

Atmospheric H₂ could be key to the development of terrestrial planets. The presence of significant hydrogen fractions has been invoked in extending the habitable zone (e.g., Sagan, 1977; Stevenson, 1999; Pierrehumbert and Gaidos, 2011; Wordsworth, 2012; Abbot, 2015; Ramirez and Kaltenegger, 2017) and providing conditions suitable for the production of prebiotic molecules via H₂ buildup then loss (Miller and Urey, 1959). Several studies have looked at the climatic consequences of adding a hydrogen fraction to the atmospheres of the early Earth (Wordsworth and Pierrehumbert, 2013b), early Mars (Ramirez et al., 2014; Batalha et al., 2015; Wordsworth et al., 2017; Hayworth et al., 2020) and terrestrial planets more widely (e.g., Ramirez and Kaltenegger, 2017). Others have looked at how hydrogen can be introduced into the earliest primary atmospheres of terrestrial bodies from proto-planetary nebular gases (Stevenson, 1999), magma oceans (Deng et al., 2020) and accretion/impact processes (Schaefer and Fegley, 2007, 2010). However, hydrogen is a light element which escapes easily to space; on terrestrial sized bodies, any primary atmosphere should be blown off by high rates of stellar irradiation within the first few million years (Pierrehumbert and Gaidos, 2011). Therefore, to maintain a hydrogen-rich atmosphere on a rocky planet, H₂ must be constantly replenished over geologic timescales to offset its continuous loss to space.

In the presence of life, methanogens and anoxygenic phototrophs can be an important source of hydrogen in the form of methane (Kharecha et al., 2005). However, in a prebiotic context geologic sources of H₂ are required to generate abiotic secondary atmospheres (i.e.,

Can Volcanism Build Hydrogen–Rich Early Atmospheres?

atmospheres generated post-accretion and magma ocean phase, and before the emergence of life). These can include the serpentinisation of ultramafic rock, metamorphic fluxes of CH₄ from hydrothermal vents, and volcanism (Kasting, 2013). It is this latter possibility of volcanic H₂ production in an early secondary atmosphere that this chapter focuses on.

A key parameter determining the build up of H₂ in planetary atmospheres is the escape rate of hydrogen to space. Were this loss rate to have been lower on the early Earth, moderate to significant fractions of hydrogen could have built up (Tian et al., 2005; Kuramoto et al., 2013). In these studies, the hydrogen source is assumed to be volcanic and is based on extrapolating from the modern volcanic hydrogen flux. The missing link for these studies is a more thorough analysis of the amount of hydrogen which could reasonably be released to an atmosphere through volcanism, as a function of planetary interior and exterior conditions. There are 3 primary controls on this; 1) the redox state of the degassing magma, 2) the pressure of degassing, and 3) the overall volcanic flux of the planet. Once these factors have been constrained, the hydrogen loss rate necessary to achieve a particular hydrogen fraction from volcanism can be evaluated. Here, we aim to address this issue by using a magma degassing code to constrain the possible range of volcanically sustained H₂ in planetary atmospheres, linking the atmospheric H₂ fraction to the potential oxidation state, geological activity and atmospheric loss rates of early Earth, early Mars and terrestrial planets.

3.2 Controls on a volcanic hydrogen atmospheres

3.2.1 Magma degassing

Volcanic gases are widely considered to be approximately in equilibrium with the oxidation state of the magma from which they exsolved (e.g., Moretti and Papale, 2004; Burgisser et al., 2015). Therefore, to change the speciation of a gas phase from oxidised (H₂O, CO₂ and SO₂ dominated) to reduced (CO, H₂ and H₂S dominated), and therefore more H₂-rich, the *fO₂* of the magma needs to be lower. A greater dissolved water content at a constant *fO₂* will result in a melt with a greater total atomic hydrogen content, and therefore will also increase the volcanic hydrogen emission.

Pressure exerts a dominant control over volatile partitioning between the melt and the gas phase in a magmatic system, and therefore also controls the composition of a volcanic gas phase (Gaillard and Scaillet, 2014). Species with a low solubility such as CO₂ and CO exsolve at higher pressures and therefore dominate the early stages of magma degassing, with more soluble and often more abundant phases such as water becoming dominant at low pressures (e.g., Dixon and Stolper, 1995). The effect of pressure on the composition of secondary

3.2 Controls on a volcanic hydrogen atmospheres

volcanic atmospheres has been examined by Gaillard and Scaillet, 2014, in which they assume average redox conditions across the solar system driven by graphite saturation buffering an ascending magma's $f\text{O}_2$,



and therefore perform all their calculations starting at FMQ -1.5. However, the average $f\text{O}_2$ of erupting MORB on Earth (a relatively oxidised planet) is FMQ -0.41±0.43 (Bézos and Humler, 2005), and values across the solar system vary down to IW-5 on Mercury (Wadhwa, 2008; Zolotov et al., 2013). Given the similar potential for $f\text{O}_2$ diversity among exoplanets (Doyle et al., 2019), here we examine a wide range of $f\text{O}_2$ values.

While pressure and magmatic $f\text{O}_2$ can control the mass and composition of the gas phase, the total amount of H_2 emitted to an atmosphere will also be controlled by the volcanic flux. A higher flux can be achieved either through a larger total volatile content of the magma, which then releases a greater volume of gas into the atmosphere per unit mass of magma degassed, or a greater total flux of magma to the surface, such as may occur in a younger volcanically active planet, or a planet experiencing tidal heating (e.g., Io in our own solar system).

3.2.2 Hydrogen escape mechanisms

The escape flux of hydrogen from an atmosphere is dictated by the rate at which hydrogen diffuses through the layer of background air between the homopause (the level below which an atmosphere is well mixed) and the exobase, above which the atmosphere becomes collisionless. I.e., the escape flux is limited by the rate at which H_2 can be supplied to the altitude where it can escape Earth's atmosphere. In a diffusion-limited escape regime, once hydrogen diffuses above the exobase it is rapidly lost from the atmosphere so that the rate of replenishment from below is the limiting factor. These removal processes can be thermal, with two end-member approximations, or involve suprothermal mechanisms (e.g., photochemical escape, charge exchange and polar wind) which we do not consider here.

Thermal escape can occur as Jeans' escape; where molecules from the high-energy tail of the molecular thermal distribution attain enough kinetic energy to escape from the exobase; and hydrodynamic escape, occurring when heating of the atmosphere below the exobase by stellar extreme ultraviolet radiation (XUV) causes an upward pressure gradient driving a bulk, radial outflow. Jeans' escape occurs with a high temperature exobase, and is responsible for a non-negligible fraction of hydrogen escape occurring today on Earth and Mars (Catling and Kasting, 2017). Hydrodynamic escape becomes dominant when the XUV flux is sufficient to

Can Volcanism Build Hydrogen–Rich Early Atmospheres?

drive a bulk outflow, and is key early in the lifetime of planetary systems, when the parent star is more active (Tu et al., 2015).

Hydrogen escape from Earth is generally assumed to be diffusion-limited, and this diffusion rate can be linked to the concentration of hydrogen in an atmosphere (Walker, 1977). However, some models of the early atmosphere suggest a cold exobase, and insufficient stellar XUV, resulting in a less efficient, energy limited escape regime (Tian et al., 2005; Kuramoto et al., 2013). Estimates for the hydrogen mixing ratio in the Archean atmosphere range from <0.1 % (e.g., Walker, 1977; Kasting, 1993), through $\leq 1\%$ H₂ (Kuramoto et al., 2013; Zahnle et al., 2019) up to $\sim 30\%$ (Tian et al., 2005). To reflect uncertainty around the escape rate of H₂, we model cases both at and below the diffusion limit in this chapter. This is initially carried out in manner which is agnostic of the specific physics of hydrogen escape, so that the reduction from the diffusion limit into an energy limited scenario can be applied to planets generally, including those in different stellar regimes (and therefore different high energy UV spectra). However, escape fluxes below the diffusion limited rate are later compared to XUV-limited escape to physically inform results for the early Earth and Mars.

3.3 Modelling volcanic outgassing

3.3.1 Thermodynamics

The volcanic gas composition in this study is calculated according to the pressure, temperature, melt f_{O_2} and volatile content using an earlier iteration of the EVo model described in Chapter 2. However, the only major difference between the version used here, and that previously described is the treatment of sulfur solubility. Rather than the sulfide capacity system described in Section 2.1.1, the sulfur system was treated in the same way as in the DCompress model of Burgisser et al. (2015). SO₂ and H₂S are treated as soluble, with the solubility laws following the form

$$w_i^m = a_i(f_i)^{b_i}, \quad (3.2)$$

where a_i and b_i are constants taken from Burgisser et al. (2015), w_i^m is the weight fraction of the species dissolved in the melt and f_i is the fugacity of species i in the gas phase calculated according to Eq. (2.9). S₂ is treated as insoluble. We note here that this is a somewhat simplistic model for sulfur, which does not account for how sulfur degassing can impact the f_{O_2} of a melt as it erupts (hence the switch to the method described in Section 2.1.1 for later iterations of EVo). Nitrogen is excluded so the gas chemistry is comprised of 9 species in a C-O-H-S volatile system. A basaltic melt composition was used for compositionally dependent solubility laws.

3.3 Modelling volcanic outgassing

The gas composition is only calculated at the surface pressure, rather than the entire decompression pathway. This means the $f\text{O}_2$ reported is that of the melt at the surface, rather than the mantle. This removes the buffering effect of the iron and sulphur content in the melt of the expected evolution of $f\text{O}_2$ as the pressure decreases and volatiles exsolve from the melt. Source-to-surface modelling of a magma degassing H_2 would show sulphur species further complicating the relationship between mantle $f\text{O}_2$ and H_2 outgassing, as release of S_2^- can lower the $f\text{O}_2$ of a system (e.g., Gaillard et al., 2011), while sulphur degassing is enhanced under oxidising conditions. Given that the $f\text{O}_2$ conditions relevant to most planetary magmatism will have sulfur speciated as S^{2-} , the result of this simplified S degassing model is to slightly underestimate the H_2 production, if the $f\text{O}_2$'s we quote are viewed as being mantle $f\text{O}_2$.

3.3.2 Volcanic outgassing

The outgassing flux of a species can be parameterized in terms of a concentration of species X as

$$\Phi_{\text{volc}}(X) = \Phi_{\text{volc}} f_{\text{T}}^{\text{v}}(X), \quad (3.3)$$

where Φ_{volc} is the total volcanic outgassing flux [mol s^{-1}], and $f_{\text{T}}^{\text{v}}(X)$ is the total number mixing ratio of species X in the volcanic input to the base of the atmosphere.

The volcanic outgassing flux varies according to the vent pressure and melt $f\text{O}_2$ (See Appendix B and Section B.1). To account for this, Earth's modern flux ($\Phi_{V0} = 3.4 \times 10^6 \text{ mol s}^{-1}$, taken from Tables 7.1 and 7.3 in Catling and Kasting, 2017), was assumed to be equal to the amount of volcanic outgassing modelled for a magma degassing at 1 bar and $\Delta\text{FMQ}=0$, with an initial volatile content of 350 ppm H, 550 ppm C and 1000 ppm S (approx 0.3 wt % H_2O and 2000 ppm CO_2 ; this modern Earth reference run was chosen as a good approximation of the average modern melt compositions degassing at mid-ocean ridges, Michael and Graham, 2015; Wallace et al., 2015). In all cases, the initial volatile content refers to an undegassed magma, rather than a mantle source. The number of moles from all other model runs were then scaled against the total number of moles of gas (of all species) released by this reference run for the modern Earth,

$$\Phi_{\text{volc}} = \frac{n}{n_{\text{FMQ}}} \cdot \Phi_{V0}, \quad (3.4)$$

Can Volcanism Build Hydrogen–Rich Early Atmospheres?

where n is the total number of moles of gas released by any one model run, and n_{FMQ} is the number of moles released by our reference modern Earth run. This ratio is used to adjust the volcanic flux to account for the effect of redox and surface pressure on volcanic degassing.

Volcanic outgassing of hydrogen is discussed here as $f_T^v(\text{H}_2)$, the total hydrogen (H, tracked as H₂ molecules) number mixing ratio of the volcanic gases input to the base of the atmosphere. This value can be parameterized in several different ways,

$$f_T^v(\text{H}_2) \approx \begin{cases} f^v(\text{H}_2), & (3.5\text{a}) \\ f^v(\text{H}_2) + 4f^v(\text{CH}_4) + 3f^v(\text{H}_2\text{S}), & (3.5\text{b}) \\ f^v(\text{H}_2) + 2f^v(\text{CH}_4) + f^v(\text{H}_2\text{S}), & (3.5\text{c}) \end{cases}$$

where $f^v(X)$ is the mixing ratio of each individual species X (i.e., H₂, CH₄ etc) in the volcanic gas. The three different cases in Eq. (3.5), summarised here, are discussed in more detail in Appendix B and Section B.2.

Case a: Only molecular H₂ from volcanic outgassing is considered as providing a H₂ input to the base of the atmosphere. All other hydrogen-bearing species, e.g., CH₄ and H₂S are assumed to be removed rapidly via deposition to the surface.

Case b: All the reduced hydrogen-bearing volcanic gases i.e., H₂, CH₄ and H₂S contribute to $f_T^v(\text{H}_2)$. This is equivalent to assuming that all the CH₄ and H₂S is oxidised to CO₂ and SO₂ respectively, before reaching the homopause, providing an additional volcanically derived flux of H₂ (Catling and Kasting, 2017). As H₂O is the oxidant in both cases, this case requires a large enough reservoir of atmospheric water to oxidise all the CH₄ and H₂S released, to maintain the photochemically-derived H₂ over the geological timescales of interest.

Case c: Some volcanic H₂S will be deposited to the surface, and some volcanic H₂ will be removed from the atmosphere as it undergoes subsequent photochemical and thermochemical reactions followed by rainout of any soluble species produced. The rest of the CH₄ and H₂S reacts as in case b, leaving $f_T^v(\text{H}_2)$ in this case to be the sum of the H-bearing species, weighted by the number of moles of H₂ each species contains (equivalent to all the H-bearing species being photodissociated in the upper atmosphere).

In a natural system, it is very unlikely that all the outgassed CH₄ and H₂S will be efficiently converted to H₂ with no deposition to the surface. We therefore adopt the definition of case c here, with $f_T^v(\text{H}_2)$ defined in Eq. (3.5c). This provides a compromise that is intermediate between the definitions of Eqs. (3.5a) and (3.5b) (See Appendix B and Section B.2 for examples of how the choice of photochemical regime impacts results).

3.4 Relating outgassing to atmospheric H₂ mixing ratios

$\Phi_{\text{volc}}(\text{H}_2)$, the total flux of molecular hydrogen from volcanic sources, can therefore be calculated as:

$$\Phi_{\text{volc}}(\text{H}_2) = \Phi_{\text{volc}} \cdot f_T^v(\text{H}_2) = \Phi_{\text{volc}} (f^v(\text{H}_2) + 2f^v(\text{CH}_4) + f^v(\text{H}_2\text{S})). \quad (3.6)$$

In order to consider atmospheric escape, it is convenient to convert from geological units of mol s⁻¹ to the photochemical units molecules cm⁻² s⁻¹.

Although volcanic CO can generate H₂ through



We treat volcanic CO outgassing as compensated for by CO deposition, i.e.,

$$\Phi_{\text{volc}}(\text{CO}) = v_{\text{dep}}(\text{CO})f(\text{CO}), \quad (3.8)$$

as the deposition rate is expected to overwhelm the photochemistry. $\Phi_{\text{volc}}(\text{CO})$ is the volcanic flux of CO, $v_{\text{dep}}(\text{CO})$ the deposition velocity [cm s⁻¹] and $f(\text{CO})$ the atmospheric mixing ratio of CO.

3.4 Relating outgassing to atmospheric H₂ mixing ratios

We initially assume the rate of escape of H₂ to space is limited by the diffusion rate across the homopause, as is the case on the modern Earth. The diffusion limited flux is given by Walker (1977) as

$$\Phi_{\text{esc}}(X) \cong \frac{b_X}{H_a} \cdot \frac{f_T(X)}{1 + f_T(X)} \quad (3.9)$$

where b_X is the binary diffusion parameter for species X, H_a is the scale height of the atmosphere, and $f_T(X)$ is the total number mixing ratio of X in the atmosphere (as opposed to $f_T^v(X)$, which is the mixing ratio in the volcanic gas).

$f_T(X)$ here is $f_T(\text{H}_2)$, the sum of the mixing ratios of all H₂-bearing atmospheric constituents above the tropopause (e.g., Kharecha et al., 2005). $f_T(\text{H}_2)$ is evaluated above the stratospheric cold trap, where H₂O has been removed by condensation,

$$f_T(\text{H}_2) \approx f(\text{H}_2) + 2f(\text{CH}_4) + f(\text{H}_2\text{S}). \quad (3.10)$$

We use a well established convention for the escape of H₂ (Walker, 1977; Kasting, 1993; Kharecha et al., 2005), by balancing the volcanic outgassing flux Φ_{volc} with escape, i.e.,

$$\Phi_{\text{volc}}(\text{H}_2) \cong \Phi_{\text{esc}}(\text{H}_2) = \alpha \cdot \Phi_{\text{diff}}(\text{H}_2). \quad (3.11)$$

The escape flux Φ_{esc} can be less than or equal to the diffusion limited case Φ_{diff} , with the difference parameterized by an escape efficiency factor α bound between 0 and 1.

Volcanic flux is also a variable, so this is examined using an outgassing flux factor β , indicating the factor of increase in volcanic outgassing rate compared to the modern Earth. This maintains a steady-state atmosphere, with the total fraction of H_2 in the atmosphere defined as

$$\frac{f_T(\text{H}_2)}{1 + f_T(\text{H}_2)} = \frac{\beta \Phi_{\text{volc}}(\text{H}_2) H_a}{\alpha b_{H_n}}. \quad (3.12)$$

b_{H_n} is the binary diffusion parameter at $1.8 \times 10^{19} \text{ cm}^{-1} \text{ s}^{-1}$, the weighted average of b_{H} ($2.73 \times 10^{19} \text{ cm}^{-1} \text{ s}^{-1}$) and b_{H_2} ($1.46 \times 10^{19} \text{ cm}^{-1} \text{ s}^{-1}$) based on the modern relative abundances of H and H_2 at the homopause. In detail, these values will vary slightly depending on the homopause temperature and background atmospheric composition. To find the reduction in escape efficiency necessary to achieve a given $f_T(\text{H}_2)$, we solve for α

$$\alpha = \frac{\beta \Phi_{\text{volc}}(\text{H}_2) H_a}{b_{H_n}} \cdot \frac{1 + f_T(\text{H}_2)}{f_T(\text{H}_2)}, \quad (3.13)$$

setting $f_T(\text{H}_2)$ to a desired atmospheric mixing ratio of H_2 and keeping in mind that α is an efficiency factor bound between 0 and 1, defining how far below the diffusion limited loss rate H_2 escape is occurring.

3.5 $f_T(\text{H}_2)$ systematics with $f\text{O}_2$ and pressure

We initially examine how $f_T(\text{H}_2)$ varies with $f\text{O}_2$ and vent pressure alone, across three different initial volatile contents. Different pressures are considered to cover the range of vent pressures relevant for the Archean (from 3 to <0.5 bar, e.g., Goldblatt et al., 2009; Som et al., 2016; Rimmer, Shorttle, et al., 2019). They also cover pressures relevant to vents in submarine settings under shallow oceans, a possible scenario for the Archean (Flament et al., 2008).

Depending on the initial volatile content of the melt (see Appendix B, Section B.1) and the vent pressure, more reduced melts can sustain an atmosphere with a greater fraction of H_2 (Fig. 3.1), with a decrease in $f\text{O}_2$ of 2 log units providing a $15\times$ increase in $f_T(\text{H}_2)$. $f_T(\text{H}_2)$ converges on a maximum value at low $f\text{O}_2$, which is dependent on greatest achievable $f_T^v(\text{H}_2)$ for a melt's volatile content and vent pressure (see Appendix B and Section B.1). $f_T(\text{H}_2)$ for a fixed $f\text{O}_2$ decreases with increasing surface pressure, although there is very little difference

3.5 $f_T(H_2)$ systematics with fO_2 and pressure

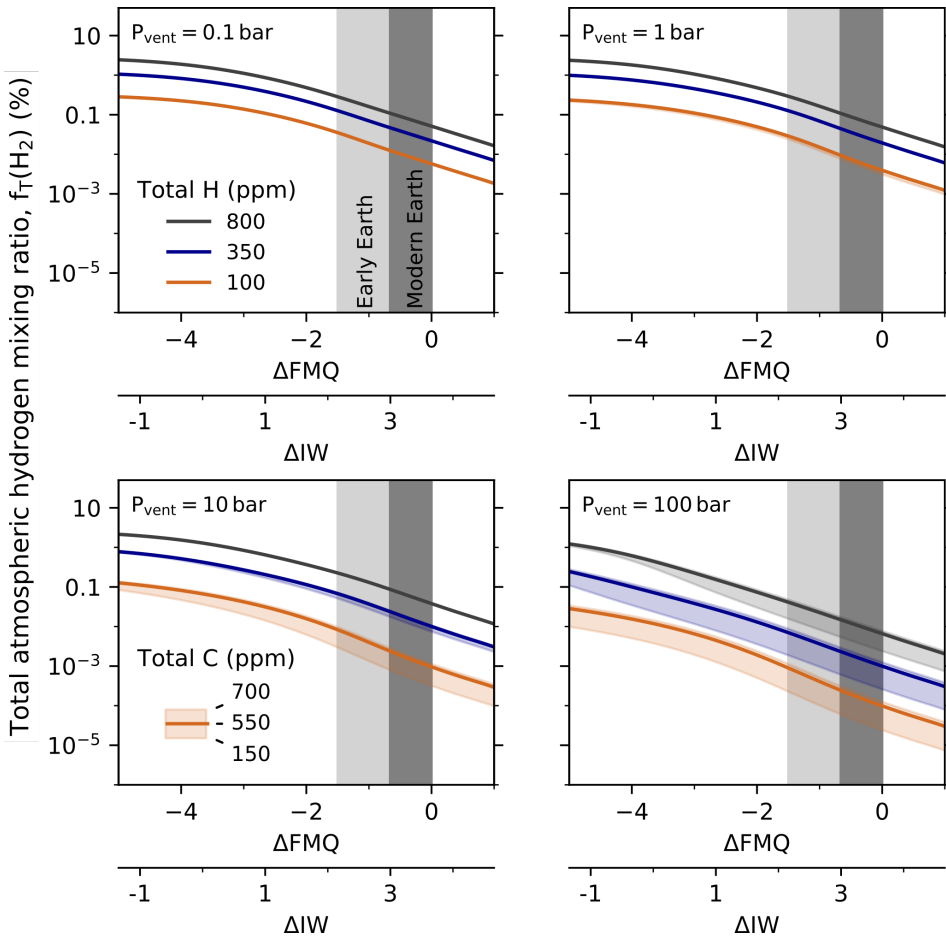


Fig. 3.1 Total hydrogen mixing ratio sustained in the troposphere according to the oxygen fugacity of the degassing magma. Calculations assume the loss of hydrogen to space is diffusion limited ($\alpha=1$), and consider four different vent pressures all with a volcanic flux equal to the modern Earth ($\beta = 1$). Results are shown for three different H contents, all with 1000 ppm S and, and indicating the effect of a variable C content between bounds of 150 and 700 ppm C. At FMQ and 1 bar pressure, 150, 550 and 700 ppm C correspond to approx 550, 2000 and 2500 ppm total CO₂ in the system, and 0.09, 0.3 and 0.7 wt % H₂O for 100, 350, 800 ppm H respectively. Both the CO₂ and H₂O contents are almost entirely partitioned into the gas phase at 1 bar pressure. The modern range in MORB fO_2 is highlighted as a dark grey bar (Bézos and Humler, 2005), with a possible lower bound on Archean fO_2 represented in light grey (Aulbach and Stagno, 2016; Nicklas et al., 2019).

in the results for 0.1 and 1 bar. This is due to the pressure dependent solubility of water and sulphur species; at high vent pressures a smaller fraction of the system's volatiles have exsolved and are available to form the $f_T^V(H_2)$ fraction, effectively decreasing the volcanic flux. Atmospheres fed by H-poor magmas show a greater decrease in $f_T(H_2)$ as surface pressure

Can Volcanism Build Hydrogen–Rich Early Atmospheres?

is increased. The scale of this decrease is greater the more oxidised the system is. H-poor systems are particularly sensitive, as water is very soluble in basalt: for a 100 ppm H system at $f\text{O}_2 > \text{FMQ-3}$, 45 % of the H content (almost entirely speciated as water) can remain dissolved in the melt even at 1 bar pressure. In contrast, for an 800 ppm H system, < 10 % of the total hydrogen is still stored in the melt at 1 bar and with an $f\text{O}_2 > \text{FMQ-1}$.

Higher pressure also results in greater variability of $f_T(\text{H}_2)$ with carbon content. At low pressures, and to some extent low $f\text{O}_2$, a carbon content change of $\sim 4.5 \times$ produces a negligible impact on atmospheric $f_T(\text{H}_2)$. However, at high pressures and higher $f\text{O}_2$, this range changes the $f_T(\text{H}_2)$ by almost 1 order of magnitude. $f_T(\text{H}_2)$ increases with C content at high pressures because the magma reaches CO_2 saturation earlier, and forms a gas phase within the melt at higher pressures. Hydrogen bearing species can then partition into this gas phase and be degassed at higher pressures than they would be in a C-poor magma.

3.6 Achieving volcanically-sustained H_2 atmospheres

Figure 3.1 suggests that for a very reduced planet with a moderate to low pressure atmosphere and with a mantle volatile budget, volcanic flux, and stellar environment otherwise similar to the modern Earth, the maximum $f_T(\text{H}_2)$ achievable is 3.2 %. More conservatively, considering the range of magma $f\text{O}_2$ likely across Earth history (e.g., Bézos and Humler, 2005; Aulbach and Stagno, 2016; Nicklas et al., 2019), represented as the dark and light grey bars in Fig. 3.1, the maximum possible $f_T(\text{H}_2)$ from this model would be 0.4 %, assuming ≤ 1 bar surface pressure and a high H content. This result is consistent with the 0.1 % $f_T(\text{H}_2)$ often quoted for the Archean (Walker, 1977; Kasting, 1993), but it requires degassing pressures of less than 10 bar and > 350 ppm H in the melt. To achieve values of $f_T(\text{H}_2)$ more conducive to greenhouse heating, prebiotic chemistry, and to match evidence for ~ 1 % $f_T(\text{H}_2)$ (Zahnle et al., 2019), an increase in the volcanic flux ($\beta > 1$, Fig. 3.2), or a reduction in the loss efficiency, $\alpha < 1$ (Fig. 3.3) must be invoked. We therefore explore varying these two parameters in this section.

3.6.1 Changing the volcanic flux

A change in the volcanic flux can modify the H_2 flux to an atmosphere (see Eq. (3.12) and Fig. 3.2) and is representative of either, 1) a change in the magma’s initial volatile content, 2) a greater proportion of magma reaching low pressure, or 3) increased magma production. Here, we have examined a range of volcanic fluxes from modern to $20 \times$ the modern rate. As expected, increasing the volcanic flux produces a nearly proportional increase in $f_T(\text{H}_2)$ (Fig. 3.2); proportional where $f_T(\text{H}_2) \ll 1$, and slightly less than a proportional as $f_T(\text{H}_2)$

3.6 Achieving volcanically-sustained H₂ atmospheres

increases above this point. Increasing the H content from 350 ppm to 800 ppm is equivalent to increasing the volcanic flux by 2-3×. For a magma at FMQ -1.5, increasing the volcanic flux to 10× modern produces an $f_T(\text{H}_2)$ of 1.6 - 3.4 % for 350 ppm H and 800 ppm H, respectively.

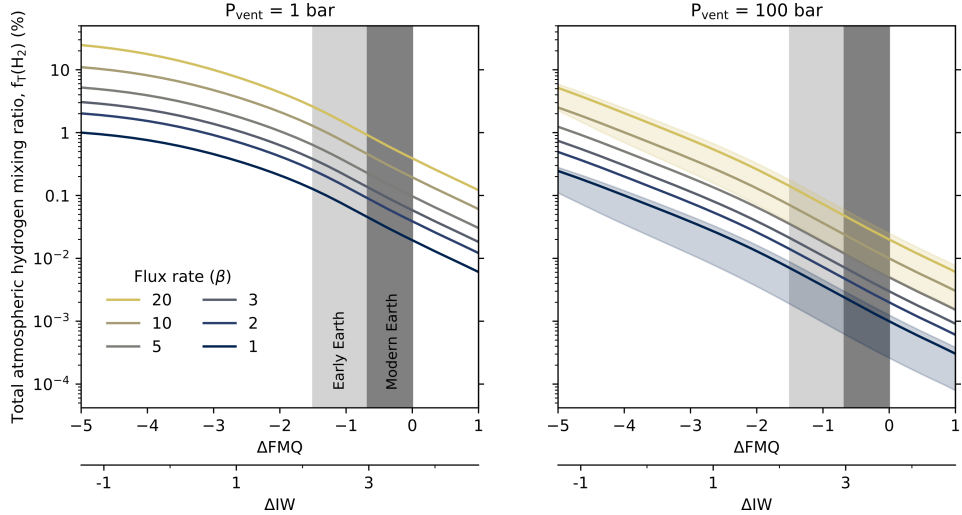


Fig. 3.2 The effect of a higher volcanic flux on the hydrogen mixing ratio, $f_T(\text{H}_2)$, in the atmosphere. Calculated with a volatile content of 350 ppm H, 550 ppm C and 1000 ppm S at 1 and 100 bar, $\alpha=1$. Lines are coloured according to the flux, and the dark/light grey bars represent the fO_2 of modern Earth MORB and possible early Earth basalts respectively. Shaded bands of uncertainty in the 100 bar panel represent the area of 150 - 700 ppm C in the melt for flux rates of 1 and 20×.

The 100 bar panel in Fig. 3.2 indicates that even with very high fluxes and a reduced Archean melt, the maximum achievable $f_T(\text{H}_2)$ would be around 0.2 %. Only a highly reduced planet erupting melts around the IW buffer, with a high volatile content (equivalent to >400 ppm H) would see $f_T(\text{H}_2)$ contents above 1 % in an atmosphere if the average vent pressure is at 100 bar. We therefore suggest that without significant modification to the hydrogen escape rate, it is unlikely that an early Earth scenario with the majority of its volcanism occurring in submarine settings could attain a hydrogen-rich secondary atmosphere. Exoplanets covered by global oceans, and those with dense atmospheres (e.g., CO₂-rich atmospheres similar to that of Venus) would similarly have to be erupting highly reduced melts with a high volcanic flux, and/or have a lower hydrogen escape rate to achieve an atmosphere with an $f_T(\text{H}_2)$ on the order of 1% or above.

3.6.2 Changing the H₂ escape rate

Rather than modifying the volcanic input term to the atmosphere, hydrogen can be built up in the atmosphere by reducing the loss rate to space. So far, we have considered loss rate to be purely diffusion-limited, as it is on the modern Earth (Catling and Kasting, 2017). However, if the loss rate were less efficient, a greater $f_T(H_2)$ could be achieved for the same fO_2 and volcanic flux. We have parameterized the reduction in loss efficiency as α , and calculated the value of α required to achieve a certain $f_T(H_2)$, for a given magma fO_2 and $\beta=1$ (Fig. 3.3).

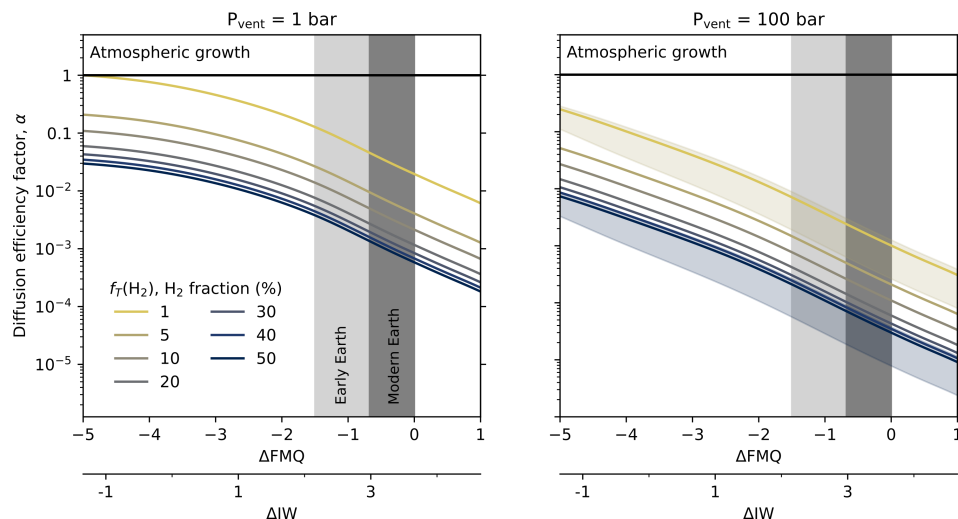


Fig. 3.3 Values of alpha required to achieve a certain hydrogen mixing ratio in the atmosphere, dependent on the fO_2 of the degassing melt. For melt with 350 ppm H, 550 ppm C, 1000 ppm S, degassing at either 1 or 100 bar vent pressure, $\beta = 1$. Shaded bands of uncertainty in the 100 bar panel represent the area of 150 - 700 ppm C in the melt for $f_T(H_2) = 1$ and $f_T(H_2) = 50$. An α value > 1 indicates a diffusion limited loss rate greater than today's would be necessary to limit the H₂ content of the atmosphere to the specified fraction; as this is unlikely, we infer that $f_T(H_2)$ would increase until steady state is reached at $\alpha = 1$.

At the reduced end of Fig. 3.3, around IW, a loss rate of $\alpha=0.1$ (i.e., 10 % of modern) is enough to build up an $f_T(H_2)$ of 10 %. In contrast, across the more oxidised magmatic conditions prevailing over Earth history, an α of 0.16 - 0.025 is needed to build up a 1 % mixing ratio of H₂ in a 1 bar atmosphere. Increasing the volatile content to 800 ppm H allows α to increase to 0.4-0.06 while still generating 1 % H₂ at 1 bar. However, once the vent pressure has been increased to 100 bar, $\alpha < 8 \times 10^{-3}$ is required to achieve 1 % $f_T(H_2)$ given Earth's magmatic fO_2 . Large reductions in escape efficiency below the diffusion limit are required to obtain $f_T(H_2)$ at the percent level. We discuss whether such values for α are plausible in the following section, but this suggests that the volatile content and rate of volcanism could be the

key variables in achieving a hydrogen-rich secondary atmosphere, rather than large changes in the atmospheric loss rate.

3.7 H₂ on the early Earth

Using a thermodynamic magma degassing model, we have mapped the parameter space for producing a terrestrial atmosphere with a significant H₂ mixing ratio. The parameters we have considered are magma *fO*₂, volatile content, volcanic outgassing flux, and atmospheric escape efficiency as variables. A 6 log unit change in *fO*₂ can produce a change in *f_T(H₂)* of around a factor of 100. On planetary bodies with a reduced mantle such as Mars, volcanic fluxes comparable to those likely over the evolution of the Earth (1-12× modern e.g., Sleep and Zahnle, 2001; Korenaga, 2006; Avice et al., 2017) could result in secondary atmospheres with hydrogen fractions on the order of 1-10's of percent. However, over the restricted range of *fO*₂ likely for the Archean Earth, the most effective way to achieve an *f_T(H₂)* > 1% is to vary both the outgassing flux and the loss efficiency within ranges closer to modern.

3.7.1 Likely escape rates on the early Earth

The escape rate of hydrogen from an atmosphere with a given *f_T(H₂)* will decrease below the diffusion limited escape rate, if removal of H₂ from above the homopause becomes less efficient. In this scenario, H₂ escape becomes energy limited by the incident XUV flux (e.g., Tian et al., 2005). Luger and Barnes, 2015 describe the energy-limited mass loss rate (*m_{XUV}*) as

$$\dot{m}_{\text{XUV}} = \frac{\varepsilon_{\text{XUV}} \pi \mathcal{F}_{\text{XUV}} R_p R_{\text{XUV}}^2}{GM_p K_{\text{tide}}} \quad (\text{gs}^{-1}), \quad (3.14)$$

where ε_{XUV} is the absorption efficiency of XUV, \mathcal{F}_{XUV} is the XUV flux at the top of atmosphere, M_p is the mass of the planet, R_p is the planet radius, R_{XUV} is the radius where the bulk of the energy is deposited (which, for simplicity, we take to be equal to R_p), and K_{tide} is a tidal correction term of order unity. We convert this equation into units of flux,

$$\Phi_{\text{XUV}} = \frac{\varepsilon_{\text{XUV}} S \mathcal{F}_{\text{XUV}} R_p N_A}{4GM_p M_{\text{H}_2}} \quad \text{H}_2 \text{ (molecules cm}^{-2} \text{s}^{-1}\text{)}, \quad (3.15)$$

where S is the XUV irradiation relative to modern Earth, \mathcal{F}_{XUV} is the modern XUV flux of 4.5 ergs cm⁻² s⁻¹ for Earth (Ribas et al., 2005), N_A is Avogadro's constant (6.022×10^{23} mol⁻¹) and M_{H_2} is the molecular mass of a H₂ molecule (2.02 g mol⁻¹). Equation (3.15) shows that as planetary mass decreases, the Φ_{XUV} increases, getting closer to the diffusion limited rate (Φ_{diff}).

Can Volcanism Build Hydrogen–Rich Early Atmospheres?

At the same time, the diffusion limited flux decreases as $\Phi_{\text{diff}} \propto$ gravitational strength. Hence as planetary mass decreases, the difference between the energy limited and diffusion limited fluxes decreases, and the resulting H₂ escape flux is reduced. Equation (3.15) is also highly dependent on the absorption efficiency of XUV, ϵ_{XUV} . This value is typically fixed at 0.1 for terrestrial planets with high molecular weight atmospheres (e.g., Lopez et al., 2012; Owen and Alvarez, 2015; Bourrier et al., 2017), and is linked to the availability of different atmospheric species. For example, high H₂ fractions cause more efficient XUV absorption, a greater heating rate and faster escape; the presence of IR cooling molecules such as CO₂ reduces the amount of thermal energy which can be converted into atmospheric escape, reducing the loss rate.

Modelling of the hydrogen escape flux compared to diffusion limited and energy limited escape rates, depending on the activity of the Archean sun, has been carried out by Tian et al., 2005; Kuramoto et al., 2013 and Zahnle et al., 2019 (with these results summarised in Fig. 3.4). These models of the early Earth use a very low temperature for the exobase (250 K compared to the modern 1000 K), after assuming an anoxic and CO₂-rich atmosphere, similar to Mars and Venus today. A cold exobase makes the Jeans' escape rate minimal, so that hydrodynamic escape controls escape efficiency. However, the temperature of the Archean upper atmosphere is highly debated, and will strongly depend on the atmospheric composition (Catling, 2006) and non-LTE effects, the operation of which in the Archean atmosphere are poorly constrained. A warmer exobase would increase the overall rate of loss, making it more likely the loss occurred at, or close to, the diffusion limit; therefore the hydrodynamic loss rates seen below should be considered a lower limit of escape rate and α .

In Fig. 3.4 the escape flux from the model of Zahnle et al., 2019 is compared to both the diffusion limited escape rate, and an XUV energy-limited rate. Young stars are more active, and therefore emit more XUV radiation earlier in their life-cycles, so the average incident XUV (\mathcal{F}_{XUV}) at 2.5 Ga is thought to be around 2.5-3× today's, up to 5 -10× modern at 3.5 Ga depending on whether the Sun was a slow or fast rotator early in its lifetime (Tu et al., 2015). Higher radiation levels drive higher rates of hydrogen loss above the exobase following the slope of XUV limited escape, until loss starts to asymptote to the diffusion limit, i.e., is limited by supply of H₂ to the hydrogen escape region. During the solar cycle today, the XUV flux can vary by up to a factor of 5 between a quiet and active sun; however, this variation occurs on a high frequency ∼11 year cycle, so has been ignored in preference for an average XUV flux to calculate $f_T(\text{H}_2)$. α is defined as

$$\alpha = \frac{\text{hydrodynamic loss rate}}{\text{diffusion limited loss rate}}, \quad (3.16)$$

which is plotted in Fig. 3.4, representing a fractional reduction in the escape efficiency from the diffusion limited case. Figure 3.4 suggests that a reasonable range for α on the early Earth,

assuming an $f_T(H_2)$ of 10 % or less, is ~ 0.2 at 2.5 Ga, and 0.5-0.6 at 3.5 Ga. Comparing these values of α to those explored in Fig. 3.3, suggest that achieving an $f_T(H_2)$ on the order of 1 % or higher seems implausible for a high pressure degassing scenario on the early Earth, and indicates that an increase in the volcanic flux compared to modern is likely to be necessary even at lower degassing pressures.

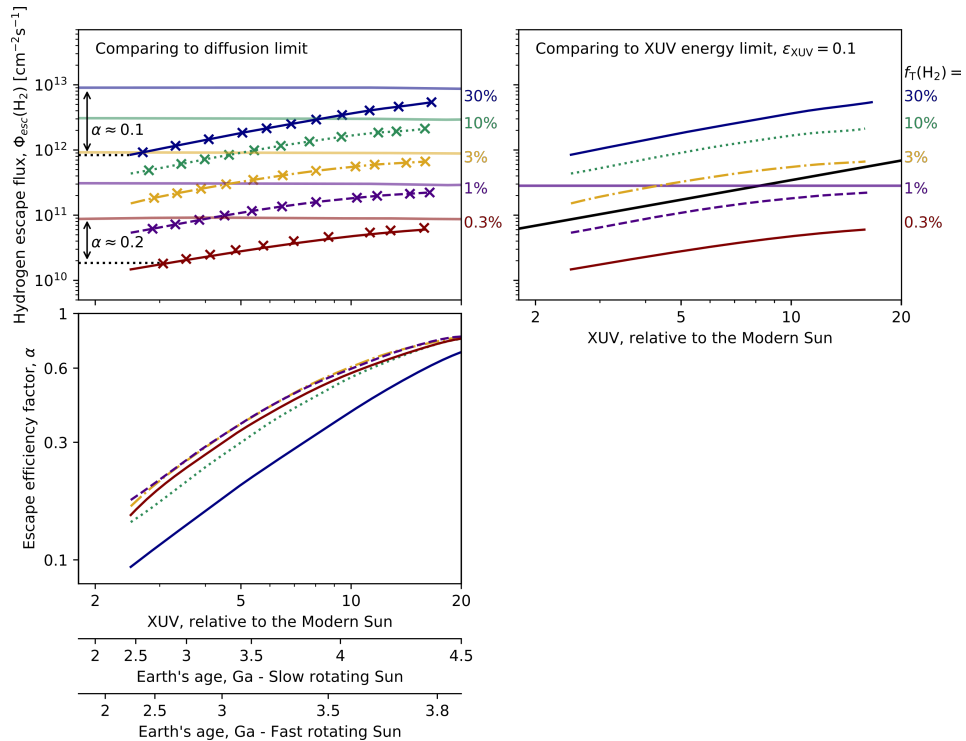


Fig. 3.4 Top left: Crossed lines represent the hydrodynamic hydrogen flux from an atmosphere with an exobase temperature of 250 K, with the solid lines representing the diffusion limited flux for the same atmosphere. Escape fluxes have been calculated for several different values of $f_T(H_2)$ (taken from Zahnle et al., 2019), represented by changing colour and dash type, as a function of XUV flux (Extreme UV). Top right: The same hydrodynamic fluxes are shown, this time compared to an XUV limited flux (diagonal black line) calculated using Eq. (3.15), $\varepsilon_{\text{XUV}} = 0.1$ and the diffusion limit for 1 % $f_T(H_2)$ (horizontal line) as a reference. Bottom: The difference between the diffusion limited flux and the hydrodynamic loss rate gives α ($\alpha = \frac{\text{hydrodynamic loss rate}}{\text{diffusion lim. loss rate}}$), which is primarily a function of XUV flux, and largely insensitive to $f_T(H_2)$ for most values below 30 %. An α of 1 is an escape efficiency equal to the diffusion limited escape rate.

3.7.2 Hydrogen mixing ratios on the Archean Earth

In the previous sections, we have demonstrated that varying both the volcanic flux and the atmospheric loss rate can result in significant variation in atmospheric $f_T(H_2)$ at a given magmatic fO_2 , compared to $f_T(H_2)$ calculated with a modern volcanic flux and $\alpha = 1$. Here, we explore the range of potentially achievable H_2 mixing ratios for a planet with similar stellar and volcanic flux parameters to those suggested for the early Earth, examined over a wide range of fO_2 (Fig. 3.5).

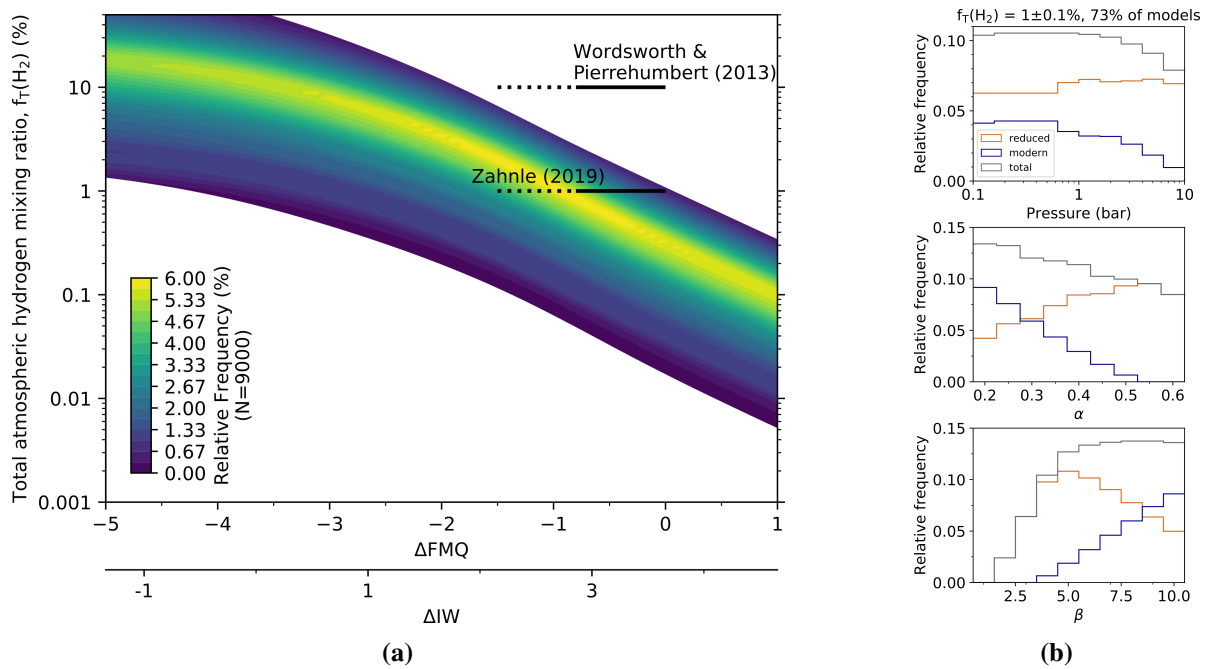


Fig. 3.5 (a) The relative frequency of hydrogen mixing ratios in an atmosphere as a function of the magma fO_2 , represented as a 2D density surface. This calculation considers varying parameters uniformly over the ranges, $\alpha = 0.2-0.6$, $\beta = 1 - 10$ and surface pressures of 0.1 - 10 bar. White regions are unphysical. Horizontal bars indicate 1 and 10 % $f_T(H_2)$, plotted across the modern Earth (solid bar Bézos and Humler, 2005) and early Earth (dashed bar Aulbach and Stagno, 2016; Nicklas et al., 2019) mantle fO_2 range. (b) Relative frequency distributions for the three parameters varied in panel (a), for models which can achieve $1\pm0.1\%$ $f_T(H_2)$ within the magmatic fO_2 range of Earth, labelled with the percentage of model runs which meet these constraints. The plots show a breakdown of the total distribution between models which calculate 1 % $f_T(H_2)$ within the modern (blue) or early Earth (red) fO_2 ranges (grey is total).

Figure 3.5 suggests that for a single value of magma fO_2 , varying surface pressure, volcanic flux and loss rate over plausible ranges can result in a change in the mixing ratio by around a factor of 100. Assuming an Archean magma fO_2 between FMQ-1.5 and FMQ, a 2.5-10× increase in solar XUV (and therefore a range for α of 0.2-0.6 for an atmosphere with less than

30 % $f_T(H_2)$), a volcanic flux of 1-10× present and a vent pressure of 0.1-10 bar, the range of H₂ mixing ratios predicted for the Archean Earth is $\sim 0.02 - 7\% H_2$, with most models falling in the range 0.2 to 3 % $f_T(H_2)$ (0.18 - 4.5 % accounting for photochemical uncertainty, see Appendix B and Section B.2).

Results from Zahnle et al., 2019 have suggested H₂ mixing ratios on the early Earth of $\sim 1\%$. The parameter sweep shows that this can be achieved with a magmatic fO_2 within the range proposed for the Archean, and with only a weak dependence on degassing pressure and a moderate dependence on volcanic flux and loss rate (Fig. 3.5b). My results also show the trade offs between parameters which achieve this fit to $f_T(H_2) = 1\%$. Assuming an fO_2 similar to modern, the number of model runs which achieve 1 % $f_T(H_2)$ decreases with increasing pressure, strongly decreases as α increases with no runs above $\alpha = 0.5$, and increases when $\beta > 3$; no model runs within the modern fO_2 range meet $f_T(H_2)=1\%$ using the modern value of β . For a more reduced melt, the trends are more or less reversed, with a peak in model frequencies at around $\beta = 5$. The peak in the frequency distribution (Fig. 3.5) falls between FMQ -0.8 and FMQ -1, with a bias to the reduced fO_2 range. Our model indicates that 1 % $f_T(H_2)$, which Zahnle et al., 2019 posit Xenon isotope fractionation is indicative of, is easily achievable for the early Earth (Fig. 3.5) with 73 % of models obtaining 1 % $f_T(H_2)$ within Earth's mantle fO_2 range.

Wordsworth and Pierrehumbert, 2013b suggest that for an Archean atmosphere with CO₂ levels similar to modern, 10 % H₂ and 3× modern N₂ would be needed to raise the surface temperature above freezing, given the faint young sun. However within our parameter ranges, 10 % $f_T(H_2)$ cannot be achieved (Fig. 3.5). We therefore suggest that without alternative sources of H₂, or a large increase in the N₂ and CO₂/CH₄ atmospheric partial pressures compared to modern, it is unlikely that sufficient H₂-enhanced greenhouse warming was occurring to raise Archean surface temperatures above freezing.

3.7.3 Alternative H₂ sources on the early Earth

Our calculations so far have assumed that volcanic emissions are the only source of H₂ to the atmosphere in the Archean. However, while it may be true that the volcanic flux is likely to be the largest steady H₂ input, there are several other sources which may have contributed to the global H₂ budget, summarised in Fig. 3.6.

A particularly large source of uncertainty comes from the sources and sinks of hydrogen introduced by adding life into the model considerations. Kharecha et al., 2005 and Haqq-Misra et al., 2008 have suggested that up to 1000 ppmv CH₄ could be sustained by methanogenic biota in the late Archean. The H₂ flux this methane production is equivalent to, makes methanogens a potentially equal contributor to volcanism (at high volcanic fluxes) in sustaining atmospheric

Can Volcanism Build Hydrogen–Rich Early Atmospheres?

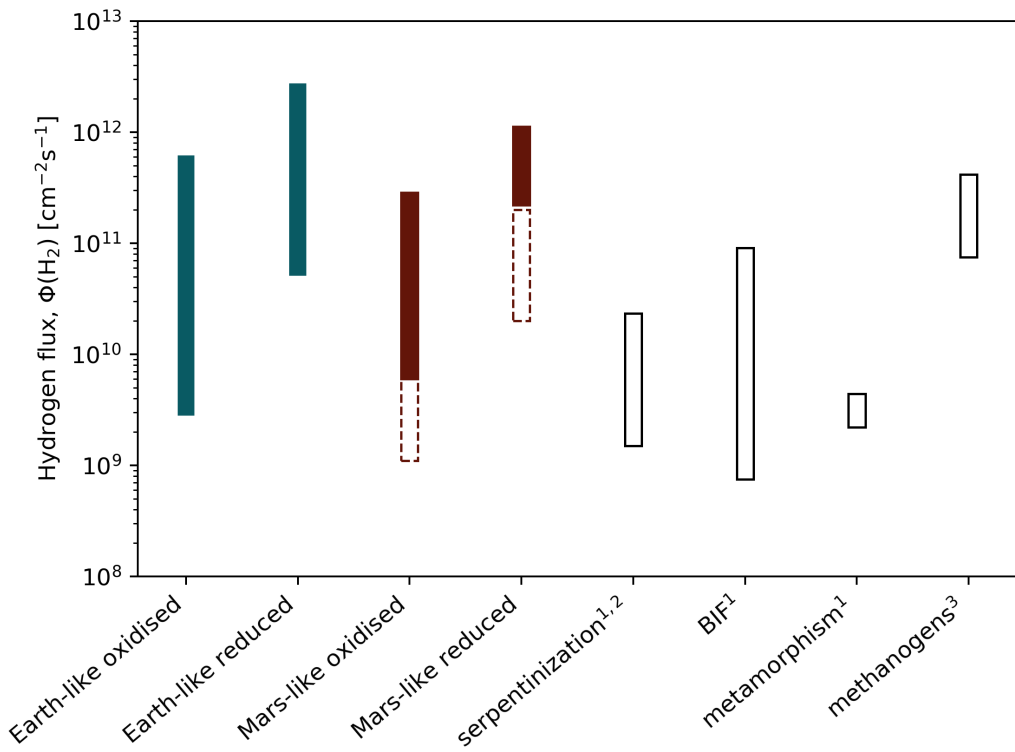


Fig. 3.6 A comparison of the fluxes of alternative sources of H₂ on the early Earth, and volcanic H₂ sources for planets similar to early Earth or early Mars. Solid bars represent a volcanic input, the range in possible $f_T(\text{H}_2)$ given by our volcanic H₂ model for 4 different conditions. Oxidised means FMQ to FMQ-2, reduced is FMQ -2.5 to FMQ -4.5 (IW -1 to IW +1). Earth conditions are for a range of 1-10 bar pressure and 1-10× modern flux using the previously described volatile content. Mars data uses the melt composition described in the main text, for vent pressures of 0.5 - 2 bar and 0.5 to 2× modern Earth volcanic flux. For Mars, solid bars represent hydrous conditions, dashed bars the dry conditions. Alternative sources of H₂ are represented by open bars. Data taken from: 1. Kasting, 2013, 2. Batalha et al., 2015, 3. Kharecha et al., 2005.

3.8 Atmospheric warming of early Mars

H_2 . Methanogens could therefore potentially significantly increase both the total input of hydrogen to the atmosphere and therefore the $f_T(H_2)$. However, adding methanogens also produces a sink of hydrogen in the form of organic carbon burial, potentially between 6×10^9 to 1.5×10^{10} molecules $\text{cm}^{-2} \text{s}^{-1}$ (Kasting, 2013). Although this is a fairly low flux compared to H_2 sources, it could become significant in cases where the volcanic hydrogen flux is low. Despite the important supply of H_2 life can provide to an atmosphere, methanogens of course cannot contribute to either a greenhouse atmosphere in a prebiotic system, nor to generating a reducing atmosphere required for prebiotic chemistry. If H_2 atmospheres are needed at this early stage of Earth's history, other sources must be considered.

Other geological sources of hydrogen include the serpentinisation of mafic and ultramafic oceanic crust, metamorphic outgassing, and release of H_2 during the formation of banded iron deposits (Kasting, 2013). Not included in Fig. 3.6 is the flux of hydrogen which could be delivered by a large impactor. This has been excluded as an impactor would provide a point source of hydrogen decaying over time, rather than a long-term steady flux, making this a significantly different proposition in comparison to other long term H_2 fluxes. However, the scale of the flux, a single point injection of possibly 3×10^{18} mols (assuming injection over the course of a year, this would be a point flux of 1×10^{16} molecules $\text{cm}^{-2} \text{s}^{-1}$ for a year; Zahnle et al., 2019), means that impactors could be important for transient high levels of hydrogen in the atmosphere.

3.8 Atmospheric warming of early Mars

At 3.8-3.6 Ga (during the Noachian period), Mars' climate appears to have been warm enough to sustain liquid water at the surface (e.g., Hoke et al., 2011). However, a pure CO_2 Martian atmosphere provides insufficient warming under a faint young sun (Forget et al., 2013). To address this, Hayworth et al., 2020 suggest that a range of H_2 contents of 5 - 8%, in 1.2 to 3 bar CO_2 atmospheres, could be sufficient to deglaciate the Martian surface in a cyclical manner. We therefore perform a similar parameter sweep to that conducted above for Earth, adjusted to be suitable for an early Mars-like planet, to assess the plausibility of this occurring given volcanic constraints. Here we compare 8 % $f_T(H_2)$ in a 1.25 bar atmosphere to the results of a parameter sweep similar to that conducted above. We account for the different scale height and diffusion rate of the Martian atmosphere by using a b_{H_n}/H_a ratio taken from Ramirez et al. (2014), of $1.6 \times 10^{13} \text{ cm}^{-2} \text{s}^{-1}$, which applies for a homopause temperature of ~ 160 K. Using values relevant to 3.8-3.6 Ga and accounting for the decay in XUV flux with orbital distance (irradiance at Mars is 36-53% weaker than at 1 AU Thiemann et al., 2017), the incident XUV flux at Mars would have been be in the range $\sim 2.2 - 9 \times$ that of the modern Earth, giving a

Can Volcanism Build Hydrogen–Rich Early Atmospheres?

similar range in α to those used for Earth (see Fig. 3.4; Tu et al., 2015). We therefore adopt the same range of alpha as used above, accepting that the XUV flux might have a significantly different effect on the escape rate of Mars compared to Earth, with the escape rate possibly being much higher (and therefore a larger value of alpha closer to 1) after scaling for Mars’ lower gravity.

We account for the different scale height and diffusion rate of the Martian atmosphere by using a b_{H_n}/H_a ratio taken from Ramirez et al. (2014), of $1.6 \times 10^{13} \text{ cm}^{-2} \text{ s}^{-1}$, which applies for a homopause temperature of ~ 160 K. Although the XUV flux at Mars is 36–53% weaker than at 1 AU (Thiemann et al., 2017), at 3.6–3.8 Ga the solar XUV flux is approximately double that of the period modelled for Earth. Both of these factors conspire to decrease the difference between the diffusion and energy limited flux regimes on Mars at the relevant time period, leading to increased α . By comparing the diffusion limited flux with XUV-limited escape using Eq. (3.15) and $\varepsilon_{\text{XUV}} = 0.1$, we plot α in Fig. 3.7.

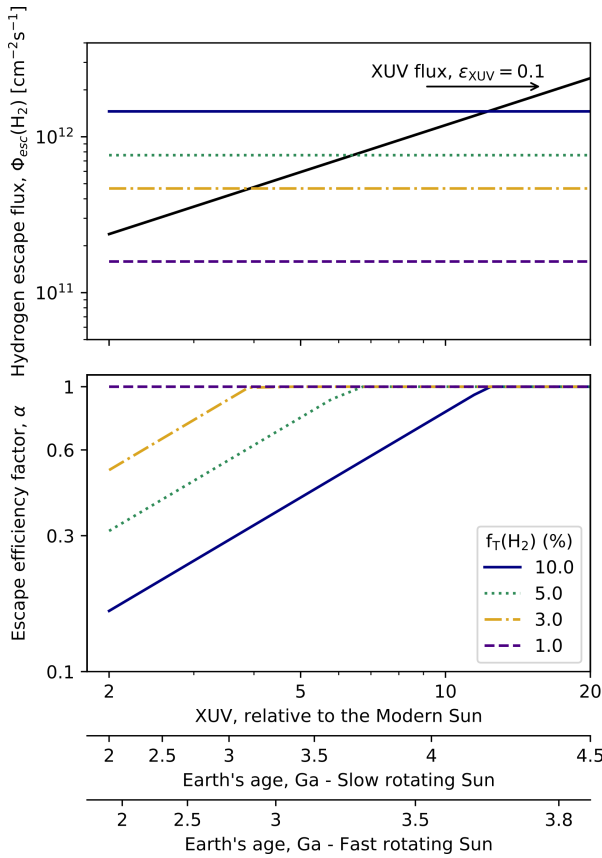


Fig. 3.7 Top: Comparing the diffusion limited escape rate (horizontal lines) to the energy limited escape rate (diagonal line) calculated using Eq. (3.15) Bottom: α calculated as XUV flux/diffusion limited flux.

If we assume that the H_2 loss rate proceeds exactly at the XUV limited rate until it intersects the diffusion limit (Fig. 3.7), for the period 3.8–3.6 Ga α would only be < 1 when $f_T(\text{H}_2) \geq 5\%$, with the greatest reduction below the diffusion limit being $\alpha=0.6$ for $f_T(\text{H}_2)=10\%$. However, this is not quite accurate; the true H_2 loss rate is likely to drop below the XUV limit

3.8 Atmospheric warming of early Mars

as the flux asymptotes towards the diffusion limit, prolonging the period where $\alpha = 0.7 - 0.9$ beyond that seen in Fig. 3.7 (see Fig. 3.4). We therefore use a range of 0.6 - 1 for α in Fig. 3.8.

The volcanic fluxes considered are 0.5-2× the modern Earth, in keeping with the idea that the heat flux in the Noachian was probably similar to the modern Earth's (Ramirez et al., 2014; Batalha et al., 2015). On this basis, we consider that the volume of magma reaching the surface per unit area should therefore be similar. However, this assumption relies on similar magmatic volatile contents between the two planets, and the primary volatile contents of early Martian magmas are very poorly constrained. Estimates of the pre-eruptive water contents of Martian magmas have ranged from nearly anhydrous through to around 2 wt % based on analysis of the SNC meteorites (e.g., McSween et al., 2001; McCubbin et al., 2012; Usui et al., 2012; Filiberto, Gross, et al., 2016), which sample magmas which were erupted at < 2 Ga (Nyquist et al., 2009). While differences in analytical technique may explain some of this variation, there are a large number of unknowns for Mars which could contribute to this uncertainty, including the extent of volatile recycling (e.g., Batalha et al., 2015; Magna et al., 2015), heterogeneous distributions of water in the mantle (McCubbin et al., 2016), the potential for volatile enrichment in magmas via crustal assimilation (McCubbin et al., 2016), and the evolution of mantle (and therefore magmatic) water contents through time (e.g., Filiberto, Baratoux, et al., 2016).

In light of the large uncertainty around the water contents of Martian magmas, we ran two parameter sweeps to find upper and lower limits on the potential atmospheric hydrogen content of Noachian Mars. The hydrous scenario, valid if volatile cycling (via crustal assimilation or other processes) or a large initial mantle water budget was present, is run with 550 ppm H, 200 ppm C, and 4000 ppm S, equivalent to 0.3 wt % H₂O and 600 ppm CO₂ dissolved prior to degassing at IW (e.g., upper limit of McCubbin et al., 2012). The dry scenario is run with equal C and S contents, and with 120 ppm H, equivalent to 0.03 wt % H₂O and 400 ppm CO₂ (Filiberto, Gross, et al., 2016; McCubbin et al., 2016). While the C content of Mars is equally uncertain, a variation in the magma carbon content of several hundred ppm would have a negligible effect on $f_T(H_2)$ at ∼ 1 bar pressure (Fig. 3.1) so the C content between the two runs remains fixed. Our results are summarised in Fig. 3.8.

Figure 3.8 indicates that across the likely range of magmatic fO_2 on Mars, the range of H₂ mixing ratios predicted for the hydrous scenario is ∼0.6 - 11 % H₂, with most models falling in the range 2 to 8 % $f_T(H_2)$ (0.9 - 15 % accounting for photochemical uncertainty, see Appendix B and Section B.2). We find that 42 % of models run at 1.2 ± 0.1 bar achieve a 5 % $f_T(H_2)$ within Mars' likely magmatic fO_2 range. The number of hydrous model runs which achieve 5 % $f_T(H_2)$ decreases as α increases, and Fig. 3.8 (b) shows a strong bias towards high values of β ; no model runs within Mars' fO_2 range meet $f_T(H_2) = 5\%$ with $\beta \leq 1$. Under a dry scenario, the most frequent results fall to 0.4 - 1.2 % $f_T(H_2)$ (0.1 - 3 with photochemical

Can Volcanism Build Hydrogen–Rich Early Atmospheres?

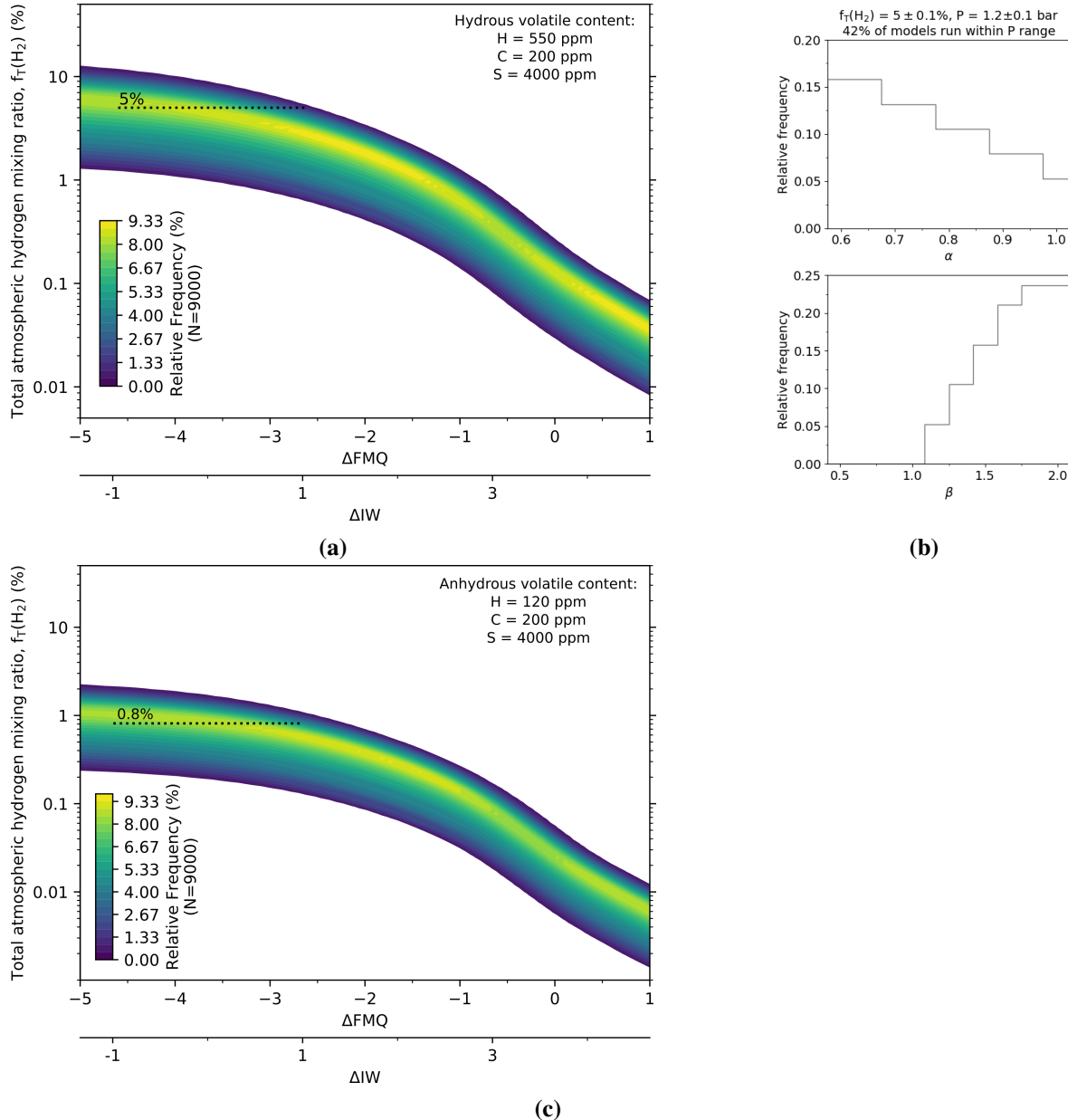


Fig. 3.8 (a) The relative frequency of model predictions of H_2 mixing ratios in the atmosphere of a Mars-like planet under the hydrous scenario as a function of the magma fO_2 , represented as a 2D density surface, assuming: $\alpha = 0.6 - 1$, β of $0.5 - 2$ and a surface pressure of $0.5 - 2$ bar (Kurokawa et al., 2018; Warren et al., 2019). White regions are unphysical. Horizontal bar indicates the estimated Martian fO_2 range. (b) Relative frequency distributions for the two parameters varied in the calculations presented in panel (a), for models which can achieve $5\% f_T(H_2)$ at 1.2 ± 0.1 bar pressure within the fO_2 range of Mars, labelled with the percentage of model runs which meet these constraints. (c) Relative frequency plot equivalent to (a) but for a dry scenario.

uncertainty, see Appendix B and Section B.2). Given the relative frequency with which hydrous degassing models with Martian parameters can generate $f_T(H_2) = 5\%$, it is plausible that a volcanically-driven hydrogen greenhouse effect contributed to the warm and wet Noachian period on Mars, particularly if erupting magmas are at or below the IW buffer (Fig. 3.8(a)). While under dry conditions this seems to be highly unlikely, as with Earth, there may also have been other geological sources of H₂ to the Martian atmosphere, such as weathering of white rust (Fe(OH)₂, Tosca et al., 2018).

A key requirement of H₂-driven warming on Mars is that the atmosphere is dominantly CO₂. However, under reducing conditions with a high S content and a hydrous melt, most of the gas emission occurs as H₂ and H₂S, with C-bearing species only making up $\sim 5\%$ of the gas emitted (as a molar fraction). Ramirez et al., 2014 suggest that the CO₂ in the atmosphere could be sourced from volcanism through indirect CO and CH₄ reactions, but if less than 5 % of the volcanic emissions are carbon-bearing species, then it may pose a challenge for a CO₂-H₂ atmosphere to be maintained solely through volcanism.

Ramirez et al., 2014 also suggest that the atmospheric CO₂ could have been sourced earlier in Mars' history through the initial solidification of the upper 50 km of Mars' crust. However, carbon in Mars' atmosphere is thought to have been lost via hydrodynamic escape prior to 4.1 Ga, suggesting a CO₂-rich atmosphere from crustal solidification could not have been maintained (Tian et al., 2009). One possible solution to this is an intrinsically more carbon-rich martian mantle; this would have a minimal effect on the hydrogen fraction produced (Fig. 3.1), but could increase the flux of C-bearing species to the atmosphere. As the constraints on the volatile content of the Martian interior are very uncertain, it is difficult to rule this out.

3.9 Conclusions

We have investigated the possibility of volcanism sustaining secondary atmospheres with a high H₂ mixing ratio. We have found that $f_T(H_2)$ values of several percent can be maintained, even with relatively oxidised magmatic sources such as those seen on Earth. As the magmatic fO_2 decreases, the $f_T(H_2)$ sustained increases, to the point where the assumption that H₂ is a minor species breaks down as $f_T(H_2)$ approaches 50 %. These high H₂ fractions are very unlikely to be formed where the volcanic degassing occurs under high atmospheric pressure or underwater, and for more oxidising magmas a greater volcanic flux and/or a less efficient H₂ loss to space is necessary to maintain significant atmospheric H₂ fractions.

We have found that a sustained $\sim 1\%$ hydrogen atmosphere is plausible for the early Earth, given the likely range of magmatic and surface conditions, and does not require a mantle source reduced beyond that seen today. However, H₂ mixing ratios at the 10% level cannot

Can Volcanism Build Hydrogen–Rich Early Atmospheres?

be achieved given the likely conditions and magmatic $f\text{O}_2$ on the early Earth, without supply from another source or suppression of escape beyond that which we consider is plausible. H₂-enhanced warming is therefore unlikely to have significantly contributed to counteracting the faint young sun. In the case of Mars, we suggest that sufficient H₂ could be degassed to carry out greenhouse warming if primary Martian magmas are relatively water-rich. However, the challenge under this scenario is that there may not have been a sufficient CO₂ source for this greenhouse mechanism to be viable; only ~ 5 mol % of volcanically degassed species are carbon-bearing under hydrous conditions according to our model, and any CO₂ from early crustal solidification is likely to have already been lost. The sensitivity of these results to primary magmatic water contents shows the importance of improving constraints on the volatile content of Mars' mantle, for understanding the planet's early climate.

4

Secondary Volcanic Atmospheres: Growth and Evolution on Hot Rocky Planets

4.1 Introduction

Planetary atmospheres can have three different origins: nebular gas accreted from the protoplanetary disk (primordial); early, syn-accretionary gas release from planetesimal accretion or outgassing during the cooling of a magma ocean (primary); or long-term release of volatiles from the planetary interior e.g., through volcanism (secondary). The atmospheres of rocky planets may evolve from primordial/primary to secondary as they undergo significant modification by geological and atmospheric processes, altering the atmosphere's mass fraction and chemical composition. Modification processes include hydrodynamic escape, erosion and volatile addition from impacts, and volcanic outgassing of volatiles from the interior (see Table 4.1 for references). A more extensive list of processes which can modify planetary atmospheres, and associated literature which has investigated these effects, can be found in Table 4.1.

Here, we focus on secondary atmospheres which form as a result of volcanic outgassing. The chemistry of volcanic gases is dependent on the oxygen fugacity ($f\text{O}_2$) of the magma (and likewise the mantle from which the magma was formed, e.g., Burgisser et al., 2015; Gaillard et al., 2015; Ortenzi et al., 2020), surface pressure through volatile solubility in magmas (Gaillard and Scaillet, 2014), and the relative abundance of volatile elements (i.e., H, C, O, S and N) within the magma. The secondary atmospheres of volcanically active rocky planets are therefore inextricably linked to their geological state. This is particularly useful when

Secondary Volcanic Atmospheres: Growth and Evolution on Hot Rocky Planets

considering studies of exoplanets, where secondary atmospheres could provide key insight into planetary interiors through the window of volcanic activity.

The geological properties of a planet, such as size, mantle fO_2 and volatile H/C ratio in the bulk silicate planet (the ratio of H/C in the planet's earliest mantle), are both dependent on, and in turn help to control, many facets of rocky planet evolution. The mass of a planet may control mantle fO_2 (Wade and Wood, 2005), along with the planet's location in the protoplanetary disk and core formation processes (Frost et al., 2008). The bulk silicate H/C ratio could be dependent on the initial ^{26}Al content of the protoplanetary system (Lichtenberg et al., 2019), degassing during early planetary differentiation (Hirschmann et al., 2021) and the quantity of both water and carbon in the magma ocean during core formation, which results in the sequestration of hydrogen and carbon within the core (Grewal et al., 2021; Tagawa et al., 2021). The predicted atmospheric compositions of rocky exoplanets based on geological properties, such as mantle fO_2 and initial volatile content, can in principle be compared to observations to test planetary formation and evolution scenarios. While properties such as the size and interior structure of a planet can already be observed, or may be inferred using mass radius observations (e.g., Dorn et al., 2017), establishing the mantle fO_2 or the bulk silicate H/C ratio will require observations of atmospheric chemistry.

The composition and speciation of volcanic gases can be linked to the fO_2 and volatile content of the magmas they originate from (e.g., Holloway, 1987; Gerlach, 1993; Moretti and Papale, 2004; Iacovino, 2015). However, when degassed into an atmosphere these gases mix and are subject to various processes which will act to complicate the link between the mantle of a planet and its volcanic atmosphere (See Table 4.1). For example, as volcanic outgassing proceeds, the surface pressure increases, which in turn affects the volume and composition of the volcanic gases being emitted. At higher atmospheric pressures, water outgassing is suppressed (Gaillard and Scaillet, 2014), making the emitted gases proportionally more carbon-rich. If atmospheric escape is occurring concurrently, then mass is also being lost from the atmosphere, and is acting to decrease the surface pressure. The loss of H atoms via hydrogen escape (explored in Chapters 3 and 6) will modify the redox chemistry of the atmosphere (e.g., Kasting, 1993; Wordsworth and Pierrehumbert, 2014), while drawdown processes which preferentially remove certain species (e.g., the carbonate-silicate cycle removing CO_2) will affect the atmospheric composition by leaving behind elements which are less sensitive to drawdown processes to build up in the atmosphere (e.g., N; Hu and Diaz, 2019).

Volcanic gases, once input to an atmosphere, will be cooled to the temperature of the planet's surface environment, changing their speciation compared to that at their eruptive conditions (Gaillard et al., 2021). There will be limits on the extent of volcanic gas re-equilibration at lower atmospheric temperatures, where gases may quench at their high temperature speciations and

4.1 Introduction

remain in disequilibrium within the atmosphere on long timescales. Here, we focus on planets with high atmospheric temperatures, $\geq 800\text{ K}$, where quenching is likely to be insignificant on long timescales. Hot rocky planets are a key class of rocky exoplanet of which there is only one example in the solar system (Venus), and are the most amenable to observation in the next 5-10 years as their short period orbits increase the observational duty cycle. At 800 K it is plausible that volcanic gasses, once added to and mixed with the atmosphere, will be able to evolve to low temperature thermochemical equilibrium. See Chapter 5 for a complete analysis of the reactions that regulate the attainment of thermochemical equilibria in secondary volcanic atmospheres, and the temperature requirements for thermochemical equilibrium to be achieved.

Previous investigation into the formation of secondary volcanic atmospheres has focused on factors such as the mass, bulk composition, tectonic regime, early volatile content, graphite saturation of magmas, and orbital distance of a planet can affect volcanic outgassing and the resultant secondary atmosphere composition. These past studies have identified several key features of volcanic secondary atmospheres and how they relate to the broader geodynamic state of the planet: planets which are more massive ($>2\times$ the mass of Earth, Noack et al., 2017; Dorn et al., 2018), which have graphite saturated magmas (Guimond et al., 2021), or which have a high iron to silicon ratio (Spaargaren et al., 2020) will have lower outgassing rates; stagnant lid planets may grow more massive atmospheres than those with plate tectonics (Spaargaren et al., 2020) (although this is controversial, e.g., Kite et al., 2009; Noack et al., 2014); and rocky planets which form with thick primordial atmospheres are less likely to have long-lived secondary atmospheres (Kite and Barnett, 2020). Ortenzi et al. (2020) have also recently investigated the effect of mantle $f\text{O}_2$ on the atmospheres of rocky planets; however, their modelling focused on the atmospheric composition in terms of the outgassed mass of H_2O , CO_2 , CO and H_2 at very high temperatures (around 2000 K) and without considering adjustment of the atmosphere to thermochemical equilibrium at surface temperatures.

Here, we model how secondary atmospheres on hot stagnant lid planets will grow and evolve over time. This regime is chosen as high surface temperatures ($>400\text{-}600\text{ K}$) are likely to inhibit the initiation of plate tectonics, due to the lack of surface water and a reduced temperature difference between the mantle and lithosphere (see Foley and Driscoll, 2016, and references within). The influence of mantle $f\text{O}_2$, the bulk silicate H/C ratio, and atmospheric temperature is investigated, using a C-O-H-S-N volcanic outgassing model. This expands on previous work (e.g., Gaillard and Scailet, 2014; Ortenzi et al., 2020) by including both sulfur and nitrogen species in the atmosphere, and accounting for the changes in speciation of gases which occur as a function of temperature. This also differs from the previous work discussed above by allowing the $f\text{O}_2$ of erupted magmas (and therefore the chemistry of their associated gas phase) to evolve as they are erupted, rather than fixing them at the $f\text{O}_2$ of the mantle.

Secondary Volcanic Atmospheres: Growth and Evolution on Hot Rocky Planets

In this chapter, we investigate the base case of volcanic secondary atmosphere formation and how these atmospheres may reflect planetary geochemistry; specifically, the mantle $f\text{O}_2$ and bulk silicate H/C mass ratio. The atmosphere is solely influenced by progressive volcanic degassing, and instantaneous cooling of the atmosphere to 800 K. These base atmospheres we present are therefore a foundation upon which additional physical and chemical atmospheric processes should be tested (e.g., the kinetics of cooling atmospheres, explored in Chapter 5, and H_2 escape in Chapter 6). In Section 4.2, we present our modelling technique. Results are shown in Section 4.3, with discussion and conclusions presented in Sections 4.4 and 4.5.

4.1 Introduction

Table 4.1 Processes which can modify the chemical composition and speciation of an atmosphere, and examples of previous papers which have discussed these processes in the context of exoplanet atmospheres.

Atmospheric modification processes on rocky planets	Considered here?	Other references
Volcanic outgassing	Yes	Gaillard and Scaillet (2014), Hoolst et al. (2019), Kite and Barnett (2020), Liggins et al. (2020), and Ortenzi et al. (2020)
Non-volcanic outgassing (e.g., serpentinization)	No	Guzmán-Marmolejo et al. (2013)
Thermochemical kinetic re-equilibration	See Chapter 5	Sossi et al. (2020) and Zahnle et al. (2020)
Atmospheric escape	See Chapter 6	Hunten (1973), Walker (1977), Lammer et al. (2014), and Tian (2015a)
Photochemistry	No	Kasting and Catling (2003), Hu et al. (2012), Catling and Kasting (2017), Wogan and Catling (2020), and Jordan et al. (2021)
Deposition, condensation & rainout	No	Pinto et al. (1980), Hu et al. (2012), Ranjan et al. (2019), Rimmer, Shortle, et al. (2019), and Huang et al. (2022)
Impact erosion, transformation & volatile delivery	No	Kasting (1990), Liu et al. (2015), Schlichting et al. (2015), Rimmer, Ferus, et al. (2019), Sinclair et al. (2020), Todd and Öberg (2020), and Zahnle et al. (2020)
Drawdown processes (e.g., silicate weathering causing CO ₂ drawdown)	No	Walker et al. (1981)
Biological processes	No	Kharecha et al. (2005)

4.2 Methods

To simulate the evolution of a planet's atmosphere, we have constructed EVolve, a 3-part model linking mantle to atmosphere via a volcanic system, as described in Chapter 2 and Section 2.2. In brief: during a single time-step, a portion of the mantle is melted, and volatiles partition from the bulk mantle into the melt phase according to the batch melting equation (Section 2.2.1). The mass and volatile content of this magma, along with the $f\text{O}_2$ of the mantle, is used as an initial condition for EVo, the volcanic outgassing model, which forms Part 2 of EVolve (Section 2.2.2). EVo returns the mass, composition, and speciation of the volcanic gas, as a mixture of 10 C-O-H-S-N species, at the current surface pressure. In the third model component (Section 2.2.3), representing the atmosphere, the volcanic gas is mixed with the pre-existing atmosphere, the surface pressure is updated, and the equilibrium speciation for this atmosphere is determined using FastChem 2.0 (Stock et al., 2018; Stock and Kitzmann, 2021).

All models presented begin their calculations with 0.01 bar surface pressure (this is an arbitrary value which is small enough not to affect results, as EVo cannot be initiated with zero atmospheric pressure) from a pure N₂ gas, i.e., minimal pre-existing atmosphere. This assumes that any primordial or primary atmosphere from before magma ocean solidification has been lost, or replaced by outgassing over time. Initialising a planet which retains a massive atmosphere would effectively imply the presence of a magma ocean (Nikolaou et al., 2019), because of the strong greenhouse effect of a thick reducing atmosphere (e.g., Wordsworth and Pierrehumbert, 2013b). Such a scenario is outside the scope of this work. The escape of hydrogen to space is also neglected here, and the effects of escape are considered in detail in Chapter 6; this means that the results of this chapter are relevant for an end-member of planetary evolution where current atmospheric escape is negligible – an important basis on which to build models incorporating more physical/chemical processes.

All models also use a single rate of melt production in the mantle. While planets are more likely to have a rate of melt production which wanes with time, as the interior of the planet cools, different rates of melt production would in practise simply change the timescale over which various points in atmospheric evolution are reached. This will not affect the interpretation of our results, as we do not aim to make detailed predictions of planets at particular points in their history. Finally, atmosphere-interior volatile cycling is assumed to be inefficient, i.e., volatiles remain in the atmosphere once outgassed (Tosi et al., 2017). This is appropriate for the hot planets here, on which low temperature, aqueous drawdown processes, such as the carbonate-silicate cycle, do not operate (including those suggested by Foley, 2019; Höning et al., 2019, for stagnant lid planets).

4.3 Results

Here we investigate the effects of mantle $f\text{O}_2$ and atmospheric temperature on the atmospheric growth and evolution of Earth-sized, stagnant lid planets. A single starting mantle volatile content is initially considered, based on the H_2O and CO_2 content of the mantle after magma ocean solidification in a volatile-rich delivery scenario (450 ppm H_2O and 50 ppm CO_2 ; Elkins-Tanton, 2008). The mantle volatile contents of exoplanets are highly uncertain, and in the absence of any other reliable data on the S and N contents of planetary mantles the initial concentrations of sulfur and nitrogen in the model mantles are set by scaling estimates of Earth's depleted MORB (mid-ocean ridge basalt) source mantle content (Le Voyer et al. (2017, 140 ppm CO_2); Ding and Dasgupta (2017, 150 ppm S:); Marty and Dauphas (2003, 1 ppm N:)), to match the CO_2 value from Elkins-Tanton (2008). A single rate of mantle melting is considered, so all times since the onset of volcanism discussed here are linearly dependent on the melt production rate – i.e., time and cumulative eruptive melt volume are interchangeable, and our use of time to track atmospheric evolution is simply indicative (see Fig. 4.7 for examples of melt volumes implied by a given age). All planets are assumed to be Earth-sized, and are initialised with a 0.01 bar N_2 atmosphere. Atmospheric chemical compositions are presented at surface pressure.

We explore the effect of atmospheric temperature on volcanic atmospheres at thermochemical equilibrium (Section 4.3.1); how the resulting speciation of the lower temperature volcanic atmospheres fall into distinct atmospheric classes depending on their mantle $f\text{O}_2$ (Section 4.3.2); the effect of the bulk silicate H/C ratio on these atmospheric classes (Section 4.3.3) and how volcanic atmospheres evolve over long timescales (Section 4.3.4).

4.3.1 Volcanic atmospheres in thermochemical equilibrium

We first compare results where volcanic gases have reached thermochemical equilibrium at three different planetary surface temperatures: 2000, 1500 and 800 K.

The surface pressure, scale height, mean molecular mass, and major atmospheric chemistry for three different surface temperature cases are shown in Fig. 4.1, as functions of mantle $f\text{O}_2$. Results are shown after 1 Gyr of volcanic activity. Figure 4.1a shows that the surface pressure, while unaffected by temperature, increases non-linearly with mantle $f\text{O}_2$. The increase in surface pressure with mantle $f\text{O}_2$ is controlled by a number of factors: (1) a more oxidised mantle will produce more oxygen-bearing gas species, with a correspondingly higher mean molecular weight (e.g., CO_2 replacing CO). (2) The partitioning of both C and N into the melt phase during mantle melting is $f\text{O}_2$ dependent, where a smaller fraction of the volatile budget enters the melt at low $f\text{O}_2$ (see Section 2.2.1). (3) The $f\text{O}_2$ dependence of many gas-melt

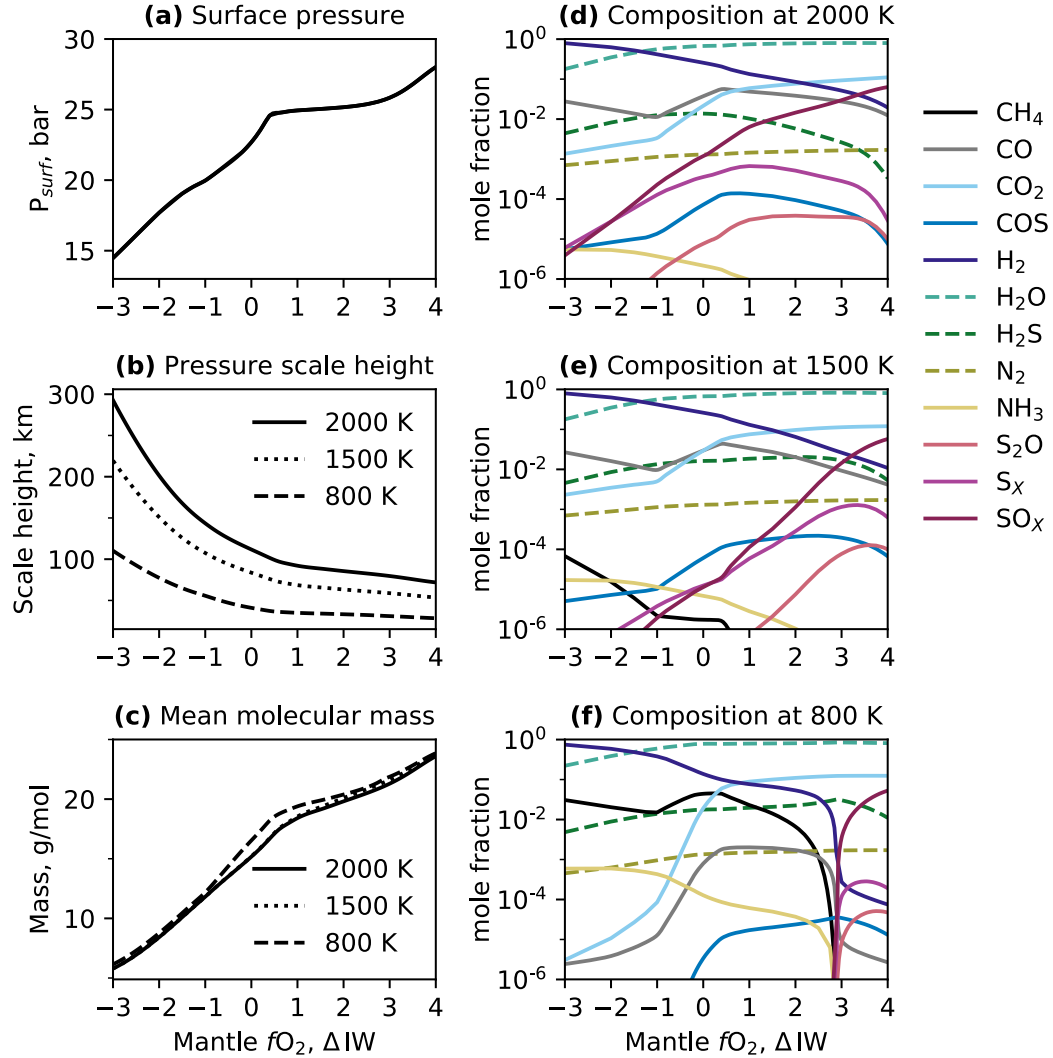


Fig. 4.1 The effect of isothermal atmospheric temperature on the physical properties: (a) surface pressure, (b) scale height, and (c) mean molecular mass; and atmospheric chemistry at surface pressure: (d) at 2000 K, (e) at 1500 K, and (f) at 800 K, after 1 Gyr of volcanic activity. Atmospheres ≥ 1500 K have greater scale heights and a more gradual change in atmospheric chemistry with mantle fO_2 compared to 800 K isothermal atmospheres. Ions (notably OH^- , HS^- and O^{2-}) have been excluded from the 2000 K chemistry plot, but are present at approximately constant levels across the fO_2 range presented here. The full data results for these plots, including ions, are available in the data repository.

4.3 Results

solubility laws; at low $f\text{O}_2$, nitrogen outgassing from the melt phase is suppressed (it becomes much more soluble by speciating into the melt as N^{3-} Libourel et al., 2003), while at high $f\text{O}_2$ sulfur outgassing is enhanced (the sulphide capacity of the melt lowers under more oxidising conditions, e.g., O'Neill, 2021). This creates the stepped trend in surface pressure, with more massive atmospheres formed at higher mantle $f\text{O}_2$.

Conversely, the atmospheric scale height decreases with increasing mantle $f\text{O}_2$, reflecting the lower mean molecular weight of atmospheres on planets with reduced mantles, and particularly their increased abundance of H_2 (Miller-Ricci et al., 2008). The effect of atmospheric temperature on the mean molecular weight of the atmosphere is small (maximum 3 g/mol for a given $f\text{O}_2$, Fig. 4.1(c)), and therefore the differences in scale height between the three atmospheres are almost entirely due to thermal expansion with the 2000 K atmosphere having a scale height $\approx 2.5 \times$ greater than the 800 K atmosphere across the $f\text{O}_2$ range.

Figures 4.1d to 4.1f demonstrate that the atmospheric chemistry of volcanic atmospheres changes systematically as a function of $f\text{O}_2$ and surface temperature. The atmospheric chemistry of the 1500 K atmosphere agrees with trends shown in previous work (e.g., Ortenzi et al., 2020); there is a smooth transition from the atmosphere being rich in H_2O , CO_2 and SO_x (in this case speciated almost entirely as SO_2) under oxidised mantle scenarios, to being more rich in H_2 and CO under reduced scenarios, and with CH_4 abundance increasing as mantle $f\text{O}_2$ reduces below IW+1. The atmospheric chemistry of the 2000 K atmosphere shows less variability with mantle $f\text{O}_2$ than that of the 1500 K atmosphere; CH_4 is absent at the ppm level across the entire $f\text{O}_2$ range, while SO_x species are present even at the most reduced mantle $f\text{O}_2$ conditions. Ions are also present in the 2000 K atmosphere (including OH^- and HS^-). As none of the ions show a strong change in abundance with mantle $f\text{O}_2$, they have been omitted from Fig. 4.1 for clarity of results.

In contrast, the atmospheric chemistry of the 800 K atmosphere shows much more variability with mantle $f\text{O}_2$, compared with both the 2000 K and the 1500 K atmospheres. Rather than a smooth transition from oxidising to reducing atmospheres, the atmospheric chemistry shows distinct transitions in the abundance of certain species, which coincide with inflections in the total atmospheric pressure (Fig. 4.1a). A sharp transition in the atmospheric speciation can be seen at high $f\text{O}_2$ (IW+3), where oxidised sulfur species (SO_x , S_2O , S_x) drop below ppm abundances, and the CH_4 content rapidly increases to $\sim 1\%$. Another, more gradual transition can be seen at low $f\text{O}_2$ (IW), where the CO_2 and CO abundances drop sharply to less than 10 ppm, COS decreases to below ppm levels and the H_2 content increases again to $> 10\%$. At this point, the NH_3 abundance also exceeds CO , reaching > 500 ppm at a mantle $f\text{O}_2$ of IW-2.

4.3.2 Atmospheric classes on warm planets

The results of Section 4.3.1 have shown that once volcanic atmospheres cool to below eruptive temperatures, they start to form more distinct compositional groups, linked to the $f\text{O}_2$ of the mantle supplying the degassing magmas (Fig. 4.1). Here we explore how these compositional groups can be classified in an 800 K atmosphere, after 1 Gyr of outgassing (at which point these atmospheric compositions become stable in time).

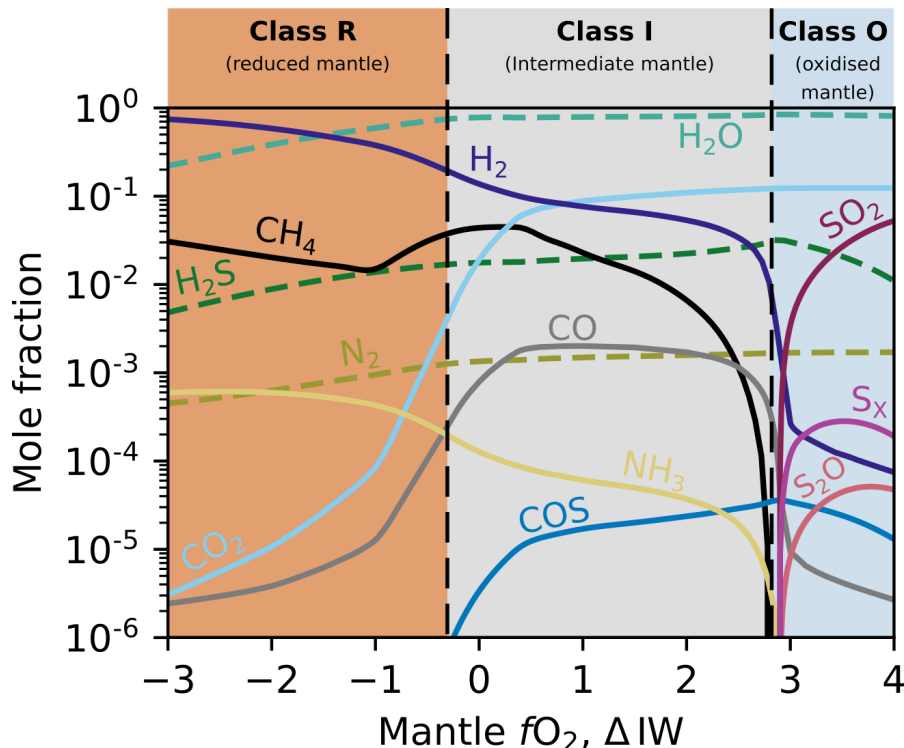


Fig. 4.2 The three secondary volcanic atmosphere classes. Each atmospheric class is indicative of the underlying mantle $f\text{O}_2$, with each distinguished by the changing abundance of key species: SO_2 , S_2O and S_x for Class O; CH_4 , CO_2 , CO and COS for Class I; and H_2 , CH_4 and NH_3 for Class R. The species irrelevant to the class definitions (H_2O , H_2S , N_2) have been plotted in dashed lines. Compositions shown for an 800 K atmosphere after 1 Gyr of volcanic outgassing.

By considering the species which vary by more than an order of magnitude in abundance across the mantle $f\text{O}_2$ range for the 800 K atmosphere, three classes of secondary volcanic atmospheres can be defined (Fig. 4.2):

Class R atmospheres, present on planets with reduced mantles ($<\text{IW}-0.5$), are defined by the presence of H_2 and CH_4 with mixing ratios $>1\%$, alongside NH_3 and very low or declining levels of CO_2 and CO . Class R atmospheres are also more extended, with significant H_2 inflating the scale height.

4.3 Results

Class I atmospheres, produced by planets with intermediate mantle fO_2 between approximately IW-0.5 and IW+2.7, are characterised by the presence of CO₂, CH₄ at mixing ratios <1%, alongside smaller amounts of CO and COS.

Class O atmospheres, are formed by planets with oxidised mantles (>IW+2.7), and are classified by the presence of SO₂ and sulfur allotropes (S_x).

H₂O, H₂S and N₂ are present across the entire fO_2 range here and are found in all three atmospheric types. These three classes show the chemistry of an atmosphere can be directly linked to the mantle fO_2 of a planet, even after volcanic gases are allowed to react in the atmosphere and cool down from their eruptive temperatures – subject to no further modification processes such as escape.

The EVolve results presented in this chapter (and the rest of this thesis) are all calculated assuming a single pressure of melting (2 GPa) and a single mantle melt fraction (0.1). As the concentration of volatiles in a melt phase generated by batch melting of the mantle is dependent on the pressure of melting (for carbon partitioning under graphite saturated conditions, as per Eqs. (2.47) and (2.48)) and the local melt fraction (for all species, Eq. (2.46)), the sensitivity of the atmospheric classes presented in Fig. 4.2 to these mantle parameters is tested in Fig. 4.3. The model scenario shown in Fig. 4.2 is highlighted in bold. Varying the pressure of melting between 1 and 3 GPa produces a negligible change in the mantle fO_2 at which the class transitions occur. As the local melt fraction increases, the effect on the I-O class transition is again negligible, while it slightly increases the width of the I-R transition zone by moving the point at which NH₃ becomes more abundant than CO to slightly more reduced conditions. The results presented here are therefore robust to a range of melting conditions within the mantle.

As shown in Figs. 4.1d to 4.1f, the fO_2 dependence of atmospheric speciation diminishes at higher temperatures. Therefore, not all of the three atmospheric classes defined in Fig. 4.2 (for an 800 K atmosphere) will be present for planets with higher atmospheric temperatures Fig. 4.4. As the surface temperature increases, Class R and then Class I atmospheres are no longer produced, regardless of mantle fO_2 . Figure 4.4c shows that at 950 K a transitional Class R atmosphere can be formed on planets with reduced mantles; the speciation displays almost all of the properties of a Class R atmosphere (e.g., high H₂, COS below ppm abundances), but as NH₃ is not more abundant than CO, it cannot be classified as a true Class R.

Secondary Volcanic Atmospheres: Growth and Evolution on Hot Rocky Planets

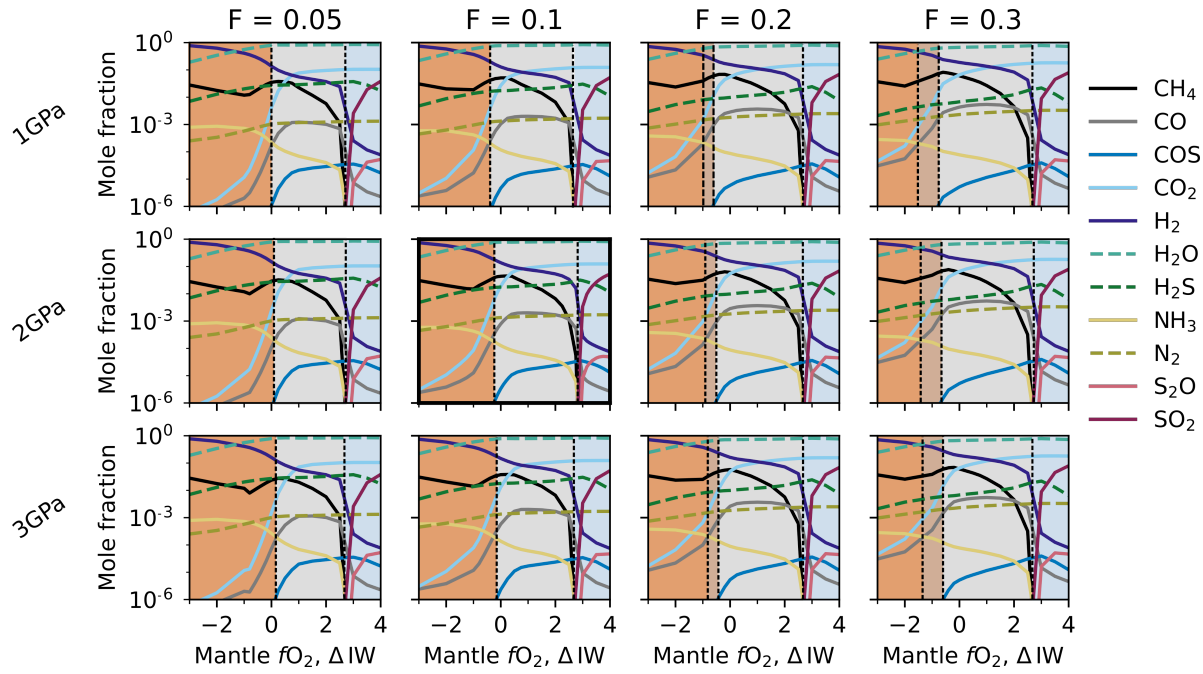


Fig. 4.3 The sensitivity of our atmospheric classes to changes in the mantle melt fraction (F) and the pressure of mantle melting. The model discussed in the main text ($F=0.1, P=2\text{GPa}$) is highlighted in bold.

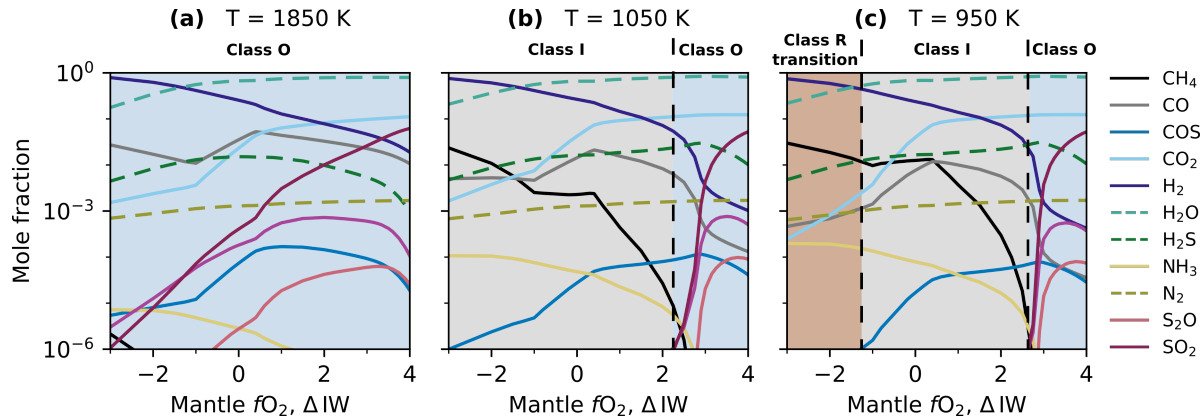


Fig. 4.4 Atmospheric classes which are produced as the temperature is varied, used to define limits in Fig. 4.5. As the atmospheric temperature increases, the speciation of the atmosphere starts to resemble those of planets with oxidised mantles at 800 K.

Figure 4.5 shows the approximate equilibrium temperature of a planet according to the luminosity of its parent star (a function of stellar radius and temperature), and its orbital distance in AU. Superimposed on top are the atmospheric classes which could be present

(over the mantle fO_2 range IW-3 to IW+4), assuming the atmospheric temperature is equal to the equilibrium temperature. Cooler planets can exhibit the characteristics of a Class R atmospheres if the mantle fO_2 is sufficiently low, however once the atmosphere is hotter than ~ 1850 K the atmospheric chemistry will resemble a Class O atmosphere, regardless of how reduced the planetary mantle is (Fig. 4.4 for plots showing these T-dependent class changes). Above 2000 K, atmospheres start to contain a significant abundance of ions not considered here, so no longer fit into the Class O classification well. Discussions of atmospheres below 800 K are left to Chapter 5.

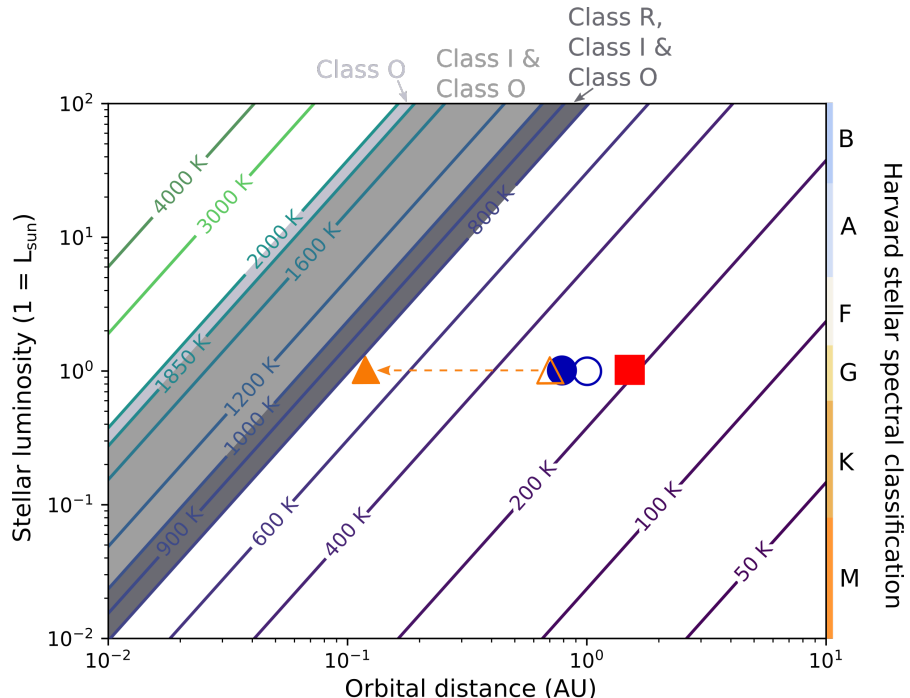


Fig. 4.5 Equilibrium temperature of planets assuming an Earth-like Bond albedo, with atmospheric classes possible (over an IW-3 to IW+4 mantle fO_2 range) according to the luminosity of the star with respect to the Sun (a property controlled by their effective temperature and radius), and the orbital distance of the planet superimposed. Temperature contours are for the equilibrium temperature of a planet in kelvin. Earth (blue circle) and Venus (orange triangle) and Mars (red square) are plotted at their orbital distances, indicating their equilibrium temperature if they had a Bond-albedo similar to Earth's (empty symbol) and their actual surface temperatures (filled symbol) as controlled by the climatic conditions created by their atmospheres. The formation history, and therefore initial volatile content of planets is assumed to be constant, regardless of the planet's distance from the star.

The atmospheric temperature of a planet may also be warmer than the equilibrium temperature plotted here, depending on the composition and thickness of it's atmosphere. As an example of this, the greenhouse effect of the present atmospheres of Venus, Earth and Mars are shown in Fig. 4.5 with triangles, circles and squares, respectively. The empty symbols indicate each planet's equilibrium temperature based on their orbital distances from the Sun,

while the filled symbols indicate the true surface temperature of each planet that results from atmospheric greenhouse warming. Planets further out from their stars may therefore also fall into the temperature bands shown here where our classification system applies, depending on their climate.

4.3.3 Effect of the bulk silicate H/C ratio

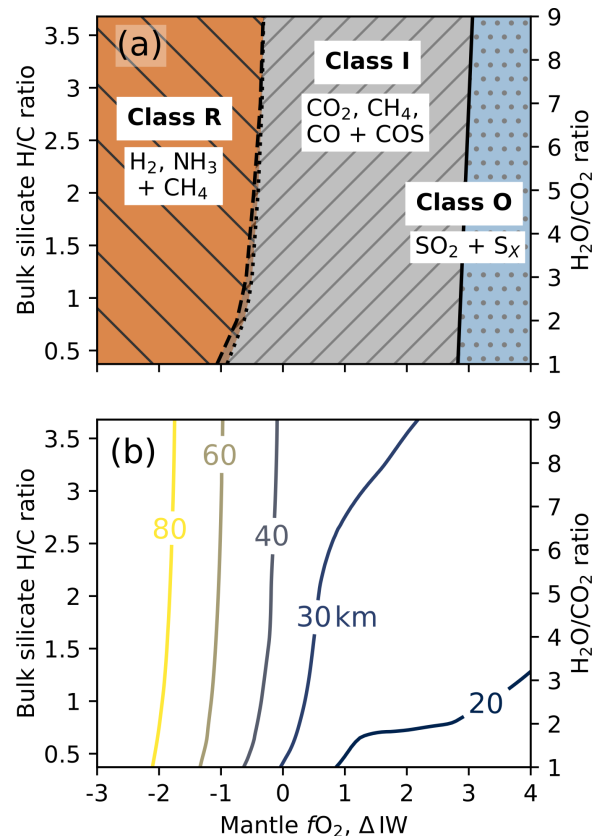


Fig. 4.6 (a) Volcanic secondary atmosphere regime diagram. The three identified secondary volcanic atmosphere classes on mature planets at 800 K are shown, varying with mantle $f\text{O}_2$ and initial H/C ratio, after 3 Gyr of outgassing. Two dashed lines indicate the two different markers for a class R atmosphere; the dotted line indicates the point where NH_3 becomes more abundant than CO , the dashed where the COS abundance drops below 1×10^{-6} (these lines fall very close to each other). The bulk silicate H/C ratio is also presented as its equivalent $\text{H}_2\text{O}/\text{CO}_2$ mass ratio on the right-hand axis, assuming all hydrogen in the mantle is speciated as H_2O , and all carbon as CO_2 . (b) Pressure scale height (km) at 3 Gyr with mantle $f\text{O}_2$ and bulk silicate H/C ratio.

The ratio of different volatiles in a planet's mantle can also affect the chemistry of volcanic gases released by making them more or less carbon rich, for example. The robustness of the atmospheric classifications listed above (calculated using a bulk silicate H/C ratio of approximately 3.5) to a variable bulk silicate H/C mass ratio is tested in Fig. 4.6. The ratio of C:S:N remains fixed, so the only variable changing is the proportional hydrogen content. We present results for atmospheres after 3 Gyr of volcanic activity, because in some simulations with a mantle $f\text{O}_2$ close to class transitions and a low H/C ratio (water-poor), it took longer than 1 Gyr to reach a class composition. In each case after 3 Gyr the class transitions were

then maintained out to 10 Gyr. This effect of a compositional dependence on the timescale of atmospheric evolution, and the few edge cases which remain where the atmospheric class continues to change after 3 Gyr, are explored further in Section 4.3.4.

Class O atmospheres ($\text{CH}_4 < 1 \times 10^{-6}$, high SO_2 and S_X) appear for a mantle $f\text{O}_2$ more oxidised than $\sim \text{IW}+3$ across a wide range of bulk silicate H/C ratios. The transition from Class R to I is also largely constant at IW-0.5, although at H/C=1 and below this occurs at slightly more reducing conditions, towards IW-1. Figure 4.6 shows that while mantle $f\text{O}_2$ may be classified using the atmospheric speciation, the same cannot be said for the bulk silicate H/C ratio. Over the H/C range shown here, there are no distinct changes in either the speciation of the atmosphere, or the pressure scale height which might indicate the initial H/C ratio. Pressure scale heights (directly proportional to atmospheric extent) of ≥ 60 km indicates a class R atmosphere for an 800 K isothermal atmosphere.

4.3.4 Long-term atmospheric evolution

The chemical composition of volcanic atmospheres is expected to slowly change through time as the surface pressure of the planet increases, driving preferential degassing of the most insoluble species (e.g., carbon Gaillard and Scaillat, 2014). Three examples of long-term atmospheric evolution are shown in Fig. 4.7. As previously discussed in Sections 4.3.2 and 4.3.3, we find that in most cases atmospheric chemical compositions have stabilised with respect to the classes presented here after 1-3 Gyr of volcanic outgassing (e.g., Fig. 4.7b). Although compositions continue to slowly evolve beyond this age, most notably in terms of which molecule makes up the dominant atmospheric species (e.g., Fig. 4.7b shows CO_2 becoming dominant after ~ 6 Gyr, see Fig. 4.8 for more detail), class boundaries are not crossed.

However, for planets which sit close to a class boundary after 3 Gyr (see Fig. 4.6a), the speciation of the atmosphere can change more dramatically over long timescales (Figs. 4.7a and 4.7c). My results show model atmospheres on the Class I - O boundary which start in Class O can transition into Class I over long timescales from volcanic degassing alone (i.e., discounting atmospheric loss and volatile cycling processes; Fig. 4.7c). Similarly, atmospheres on the R-I boundary categorised as Class R after 3 Gyr can transition into Class I over time (Fig. 4.7a); although given the two criteria for a Class R atmosphere ($\text{COS} < 1 \times 10^{-6}$ and $\text{CO} < \text{NH}_3$) this transition can be much more gradual, over several Gyr, in comparison to the transition shown in Fig. 4.7c. It is important to note that despite the apparent sharp change in atmospheric composition seen particularly clearly in Fig. 4.7c, there is no sudden change in the gasses being added to the atmosphere (Figs. 4.7d to 4.7f). Over time, the pressure-sensitive nature of degassing means that sulfur and then water degassing is limited, so the

Secondary Volcanic Atmospheres: Growth and Evolution on Hot Rocky Planets

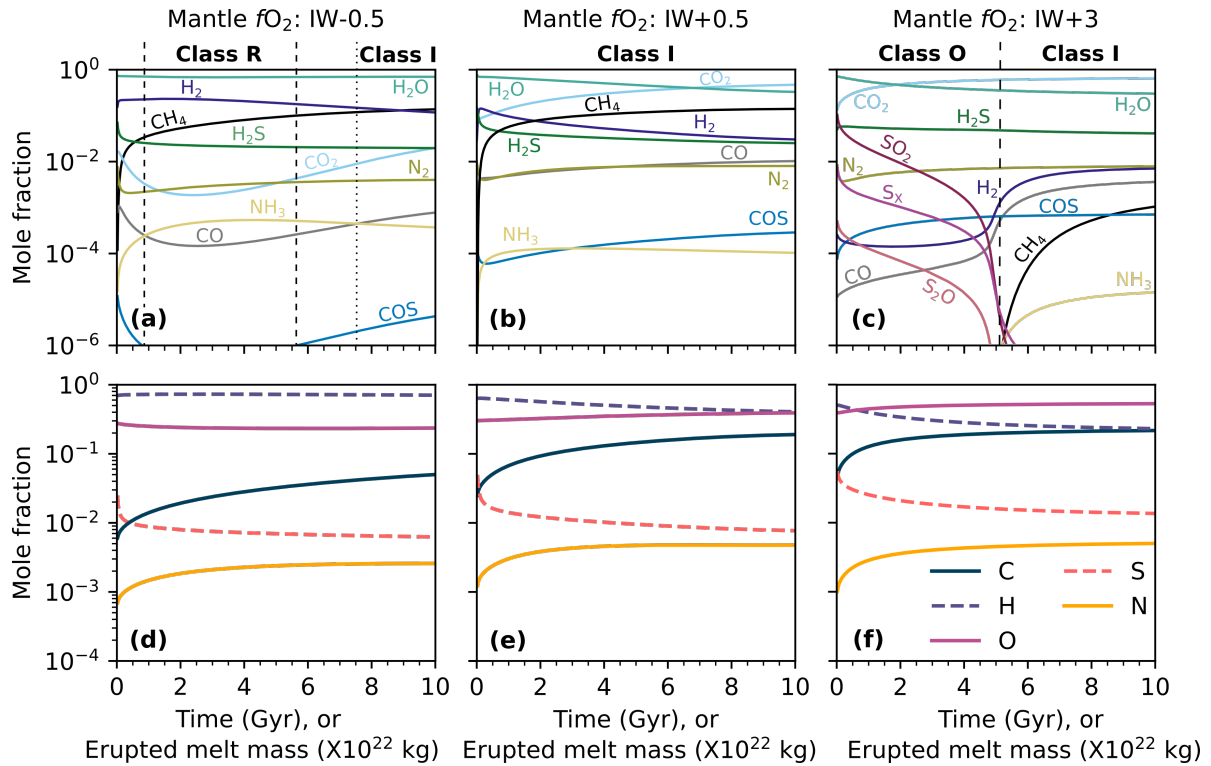


Fig. 4.7 The evolution of three different 800 K atmospheres over 10 Gyr of time, showing the speciation of the atmosphere (a-c) and the atmospheric composition as mole fractions of each atomic element (d-f). (a) and (c) have a H/C=2, (b), (c) (e) and (f) have H/C=1. Most scenarios follow the pattern of (b), stabilising into a single compositional class after 1-3 Gyr. Models which sit at the edge of classes, such as those in (a) and (c), may change groups over longer time periods.

slowly changing ratios of elements in the atmosphere seen in Figs. 4.7d to 4.7f eventually trigger a change in the thermochemical equilibrium balance of the atmosphere so that more reduced species are favoured.

Figure 4.8 shows the length of time a planet has to be volcanically active for, at a constant rate, in order for the atmosphere to become dominated by a species other than water. H_2O is much more soluble than either carbon-bearing species, or H_2 . As the surface pressure increases over time, volcanic gases become increasingly dry, leading to atmospheres which gradually become either H_2 or CO_2 dominated, as seen in Figs. 4.7b and 4.7c, with the shaded areas of Fig. 4.8 indicating a non- H_2O species becoming dominant in < 1 Gyr. In the case of highly reduced mantles ($\lesssim \text{IW}-2$) the low $f\text{O}_2$ means H_2O is never the dominant species after a few time-steps, as most of the H in the mantle is stored and outgassed as H_2 .

The timescale water replacement occurs over is a function of the mantle $f\text{O}_2$, the bulk silicate H/C ratio, and the melt flux to the surface (i.e., the intensity of volcanic activity on

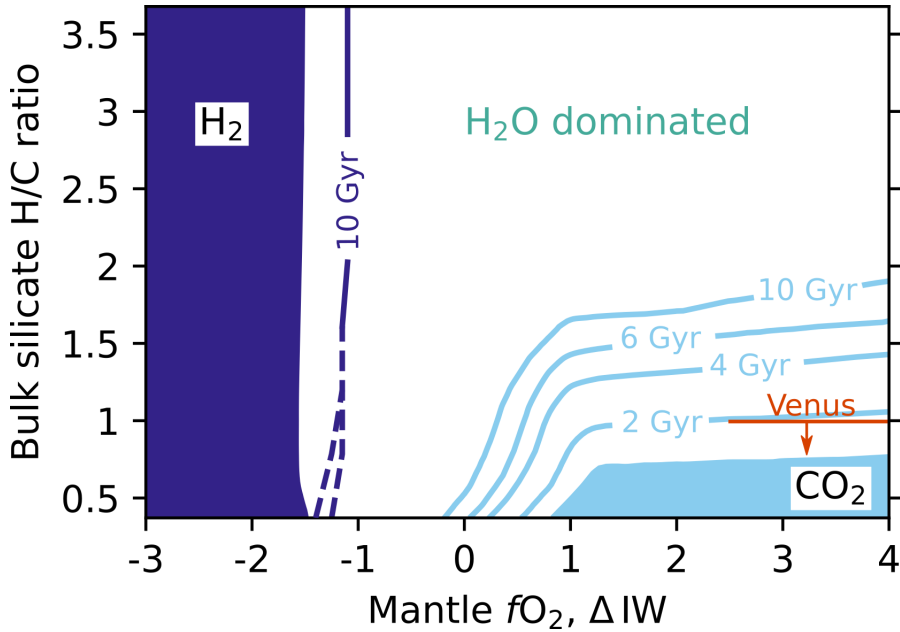


Fig. 4.8 The time taken (in Gyr) for a planetary atmosphere to become dominated by a species other than H₂O, for a given bulk silicate H/C ratio and mantle *f*O₂, assuming a modern Earth-like flux of magma to the surface. The shaded areas indicate that H₂ or CO₂ domination was achieved within 1 Gyr. Venus is plotted at the BSE H/C ratio, over a range of mantle *f*O₂'s suggested for the ancient and modern Earth (Bézos and Humler, 2005; Aulbach and Stagni, 2016) as a reference value. The dashed lines for H₂ indicate bounds (thinner than the linewidth at higher H/C) where H₂O is dominant at 10 Gyr, but H₂ has previously been the dominant species. The lower bound acts as the 10 Gyr H₂ dominant contour.

a planet). The timescales for a given species to achieve dominance shown in Fig. 4.8 are calculated using a single melt flux to the surface ($1 \times 10^{14} \text{ kg yr}^{-1}$, similar to that of the modern Earth); the timings shown in Fig. 4.8 are inversely proportional to this melt flux. This means a planet which is twice as volcanically active as Earth, with a H/C ratio of 1 and a mantle *f*O₂ of IW+3 would attain a CO₂ dominated atmosphere in 1 Gyr, rather than the 2 Gyr shown in Fig. 4.8.

For higher H/C ratios, a carbon-rich atmosphere is never achieved even under oxidised scenarios. This is best understood by imagining a simple case where the only volatiles considered are H₂O and CO₂. Under high H/C conditions, the overabundance of H is such that even accounting for the greater fraction of C which can reach the atmosphere (due to its lower solubility; in our simulations > 90% of the H remains in the mantle after 10 Gyr of outgassing at IW+4, compared to 18% of the C), the amount of water extracted from the mantle will be greater than the amount of CO₂, and a CO₂ dominated atmosphere will not occur by closed system volcanic degassing alone.

4.4 Discussion

We have identified three atmospheric classes for hot, volcanically-derived atmospheres. These apply for planets where minimal escape or volatile cycling is occurring. These classes are robust to a wide range of water-rich to water-poor volatile inventories and show that planetary interiors, specifically the mantle fO_2 , can impose constraints of the chemistry of a planet's atmosphere even after significant temperature changes and thermochemical re-equilibration is applied.

The presence of distinct groups in atmospheres with 800 K surface temperatures, which are not present at 1850 K and above, suggests that planets which are cool enough to have a solid surface, rather than a magma ocean, would be more amenable to having their mantle fO_2 characterised. All three groups have species markers at abundances above $1 \times 10^{-4}/100$ ppm (SO_2 for Class O, CH_4 combined with CO_2 for Class I, and CH_4 combined with a low mean molecular weight indicating substantial H_2 for Class R) which would put them above the detectability limit for the James Webb Space Telescope (JWST) (e.g., Batalha et al., 2018; Krissansen-Totton et al., 2019). However, directly applying these model atmospheres to exoplanet observations is only valid under specific scenarios, i.e. where a planet has lost its primordial/primary atmosphere and is building a secondary atmosphere back through volcanism in a low-escape environment. Even under these constraints, uncertainties remain over atmosphere-surface interactions and photochemistry (Jordan et al., 2021) on hot planets, which may lead to significantly different atmospheric chemistry's to those presented here.

The atmospheres of rocky planets are highly complex and subject to a range of processes which modify their chemistry (e.g., see Table 4.1). The atmospheric classes discussed in this work provide an important baseline from which the effects of further atmospheric processing, such as H_2 escape and photochemistry, can be evaluated. We examine the effect of varying rates of hydrogen escape on these atmospheric classes in Chapter 6, as this process will likely have the strongest effect on the redox state of the atmosphere, potentially weakening the link between mantle and atmosphere.

4.5 Conclusions

Atmospheric temperature has a significant impact on the chemistry of volcanic atmospheres, and should be considered during future modelling of secondary atmospheres. Hot volcanic atmospheres at 800 K show three distinct atmospheric classes defined according to their chemical speciation and scale height. These classes are dictated by the fO_2 of the mantle, and are robust to a wide range of bulk silicate H/C ratios. These classes may be used as a

4.5 Conclusions

simple base for future research, exploring the effects of other processes on volcanic secondary atmospheres as produced by a range of geological conditions.

5

Secondary Volcanic Atmospheres: The Importance of Kinetics

Models simulating volcanic growth of atmospheres often make one of two assumptions: either that atmospheric speciation is set by the high-temperature equilibrium of volcanism; or, that volcanic gases thermochemically re-equilibrate to the new, lower, temperature of the surface environment. In the latter case it has been suggested that volcanic atmospheres may create biosignature false positives. In this chapter, we test the assumptions underlying such inferences by performing chemical kinetic calculations to estimate the relaxation timescale of volcanically-derived atmospheres to thermochemical equilibrium, in a simple 0D atmosphere neglecting photochemistry and reaction catalysis. We demonstrate that for planets with volcanic atmospheres, thermochemical equilibrium over geological timescales can only be assumed if the atmospheric temperature is above ~ 700 K. Slow chemical kinetics at lower temperatures inhibit the relaxation of redox-sensitive species to low-temperature thermochemical equilibrium, precluding the production of two independent biosignatures through thermochemistry alone: 1. ammonia, and 2. the co-occurrence of CO₂ and CH₄ in an atmosphere in the absence of CO. This supports the use of both biosignatures for detecting life. Quenched at the high temperature of their degassing, volcanic gases also have speciations characteristic of those produced from a more oxidized mantle, if interpreted as being at thermochemical equilibrium. This therefore complicates linking atmospheres to the interiors of rocky exoplanets, even when their atmospheres are purely volcanic in origin.

5.1 Introduction

Exoplanet science will provide many fascinating insights into planet formation and evolution, one of which will be a greater understanding of the origin and nature of rocky planet atmospheres – a possibility that recently became a lot closer to being realised with the launch of the James Webb Space Telescope (Lustig-Yaeger et al., 2019). Of particular importance for linking to planetary habitability, and in the search for life, is developing an understanding of how atmospheric observations of exoplanets might be used to infer their geological properties and processes. As such, many models of the atmospheres of rocky exoplanets have been developed to allow future observations to be interpreted in the context of different geological paradigms: magma ocean worlds (Elkins-Tanton, 2008; Hirschmann, 2012; Hamano et al., 2013, 2015; Katyal et al., 2020; Sossi et al., 2020; Lichtenberg et al., 2021; Gaillard et al., 2022); stagnant lid tectonics (e.g., Noack et al., 2017; Tosi et al., 2017; Dorn et al., 2018); impact events (Schaefer and Fegley, 2010; Kuwahara and Sugita, 2015; Schlichting et al., 2015; Sinclair et al., 2020; Zahnle et al., 2020); interior structure and chemistry (Abe, 2011; Noack et al., 2014; Schaefer and Fegley, 2017; Dorn et al., 2018; Ortenzi et al., 2020; Spaargaren et al., 2020); surface chemistry (Schaefer et al., 2012; Herbst et al., 2020; Yu et al., 2021); atmospheric escape (Wordsworth and Pierrehumbert, 2014; Kislyakova et al., 2015; Tian, 2015b; Dong et al., 2018; Kite and Barnett, 2020); or volcanism (Gaillard and Scaillet, 2014; Kadoya and Tajika, 2015; Liggins et al., 2020; Wogan et al., 2020).

Chapters 4 to 6 explore an important end-member case of hot rocky planet atmospheric evolution, where their atmospheres have been formed and evolved purely under the influence of volcanic gas supply: i.e., without the oceans, aqueous geochemistry or life that exert strong controls on Earth's atmosphere. As has already been explored in Chapter 4, these planets are of particular interest because they can form classes of volcanic atmosphere which are linked to the interior conditions (particularly, how oxidised planetary mantles are) which may reflect core formation history, planetary mass, and formation location within the protoplanetary disk (Wade and Wood, 2005; Frost et al., 2008). Chapter 6 will expand on the results in Chapter 4 by including considerations of atmospheric escape. These end-member models will be important to inform evidence of volcanic activity in future atmospheric abundance estimates made for exoplanet spectra.

A key question in making this link between a planet's atmosphere and interior is to what extent the lower pressures and temperatures of a planet's atmosphere will allow its chemistry to reflect information about the geochemistry of its interior. A commonly used approximation for modelling rocky planet atmospheres is to assume that they will exist in thermochemical equilibrium, either homogeneous (equilibrium within the gas phase only, e.g., Liggins et al., 2020; Ortenzi et al., 2020; Wogan et al., 2020) or heterogeneous (equilibrium is extended

5.1 Introduction

to include surface interactions, e.g., Herbort et al., 2020; Sossi et al., 2020; Woitke et al., 2021). However, in volcanically-derived atmospheres, gases will typically be injected into the atmosphere at higher temperatures than the ambient surface temperature. The extent to which these high temperature volcanic gases will relax and re-equilibrate to a new, low temperature equilibrium is unclear, but is important for understanding how interior conditions may be inferred from an atmosphere. For example in Chapter 4, we found that clear atmospheric classes (defined according to the speciation of the atmosphere at thermochemical equilibrium) can emerge in volcanically-derived atmospheres as a function of mantle $f\text{O}_2$. However, while these classes form most clearly under lower atmospheric temperature conditions, they require thermochemical equilibrium to have been reached in order to be valid.

Thermochemical equilibrium in low temperature atmospheres derived by outgassing of silicate materials has previously been invoked as a potential source of false-positive biosignatures. Woitke et al. (2021) found that at thermochemical equilibrium with temperatures ≤ 600 K, gases released by “common rock materials” (carbonaceous chondrites and mid-ocean ridge basalt) produced an atmosphere where CO_2 and CH_4 could coexist with only trace amounts of CO , producing a geological false-positive for the CO_2+CH_4 biosignature of Krissansen-Totton et al. (2018). However, this conclusion depends heavily on the timescale over which a low temperature equilibrium can be achieved.

In a system modelled at thermochemical equilibrium (as would be the case for calculations performing Gibbs-free energy minimisation), the timescale for gas chemistry to adjust to the surface P-T conditions is necessarily just the cooling rate of the gas. The (sometimes implicit) assumption here is that reaction rates are fast enough to adjust speciation to the new equilibria. However, as the temperature and pressure of a volcanic gas decreases towards ambient surface conditions, both the frequency of molecular collisions, and the energies with which these collisions occur, decrease. The timescale over which a new equilibrium can be achieved thus lengthens. The consequence of this is that volcanic gases as observed on Earth, which are erupted at high temperatures into a cold environment and cool rapidly, usually have their chemistry ‘quenched’ (Le Guern et al., 1982; Gerlach and Casadevall, 1986): their gas-phase speciation is frozen in at the temperature where chemical reactions become slow enough that the speciation of the gas is effectively constant over the timescale of interest. In detail, this quench temperature will vary by species, so that the resultant quenched gas entering and mixing with the atmosphere reflects the equilibrium state of no single temperature (or pressure).

In defining quenching to have occurred, the timescale of interest is critical. If it takes a thousand years for a volcanic gas to re-equilibrate at a cooler temperature, it may be considered quenched over the timescale of observations on Earth (usually minutes to a few days while the gas mixes into the background atmosphere), but not when looking at gas chemistry over

Secondary Volcanic Atmospheres: The Importance of Kinetics

geological time (i.e., on the order of billions of years). Depending on the rate at which a cooled volcanic gas re-attains thermochemical equilibrium, volcanically-derived atmospheres of rocky planets may be either in thermochemical equilibrium, as many modelling results assume, or a disequilibrium gas mixture, where volcanic gases are present in a quenched composition from some higher temperature than the background atmosphere.

Here, we identify the temperature below which chemical equilibrium is no longer a valid assumption, and use this to comment on the implications for various approaches to both modelling volcanic atmospheres, and applying potential biosignatures. In Section 5.2, we present a brief recap of the EVolve model used to produce synthetic atmospheres, which is described in full in Chapter 2, along with our methods for calculating chemical timescales. Results are shown in Section 5.3, including a description of the rate limiting steps we identify as preventing the chemical relaxation of volcanic atmospheres (Section 5.3.2). The discussion includes an assessment of model limitations, and a demonstration that the key results of this study are independent of the chemical network chosen to perform the modelling (see Section 5.4.2). Conclusions follow in Section 5.5.

5.2 Methods

The conceptual model applied here is similar to those used in previous studies which assume thermochemical equilibrium in an atmosphere; we model the thick, near-surface layer of the atmosphere, conceptually a 0D box at a single (surface) temperature and pressure. This box ignores surface-atmosphere interactions outside of input by volcanic outgassing. We also ignore the effects of vertical mixing and photochemistry within the atmosphere, both of which would introduce disequilibrium into the near-surface environment.

5.2.1 Evolving volcanic atmospheres

The evolution and chemical composition of volcanically-derived atmospheres in thermochemical equilibrium is modelled here using the EVolve atmospheric evolution model, previously described in Chapter 4. In brief, EVolve is a 3-part model linking the mantle to the atmosphere using EVo Liggins, 2022a, a volcanic degassing model for elements C, O, H, S and N. In every time-step, a portion of the mantle is melted and volatiles partition from the bulk mantle into the melt phase according to the batch melting equation. The mass and volatile content of this magma, along with how oxidising the planet's upper mantle is (measured by its oxygen fugacity, the $f\text{O}_2$ relative to the iron-wüstite, IW, rock buffer) are used as initial conditions in EVo. EVo finds the volatile saturation pressure of this magma, then calculates

the volatile element chemistry of the two-phase magma and exsolved gas mixture at both the saturation pressure, and the surface at a constant temperature of 1200°C. This is done by simultaneously solving a system of 5-7 heterogeneous equilibria (between silicate melt and gas, described using solubility laws), 5 homogeneous gas-phase equilibria and the balance between oxygen stored in the melt as Fe₂O₃ or FeO, and oxygen within the volatile species. The end point of the volcanic outgassing is defined as the surface atmospheric pressure, which gradually increases with every time-step as volatile mass is added to the atmosphere.

The FastChem 2.0 equilibrium chemistry model (Stock et al., 2018; Stock and Kitzmann, 2021) is next used to calculate the chemistry of the atmosphere at the recalculated surface pressure and temperature of the planet for the new, mixed atmosphere. It is this 0D atmospheric temperature which is varied to determine the timescales to equilibrium for different species, while keeping the temperature of the volcanic melt+gas system constant. We note that FastChem 2.0 assumes an ideal gas equation of state, but with the maximum pressure investigated in this chapter of <30 bar little deviation between fugacities and partial pressures are expected.

The results presented in this chapter are all for a single set of initial mantle volatile contents, with a H₂O/CO₂ mass ratio of 9 and a C:S:N ratio similar to modern MORB magmas on Earth (see Chapter 4). This results in an initial mantle volatile content of 450 ppm H₂O, 50 ppm CO₂, 54 ppm S, and 0.36 ppm N. Results are always presented relative to a mantle *f*O₂, reflecting the redox state in the mantle at the pressure of melt production. The final *f*O₂ of a melt+gas parcel will change according to the degree of volatile outgassing which occurs (for example, see Carmichael, 1991; Oppenheimer et al., 2011; Brounce et al., 2017) and will therefore vary through time as the volatile content of the melt and outgassing pressure changes; the constant *f*O₂ of the mantle is therefore provided as a fixed independent reference point for a specific planet.

5.2.2 Calculating chemical timescales

To test how long it may take for a volcanic atmosphere to reach thermochemical equilibrium we used a chemical-kinetics code for planetary atmospheres. This code consists of a solver, ARGO (Rimmer and Helling, 2016; Rimmer and Helling, 2019), and a chemical network, STAND2020 (Hobbs et al., 2021; Rimmer et al., 2021). The reactions listed in the chemical network are solved by ARGO as a set of time-dependent, coupled, nonlinear differential equations, with reaction rates calculated as functions of pressure, temperature, and concentrations of the reactant species. As the solver proceeds, and the chemical composition of the atmosphere tends closer to its equilibrium speciation, the chemical timescales can become very long and, in certain cases, the solver subroutine can stall before chemical equilibrium is achieved. This

Secondary Volcanic Atmospheres: The Importance of Kinetics

is generally the result of the chemical speciation reaching a quasi-steady state, intermediate between the initial speciation and the equilibrium speciation. Stalling at quasi-steady state is a common problem in numerical modelling of chemical kinetics, which are typically stiff systems of differential equations (Leal et al., 2017).

Where ARGO could not reach equilibrium, i.e., where it stalled with a quasi-steady state speciation different from that predicted for thermochemical equilibrium, instantaneous chemical timescales were calculated. The chemical timescales provide an estimate of the length of time it would take for each species to reach its abundance at chemical equilibrium, calculated as

$$t_{i,chem} = \frac{|n_i - n_{i,eq}|}{\frac{dn_i}{dt}}, \quad (5.1)$$

where $t_{i,chem}$ (s) is the chemical timescale, n_i (cm^{-3}) is the final number density of species i calculated using ARGO, $n_{i,eq}$ (cm^{-3}) is the equilibrium number density of species i calculated using FastChem 2.0 (Stock et al., 2018; Stock and Kitzmann, 2021), and dn_i/dt ($\text{cm}^{-3}\text{s}^{-1}$) is the rate of change of the number density of species i as calculated by ARGO. For these simulations, ARGO was given as initial conditions: the equilibrium speciation of the gas at 1473 K (the temperature of the gas in the volcanic system) calculated using FastChem, the atmospheric temperature (between 500 – 2000 K), and the pressure was set at the final pressure of the gas that would result after 1 Gyr of volcanic activity.

In all timescale calculations, the starting gas composition was taken as the speciation of a volcanically constructed atmosphere with a temperature of 1473 K after 1 Gyr of volcanic activity. The atmosphere was then assumed to be instantaneously cooled (or heated) to a new surface temperature, and ARGO was used to calculate the chemical speciation of the gas as a function of time as it adjusted towards the new thermochemical equilibrium. A discussion of how this relates to more realistic natural scenarios, and limitations of the approach, can be found in Section 5.4.2.

As n_i approaches $n_{i,eq}$, the rate of change of n_i diminishes and Eq. (5.1) approaches a singularity, causing the estimated chemical timescales to become very long. Equation (5.1) is therefore only an appropriate estimate of the timescale to equilibrium if the system has not yet neared its equilibrium state. We therefore use Eq. (5.1) to estimate the timescale to equilibrium only for the systems that have not reached chemical equilibrium and the solver has instead stalled with some quasi-steady state abundance. For the systems that have reached chemical equilibrium we need only record the time taken for the solver to achieve this state. We can then compare the timescales to equilibrium, either explicitly solved for or estimated using Eq. (5.1), to relevant geological timescales to determine whether or not a species will quench with a non-equilibrium abundance at a given atmospheric temperature. These calculations are

performed for atmospheres with a temperature range 500 – 2000 K. Examples of the kinetic evolution of the atmosphere are shown in Section C.1. In Fig. C.1 we demonstrate the chemical relaxation in a ‘hot’ (2000 K), ‘warm’ (1000 K), and ‘cool’ (500 K) case, and we validate the instantaneous timescale calculation in cases where the timescales to true equilibrium were reached.

5.3 Results

If planetary atmospheres are assumed to be in pure thermochemical equilibrium, then the speciation of gases in the atmosphere will change continuously with temperature (Fig. 5.1; note that water condensation at low temperatures in these plots is ignored). The chemical speciation of the atmosphere tends to diminish in complexity as the temperature decreases, so that by 300 K, regardless of the mantle $f\text{O}_2$, the atmospheric speciation above the ppm level can be described by ~ 5 species, as opposed to the >10 species which are present above ppm levels at 1500 K.

Secondary Volcanic Atmospheres: The Importance of Kinetics

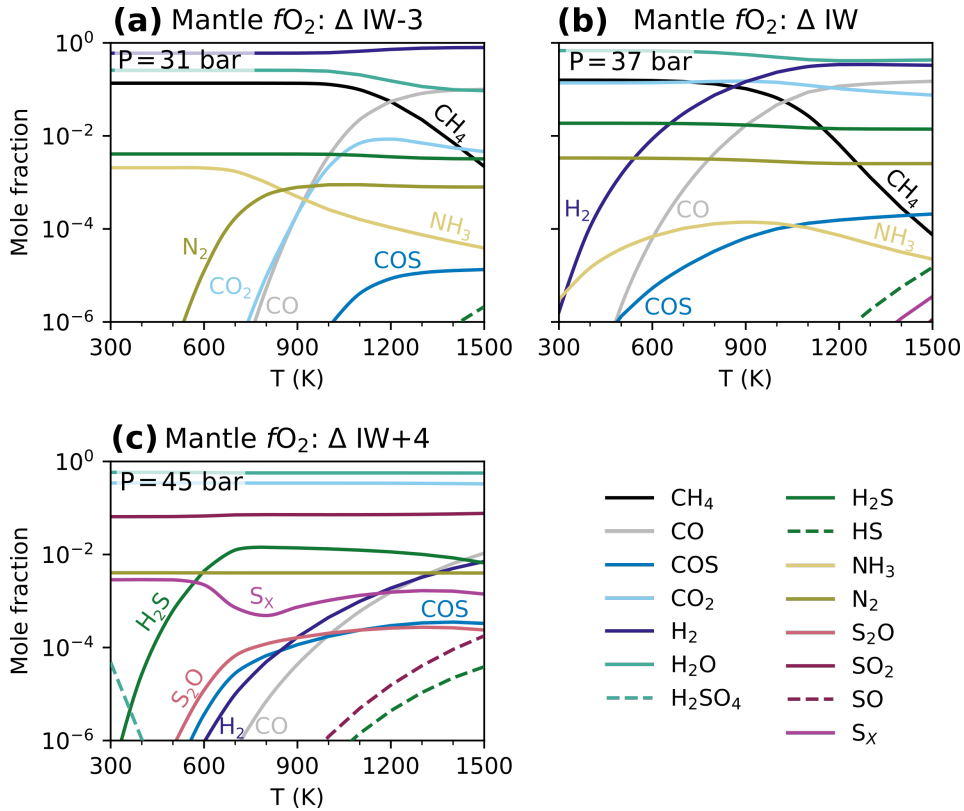


Fig. 5.1 The chemical speciation of a volcanic atmosphere at the surface after 1 Gyr of outgassing, shown for three values of the fO_2 of the mantle supplying those gases and plotted as a function of the 0D atmospheric temperature. The surface pressure is labelled on each panel, as controlled by the mass of volatiles outgassed after 1 Gyr. Thermochemical equilibrium is assumed, and other processes such as water condensation and photochemistry are ignored.

Two notable transitions in atmospheric composition during cooling are (i) the decrease in CO due to its hydrogenation to CH_4 , and (ii) the decrease in N_2 as it is hydrogenated to make NH_3 (Figs. 5.1a and 5.1b). These changes in some of the major atmospheric species are key discriminators of different atmospheric classes, and a planet's mantle fO_2 (see Chapter 4). However the efficient operation of these reactions is strongly inhibited by low temperatures.

The extent to which CH_4 and NH_3 can be produced abiotically in planetary atmospheres has been a subject of debate over recent years (Seager et al., 2013; Schaefer and Fegley, 2017; Wogan et al., 2020; Zahnle et al., 2020; Woitke et al., 2021; Huang et al., 2022), and again here we see that the behaviour of these gases is central to understanding the chemistry of volcanic atmospheres on hot rocky exoplanets. The production of NH_3 and CH_4 from high-temperature volcanic precursors is ultimately dependent on both the chemical timescales of the reactions, and the time period over which gases have to relax (either the time period of observation,

or the cooling rate of the gas if the temperature is changing). The next step is therefore to constrain the kinetics of these reactions, in order to understand how high temperature volcanic gas chemistry translates to lower temperature planetary atmospheres.

5.3.1 Timescales to thermochemical equilibrium

The chemical timescales to new equilibrium abundances for CH₄, CO and NH₃ are plotted in Fig. 5.2. These calculations show an atmospheric composition produced by volcanic degassing from a mantle with $f\text{O}_2$ equal to the iron-wüstite (IW) buffer. This atmosphere has then been instantaneously cooled/heated to the given temperature from its magmatic temperature of 1473 K. We note that a physical scenario where the atmospheric temperature is significantly hotter than that of magmatic gases (and therefore the interior of the planet) is unlikely, but it is nonetheless useful to test the reaction kinetics at higher temperatures.

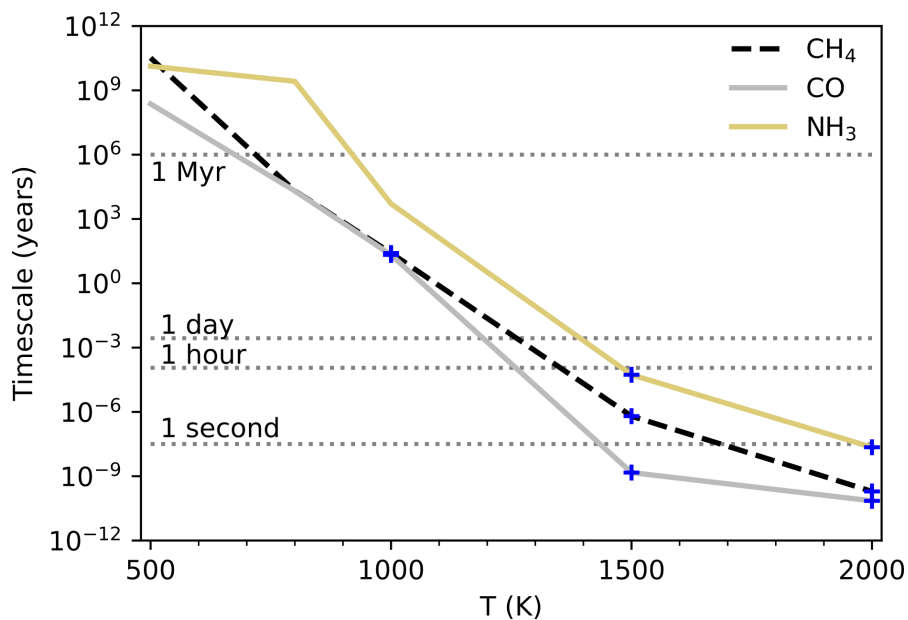


Fig. 5.2 The chemical timescales for CH₄, CO and NH₃ to reach thermochemical equilibrium for instantaneous cooling/heating of the 0D atmosphere at 23 bar from a starting temperature of 1473 K. Timescales were evaluated for final temperatures of 500, 800, 1000, 1500 and 2000 K. The starting atmospheric composition is that produced by 1 Gyr of degassing from a mantle with an $f\text{O}_2 = \text{IW}$. Where thermochemical equilibrium was reached by ARGO (indicated by blue crosses) the time taken to reach equilibrium is plotted; otherwise, instantaneous chemical timescales are used to estimate time to equilibrium. Timescales are given in years, and are estimated to vary over nearly 24 orders of magnitude.

At temperatures of 1100 K and higher, the atmosphere (at surface pressure, 23 bar in this case) will re-equilibrate in less than one hundred years, a geological blink of an eye. Above 1500 K, these timescales drop to minutes, down to less than a second at 2000 K.

Secondary Volcanic Atmospheres: The Importance of Kinetics

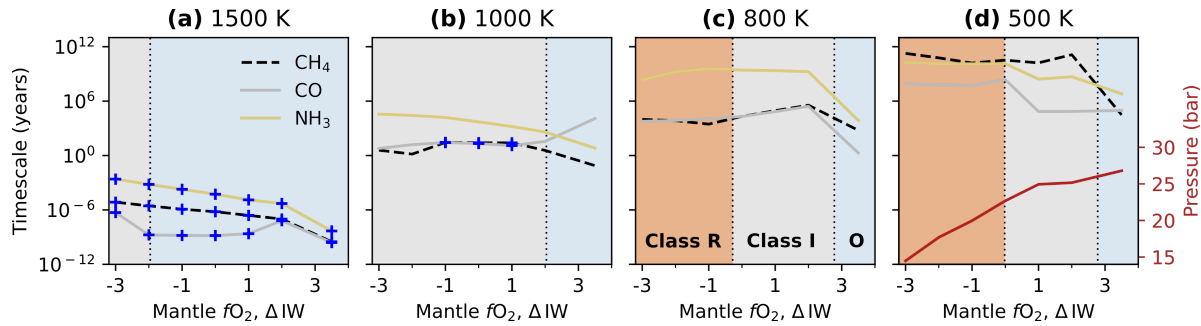


Fig. 5.3 Estimates of the chemical timescales for CH_4 , CO and NH_3 to reach thermochemical equilibrium for instantaneous cooling/heating of the 0D atmosphere from 1473 K to 1500, 1000, 800 and 500 K respectively. Blue crosses indicate simulations where ARGO achieves the FastChem equilibrium number density of the given species. Timescales are given in years, increasing from minutes at 1500 K, to hundreds of Gyr at 500 K. Background colours denote the atmospheric classes derived in Chapter 4 for the fully re-equilibrated atmosphere at each temperature, labelled in (c). The surface pressure (P_{surf}) trend (identical for all 4 temperature scenarios) is plotted as a red line in (d).

With timescales this short, processes other than chemical kinetics will be the rate limiting step for thermochemical equilibrium being reached within the atmosphere, such as the mixing/circulation time for the atmosphere. At 800 K, while CH_4 and CO re-equilibrate on the order of thousands of years, NH_3 will now take 2.6 Gyr to reach its new equilibrium abundance. However, once the surface temperature has dropped to 500 K, all three species take on the order of a Gyr to reach their equilibrium abundances. At this temperature, still well above what would usually be considered ‘habitable’, CH_4 has a chemical timescale of 33 Gyr to equilibrium; over 30 \times longer than the period of volcanic outgassing which produced the atmosphere. At 500 K and without reaction catalysis, this atmosphere would therefore take more than double the age of the universe to fully re-equilibrate.

The speciation of volcanic gases, and therefore the atmospheres they form, is dependent on the mantle fO_2 of the planet (see Fig. 5.3 and Chapter 4 for more discussion). Figure 5.3 shows how the timescales to equilibrium shown in Fig. 5.2 are affected by the different atmospheric conditions imposed by varying the fO_2 of the mantle from which outgassing has occurred, at 1500, 1000, 800 and 500 K.

The different atmospheric speciations and surface pressures that result from varying mantle fO_2 have minimal effects on the results already described (although this ignores any climate effects induced by the changing atmospheric speciation, see Section 5.4.2). Over 9 log-units of fO_2 change, the timescales to equilibrium stay broadly grouped at similar values; at 1500 K, full thermochemical equilibrium is reached after a maximum of around 1 week at $IW-3$, down to a few minutes at $IW+3.5$ (and less than a second at $IW+2$). In contrast, at 500 K the very

fastest timescales are around 0.2 Myr, while at lower mantle $f\text{O}_2$ conditions NH_3 and CH_4 have chemical timescales of 10's to 100's of Gyr. It should be noted that these values are estimated timescales, which, as discussed in Section 5.2, may overestimate the time to equilibrium if the solver has stalled close to the true equilibrium composition. However, reducing the timescales of most of the $f\text{O}_2$ range shown in Fig. 5.3d even by a factor of 10-100 would still result in an atmosphere at disequilibrium after several Gyr: i.e., comparable to the age of planets we will observe over the coming decades.

Aside from the trend of timescale with temperature, there is also a slight trend to shorter timescales under more oxidised conditions (Fig. 5.3), particularly at lower temperature conditions. This is a result of the higher pressure volcanic atmospheres generated by outgassing of more oxidised mantles (see Chapter 4 and Fig. 5.3d) and hence more frequent molecular collisions. Linking these results back to the atmospheric classes introduced in Chapter 4 for an 800 K atmosphere, Class O (oxidised mantle) atmospheres tend to have faster, but more variable rates to equilibrium at a given surface temperature, while Classes I and R (intermediate and reduced mantles, respectively) have slightly slower, but more consistent timescales.

5.3.2 Rate-limiting reactions

The key abundant and redox sensitive species exhibiting quenching are CO , CH_4 and NH_3 . The interconversions of $\text{CO} \rightleftharpoons \text{CH}_4$ and $\text{N}_2 \rightleftharpoons \text{NH}_3$ proceed via networks of reactions with multiple intermediate steps and several possible reaction pathways. In this web of reactions, the kinetically limiting step converting one species to another is that step which progresses at the slowest rate along the overall fastest reaction pathway. The model discussed here ignores any inhibiting or catalysing processes such as photochemistry or atmosphere-surface reactions; accordingly, identifying the limiting step in each interconversion can indicate if, and via which step directly, such processes might affect the rate of re-equilibration.

The dominant reaction pathways and limiting reactions for both the $\text{CO} \rightleftharpoons \text{CH}_4$ and $\text{N}_2 \rightleftharpoons \text{NH}_3$ interconversions have been debated in the literature, with the primary focus being on explaining disequilibrium chemistry observed in the atmospheres of giant planets (e.g., HD189733b, HD209458b, GJ436b, Gliese 229b) (Line et al., 2011; Moses et al., 2011; Visscher and Moses, 2011; Zahnle and Marley, 2014). Tsai et al. (2017, 2021) perform a detailed model intercomparison for the above conversions and demonstrate that the differences between the results of previous studies are primarily due to different choices of reaction rate coefficients for key reactions, despite the use of a less extensive chemical network by Tsai et al. (2017, 2021). The rates of each reaction involved in the overall conversion of CO and N_2 depend on often poorly constrained rate coefficients; a further motivation for performing a detailed analysis into the reaction pathways and rate-limiting steps is to identify the underlying

Secondary Volcanic Atmospheres: The Importance of Kinetics

experimentally/theoretically constrained rate coefficients that drive our results. A more detailed description and analysis of the reactions and rates we discuss, including full reaction pathways and temperature and fO_2 dependencies, can be found in Section C.2 and Section C.3 for the CO \rightarrow CH₄ system and N₂ \rightarrow NH₃ system, respectively. In the following two sections we now briefly examine the reaction pathways and rate-limiting steps that are ultimately responsible for the quenching of CO, CH₄, and NH₃ in our reaction network.

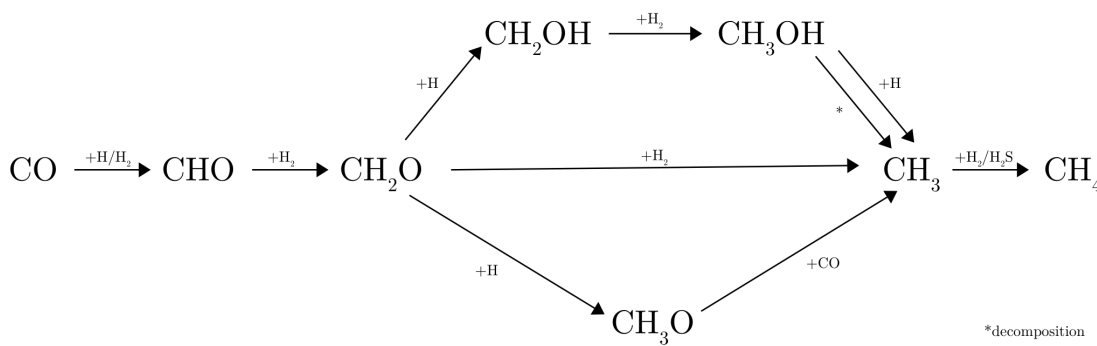
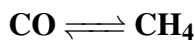


Fig. 5.4 Network of important reactions linking CO to CH₄ in the chemical-kinetics network.

In Fig. 5.2 we showed that CO and CH₄ do not reach their equilibrium abundances in under 1 Myr at 700 – 800 K and below. This is due to the slowest step along the reaction pathway causing a bottleneck in the conversion at these temperatures. The major chemical pathways linking CO to CH₄ are shown in Fig. 5.4. We find that the dominant reaction pathway for the CO → CH₄ conversion changes as a function of temperature but maintains the same net reaction:



At 1000 K and 800 K, we find that the rate-limiting step of the dominant reaction pathway for the $\text{CO} \longrightarrow \text{CH}_4$ conversion (rate coefficient, k ($\text{cm}^3 \text{ s}^{-1}$), taken from Rimmer and Helling (2016)) is



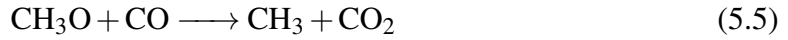
$$k = 9.41 \times 10^{-9} \exp(-124000/T), \quad (5.4)$$

corresponding to the breaking of the C–O bond. This set of reactions has also been identified as important for giant planets (Yung et al., 1988; Visscher et al., 2010; Line et al., 2011). While others have identified alternative rate-limiting steps, the difference is likely due to the inclusion of photochemistry in their systems (Yung et al., 1988; Visscher et al., 2010), as e.g., Tsai et al.

5.3 Results

(2018) identify the same rate-limiting step as Eq. (5.3) for equivalent temperature and pressure conditions.

At 500 K, we find that the rate-limiting step of the dominant reaction pathway for the $\text{CO} \longrightarrow \text{CH}_4$ conversion is



$$k = 2.61 \times 10^{-11} \exp(-5940/T), \quad (5.6)$$

with the rate coefficient taken from Tsang and Hampson (1986). This pathway has not been discussed in previous literature regarding the $\text{CO} \rightleftharpoons \text{CH}_4$ interconversion.

At 800 K, in the most reduced case, $f\text{O}_2 = \text{IW-3}$, the pathway in Eq. (5.5) is one order of magnitude slower than reaction (5.3). However, this reaction increases in importance for volcanic atmospheres built from increasingly oxidised mantles, and becomes comparable in rate to reaction (5.3) by $f\text{O}_2 \geq \text{IW}$. At 500 K, the reaction rates become extremely small and the pathway along Eq. (5.5) becomes almost entirely responsible for the little production of CH_4 that occurs. This is the reaction ultimately responsible for the quenching of CO and CH_4 abundances at low temperatures. The relative importance of all the significant reaction pathways as a function of atmospheric temperature and mantle $f\text{O}_2$ can be found in Fig. C.2.

$\text{N}_2 \rightleftharpoons \text{NH}_3$

The interconversion of $\text{N}_2 \rightleftharpoons \text{NH}_3$ has historically been more difficult to assess compared to that of $\text{CO} \rightleftharpoons \text{CH}_4$, with less well understood reaction schemes (Moses et al., 2010, 2011). We have found that at temperatures ≤ 1000 K, NH_3 does not reach its equilibrium abundance after 1 Myr, due to the slowest step in the interconversion causing a bottleneck at these temperatures (Fig. 5.2). The major chemical pathways linking N_2 to NH_3 are shown in Fig. 5.5.

We find that the dominant reaction pathway for the $\text{N}_2 \longrightarrow \text{NH}_3$ conversion remains the same over all temperatures, with net reaction:



and the rate-limiting step and coefficient (Tomeczek and Gradoń, 2003) of



$$k = 3.32 \times 10^{-11} \exp(-12630\text{K}/T). \quad (5.9)$$

Secondary Volcanic Atmospheres: The Importance of Kinetics

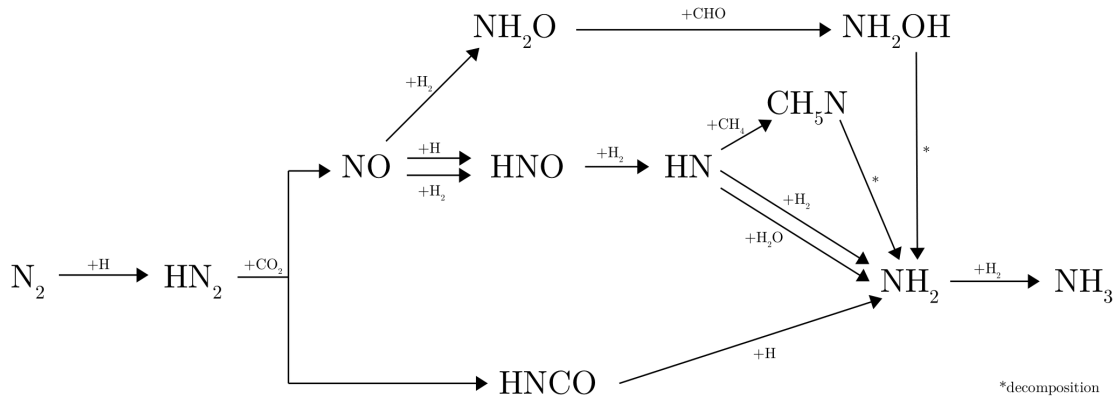


Fig. 5.5 Network of important reactions linking N_2 to NH_3 in our chemical-kinetics network.

Reaction 5.8 is endothermic and therefore the numerator of the exponent in Eq. (5.9) depends on the change in Gibbs free energy, which changes as a function of temperature. Here we evaluate it at $\sim 900\text{ K}$, the approximate quench temperature found for NH_3 . We note the rate constant we use for reaction 5.8 assumes no barrier, therefore if there is a significant activation barrier to $\text{HN}_2 + \text{CO}_2 \rightarrow \text{HNCO} + \text{NO}$, then another reaction may set the rate limiting step or overall conversion pathway. However, we note (1) that even if we remove this reaction from the network altogether, we obtain the nearly the same timescale, and (2) consistent with this observation is that similar results have been found by different models with different chemical networks. Together, these imply that $\text{N}_2\text{--NH}_3$ quenching is insensitive to the precise details of the reaction scheme.

While the net reaction (5.7) matches that of previous schemes Line et al. (2011), Moses et al. (2011), and Tsai et al. (2018), the mechanism of conversion differs. Instead of sequential reactions of N_2 with H and H_2 Line et al. (2011) and Moses et al. (2011), our reaction scheme follows the addition of a H atom with the breaking of the $\text{N}=\text{N}$ bond, resulting in two separate branches, one following HCNO , and the other following NO (See Fig. 5.5 and Section C.3).

At 2000 K and 1500 K both branches contribute, and the pathways are limited by reaction (5.8). As the temperature lowers, further limiting reactions emerge along the NO branch and this becomes subdominant compared to the HCNO branch, which remains limited by (5.8) over our whole temperature and $f\text{O}_2$ range. Reaction (5.8) is thus the reaction ultimately responsible for the quenching of NH_3 abundances at low temperatures. The relative importance of all the significant reaction pathways as a function of atmospheric temperature and mantle $f\text{O}_2$ can be found in Fig. C.3.

5.4 Discussion

The results shown here demonstrate that for a volcanically-derived atmosphere, the surface temperature has to be in excess of 1000 K in order for the chemical timescales of all three species considered here to be shorter than 1 Myr, across all of the mantle $f\text{O}_2$ -dependent atmospheric classes identified in Chapter 4. As this is $1000 \times$ shorter than the age of the atmospheres considered in Figs. 5.2 and 5.3 (which are calculated for an atmosphere 1 Gyr old), we consider chemical timescales of 1 Myr to be the cutoff point for assuming equilibrium, where longer timescales indicate that the abundance of the species in the atmosphere will start to significantly diverge from the abundance predicted by thermochemical equilibrium.

When this assumption is applied to the results shown in Figs. 5.2 and 5.3, it can be seen that there is a temperature range where only NH_3 has a calculated timescale greater than 1 Myr, while CO and CH_4 have timescales shorter than this cutoff. This reflects a limiting-step reaction rate for the $\text{N}_2 \rightleftharpoons \text{NH}_3$ conversion which is systematically many orders of magnitude lower than that of the $\text{CO} \rightleftharpoons \text{CH}_4$ conversion. In this scenario, the atmosphere can be thought of as being in partial equilibrium; where C-H-O species, forming the bulk of the atmosphere, should be approaching thermochemical equilibrium, but major nitrogen species such as NH_3 have their abundances dictated by their freezeout temperatures, reflecting a higher temperature equilibrium.

At higher temperatures, ≥ 1000 K, all species have timescales shorter than 1 Myr and so the atmosphere is assumed to be closely approaching thermochemical equilibrium (discounting photochemistry and vertical mixing). At lower temperatures, below ~ 700 K, NH_3 , CO and CH_4 all have timescales longer than 1 Myr so we assume an entirely ‘kinetically limited’ volcanic atmosphere where even over very long timescales, the atmosphere will no longer reflect thermochemical equilibrium, and instead the kinetics of different reactions control the atmospheric speciation.

The presence of different temperature zones where atmospheres may be in full/ partial/ kinetically limited thermochemical equilibrium requires that certain stars, and orbital zones around those stars, will be optimal for finding planets with atmospheres which are in specific equilibrium regimes. These zones are shown in Fig. 5.6, according to the equilibrium temperature of a planet relative to the luminosity of its star and its orbital distance. Also shown is the point at which water will start to condense from the atmosphere, allowing aqueous chemistry within water droplets. Figure 5.6 indicates that many exoplanets orbiting M stars (which are the most amenable to observations of secondary atmospheres, due to the low planet–star size ratio) will have to have a significant greenhouse effect to have atmospheres which can be modelled as approaching thermochemical equilibrium near their surfaces.

Secondary Volcanic Atmospheres: The Importance of Kinetics

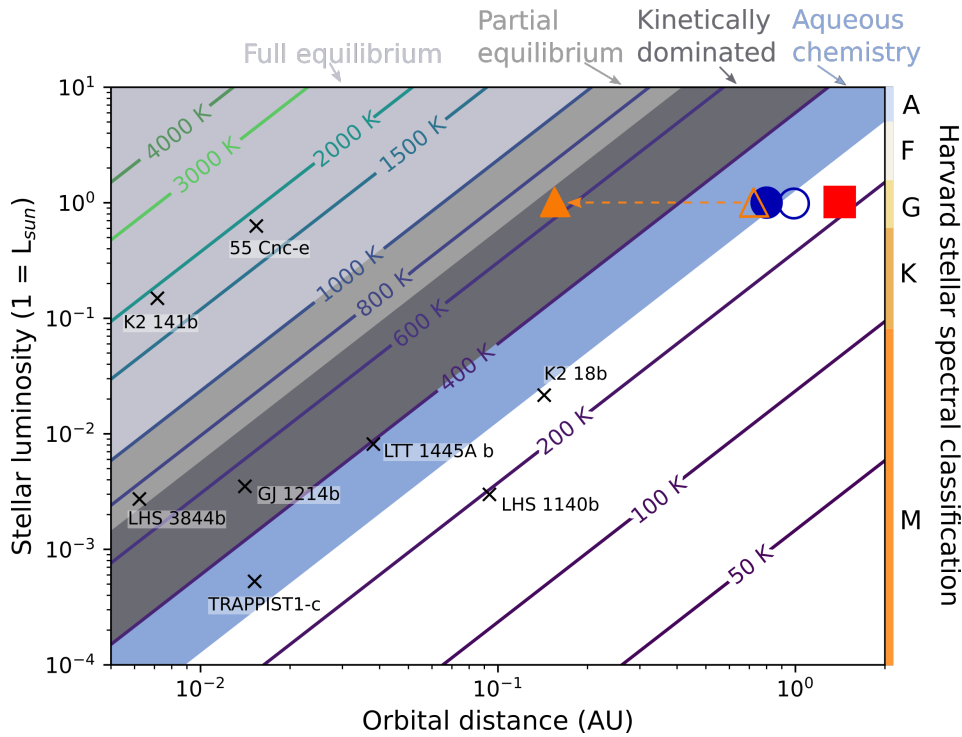


Fig. 5.6 Regions in stellar luminosity–orbital distance space where volcanic gases injected into atmospheres may reach either full, partial or minimal thermochemical equilibrium at a given atmospheric temperature. Temperatures are plotted as the equilibrium temperature of a planet assuming a Bond albedo of 0.3. Atmospheres in partial equilibrium will have species such as NH₃ with abundances dictated by their ‘freezeout’ temperatures, while the rest of the species will be present at abundances predicted by thermochemical equilibrium for that temperature. The liquid water zone is also marked, indicating the point where aqueous chemistry will become relevant for influencing atmospheric chemistry and determining the lifetime of atmospheric species. Earth (blue circle) and Venus (orange triangle) and Mars (red square) are plotted both at their correct orbital distances (open symbols), and their actual surface temperatures (filled symbols), the latter as controlled by the climatic conditions created by their atmospheres. Also marked are a number of rocky exoplanets (all due to be studied during the first round of JWST observation), plotted according to their orbital distance and stellar luminosity; exoplanet data taken from www.exoplanet.eu.

The cutoff temperatures presented in Fig. 5.6 are based on timescales for the end-member case of instantaneously cooling a 0D atmosphere from its high temperature state of thermochemical equilibrium. However in nature, atmospheres will progressively gain mass over time, unless they reach a steady state where gas input is matched by removal processes (e.g., hydrogen escape, see Chapter 6). At any given time an atmosphere is thus a mix of older gases which have had time to approach equilibrium at surface temperatures, along with newly erupted gases which still reflect their high temperature origins. As volcanic gases tend to have characteristics of more oxidised atmospheres at higher temperatures, according to the class definitions of Chapter 4, quenching the chemistry of hot volcanic gases and mixing them into

the atmosphere will make the mantle $f\text{O}_2$ appear more oxidised if the volcanic atmosphere was interpreted as being in thermochemical equilibrium (e.g., Fig. 5.3, also see Fig. 4.4 in Chapter 4).

Even on planets sitting within the ‘full equilibrium’ regime in Fig. 5.6, rapid alteration processes such as escape (see Chapter 6) and photochemistry will be occurring in the atmosphere, which are not accounted for here. Photochemical processing will be particularly important on planets which are subject to intense UV radiation but have atmospheres in the partial equilibrium zone, where the surface temperatures are high enough to approximate equilibrium. In these cases the stratosphere may still be cool enough that photochemistry can significantly affect the abundances of observable species. Surface-atmosphere interactions and any potential biological activity have also been neglected in this study, along with any possible catalysis of reactions. Each of these processes will likely act to pull the chemistry of an atmosphere away from thermochemical equilibrium, and towards some new steady-state. Given that, the results presented here likely represent the most favourable case for volcanic atmospheres achieving thermochemical equilibrium. The suggested temperature zones for partial equilibrium and kinetic dominance (shown in Fig. 5.6) should therefore be taken as the coolest possible temperature estimations of such boundaries.

5.4.1 Can volcanic atmospheres produce biosignature false positives?

Results presented here suggest that 700 K is the minimum atmospheric temperature where a volcanic atmosphere might in principle be able to relax to thermochemical equilibrium (if given ≤ 1 Myr to do so). Above this temperature, it is appropriate for the atmosphere to be modelled as being close to thermochemical equilibrium. This limit is presented for the simplest, most favourable case for achieving equilibrium, as the surface pressure (the highest pressure found in an atmosphere) is assumed for the reaction conditions, and all factors confounding attainment of local thermochemical equilibrium (e.g., transport, photochemistry) have been neglected. For atmospheres with surface temperatures much lower than 700 K, such as some of those presented by Herbort et al. (2020) and all in Woitke et al. (2021), significant amounts of catalysis must be assumed for the atmosphere to remain in thermochemical equilibrium. The results of this chapter therefore bring into question the validity of using purely thermochemical modelling when considering planets with cooler surface temperatures.

The results of this chapter also support the use of co-occurring CH₄ and CO₂ in the absence of CO as a biosignature (Krissansen-Totton et al., 2018). CH₄ and CO₂ are present together in our modelled volcanically-derived atmospheres (mantle $f\text{O}_2 < \text{IW}+3$, corresponding to Class I and R, see Chapter 4), but in these cases CO is also present at abundances between 10 ppm and 0.1%. To completely remove CO to below ppm abundances in the atmospheres modelled

Secondary Volcanic Atmospheres: The Importance of Kinetics

here, while retaining both CH₄ and CO₂, the surface temperature has to be below ~ 500 K. As shown in Figs. 5.2 and 5.3, the timescales required to achieve thermochemical equilibrium, and therefore remove CO, at temperatures ≤ 500 K are sufficiently long (over a Gyr at 500 K) that such an abiotic atmosphere is implausible. This result is also in agreement with that of Huang et al. (2022), who suggest that ammonia can act as a good biosignature gas on warm to cool planets; while the production of NH₃ from volcanic gases is thermodynamically favoured at low temperatures (Fig. 5.1), the timescales to equilibrium through the conversion of N₂ to NH₃ at temperatures below 1000 K are longer than the age of most planets. A volcanic source of ammonia in warm or cool atmospheres is therefore implausible.

In contrast, the claim of Wogan et al. (2020) that methane-rich atmospheres cannot be generated through volcanism may not hold for hot terrestrial atmospheres. Certainly, the results of this chapter and Chapter 4 (Liggins et al., 2022c) indicate that when considered over geologically relevant timescales and in atmospheres of between 1000 and 700 K, significant CH₄ fractions can be built up to a maximum of around 10 % where the mantle $fO_2 \leq IW+2.5$. However, without additional modelling of photochemical processing within the example atmospheres shown here, the two results cannot be directly compared. Of course, this does not affect their claims around a strengthened case for a methane biosignature (which we agree with, as discussed above); 700 K is not a temperature that would usually be considered ‘habitable’.

5.4.2 Model Limitations

There are a number of potentially important processes not included in our modelling that should be investigated in future work.

Evolving atmospheric pressure. The results presented here omit the effect of lower atmospheric pressures earlier in the planet’s lifetime, while the atmosphere is still growing. These lower pressures would promote correspondingly longer timescales to reach equilibrium, with the reaction rates then increasing with atmospheric growth and the associated increase in surface pressure.

Self-consistent climate. Our modelled volcanic atmospheres are not calculated with a self-consistent climate model, meaning that the temperature zones relative to stellar luminosity and orbital distance shown in Fig. 5.6 are liable to move according to the speciation of the atmosphere. For example, CO₂-rich atmospheres such as those produced by oxidised and intermediate mantle fO_2 ’s (Chapter 4) will result in strong greenhouse warming, meaning planets with equilibrium temperatures presently plotted within the kinetically-dominated or aqueous zones of Fig. 5.6 may be sufficiently greenhouse heated so as to have an atmospheric temperature suitable for equilibrium based modelling. Venus demonstrates this behaviour in Fig. 5.6, although with an atmosphere containing close to 90 bar of CO₂, Venus is a

somewhat extreme example. Climate effects would likely also result in increasing surface temperatures through time as a volcanically derived atmosphere grew. The continued outgassing of greenhouse gases, such as CO₂ and H₂ would mean a warming of the planet and an increasing reaction rate and progress towards thermochemical equilibrium over time.

Dependence on chemical networks and chemical models. The findings presented here can differ from previous studies that employ different chemical-kinetics networks for three primary reasons: inclusion of other disequilibrium processes not considered in this work (e.g., transport-induced quenching, photochemistry); the different redox ranges within the atmosphere (past studies often focus on the highly reducing hydrogen dominated atmospheres of irradiated giant planets, brown dwarfs, or post-impact worlds); and the use of different thermochemical data that determine reaction rate coefficients. It is possible that the inclusion of other disequilibrium processes may alter our results for rate-limiting reactions and quench temperatures of the CO \rightleftharpoons CH₄ system and the N₂ \rightleftharpoons NH₃ system, however, disregarding photochemistry, the dominant pathways and rate-limiting reactions identified in Section 5.3.2 are mostly consistent with conclusions from recent previous studies (Moses et al., 2011; Zahnle and Marley, 2014; Zahnle et al., 2020). Moreover, the quench temperatures identified for the CO \rightleftharpoons CH₄ system and the N₂ \rightleftharpoons NH₃ system, $\sim 700\text{K}$ and $\sim 1000\text{K}$ respectively, are in agreement with results from Zahnle et al. (2020) within 100 K, who quote that quench temperatures are of the order $\sim 800\text{K}$ and $\sim 1100\text{K}$ respectively. The temperatures found by Zahnle et al. (2020) relate to transport-induced quenching (when the vertical transport timescale by eddy diffusion becomes equal to the chemical timescale), whereas this study examines quenching purely due to the limit of chemical kinetics on planetary timescales ($\sim \text{Myr}$). It is therefore expected that the quench temperatures we identify are systematically lower than the estimates of Zahnle et al. (2020): our results will apply generally as a lower limit on the quench temperature of any kinetically-limited system, within the accuracy of the thermochemical data used in the chemical-kinetics network.

We look specifically at the generality of our reaction timescale limits in the next section.

Network-independent limits on reaction timescales

We can find a network-independent minimum estimate of reaction timescales, by noting that a necessary first step for transitioning from one equilibrium state to another is the thermal dissociation of a molecule. The atoms and radicals that form from this first dissociation may react with other molecules as the system transitions into a new equilibrium state, but the system will not change until that first thermal dissociation reaction takes place. Therefore, the most rapid thermal dissociation of a major species sets the minimum possible timescale for a system to transition into a new equilibrium state. As we saw above with our complete

Secondary Volcanic Atmospheres: The Importance of Kinetics

chemical network, it is intermediate reactions which ultimately provide the bottleneck on a conversion rate from, e.g., $\text{CO} \rightleftharpoons \text{CH}_4$, hence why considering only the first dissociation of a major species provides a lower bound on reaction timescales. To assess the extent to which our results are network-dependent, we provide an estimate for this first dissociation timescale.

The equilibrium species from Fig. 5.1 with the weakest bond strength (and which will therefore likely react first) is H_2S , with a S-H bond strength of $\approx 335 \text{ kJ/mol}$ (Rumble, 2022). This approximates the activation energy for a collision with another molecule to break the S-H bond. The rate constant for this reaction (s^{-1}) is

$$k = \langle n\sigma V \rangle e^{-E_a/RT}, \quad (5.10)$$

where n (cm^{-3}) is the number density of the H_2S molecule, σ (cm^2) is the collisional cross-section, V (cm/s) is the velocity of the molecules, E_a (kJ/mol) is the activation energy, T (K) is the gas temperature, and $R = 8.3145 \text{ J mol}^{-1} \text{ K}^{-1}$ is the gas constant.

We assume that the gas is in a Maxwell-Boltzmann distribution with a well-defined temperature. To provide an upper limit for the rate constant (and therefore a lower limit for the reaction timescale), we choose an average velocity for a small molecule (in this case, H_2) and a collisional cross-section equal to the geometric cross-section for a large molecule ($\sigma = 3 \times 10^{-15} \text{ cm}^2$, similar to Benzene), and set n equal to the number density of the gas at the planet's surface, assuming a 1 bar ideal gas. The abundance of H_2S will always be less than this, and therefore the rate constant will be proportionately lower. Applying all these assumptions, and noting that the timescale τ (s) = $1/k$:

$$\tau = \frac{\sqrt{\pi m_p k T}}{2\sigma p} e^{E_a/RT}, \quad (5.11)$$

where $p = 1 \text{ bar}$ is the gas pressure at the surface, $m_p = 1.67 \times 10^{-24} \text{ g}$ is the proton mass, and $k = 1.38 \times 10^{-16} \text{ erg/K}$ is Boltzmann's constant. We plot τ as a function of T in Fig. 5.7.

The temperature at which it will take longer than 1 Gyr for the weakest bond in the system to break is 661 K (Fig. 5.7). This is less than 50 K lower than our minimum temperature of 700 K for thermochemical equilibrium to be achieved over geological timescales, as found by applying the full chemical network. We therefore find that even with an alternative chemical network, or by assuming equilibrium can be achieved with chemical timescales of over 1 Myr, a significantly lower temperature for maintaining atmospheric thermochemical equilibrium is physically unfeasible.

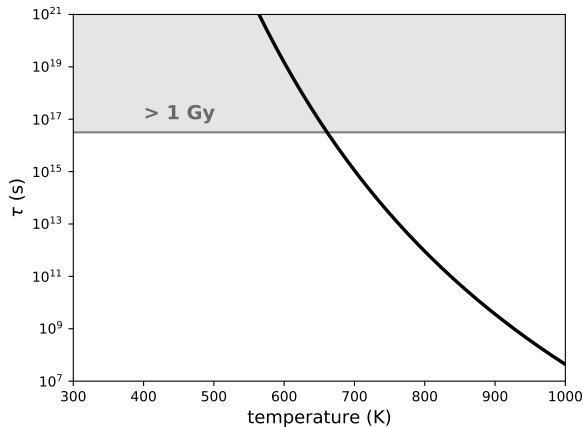


Fig. 5.7 Minimum chemical timescale τ (s) as a function of temperature (K). The black line is τ , from Eq. (5.11), with $E_a = 335$ kJ/mol, based on the bond strength of S-H, the lowest bond strength out of the bonds for equilibrium species (see Fig. 5.1). The grey line and shaded region show where timescales exceed 1 Gy, with the crossover temperature at 661 K.

5.5 Conclusions

This chapter has investigated the timescales over which volcanically-derived atmospheres can relax to a new thermochemical equilibrium, as dictated by the current atmospheric temperature and pressure. We find that the speciation of volcanic atmospheres will be quenched over geological time to those set by higher temperature thermochemical equilibria, if the atmospheric temperature is much below 700 K. Below this threshold, slow chemical kinetics preclude the reactions of key species CO, CH₄ and NH₃, preventing the atmosphere from reaching low-temperature thermochemical equilibrium. As such, the modelling of temperate exoplanet atmospheres where thermochemical equilibrium is assumed must also invoke significant catalysis of reactions in order for results to be plausible. Temperate planets with warm, or cool, quenched volcanic atmospheres will likely not show clear fingerprints of the mantle $f\text{O}_2$, particularly if the mantle is highly reduced: the volcanic gases from reducing mantles are a closer match to those from more oxidised mantles when they are still hot, meaning that if such atmospheres were interpreted according to the classes derived in Chapter 4 (reduced–intermediate–oxidising) they would be classed as being derived from more oxidising mantles than they really were (e.g., Fig. 5.3, also see Fig. 4.4). Quenching of volcanically-derived atmospheres at the relatively high temperature of 700 K also precludes the production of CO₂+CH₄ without CO, meaning that false-positive biosignatures are unlikely to be achieved in volcanic atmosphere by thermochemistry alone.

6

Secondary Volcanic Atmospheres: Hot Atmospheres Undergoing Escape

6.1 Introduction

The secondary volcanic atmospheres of rocky planets can undergo a number of processes which modify the atmosphere away from its initial, purely volcanic composition. As discussed in Chapter 4 and Table 4.1, these processes can include: kinetically limited thermochemical re-equilibration (Chapter 5); photochemistry (e.g., Kasting and Catling, 2003; Wogan and Catling, 2020; Jordan et al., 2021); impact driven erosion, transformation and volatile delivery (e.g., Liu et al., 2015; Sinclair et al., 2020; Zahnle et al., 2020; Itcovitz et al., 2022); and atmospheric escape (e.g., Hunten, 1973; Kasting, 1993; Tian et al., 2005; Wordsworth and Pierrehumbert, 2014). Of these processes, potentially the most important to consider when linking the chemistry of an atmosphere to its mantle $f\text{O}_2$, is escape. As hydrogen escapes more easily than, e.g., oxygen, escape tends to oxidise planets, starting with their atmospheres (Catling et al., 2001; Zahnle et al., 2013). This oxidation effect will act to affect the $f\text{O}_2$ -dependent atmospheric chemistry, and is therefore an important aspect to consider before models such as those presented in Chapter 4 can be applied to interpret observations of atmospheres, and link them to planetary interiors.

As has been previously discussed in Chapter 3 and Section 3.2.2, the maximum rate of hydrogen loss from an atmosphere that isn't hydrogen dominated is referred to as diffusion-limited escape. This maximal loss flux is controlled by the rate of upward molecular diffusion of hydrogen-bearing species through the background atmosphere, the hydrogen mixing ratio (the abundance of hydrogen in all its forms) and the pressure scale height (see Eq. (6.1)). The

actual rate of hydrogen loss is then controlled by the amount of incident stellar XUV radiation, which is a function of several factors such as stellar age, rotation rate, and activity (Johnstone et al., 2015), and the planet’s proximity to the star. If sufficient XUV (extreme UV) radiation is present to remove all the hydrogen from above the exobase, escape proceeds at the diffusion limited rate. Otherwise, escape is ‘energy limited’, and occurs at some fraction of the diffusion limit proportional to the XUV flux. In order to reduce the number of variables considered here, only hydrogen escape occurring at the maximum, diffusion limited rate is considered. This represents an upper limit on the efficiency of H escape shaping a terrestrial planet’s atmospheric chemistry.

Chapter 3 demonstrates that when a volcanic atmosphere is assumed to be in steady state (i.e., the input flux of hydrogen from volcanic sources is equal to the loss flux to space), a hydrogen-rich atmosphere can be maintained, depending on the mantle $f\text{O}_2$, volcanic flux and efficiency of escape. However, while the total hydrogen mixing ratio ($f_T(\text{H}_2) = f(\text{H}_2\text{O}) + 2f(\text{CH}_4) + f(\text{H}_2\text{S}) + 1.5f(\text{NH}_3)$, where f_i is the total number mixing ratio of species i) can be calculated using the method applied in Chapter 3, the speciation of this atmospheric hydrogen component is unknown. Knowing the speciation of this hydrogen component is key; for example, many of the climate implications attributed to a given $f_T(\text{H}_2)$ assume most of the hydrogen mixing ratio is speciated as H_2 , leading to an H_2 -enhanced greenhouse effect (e.g., Pierrehumbert and Gaidos, 2011; Ramirez and Kaltenegger, 2017). On cool planets, the assumption that most of the $f_T(\text{H}_2)$ fraction is present as H_2 is likely a valid one; as is shown in Chapter 5, atmospheres with temperatures below 700 K will quench their volcanic emissions. At 1500 K H_2 is thermodynamically favoured over e.g., CH_4 (see Figs. B.2, 4.1 and 5.1 for examples of this behaviour), and as such, while additional processes such as photochemistry are ignored, an assumption of a H_2 -dominated hydrogen fraction is reasonable.

However, this gas quenching will not occur in the hot atmospheres (800 K) explored in Chapters 4 and 5. There is therefore a question of what the chemistry of volcanic atmospheres, explored without escape in Chapter 4, will look like when hydrogen escape is considered. As has already been established, the method implemented in Chapter 3 only gives the total hydrogen mixing ratio, not the speciation; it is also only valid for an atmosphere in steady state – i.e., not actively growing/evolving. Steady state will not be a valid assumption for most atmospheres modelled by EVolve, which in the absence of most atmospheric sinks (deposition, drawdown and, previously, escape) continue to grow in mass over time as volcanic degassing continues, even if the speciation has stabilised (see Fig. 4.7).

This chapter describes a new method for modelling the speciation of an atmosphere which is undergoing hydrogen escape as it evolves through time (Section 6.2). The results of this method are compared to predicted total atmospheric hydrogen contents from Chapter 3, and scenarios

where the two contrasting model formalisms are best utilised are discussed (Section 6.2.3). The new model is then applied to the hot, volcanically-derived atmospheres described in Chapter 4 (Section 6.3).

The extent to which hydrogen speciated as water can escape from an atmosphere is constrained by the supply of H₂O to the high atmosphere, where it can be dissociated by photolysis and the hydrogen can escape (Wordsworth and Pierrehumbert, 2013a). This H₂O supply can be restricted by low temperatures at the coldest point in the atmosphere (on Earth, this is found in the stratosphere), sufficient to limit the local H₂O mixing ratio through condensation, and thus prevent the transport of water to the upper atmosphere where it would otherwise escape. As such, two hydrogen escape scenarios are considered in Section 6.3: 1) ‘dry stratosphere’, where water is prevented from escaping by a stratospheric cold trap, as occurs on modern Earth; and 2) ‘wet stratosphere’, where no cold trap is assumed and water is allowed to dissociate and escape. The presence of an atmospheric cold trap is a function of surface temperature, and the ratio of non-condensing species (e.g., CO₂, N₂, O₂) to water (Wordsworth and Pierrehumbert, 2014). High surface temperatures, such as those considered here, tend to preclude an atmospheric cold trap (Kasting et al., 2015). However, CO₂ can also cause cooling in the upper atmosphere, reducing the amount of water loss (Leconte et al., 2013; Wordsworth and Pierrehumbert, 2013a). In the absence of a full climate model to establish an atmospheric P-T profile, and thereby constrain the extent of upper-atmosphere cooling and any effects on a possible cold trap, both wet- and dry stratosphere escape are explored here as two end-member cases. Discussion and conclusions follow in Sections 6.4 and 6.5.

6.2 Methods

As in Chapters 4 and 5, the conceptual model applied here is of a 0D atmosphere at surface pressure, in thermochemical equilibrium, with a constant volcanic input driven by a rate of magma eruption to the surface of $1 \times 10^{14} \text{ kg yr}^{-1}$, approximately similar to the modern Earth (see Chapter 4). In this section, a brief overview of the EVolve model used here (described in full in Chapter 2) is given (Section 6.2.1); the method for calculating the speciation of an atmosphere which is undergoing escape while evolving in composition, as implemented in Evolve, is described (Section 6.2.2); and this new formalism is compared to previously established methods (Section 6.2.3).

6.2.1 Evolving volcanic atmospheres

The evolution and chemical composition of volcanically derived atmospheres in thermochemical equilibrium is again modelled here using EVolve, described in Chapter 2. This is a 3-part model linking the mantle to the atmosphere using EVo, a volcanic degassing model for elements C, O, H, S and N. During a single time-step, a portion of the mantle is melted and volatiles partition according to batch melting rules from the bulk mantle into the melt phase. The mass and volatile content of this magma, along with how oxidising the planet's upper mantle is (measured by its oxygen fugacity, the $f\text{O}_2$) are used as initial conditions in EVo. EVo finds the volatile saturation pressure of this magma, then calculates the volatile element chemistry of the two-phase magma and exsolved gas mixture at both the saturation pressure, and the surface. This is done by simultaneously solving a system of 5-7 heterogeneous equilibria (between silicate melt and gas, described using solubility laws), 5 homogeneous gas-phase equilibria and the balance between oxygen stored in the melt as Fe_2O_3 or FeO , and oxygen within the volatile species. The end point of the volcanic outgassing is defined as the surface atmospheric pressure, which gradually increases with every time-step as volatile mass is added to the atmosphere.

The FastChem 2.0 equilibrium chemistry model (Stock et al., 2018; Stock and Kitzmann, 2021) is next used to calculate the chemistry of the atmosphere at the recalculated surface pressure and temperature of the planet for the new, mixed atmosphere. In previous Chapters 4 and 5, this marks the end of a timestep; however, here considerations of hydrogen escape from the atmosphere are included, requiring further re-calculations of the atmospheric chemistry.

6.2.2 Formulating H_2 escape within EVolve

In EVolve, it is assumed that hydrogen escape proceeds at the diffusion limited escape rate, where the rate of hydrogen escape is proportional to the rate of movement of hydrogen-bearing gases through the upper atmosphere (see also Chapter 3). This limiting flux of hydrogen is described as (Hunten, 1973)

$$\phi_l(i) = \frac{b_i}{\mathcal{H}_a} \frac{f(i)}{1 + f(i)} \left(1 - \frac{\mu_i}{\mu_a}\right), \quad (6.1)$$

where $f(i)$ is the mixing ratio of species i in the atmosphere, \mathcal{H} is the atmospheric pressure scale height (cm), μ is mean molecular mass (g mol^{-1}) and b is a binary diffusion parameter ($\text{molecules cm}^{-1} \text{s}^{-1}$). In all cases the subscript a indicates a property of the background atmosphere minus the i constituent. b_i is calculated for each species using data and methods from Hunten (1973) for b_{H_2} , Marrero and Mason (1972) for $b_{\text{H}_2\text{O}}$, b_{CH_4} and b_{NH_3} , and [eq.

Table 6.1 Binary diffusion coefficients as calculated at 300 and 800 K within EVolve, using data and methods from Hunten (1973) and Banks and Kockarts (1973) for H₂ and H₂S respectively, and Marrero and Mason (1972) for H₂O, CH₄ and NH₃.

Species	b _i , T=300 K	b _i , T=800 K
H ₂	1.925 × 10 ¹⁹	4.016 × 10 ¹⁹
H ₂ O	6.315 × 10 ¹⁸	1.398 × 10 ¹⁹
CH ₄	5.660 × 10 ¹⁸	1.253 × 10 ¹⁹
H ₂ S	6.653 × 10 ¹⁸	1.086 × 10 ¹⁹
NH ₃	5.735 × 10 ¹⁸	1.269 × 10 ¹⁹

15.92] of Banks and Kockarts (1973) for $b_{\text{H}_2\text{S}}$. The atmosphere is assumed to be isothermal, so b_i values are calculated at the same temperature the atmosphere is equilibrated at, resulting in diffusion coefficient values as listed in Table 6.1. In this case, following Hunten (1973), $f(i) = n_i/n_a$, where n is the number density, rather than the more commonly used $f(i) = n_i/(n_i + n_a)$.

The limiting flux described in Eq. (6.1) is the rate at which a molecule will diffuse through the background atmosphere. If the molecular mass of the molecule is heavier than the mean molecular weight of the background atmosphere, the flux will be negative – as the molecule will sink, rather than rise, under the influence of the planet’s gravity. In this case, the flux of the heavy species is set to 0 as it is not contributing to the total flux of hydrogen to the top of the atmosphere.

The diffusion limited escape flux of hydrogen from the atmosphere is calculated as (Walker, 1977)

$$\phi H_{\text{esc}, \text{dry}}(C) = 2\phi_l(C_{\text{H}_2}) + 4\phi_l(C_{\text{CH}_4}) + 3\phi_l(C_{\text{NH}_3}) + 2\phi_l(C_{\text{H}_2\text{S}}) \quad (6.2\text{a})$$

$$\phi H_{\text{esc}, \text{wet}}(C) = \phi H_{\text{esc}, \text{dry}}(C) + 2\phi_l(C_{\text{H}_2\text{O}}), \quad (6.2\text{b})$$

where C is a set of all species in the atmosphere and $C_i \in C$. Water is included as contributing to the hydrogen escape flux (Eq. (6.2b)) only when simulating planets without a stratospheric cold trap, the ‘wet stratosphere’ scenario. Models which include a cold trap, and therefore exclude water from the hydrogen escape equation (Eq. (6.2a)), are described by the ‘dry stratosphere’ scenario.

The major concern which this method must account for is the change in the escape flux which would occur across a time-step. This is because as hydrogen escapes, and the amount of hydrogen in the atmosphere decreases, the diffusion limited loss flux decreases proportionally according to Eq. (6.1). Calculating a single escape flux at the end of the time-step using either Eq. (6.2a) or Eq. (6.2b) would therefore overestimate the amount of hydrogen lost. However, assuming steady state and equating the volcanic hydrogen input to the escape flux to calculate the total hydrogen mixing ratio of the atmosphere (as in Chapter 3 and, e.g., Kasting, 1993;

Secondary Volcanic Atmospheres: Hot Atmospheres Undergoing Escape

Kharecha et al., 2005), cannot tell us the actual composition of the atmosphere after escape, and by assuming steady state also does not allow the atmosphere to grow over time as would be expected.

We therefore solve for the condition that the diffusion limited escape flux, calculated for an atmosphere with a new and lower hydrogen content after escape (H_{new}), matches the loss flux needed to generate H_{new} over the time-step. An iterative method is required to achieve this; therefore, SciPy's implementation of the Brent root finding algorithm is applied to solve for H_{new} , the total abundance of atomic hydrogen in the atmosphere after escape, using

$$\Phi_{\text{loss}}(H_{\text{new}}) = \phi H_{\text{esc}}(\text{FastChem}(H_{\text{new}})), \quad (6.3)$$

where

$$\Phi_{\text{loss}}(H_{\text{new}}) = \frac{1}{dt} \frac{(M_{H_{\text{init}}} - M_{H_{\text{new}}})}{\mu_H N_A} \frac{1}{4\pi r_p^2}. \quad (6.4)$$

The Brent algorithm is used to provide physical limits to the solution, so that the atmosphere cannot gain H_2 , or lose more than was present in the atmosphere at the start of the H_2 loss iteration. This inhibits the algorithm from providing unphysical solutions to Eq. (6.3).

In Eq. (6.3) $\text{FastChem}(H_{\text{new}})$ denotes re-running the FastChem model, producing an atmospheric composition C , so the RHS of Eq. (6.3) is the diffusion limited escape flux of hydrogen, in atoms $\text{cm}^{-2} \text{s}^{-1}$, based on the current atmospheric chemical composition and resultant scale height. $\Phi_{\text{loss}}(H_{\text{new}})$ is the hydrogen loss flux over the last time-step as a function of the difference in the mass of hydrogen in the atmosphere before ($M_{H_{\text{init}}}$) and after ($M_{H_{\text{new}}}$) escape, calculated using Eq. (6.4). μ_H is the atomic mass of H, N_A is Avogadro's constant, dt is the number of years in a single time-step and r_p is the radius of the planet.

6.2.3 Validation of atmospheric escape formalism

It is useful to validate this new procedure for calculating hydrogen escape by comparing results to those calculated using more established methods. The commonly used approximation, as established and utilised in Chapter 3, is to assume a steady-state atmosphere where the input flux of hydrogen to the atmosphere is equal to the loss flux to space (Walker, 1977; Kasting, 1993; Kharecha et al., 2005). In order to validate the method described above, which was implemented to allow for an evolving atmospheric mass and composition, results generated by EVolve's H escape formalism were compared to those produced by the steady-state method used in Chapter 3, first shown in Fig. 3.1. EVolve was run under conditions which resembled as closely as possible those assumed by the steady-state calculations in Chapter 3. As in previous chapters, EVolve was initiated with a 0.01 bar N_2 atmosphere, and was allowed to

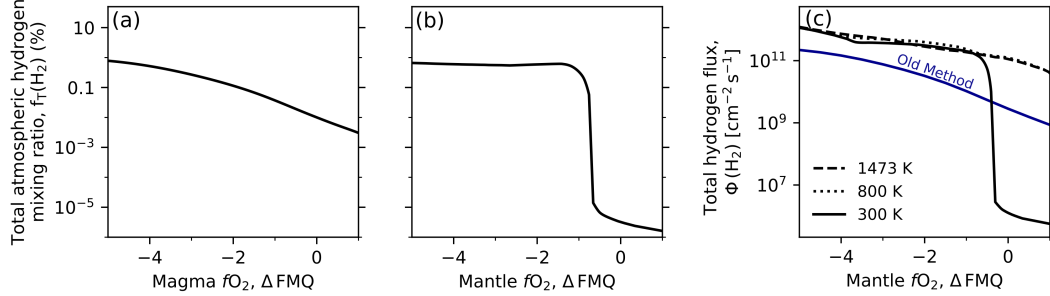


Fig. 6.1 Comparing the hydrogen mixing ratio as calculated using the methods of a) Chapter 3, where steady state is assumed, and b) this chapter. c) The total input flux of atomic hydrogen entering the atmosphere as calculated in Chapter 3 (blue) and this chapter, assuming the volcanic gas has re-equilibrated at 1473, 800 and 300 K.

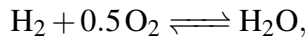
run until the atmospheric pressure reached 10 bar, with dry stratosphere escape implemented as is appropriate for a cold atmosphere. The initial mantle volatile content for EVolve was approximated so that the melt volatile content is similar to those used in Chapter 3, and the atmospheric temperature was set to 300 K. This is slightly warmer than the 210 K used to calculate the binary diffusion coefficients in Chapter 3; however, this was necessary because at lower temperatures and high fO_2 (\geq IW-1) EVolve fails to find a real solution during the root-finding portion of the hydrogen escape procedure (due to convergence failures within FastChem). At lower mantle fO_2 ($<$ IW-1), where results were produced for an atmosphere at 210 K, there is on average a $<5\%$ difference between the hydrogen mixing ratio of the 300K and 210K atmospheres. Differences due to temperature between the old and new method are therefore minimal. The two methods are compared in Fig. 6.1, at a surface pressure of 10 bar.

Comparing Fig. 6.1a to Fig. 6.1b, at low fO_2 the total hydrogen mixing ratio ($f_T(H_2) = f(H_2O) + 2f(CH_4) + f(H_2S) + 1.5f(NH_3)$) is comparable across both methods. However, unlike Fig. 6.1a which shows a gradual decrease in $f_T(H_2)$ with increasing fO_2 , Fig. 6.1b shows an almost constant $f_T(H_2)$ with fO_2 until a mantle fO_2 of FMQ-1 is reached, at which point the hydrogen mixing ratio drops by around 5 orders of magnitude. The reason for the atmospheric chemistry responding to fO_2 in this way can be seen from how the input flux of hydrogen varies with the mantle fO_2 (Fig. 6.1c), which shows an equivalent abrupt decrease in the input H flux at FMQ-1. In EVolve, volcanic gases are allowed to cool and re-establish thermochemical equilibrium before, and during, hydrogen escape. As was shown in Fig. 5.1, particularly at high fO_2 , a volcanic gas re-equilibrated to 300 K will speciate almost all (to below the ppm level) of its hydrogen as H_2O . In the dry stratosphere case explored in Fig. 6.1, H_2O does not escape and therefore is not counted as part of the hydrogen mixing ratio; this

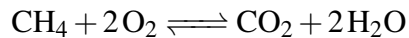
Secondary Volcanic Atmospheres: Hot Atmospheres Undergoing Escape

results in a significant drop in the flux of hydrogen into the atmosphere which can participate in escape, and a proportional decrease in the hydrogen mixing ratio within the atmosphere. In contrast, for a volcanic gas remaining at 1473 K, as is assumed in the steady-state model, no such sharp drop in the flux of hydrogen entering the atmosphere is seen and instead a gradual decrease broadly consistent with the steady-state curve is found.

Figure 6.1 also shows that a higher flux of H (speciated as either H₂, CH₄, H₂S or NH₃) into the atmosphere is required to maintain the same $f_T(H_2)$ when considering escape concurrent with volcanic outgassing in non-steady state, compared to the case where atmospheric steady state is assumed. This is a direct result of the fact that the atmosphere is allowed to thermochemically re-equilibrate *during* hydrogen escape. As H₂ (originally speciated as CH₄, H₂S etc.) escapes, equilibrium acts to restore balance by shifting reactions such as



and



to the left, the oxygen producing side, which moves hydrogen which was originally speciated as water and hence could not escape due to the cold trap, into species which are allowed to dissociate and escape. Therefore, the escape flux of hydrogen is greater than the volcanic input where water is ignored.

Two factors are important here for understanding the results shown in Fig. 6.1: 1) in the wet stratosphere case, this apparent difference between the input and output flux will strongly diminish. When H₂O is included within the $f_T(H_2)$ parametrisation, the effect of hydrogen speciation in the atmosphere is removed as all hydrogen species are now contributing to escape, and the $f_T(H_2)$ calculated using the steady-state method and the method established here for an equivalent input flux should match. 2) The method established here assumes rapid thermochemical re-equilibration during hydrogen escape, to allow H₂O-speciated hydrogen to escape in the dry-stratosphere case. While this is a valid assumption over long time periods for planets with hot atmospheres (see Chapter 5), it is not for a cool atmosphere at 300 K. The results shown in Fig. 6.1 are therefore only valid as a comparison to other formalisms for modelling escape, and the results for the remainder of this chapter are carried out assuming the same 800 K atmospheres which have been previously explored in Chapters 4 and 5. Nevertheless, Fig. 6.1 shows that the new method explored here is comparable to those which assume steady state under low temperature, reduced mantle conditions, while allowing the chemical speciation of the atmosphere to be calculated as it undergoes escape.

6.3 Results

Here, the effects of atmospheric escape on volcanic atmospheres at a temperature of 800 K are investigated. EVolve is run with the same initial conditions as in Chapters 4 and 5: initially with a single starting volatile content of 450 ppm H₂O and 50 ppm CO₂ (Elkins-Tanton, 2008), appropriately scaled S and N contents (see Chapter 4) and a single rate of melt production in the mantle. All simulations are for an Earth-sized planet, with runs initialised with a 0.01 bar N₂ atmosphere. Atmospheric compositions are for a 0D atmosphere conceptually consistent with a near-surface layer at surface pressures, and are presented for planets with a range of mantle $f\text{O}_2$ values. The total hydrogen mixing ratio ($f_T(\text{H}_2)$) for the hot, dry stratosphere scenario is shown first in Fig. 6.2, before both wet stratosphere and dry stratosphere end-member scenarios are explored in Fig. 6.3.

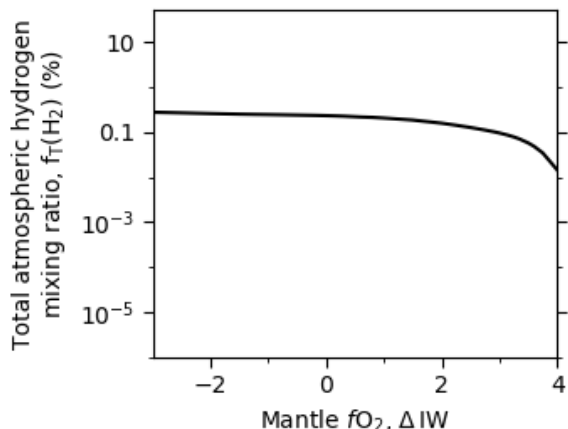


Fig. 6.2 The total hydrogen mixing ratio for a volcanic atmosphere undergoing dry stratosphere escape, after 2 Gyr of evolution. This plot shows $f_T(\text{H}_2)$ for the atmospheric speciation shown in Fig. 6.3c, and is shown with the same y-axis scale as in Figs. 6.1a and 6.1b for comparison.

The total hydrogen mixing ratio (i.e., summed across H-bearing species) for a set of hot (800 K) volcanic atmospheres with a dry stratosphere sits at around 0.1 % when mantle $f\text{O}_2$ is below IW+3 (Fig. 6.2), with hydrogen speciated almost entirely as H₂S (see below, Fig. 6.3). While the $f_T(\text{H}_2)$ values at low $f\text{O}_2$ between Figs. 6.1 and 6.2 appear to be similar, this is somewhat misleading as in Fig. 6.2 a higher escape flux (driven by higher atmospheric temperatures; the b_i/\mathcal{H}_a term in Eq. (6.1) is proportional to temperature) is counterbalanced by a greater initial H content within the mantle.

By considering atmospheric escape of H, the relationship between mantle $f\text{O}_2$ and atmospheric chemistry (Liggins et al., 2022c) becomes significantly weaker. In the dry stratosphere case (Fig. 6.3c), both SO₂ and S_X are present at abundances between slightly above 1 ppm, and 5% depending on the mantle $f\text{O}_2$, rather than only being present in atmospheres with oxidised mantles above IW+2 (e.g., Fig. 4.2). Neither CH₄ nor NH₃ is ever present above ppm abundances in the volcanic atmospheres built while undergoing escape. The atmospheric H₂ mole fraction gradually increases with decreasing mantle $f\text{O}_2$ by a factor of 100 over the 9

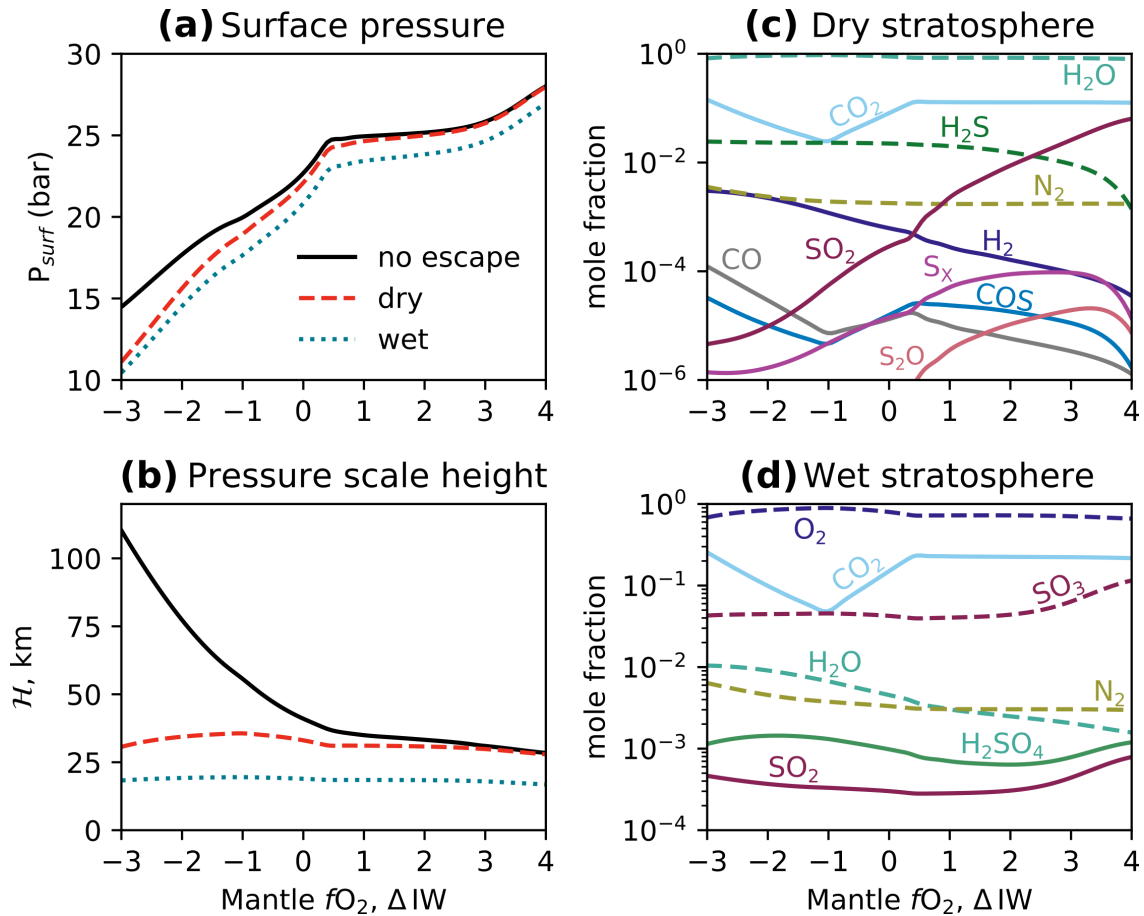


Fig. 6.3 The effect of hydrogen escape regime on the atmospheric properties of warm (800 K) volcanic atmospheres after 1 Gyr of evolution. In all cases escape is at the diffusion limited rate; in the dry stratosphere case water is not allowed to escape, whereas it is allowed in the wet stratosphere case.

log units of fO_2 change shown in Fig. 6.3c. The surface pressure remains almost unchanged under high mantle fO_2 conditions, but decreases by several bar for 2 Gyr of evolution at low mantle fO_2 in both the wet – and dry stratosphere scenarios. More significantly, the atmospheric scale height remains at ~ 25 km regardless of mantle fO_2 in the dry stratosphere case, as H_2 -induced scale height inflation (Miller-Ricci et al., 2008) no longer occurs.

The removal and relocation in relation to mantle fO_2 of the indicator species identified in Chapter 4 results in neither Class R (mantle $fO_2 < IW-0.5$, H_2 and CH_4 at $>1\%$, $NH_3 > CO$) nor Class I (mantle fO_2 between $IW-0.5$ and $IW+2.7$, includes CO_2 , CH_4 at mixing ratios $<1\%$ and an absence of oxidised S species above ppm levels) atmospheres being present in either scenario shown in Fig. 6.3. Instead, Class O atmospheres (mantle $fO_2 > IW+2.7$ in escape-free scenarios) appear across the full, 9 log units of mantle fO_2 range in the dry stratosphere case. The presence of oxidised sulfur species and sulfur allotropes, which define

6.3 Results

Class O, in the volcanic atmospheres of planets with reduced mantles is a result of too little H₂ remaining in the atmosphere to store all the atmospheric sulfur as H₂S.

If the previously established method of identifying atmospheric classes (Chapter 4, Liggins et al., 2022c) is applied to the wet-stratosphere case, the compositions presented might be classified as Class O (as oxidised sulfur species are present). However, these atmospheres have significantly different speciations to those seen earlier, as they are now oxygen dominated (an effect which has previously been described in e.g., Kasting, 1988; Leconte et al., 2013; Wordsworth and Pierrehumbert, 2014; Schaefer et al., 2016) as opposed to water dominated, and contain significant quantities of H₂SO₄. CO₂ is also the only carbon-bearing species now present. These strongly oxidising atmospheres show almost no variation across the 9 log units of mantle fO_2 change explored here, and have even lower pressure scale heights than both the dry-stratosphere case, and the escape-free atmospheres of planets with oxidised mantles, at around 20 km (Fig. 6.3b). Atmospheres which contain 10's of percent O₂ and smaller fractions of H₂SO₄, shown here to be produced by intense hydrogen escape only possible where a wet stratosphere is imposed, should therefore be considered outside the 3-class system established in Chapter 4 (Liggins et al., 2022c) and referred to as Class E (escape).

Chapter 4 showed that a change in the volatile H/C mass ratio of the initial mantle makes little difference in the atmospheric classes produced. Here, Fig. 6.4 shows that including hydrogen escape in the consideration of atmospheric evolution produces similar conclusions; in the two H/C ratios shown, there are no distinct variations either with fO_2 , or between the high and low H/C ratio cases. The most consequential difference is that planets with a high mantle fO_2 and low H/C ratio undergoing wet-stratosphere escape (Fig. 6.4f) can develop a CO₂, rather than O₂, dominated atmosphere; however, these would still be regarded as Class E as O₂ remains present at abundances $\geq 10\%$.

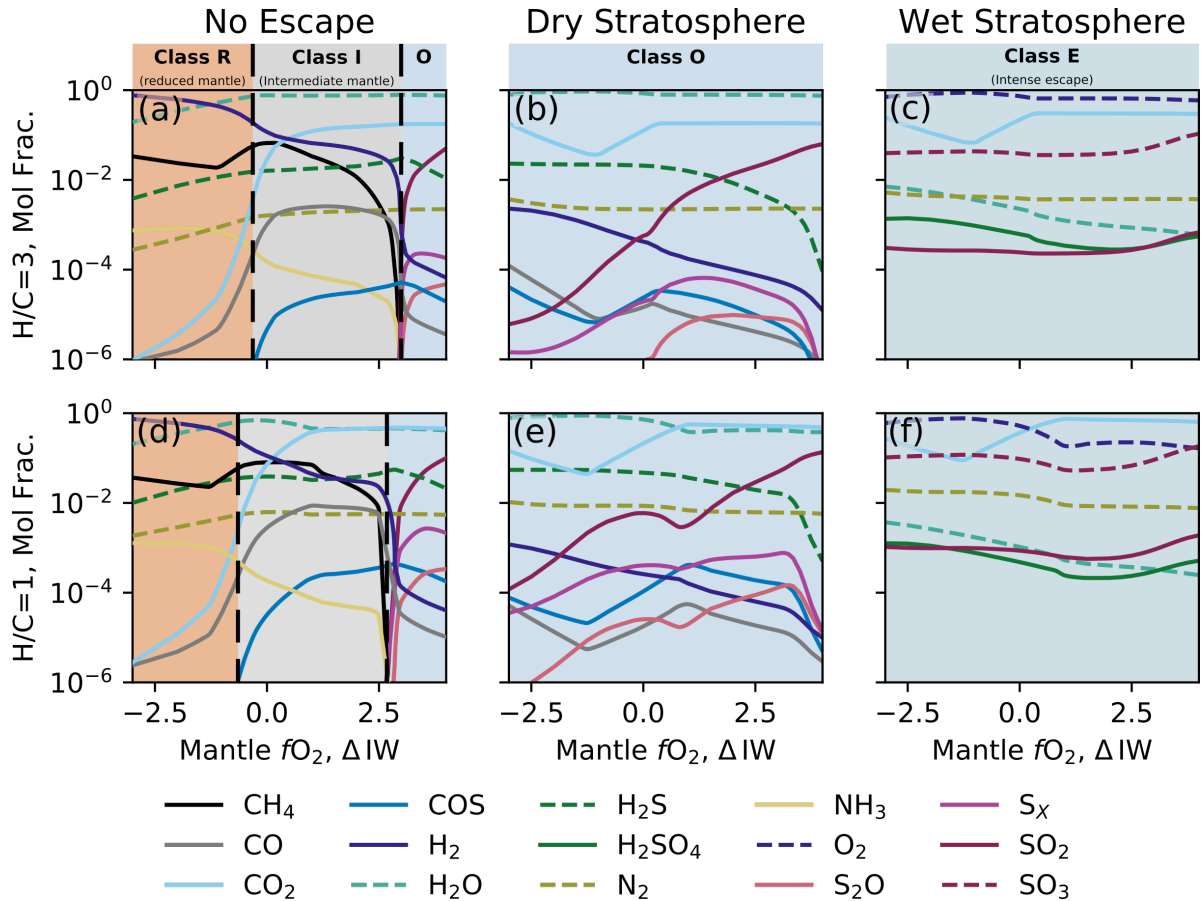


Fig. 6.4 Atmospheric speciation with mantle fO_2 given as mole fractions after 2 Gyr of evolution, for an initial mantle H/C ratio of 3 (a-c) and 1 (d-f) and absent (a and d), dry stratosphere (b and e) and wet stratosphere (c and f) escape regimes.

6.4 Discussion

In both the escape scenarios evaluated here, there is minimal to no variation in the speciation of volcanic atmospheres with mantle fO_2 , even at the lower 800 K atmospheric temperatures that show distinct, fO_2 -associated classes in escape-free scenarios. The volcanic gases being released at the surface will be very similar in all three scenarios, as the surface pressure remains largely unaffected by H₂ escape (Fig. 6.3a). However, hydrogen escape oxidises the atmosphere, essentially breaking the link between mantle fO_2 and the atmospheric composition. Even at the lower rate of escape under a dry stratosphere scenario, the escape flux of hydrogen is sufficient to functionally negate the impact of 9 log-units of mantle fO_2 change.

Atmospheres undergoing dry stratosphere escape could be particularly difficult to distinguish from an escape-free Class O atmosphere. This could lead to mis-identification of mantle fO_2 , particularly between a planet with an oxidised mantle with no atmospheric escape, and a planet with a reduced mantle undergoing dry stratosphere escape: the chemistries of the volcanic atmospheres produced on these two planets are almost indistinguishable (e.g., comparing Class O in Fig. 6.4a, and Fig. 6.4b). The oxygen-domination and presence of H₂SO₄ and SO₃ in the wet-stratosphere atmospheres are clear type-indicators for Class E, and therefore intense hydrogen escape; however, the presence of H₂SO₄ (particularly if aerosol clouds are then formed) has been shown to severely inhibit the detection of atmospheres in a simulation case study of the TRAPPIST system using JSWT (Lustig-Yaeger et al., 2019). Combined with an already reduced scale height, these high-escape atmospheres could be particularly difficult detect, let alone classify according to their mantle fO_2 .

Hydrogen escape will only proceed at the diffusion-limited rate assumed here if there is sufficient incident XUV radiation on the planet to excite and remove all the hydrogen from the top of the atmosphere, as it arrives via diffusion. If this is not the case, removal of hydrogen from the upper atmosphere becomes inefficient, as it is energy limited by the incident XUV flux (e.g., Tian et al., 2005), and the escape flux of hydrogen will decrease below the diffusion limited rate. This potential energy limit on the rate of hydrogen escape will mean that across a range of stellar systems, atmospheric compositions will fall on a continuum between the two escape regimes shown in Fig. 6.3, and the escape-free scenario explored in Chapter 4. Planets which are smaller (and therefore have weaker gravity), are on short period orbits, are in systems with an active star, and are building their atmospheres by volcanism will fall closer to the atmospheres shown in Figs. 6.4a and 6.4d. Whereas those planets that are older, larger, further from their star, are more volcanically active (and so have a greater input flux of H-bearing species to the atmosphere), or are otherwise in a low activity stellar environment will fall closer to the ‘no escape’ scenarios.

The highest rate of hydrogen escape in the models evaluated here is approximately 1.2×10^{11} atoms cm $^{-2}$ s $^{-1}$, for planets with the most reduced mantles and wet-stratosphere escape. This is several orders of magnitude higher than occurs on Earth today (3.5×10^8 atoms cm $^{-2}$ s $^{-1}$ Catling and Kasting, 2017); however, as was shown in Chapter 3 and Fig. 3.4, for a modern Earth-like incident XUV, the escape flux will be energy rather than diffusion limited which can reduce the loss flux by up to a factor of 10. To generate a Class R or Class I atmosphere while hydrogen escape is occurring at the maximum diffusion limited rate, a much higher rate of volcanism would be needed than is presented here (which is close to the modern Earth's eruption rate). However, both the maximum rate of escape, and instant thermochemical re-equilibration as H₂ is lost is assumed. This means the amount of hydrogen escape occurring is likely being over-estimated here, as it can take millions of years for equilibrium to be re-established in an escape-free system (see Section 5.3.1). For example, in the dry stratosphere case, once a large fraction of hydrogen is lost, some water would be expected to dissociate and form H₂ to regain equilibrium. In the modelling presented here, this happens instantaneously, and the dissociated H₂ can immediately be lost; in reality, this process would take much longer, and would reduce the amount of H₂ available to escape at any one time.

Further work will need to be carried out combining the kinetic modelling of Chapter 5 with the EVolve atmospheric growth and escape model, to better quantify the rate at which thermochemical re-equilibration within the atmospheric hydrogen system will fuel escape under both dry- and wet-stratosphere scenarios.

6.5 Conclusions

Here, the effect of hydrogen escape on the chemistry of volcanically derived atmospheres was investigated. Where hydrogen escape does not occur, these atmospheres have previously (Liggins et al., 2022c) been found to have speciations linked to the mantle *fO*₂ of the planet. A new method of modelling hydrogen escape occurring on planets with evolving atmospheres has been presented, which is appropriate for hot atmospheres that can rapidly relax to thermochemical equilibrium. Planets with a similar volcanic flux to the modern Earth undergoing escape with either a dry or wet stratosphere show atmospheric speciations which are largely invariant with mantle *fO*₂, showing that hydrogen escape alone is capable of breaking the redox link between the mantle of planet and its atmospheric chemistry. On planets with wet stratospheres, where water can dissociate and escape, atmospheres are oxygen-dominated and contain approximately 0.1 % H₂SO₄, sufficiently different to the speciations produced by either escape from a dry stratosphere, or atmospheres undergoing minimal escape as to be differentiated into the additional Class E. The atmospheric speciation produced by hydrogen

6.5 Conclusions

escape through a dry stratosphere, irrespective of mantle $f\text{O}_2$, is very similar to the Class O, escape-free atmospheres of Chapter 4 and so could cause planets with reduced mantles to be mischaracterised.

7

Summary and Future Directions

The main goal of this thesis was to analyse how volcanically derived or supplemented atmospheres might look and evolve, either under end-member cases where volcanism is the only factor affecting the atmosphere, or when changing surface temperatures and atmospheric escape is considered. In order to achieve this, two models were developed: 1) EVo, a new, flexible volcanic degassing model which can calculate the chemical speciation and gas/melt partitioning of a magmatic system starting from the pressure of volatile saturation. 2) EVolve, which acts as a wrapper for EVo and simulates the growth and evolution of a volcanically derived atmosphere. This is done by linking batch melting models of the mantle to EVo. EVolve subsequently relates the gaseous output of EVo to an atmosphere which grows, thermochemically re-equilibrates to a set temperature, and can undergo hydrogen escape over time.

Chapter 3 assesses the extent to which volcanism alone can act to generate hydrogen-rich atmospheres on cool planets. The presence of a hydrogen fraction has been invoked in arguments for extending the habitable zone (e.g., Stevenson, 1999; Pierrehumbert and Gaidos, 2011; Wordsworth and Pierrehumbert, 2013b; Ramirez and Kaltenegger, 2017), and providing conditions suitable for the production of prebiotic molecules (e.g., Miller and Urey, 1959). However, as hydrogen can constantly escape from the atmosphere of low-mass planets, a steady input flux is required to maintain a constant fraction of atmospheric hydrogen. In this chapter, I apply EVo as a model of magma degassing to show which combinations of magma oxidation, volcanic flux and hydrogen escape efficiency can build up appreciable levels of hydrogen in a planet's secondary atmosphere, and demonstrate that both Earth-like and Mars-like planets can sustain atmospheric H₂ fractions of several percent across relevant magmatic *fO₂* ranges. On a planet similar to the Archean Earth, I suggest that the mixing ratio of atmospheric H₂ could have been in the range 0.2-3%, from a parameter sweep over a variety of plausible surface

Summary and Future Directions

pressures, volcanic fluxes, and H₂ escape rates. On the early Earth, this would be insufficient either to counteract the climate effects of the faint young sun (Wordsworth and Pierrehumbert, 2013b), or to provide suitable conditions for prebiotic chemistry (Itcovitz et al., 2022). It does, however, fit well with suggestions by Zahnle et al. (2019) that a hydrogen mixing ratio of around 1 % may have been present on the Archean Earth. If instead, the average magma $f\text{O}_2$ being erupted was around the IW buffer, ~ 3 log units lower than the inferred values for the Archean, this hydrogen mixing ratio would increase to approximately 10-20%. For an early Mars-like planet with magmas around IW, but a lower range of surface pressures and volcanic fluxes compared to Earth, an atmospheric hydrogen mixing ratio of $\sim 2\text{-}8\%$ is possible. This hydrogen mixing ratio would have been sufficient to deglaciate early Mars. Nevertheless, the sensitivity of the results I presented in this chapter to primary magmatic water contents and volcanic fluxes show the need for improved constraints on the crustal recycling efficiency and mantle water contents of early Mars.

Chapter 4 simulates the chemical speciation of volcanic atmospheres on hot planets, to identify whether the mantle $f\text{O}_2$ of a planet can be inferred from atmospheric observations. Volcanic atmospheres are inextricably linked to the geological state of the planet, which is particularly useful when considering studies of exoplanets and their interiors. However, previous work which accounted for the redox state of the mantle (e.g., Ortenzi et al., 2020) had focussed on atmospheric compositions in terms of outgassed masses of volcanic species (i.e., summing the total amount of outgassed CO₂, H₂O etc over time), rather than the speciation of the atmosphere at a given atmospheric temperature. There are numerous factors which can modify atmospheric chemistry, therefore Chapter 4 focussed on the end-member case of an escape/impact-free scenario under hot atmospheric conditions, which inhibit lower temperature weathering processes (as they rely on the presence of liquid water, e.g., Foley, 2019; Höning et al., 2019). Hot volcanic atmospheres at 800 K were found to develop distinct compositional groups as the mantle $f\text{O}_2$ is varied, which can be identified using sets of (often minor) indicator species: Class O, representing an oxidised mantle and containing SO₂ and sulfur allotropes; Class I, formed by intermediate mantle $f\text{O}_2$'s and containing CO₂, CH₄, CO and COS; and Class R, produced by reduced mantles, containing H₂, NH₃ and CH₄ along with inflated pressure scale heights. These atmospheric classes are robust to a wide range of bulk silicate H/C ratios. The H/C ratio does however affect the dominant atmospheric constituent, which can vary between H₂, H₂O and CO₂ once the chemical composition has stabilised to a point where it no longer changes substantially with time. This final atmospheric state is dependent on the mantle $f\text{O}_2$, the H/C ratio, and time since the onset of volcanism. The results I presented provide a base set of atmospheric compositions which can be used for further

studies of volcanic atmospheres undergoing different modification processes – including those covered in Chapters 5 and 6.

Chapter 5 challenges the widely used assumption that planetary atmospheres, particularly those which are geologically derived (typically through volcanic or impact activity, e.g., Hashimoto et al., 2007; Schaefer and Fegley, 2010, 2017; Herbort et al., 2020; Ortenzi et al., 2020), can be modelled as being permanently in thermochemical equilibrium regardless of atmospheric temperature. A previous study by Woitke et al. (2021) has asserted that the CO-CH₄ biosignature of Krissansen-Totton et al. (2018) can be generated abiotically, as when re-equilibrated to 400-600 K MORB-derived volcanic gases will contain significant quantities of CH₄ and CO₂, in the absence of CO. However, simulations of atmospheric modification through impact events (Zahnle et al., 2020) show that even with slow cooling times, gas phase reactions for e.g., hydrogenation of CO to CH₄ quench at high temperatures (~ 800 K). In this chapter, chemical kinetics calculations were carried out on the atmospheric compositions derived in Chapter 4, to estimate the relaxation timescales of volcanically-derived atmospheres to thermochemical equilibrium. The results presented demonstrated that below 700 K, reactions to form CH₄ and NH₃ (which are strongly inhibited by low temperatures) will be quenched in volcanic atmospheres even over geological time. As such, the modelling of temperate exoplanet atmospheres where thermochemical equilibrium is assumed must also invoke significant catalysis of reactions in order for results to be plausible. This result also suggests that the volcanic atmospheres of many exoplanets with temperatures at and below that of Venus will therefore be quenched to chemistries reflecting the high temperatures of volcanism, even over geological time. Inferring the mantle *fO₂* of a warm to cool planet from atmospheric chemistry will be more challenging than from hot atmospheres, as the classes identified in Chapter 4 will not be formed.

Chapter 6 returns the focus to the impact of hydrogen escape on volcanic atmospheres, this time assessing how hot atmospheres, which can thermochemically re-equilibrate during degassing and escape, will change in speciation in comparison to escape-free scenarios. Results presented in Chapter 3 of this thesis showed that cool atmospheres with a steady rate of volcanism can sustain hydrogen mixing ratios of up to ~10 %, given optimal escape, volcanic flux and mantle redox conditions (Liggins et al., 2020). Other previous studies have hypothesised that on runaway greenhouse planets and/or planets with a moist greenhouse (Kasting et al., 1993), where the atmosphere is hot enough that water will dissociate and the hydrogen escapes, will produce abiotic, oxygen-rich atmospheres (e.g., Wordsworth and Pierrehumbert, 2014; Luger and Barnes, 2015; Schaefer et al., 2016). In both cases however this does not show how the remaining chemistry of the atmosphere is affected by escape, or the speciation of hydrogen in the atmosphere. In this chapter, a new method

Summary and Future Directions

of calculating the complete speciation of a volcanic atmosphere which is growing while undergoing escape is described. The results presented show that regardless of whether water-derived hydrogen is allowed to escape, atmospheric speciations are largely invariable with mantle fO_2 , showing that hydrogen escape alone is capable of breaking the redox link between the mantle of planet and its atmospheric chemistry. Moist greenhouse planets, where water is present in the stratosphere, display O₂-CO₂ dominated atmospheres across the whole mantle fO_2 range explored, coexisting with high levels of H₂SO₄ and other oxidised sulfur species to form distinctly inhospitable atmospheric conditions, and a new atmospheric Class E. Atmospheric speciations produced by dry stratosphere escape are very similar to the Class O, escape-free atmospheres of Chapter 4 and so could cause planets with reduced mantles to be mischaracterised.

Overall, this thesis presents a new volcanic degassing model and a number of use-cases, demonstrating the wide range of chemical speciations that volcanically generated atmospheres can form.

7.1 Further Work

This thesis has examined a number of base cases for the production of volcanic atmospheres, and has provided a set of example atmospheric speciations for purely volcanic, volcanic + kinetically limited, and volcanic + escape scenarios. As has been discussed across multiple chapters however, planetary atmospheres are exceedingly complex and undergo multiple competing modification processes throughout their lifetimes. As such, before the atmospheric speciations presented in this thesis can be applied to observations, it would be beneficial to consider the effects of several other processes on the base volcanic compositions.

A major consideration for volcanic systems degassing to atmospheres, which has so far been neglected in the literature, is the process of passive degassing; a significant fraction of the total mass of volcanic gases input to an atmosphere is thought to be sourced not from magma erupted to the surface, but from deep intrusive emplacements which gradually degas over time as they cool and crystallise ('second boiling' Candela and Piccoli, 1998; Shinohara, 2008; Edmonds et al., 2022). As these gases will decouple from the parent melt deep within the crust, the open-system degassing component of EVo could be utilised within EVolve to simulate this processes; however, some additional modelling of cooling and crystallisation with a model such as MELTS (Ghiorso and Sack, 1995; Asimow and Ghiorso, 1998) would also be required to drive this degassing processes.

Another useful consideration would be to implement photochemistry and kinetically limited re-equilibration within the atmospheric module of EVolve, to assess how the competing effects

of thermochemical equilibrium and photochemistry combined affect the volcanic composition. In Chapter 5, I argue that above 700 K volcanic atmospheres should remain at thermochemical equilibrium over geological time, allowing CH₄ and NH₃ to be produced and remain above ppm levels in the atmosphere. However, both species are photochemically reactive; including photochemistry within the atmospheric component may demonstrate either catalysis of the slow reactions, allowing equilibrium at lower temperatures, or efficient removal of certain species (e.g., methane is usually efficiently photochemically removed from planetary atmospheres where there is no steady input source) inhibiting equilibrium even where the kinetics of the production reactions allow it.

Similarly, it was mentioned in Chapter 4 that the atmospheric speciations calculated within EVolve are not strictly self-consistent, as the atmospheric temperature is set externally without considering climatic effects. In Chapter 4 this is acceptable as the atmospheres being discussed are for a generic example; however, a useful extension to the modelling shown here for atmospheres generally would be to build a self-consistent climate model into EVolve. This would account for the instellation a specific planet is subjected to, and would allow for calculations of both an appropriate surface temperature, given the current insolation and atmospheric chemistry, and a complete P-T profile for the atmospheric composition at varying heights. The speciation of the atmosphere would then correctly feedback into the surface temperature of the planet, enabling more accurate modelling of the locations of various atmospheric classes with stellar type and orbital distance such as the plots shown in Fig. 4.5. This more complete model of the atmosphere would then be able to produce atmospheric abundance profiles, making it suitable for calculating synthetic spectra using radiative transfer models (e.g., as has been done for rocky planets in the TRAPPIST-1 system, Turbet et al., 2020), ready for comparison with exoplanet observations.

Chapter 6 describes a new method for modelling the speciation of a volcanic atmosphere which is undergoing hydrogen escape. However, escape is assumed to proceed at the maximum, diffusion limited rate in all cases. As was established earlier in this thesis (Chapter 3), escape will often proceed at a rate lower than this upper limit, particularly on planets around older stars. Including a parametrisation for energy limited and/or more sophisticated mass-loss models (see Owen et al., 2020) within the atmospheric component of EVolve would enable a more nuanced assessment of hydrogen escape from volcanic atmospheres, particularly in scenarios where lower rates of escape may place the atmospheric speciation between the two extremes discussed in Chapters 4 and 6. Informing the rate of escape using incident radiation fluxes would also improve the ability of EVolve to simulate specific exoplanets, as would be desirable when comparing to observations.

Summary and Future Directions

Ultimately, further work would aim to produce inverse models for the interpretation of rocky planet atmospheric observations, by linking the models initially developed in this thesis to those which can produce emission and transmission spectra for, e.g., JWST. This would ultimately enable the interpretation of exoplanet observations in the context of their potential geological properties.

References

- Abbot, D. S. (2015). A Proposal for Climate Stability on H₂ Greenhouse Planets. *The Astrophysical Journal*, 815(1), L3.
- Abe, Y. (2011). Protoatmospheres and Surface Environment of Protoplanets. *Earth, Moon, and Planets*, 108(1), 9–14.
- Anenburg, M., & O'Neill, H. S. C. (2019). Redox in Magmas: Comment on a Recent Treatment of the Kaiserstuhl Volcanics (Brauner et al., *Journal of Petrology*, 59, 1731–1762, 2018) and Some Other Misconceptions. *Journal of Petrology*, 60(9), 1825–1832.
- Angelo, I., & Hu, R. (2017). A Case for an Atmosphere on Super-Earth 55 Cancri e. *The Astronomical Journal*, 154(6), 232.
- Ardia, P., Hirschmann, M. M., Withers, A. C., & Stanley, B. D. (2013). Solubility of CH₄ in a synthetic basaltic melt, with applications to atmosphere–magma ocean–core partitioning of volatiles and to the evolution of the Martian atmosphere. *Geochimica et Cosmochimica Acta*, 114, 52–71.
- Armstrong, L. S., Hirschmann, M. M., Stanley, B. D., Falksen, E. G., & Jacobsen, S. D. (2015). Speciation and solubility of reduced C–O–H–N volatiles in mafic melt: Implications for volcanism, atmospheric evolution, and deep volatile cycles in the terrestrial planets. *Geochimica et Cosmochimica Acta*, 171, 283–302.
- Asimow, P. D., & Ghiorso, M. S. (1998). Algorithmic modifications extending MELTS to calculate subsolidus phase relations. *American Mineralogist*, 83(9-10), 1127–1132.
- Aubaud, C., Hauri, E. H., & Hirschmann, M. M. (2004). Hydrogen partition coefficients between nominally anhydrous minerals and basaltic melts. *Geophysical Research Letters*, 31(20).
- Aulbach, S., & Stagni, V. (2016). Evidence for a reducing Archean ambient mantle and its effects on the carbon cycle. *Geology*, 44(9), 751–754.
- Avic, G., Marty, B., & Burgess, R. (2017). The origin and degassing history of the Earth's atmosphere revealed by Archean xenon. *Nature Communications*, 8, 15455.
- Backnaes, L., & Deubener, J. (2011). Experimental Studies on Sulfur Solubility in Silicate Melts at Near-Atmospheric Pressure. *Reviews in Mineralogy and Geochemistry*, 73(1), 143–165.
- Banks, P. M., & Kockarts, G. (1973). *Aeronomy*. Academic Press.
- Batalha, N., Domagal-Goldman, S. D., Ramirez, R., & Kasting, J. F. (2015). Testing the early Mars H₂–CO₂ greenhouse hypothesis with a 1-D photochemical model. *Icarus*, 258, 337–349.
- Batalha, N. E., Lewis, N. K., Line, M. R., Valenti, J., & Stevenson, K. (2018). Strategies for Constraining the Atmospheres of Temperate Terrestrial Planets with JWST. *The Astrophysical Journal*, 856(2), L34.
- Bézos, A., & Humler, E. (2005). The Fe³⁺/ΣFe ratios of MORB glasses and their implications for mantle melting. *Geochimica et Cosmochimica Acta*, 69(3), 711–725.
- Bourrier, V., de Wit, J., Bolmont, E., Stamenković, V., Wheatley, P. J., Burgasser, A. J., Delrez, L., Demory, B.-O., Ehrenreich, D., Gillon, M., Jehin, E., Leconte, J., Lederer, S. M., Lewis, N., Triaud, A. H. M. J., & Grootel, V. V. (2017). Temporal Evolution of the High-energy Irradiation and Water Content of TRAPPIST-1 Exoplanets. *The Astronomical Journal*, 154(3), 121.

References

- Brounce, M., Stolper, E., & Eiler, J. (2017). Redox variations in Mauna Kea lavas, the oxygen fugacity of the Hawaiian plume, and the role of volcanic gases in Earth's oxygenation. *Proceedings of the National Academy of Sciences*, 114(34), 8997–9002.
- Burgisser, A., Alletti, M., & Scaillet, B. (2015). Simulating the behavior of volatiles belonging to the C–O–H–S system in silicate melts under magmatic conditions with the software D-Compress. *Computers & Geosciences*, 79, 1–14.
- Burgisser, A., & Scaillet, B. (2007). Redox evolution of a degassing magma rising to the surface. *Nature*, 445(7124), 194–197.
- Burt, J. A., Dragomir, D., Mollière, P., Youngblood, A., Muñoz, A. G., McCann, J., Kreidberg, L., Huang, C. X., Collins, K. A., Eastman, J. D., Abe, L., Almenara, J. M., Crossfield, I. J. M., Ziegler, C., Rodriguez, J. E., Mamajek, E. E., Stassun, K. G., Halverson, S. P., Villanueva, S., ... Brasseur, C. E. (2021). TOI-1231 b: A Temperate, Neptune-sized Planet Transiting the Nearby M3 Dwarf NLTT 24399. *The Astronomical Journal*, 162(3), 87.
- Callegaro, S., Geraki, K., Marzoli, A., Min, A. D., Maneta, V., & Baker, D. R. (2020). The quintet completed: The partitioning of sulfur between nominally volatile-free minerals and silicate melts. *American Mineralogist*, 105(5), 697–707.
- Candela, P., & Piccoli, P. (1998). Magmatic Contributions to Hydrothermal Ore Deposits: An Algorithm (MVPART) for Calculating the Composition of the Magmatic Volatile Phase. In J. P. Richards & P. B. Larson (Eds.), *Techniques in Hydrothermal Ore Deposits Geology*. Society of Economic Geologists.
- Carmichael, I. S. E., & Ghiorso, M. S. (1986). Oxidation-reduction relations in basic magma: A case for homogeneous equilibria. *Earth and Planetary Science Letters*, 78(2), 200–210.
- Carmichael, I. (1991). The redox states of basic and silicic magmas: A reflection of their source regions? *Contributions to Mineralogy and Petrology*, 106(2), 129–141.
- Carroll, M. R., & Rutherford, M. J. (1988). Sulfur speciation in hydrous experimental glasses of varying oxidation state; results from measured wavelength shifts of sulfur x-rays. *American Mineralogist*, 73(7-8), 845–849.
- Catling, D. C. (2006). Comment on "A Hydrogen-Rich Early Earth Atmosphere". *Science*, 311(5757), 38.
- Catling, D. C., & Kasting, J. F. (2017). *Atmospheric evolution inhabited and lifeless worlds*. Cambridge University Press.
- Catling, D. C., Zahnle, K. J., & McKay, C. P. (2001). Biogenic Methane, Hydrogen Escape, and the Irreversible Oxidation of Early Earth. *Science*, 293(5531), 839–843.
- Charbonneau, D., Brown, T. M., Noyes, R. W., & Gilliland, R. L. (2002). Detection of an Extrasolar Planet Atmosphere. *The Astrophysical Journal*, 568(1), 377–384.
- Chase, M. W. J. (1998). NIST-JANAF Thermochemical Tables, 4th edition.
- Christie, D. M., Carmichael, I. S. E., & Langmuir, C. H. (1986). Oxidation states of mid-ocean ridge basalt glasses. *Earth and Planetary Science Letters*, 79(3), 397–411.
- Cicconi, M. R., Le Losq, C., Moretti, R., & Neuville, D. R. (2020). Magmas are the Largest Repositories and Carriers of Earth's Redox Processes. *Elements*, 16(3), 173–178.
- Cloutier, R., Charbonneau, D., Deming, D., Bonfils, X., & Astudillo-Defru, N. (2021). A More Precise Mass for GJ 1214 b and the Frequency of Multiplanet Systems Around Mid-M Dwarfs. *The Astronomical Journal*, 162(5), 174.
- Crisp, J. A. (1984). Rates of magma emplacement and volcanic output. *Journal of Volcanology and Geothermal Research*, 20(3), 177–211.

References

- Dalou, C., Hirschmann, M. M., Jacobsen, S. D., & Le Losq, C. (2019). Raman spectroscopy study of C-O-H-N speciation in reduced basaltic glasses: Implications for reduced planetary mantles. *Geochimica et Cosmochimica Acta*, 265, 32–47.
- Dauphas, N., & Morbidelli, A. (2014). 6.1 - Geochemical and Planetary Dynamical Views on the Origin of Earth's Atmosphere and Oceans. In H. D. Holland & K. K. Turekian (Eds.), *Treatise on Geochemistry (Second Edition)* (pp. 1–35). Elsevier.
- de Wit, J., Wakeford, H. R., Gillon, M., Lewis, N. K., Valenti, J. A., Demory, B.-O., Burgasser, A. J., Burdanov, A., Delrez, L., Jehin, E., Lederer, S. M., Queloz, D., Triaud, A. H. M. J., & Van Grootel, V. (2016). A combined transmission spectrum of the Earth-sized exoplanets TRAPPIST-1 b and c. *Nature*, 537(7618), 69–72.
- Deming, D., Brown, T. M., Charbonneau, D., Harrington, J., & Richardson, L. J. (2005). A New Search for Carbon Monoxide Absorption in the Transmission Spectrum of the Extrasolar Planet HD 209458b. *The Astrophysical Journal*, 622(2), 1149–1159.
- Deng, J., Du, Z., Karki, B. B., Ghosh, D. B., & Lee, K. K. M. (2020). A magma ocean origin to divergent redox evolutions of rocky planetary bodies and early atmospheres. *Nature Communications*, 11(1), 2007.
- Ding, S., & Dasgupta, R. (2017). The fate of sulfide during decompression melting of peridotite – implications for sulfur inventory of the MORB-source depleted upper mantle. *Earth and Planetary Science Letters*, 459, 183–195.
- Dixon, J. E. (1997). Degassing of alkalic basalts. *American Mineralogist*, 82(3-4), 368–378.
- Dixon, J. E., & Stolper, E. M. (1995). An Experimental Study of Water and Carbon Dioxide Solubilities in Mid-Ocean Ridge Basaltic Liquids. Part II: Applications to Degassing. *Journal of Petrology*.
- Dong, C., Jin, M., Lingam, M., Airapetian, V. S., Ma, Y., & van der Holst, B. (2018). Atmospheric escape from the TRAPPIST-1 planets and implications for habitability. *Proceedings of the National Academy of Sciences*, 115(2), 260–265.
- Dorn, C., Noack, L., & Rozel, A. B. (2018). Outgassing on stagnant-lid super-Earths. *Astronomy & Astrophysics*, 614, A18.
- Dorn, C., Bower, D. J., & Rozel, A. (2017). Assessing the Interior Structure of Terrestrial Exoplanets with Implications for Habitability. In H. J. Deeg & J. A. Belmonte (Eds.), *Handbook of Exoplanets* (pp. 1–25). Springer International Publishing.
- Doyle, A. E., Young, E. D., Klein, B., Zuckerman, B., & Schlichting, H. E. (2019). Oxygen fugacities of extrasolar rocks: Evidence for an Earth-like geochemistry of exoplanets. *Science*, 366(6463), 356–359.
- Edmonds, M., Liu, E., & Cashman, K. (2022). Open-vent volcanoes fuelled by depth-integrated magma degassing. *Bulletin of Volcanology*, 84(3), 28.
- Eguchi, J., & Dasgupta, R. (2018). A CO₂ solubility model for silicate melts from fluid saturation to graphite or diamond saturation. *Chemical Geology*, 487, 23–38.
- Elkins-Tanton, L. T. (2008). Linked magma ocean solidification and atmospheric growth for Earth and Mars. *Earth and Planetary Science Letters*, 271(1), 181–191.
- Filiberto, J., Baratoux, D., Beaty, D., Breuer, D., Farcy, B. J., Grott, M., Jones, J. H., Kiefer, W. S., Mane, P., McCubbin, F. M., & Schwenzer, S. P. (2016). A review of volatiles in the Martian interior. *Meteoritics & Planetary Science*, 51(11), 1935–1958.
- Filiberto, J., Gross, J., & McCubbin, F. M. (2016). Constraints on the water, chlorine, and fluorine content of the Martian mantle. *Meteoritics & Planetary Science*, 51(11), 2023–2035.

References

- Fincham, C. J. B., Richardson, F. D., & Goodeve, C. F. (1954). The behaviour of sulphur in silicate and aluminate melts. *Proceedings of the Royal Society of London. Series A. Mathematical and Physical Sciences*, 223(1152), 40–62.
- Fischer, T. P., & Chiodini, G. (2015). Volcanic, magmatic and hydrothermal gases. In H. Sigurdsson (Ed.), *The encyclopedia of volcanoes* (Second, pp. 779–797). Academic Press.
- Flament, N., Coltice, N., & Rey, P. F. (2008). A case for late-Archaean continental emergence from thermal evolution models and hypsometry. *Earth and Planetary Science Letters*, 275(3), 326–336.
- Foley, B. J. (2019). Habitability of Earth-like Stagnant Lid Planets: Climate Evolution and Recovery from Snowball States. *The Astrophysical Journal*, 875(1), 72.
- Foley, B. J., & Driscoll, P. E. (2016). Whole planet coupling between climate, mantle, and core: Implications for rocky planet evolution. *Geochemistry, Geophysics, Geosystems*, 17(5), 1885–1914.
- Forget, F., Wordsworth, R., Millour, E., Madeleine, J. .-, Kerber, L., Leconte, J., Marcq, E., & Haberle, R. M. (2013). 3D modelling of the early martian climate under a denser CO₂ atmosphere: Temperatures and CO₂ ice clouds. *Icarus*, 222(1), 81–99.
- Fortin, M.-A., Riddle, J., Desjardins-Langlais, Y., & Baker, D. R. (2015). The effect of water on the sulfur concentration at sulfide saturation (scss) in natural melts. *Geochimica et Cosmochimica Acta*, 160, 100–116.
- Frost, B. R. (1991). Introduction to oxygen fugacity and its petrologic importance. *Reviews in Mineralogy and Geochemistry*, 25(1), 1–9.
- Frost, D. J., Mann, U., Asahara, Y., & Rubie, D. C. (2008). The redox state of the mantle during and just after core formation. *Philosophical Transactions. Series A, Mathematical, Physical, and Engineering Sciences*, 366(1883), 4315–4337.
- Frost, D. J., & Wood, B. J. (1997). Experimental measurements of the fugacity of CO₂ and graphite/diamond stability from 35 to 77 kbar at 925 to 1650°C. *Geochimica et Cosmochimica Acta*, 61(8), 1565–1574.
- Fulton, B. J., Petigura, E. A., Howard, A. W., Isaacson, H., Marcy, G. W., Cargile, P. A., Hebb, L., Weiss, L. M., Johnson, J. A., Morton, T. D., Sinukoff, E., Crossfield, I. J. M., & Hirsch, L. A. (2017). The California-Kepler Survey. III. A Gap in the Radius Distribution of Small Planets. *The Astronomical Journal*, 154(3), 109.
- Gaillard, F., Bouhifd, M. A., Füri, E., Malavergne, V., Marrocchi, Y., Noack, L., Ortenzi, G., Roskosz, M., & Vulpius, S. (2021). The Diverse Planetary Ingassing/Outgassing Paths Produced over Billions of Years of Magmatic Activity. *Space Science Reviews*, 217(1), 22.
- Gaillard, F., Bernadou, F., Roskosz, M., Bouhifd, M. A., Marrocchi, Y., Iacono-Marziano, G., Moreira, M., Scaillet, B., & Rogerie, G. (2022). Redox controls during magma ocean degassing. *Earth and Planetary Science Letters*, 577, 117255.
- Gaillard, F., & Scaillet, B. (2014). A theoretical framework for volcanic degassing chemistry in a comparative planetology perspective and implications for planetary atmospheres. *Earth and Planetary Science Letters*, 403, 307–316.
- Gaillard, F., Scaillet, B., & Arndt, N. T. (2011). Atmospheric oxygenation caused by a change in volcanic degassing pressure. *Nature*, 478(7368), 229–232.
- Gaillard, F., Scaillet, B., Pichavant, M., & Iacono-Marziano, G. (2015). The redox geodynamics linking basalts and their mantle sources through space and time. *Chemical Geology*, 418, 217–233.

References

- Gaillard, F., Schmidt, B., Mackwell, S., & McCammon, C. (2003). Rate of hydrogen–iron redox exchange in silicate melts and glasses. *Geochimica et Cosmochimica Acta*, 67(13), 2427–2441.
- Garcia, L. J., Moran, S. E., Rackham, B. V., Wakeford, H. R., Gillon, M., de Wit, J., & Lewis, N. K. (2022). *HST/WFC3 transmission spectroscopy of the cold rocky planet TRAPPIST-1h* (arXiv:2203.13698), arXiv.
- Gaudi, B. S., Seager, S., Mennesson, B., Kiessling, A., Warfield, K., Cahoy, K., Clarke, J. T., Domagal-Goldman, S., Feinberg, L., Guyon, O., Kasdin, J., Mawet, D., Plavchan, P., Robinson, T., Rogers, L., Scowen, P., Somerville, R., Stapelfeldt, K., Stark, C., ... Zellem, R. (2020). *The Habitable Exoplanet Observatory (HabEx) Mission Concept Study Final Report* (arXiv:2001.06683), arXiv.
- Gerlach, T. M. (1993). Oxygen buffering of Kilauea volcanic gases and the oxygen fugacity of Kilauea basalt. *Geochimica et Cosmochimica Acta*, 57(4), 795–814.
- Gerlach, T. M. (2004). Comment on paper: ‘Morphology and compositions of spinel in Pu’u ’Ō’ō lava (1996–1998), Kilauea volcano, Hawaii’—enigmatic discrepancies between lava and gas-based fO₂ determinations of Pu’u ’Ō’ō lava. *Journal of Volcanology and Geothermal Research*, 134(3), 241–244.
- Gerlach, T. M., & Casadevall, T. J. (1986). Evaluation of gas data from high-temperature fumaroles at Mount St. Helens, 1980–1982. *Journal of Volcanology and Geothermal Research*, 28(1), 107–140.
- Ghiorso, M. S., & Sack, R. O. (1995). Chemical mass transfer in magmatic processes IV. A revised and internally consistent thermodynamic model for the interpolation and extrapolation of liquid-solid equilibria in magmatic systems at elevated temperatures and pressures. *Contributions to Mineralogy and Petrology*, 119(2), 197–212.
- Goldblatt, C., Claire, M. W., Lenton, T. M., Matthews, A. J., Watson, A. J., & Zahnle, K. J. (2009). Nitrogen-enhanced greenhouse warming on early Earth. *Nature Geoscience*, 2(12), 891–896.
- Grewal, D. S., Dasgupta, R., & Aithala, S. (2021). The effect of carbon concentration on its core-mantle partitioning behavior in inner Solar System rocky bodies. *Earth and Planetary Science Letters*, 571, 117090.
- Grott, M., Morschhauser, A., Breuer, D., & Hauber, E. (2011). Volcanic outgassing of CO₂ and H₂O on Mars. *Earth and Planetary Science Letters*, 308(3), 391–400.
- Guimond, C. M., Noack, L., Ortenzi, G., & Sohl, F. (2021). Low volcanic outgassing rates for a stagnant lid Archean earth with graphite-saturated magmas. *Physics of the Earth and Planetary Interiors*, 320, 106788.
- Guzmán-Marmolejo, A., Segura, A., & Escobar-Briones, E. (2013). Abiotic Production of Methane in Terrestrial Planets. *Astrobiology*, 13(6), 550–559.
- Hamano, K., Abe, Y., & Genda, H. (2013). Emergence of two types of terrestrial planet on solidification of magma ocean. *Nature*, 497(7451), 607–610.
- Hamano, K., Kawahara, H., Abe, Y., Onishi, M., & Hashimoto, G. L. (2015). Lifetime and Spectral Evolution of a Magma Ocean with a Steam Atmosphere: Its Detectability by Future Direct Imaging. *The Astrophysical Journal*, 806(2), 216.
- Haqq-Misra, J. D., Domagal-Goldman, S. D., Kasting, P. J., & Kasting, J. F. (2008). A Revised, Hazy Methane Greenhouse for the Archean Earth. *Astrobiology*, 8(6), 1127–1137.
- Harris, C. R., Millman, K. J., van der Walt, S. J., Gommers, R., Virtanen, P., Cournapeau, D., Wieser, E., Taylor, J., Berg, S., Smith, N. J., Kern, R., Picus, M., Hoyer, S., van Kerkwijk, M. H., Brett, M., Haldane, A., del Río, J. F., Wiebe, M., Peterson, P., ... Oliphant, T. E. (2020). Array programming with NumPy. *Nature*, 585(7825), 357–362.

References

- Hashimoto, G. L., Abe, Y., & Sugita, S. (2007). The chemical composition of the early terrestrial atmosphere: Formation of a reducing atmosphere from CI-like material. *Journal of Geophysical Research: Planets*, 112(E5).
- Hayworth, B. P. C., Kopparapu, R. K., Haqq-Misra, J., Batalha, N. E., Payne, R. C., Foley, B. J., Ikwut-Ukwa, M., & Kasting, J. F. (2020). Warming early Mars with climate cycling: The effect of CO₂-H₂ collision-induced absorption. *Icarus*, 345, 113770.
- Helz, R. T., Cottrell, E., Brounce, M. N., & Kelley, K. A. (2017). Olivine-melt relationships and syneruptive redox variations in the 1959 eruption of Kīlauea Volcano as revealed by XANES. *Journal of Volcanology and Geothermal Research*, 333–334, 1–14.
- Herbort, O., Woitke, P., Helling, C., & Zerkle, A. (2020). The atmospheres of rocky exoplanets - I. Outgassing of common rock and the stability of liquid water. *Astronomy & Astrophysics*, 636, A71.
- Hirschmann, M. M. (2012). Magma ocean influence on early atmosphere mass and composition. *Earth and Planetary Science Letters*, 341–344, 48–57.
- Hirschmann, M. M., Bergin, E. A., Blake, G. A., Ciesla, F. J., & Li, J. (2021). Early volatile depletion on planetesimals inferred from C–S systematics of iron meteorite parent bodies. *Proceedings of the National Academy of Sciences*, 118(13).
- Hobbs, R., Rimmer, P. B., Shorttle, O., & Madhusudhan, N. (2021). Sulfur chemistry in the atmospheres of warm and hot Jupiters. *Monthly Notices of the Royal Astronomical Society*, 506(3), 3186–3204.
- Hoeijmakers, H. J., Ehrenreich, D., Kitzmann, D., Allart, R., Grimm, S. L., Seidel, J. V., Wyttenbach, A., Pino, L., Nielsen, L. D., Fisher, C., Rimmer, P. B., Bourrier, V., Cegla, H. M., Lavie, B., Lovis, C., Patzer, A. B. C., Stock, J. W., Pepe, F. A., & Heng, K. (2019). A spectral survey of an ultra-hot Jupiter - Detection of metals in the transmission spectrum of KELT-9 b. *Astronomy & Astrophysics*, 627, A165.
- Hoke, M. R. T., Hynek, B. M., & Tucker, G. E. (2011). Formation timescales of large Martian valley networks. *Earth and Planetary Science Letters*, 312(1), 1–12.
- Holland, H. D. (2002). Volcanic gases, black smokers, and the great oxidation event. *Geochimica et Cosmochimica Acta*, 66(21), 3811–3826.
- Holland, T., & Powell, R. (1991). A Compensated-Redlich-Kwong (CORK) equation for volumes and fugacities of CO₂ and H₂O in the range 1 bar to 50 kbar and 100 - 1600 degrees C. *Contributions to Mineralogy and Petrology*, 109(2), 265–273.
- Holloway, J. R. (1987). Igneous fluids. In Thermodynamic Modeling of Geological Materials : Minerals Fluids and Melts. *Reviews in Mineralogy*, 17, 211–233.
- Holloway, J. R., Pan, V., & Gudmundsson, G. (1992). High-pressure fluid-absent melting experiments in the presence of graphite; oxygen fugacity, ferric/ferrous ratio and dissolved CO₂. *European Journal of Mineralogy*, 4(1), 105–114.
- Höning, D., Tosi, N., & Spohn, T. (2019). Carbon cycling and interior evolution of water-covered plate tectonics and stagnant-lid planets. *Astronomy & Astrophysics*, 627, A48.
- Hoolst, T. V., Noack, L., & Rivoldini, A. (2019). Exoplanet interiors and habitability. *Advances in Physics: X*, 4(1), 1630316.
- Howard, A. W., Sanchis-Ojeda, R., Marcy, G. W., Johnson, J. A., Winn, J. N., Isaacson, H., Fischer, D. A., Fulton, B. J., Sinukoff, E., & Fortney, J. J. (2013). A rocky composition for an Earth-sized exoplanet. *Nature*, 503(7476), 381–384.
- Hu, R., & Diaz, H. D. (2019). Stability of Nitrogen in Planetary Atmospheres in Contact with Liquid Water. *The Astrophysical Journal*, 886(2), 126.

References

- Hu, R., Seager, S., & Bains, W. (2012). Photochemistry in Terrestrial Exoplanet Atmospheres. I. Photochemistry Model and Benchmark Cases. *The Astrophysical Journal*, 761(2), 166.
- Huang, J., Seager, S., Petkowski, J. J., Ranjan, S., & Zhan, Z. (2022). Assessment of Ammonia as a Biosignature Gas in Exoplanet Atmospheres. *Astrobiology*, 22(2), 171–191.
- Hughes, E. C., Saper, L., Liggins, P., & Stolper, E. M. (2021). *The sulfur solubility minimum and maximum in silicate melt*.
- Huizenga, J. M. (2005). COH, an Excel spreadsheet for composition calculations in the C–O–H fluid system. *Computers & Geosciences*, 31(6), 797–800.
- Hunten, D. M. (1973). The Escape of Light Gases from Planetary Atmospheres. *Journal of the Atmospheric Sciences*, 30(8), 1481–1494.
- Hyland, J. E., Bolcar, M. R., Crooke, J., Bronke, G., Collins, C., Corsetti, J., Generie, J., Gong, Q., Groff, T., Hayden, W., Jones, A., Matonak, B., Sacks, L., West, G., Yang, K., Zimmerman, N., & Park, S. (2019). The large uv/optical/infrared surveyor (luvoir): Decadal mission concept study update. *2019 IEEE Aerospace Conference*, 1–15.
- Iacono-Marziano, G., Morizet, Y., Le Trong, E., & Gaillard, F. (2012). New experimental data and semi-empirical parameterization of H₂O–CO₂ solubility in mafic melts. *Geochimica et Cosmochimica Acta*, 97, 1–23.
- Iacovino, K., Matthews, S., Wieser, P. E., Moore, G. M., & Bégué, F. (2021). VESIcal Part I: An Open-Source Thermodynamic Model Engine for Mixed Volatile (H₂O–CO₂) Solubility in Silicate Melts. *Earth and Space Science*, 8(11), e2020EA001584.
- Iacovino, K. (2015). Linking subsurface to surface degassing at active volcanoes: A thermodynamic model with applications to Erebus volcano. *Earth and Planetary Science Letters*, 431, 59–74.
- Iacovino, K. (2021). *Ferric/Ferrous, Fe³⁺/FeT, fO₂ Converter* (Kress and Carmichael, 1991) (Version 3.2). Zenodo.
- Itcovitz, J. P., Rae, A. S. P., Citron, R. I., Stewart, S. T., Sinclair, C. A., Rimmer, P. B., & Shorttle, O. (2022). Reduced atmospheres of post-impact worlds: The early earth. *The Planetary Science Journal*, 3(5), 115.
- Johnstone, C. P., Güdel, M., Stökl, A., Lammer, H., Tu, L., Kislyakova, K. G., Lüftinger, T., Odert, P., Erkaev, N. V., & Dorfi, E. A. (2015). The evolution of stellar rotation and the hydrogen atmospheres of habitable-zone terrestrial planets. *The Astrophysical Journal*, 815(1), L12.
- Jordan, S., Rimmer, P. B., Shorttle, O., & Constantinou, T. (2021). Photochemistry of Venus-like Planets Orbiting K- and M-dwarf Stars. *The Astrophysical Journal*, 922(1), 44.
- Jugo, P. J. (2009). Sulfur content at sulfide saturation in oxidized magmas. *Geology*, 37(5), 415–418.
- Jugo, P. J., Wilke, M., & Botcharnikov, R. E. (2010). Sulfur K-edge XANES analysis of natural and synthetic basaltic glasses: Implications for S speciation and S content as function of oxygen fugacity. *Geochimica et Cosmochimica Acta*, 74(20), 5926–5938.
- Kadoya, S., Catling, D., Nicklas, R., Puchtel, I., & Anbar, A. (2020). Mantle cooling causes more reducing volcanic gases and gradual reduction of the atmosphere. *Geochemical Perspectives Letters*, 25–29.
- Kadoya, S., & Tajika, E. (2015). Evolutionary Climate Tracks of Earth-like Planets. *The Astrophysical Journal Letters*, 815(1), L7.
- Kasting, J. F. (1993). Earth's early atmosphere. *Science*, 259(5097), 920–926.
- Kasting, J. F. (1988). Runaway and moist greenhouse atmospheres and the evolution of Earth and Venus. *Icarus*, 74(3), 472–494.

References

- Kasting, J. F. (1990). Bolide impacts and the oxidation state of carbon in the Earth's early atmosphere. *Origins of life and evolution of the biosphere*, 20(3), 199–231.
- Kasting, J. F. (2013). What caused the rise of atmospheric O₂? *Chemical Geology*, 362, 13–25.
- Kasting, J. F., & Catling, D. (2003). Evolution of a Habitable Planet. *Annual Review of Astronomy and Astrophysics*, 41(1), 429–463.
- Kasting, J. F., Chen, H., & Kopparapu, R. K. (2015). Stratospheric Temperatures and Water Loss from Moist Greenhouse Atmospheres of Earth-like Planets. *The Astrophysical Journal*, 813(1), L3.
- Kasting, J. F., Whitmire, D. P., & Reynolds, R. T. (1993). Habitable Zones around Main Sequence Stars. *Icarus*, 101(1), 108–128.
- Katsura, T., & Nagashima, S. (1974). Solubility of sulfur in some magmas at 1 atmosphere. *Geochimica et Cosmochimica Acta*, 38(4), 517–531.
- Katyal, N., Ortenzi, G., Grenfell, J. L., Noack, L., Sohl, F., Godolt, M., Muñoz, A. G., Schreier, F., Wunderlich, F., & Rauer, H. (2020). Effect of mantle oxidation state and escape upon the evolution of Earth's magma ocean atmosphere. *Astronomy & Astrophysics*, 643, A81.
- Kelley, K. A., & Cottrell, E. (2012). The influence of magmatic differentiation on the oxidation state of Fe in a basaltic arc magma. *Earth and Planetary Science Letters*, 329–330, 109–121.
- Kharecha, P., Kasting, J., & Siefert, J. (2005). A coupled atmosphere–ecosystem model of the early Archean Earth. *Geobiology*, 3(2), 53–76.
- Kislyakova, K. G., Holmström, M., Lammer, H., & Erkaev, N. V. (2015). Stellar Driven Evolution of Hydrogen-Dominated Atmospheres from Earth-Like to Super-Earth-Type Exoplanets. In H. Lammer & M. Khodachenko (Eds.), *Characterizing Stellar and Exoplanetary Environments* (pp. 137–151). Springer International Publishing.
- Kite, E. S., Manga, M., & Gaidos, E. (2009). Geodynamics and Rate of Volcanism on Massive Earth-Like Planets. *The Astrophysical Journal*, 700(2), 1732–1749.
- Kite, E. S., & Barnett, M. N. (2020). Exoplanet secondary atmosphere loss and revival. *Proceedings of the National Academy of Sciences*, 117(31), 18264–18271.
- Korenaga, J. (2006). Archean Geodynamics and the Thermal Evolution of Earth. In *Archean Geodynamics and Environments* (pp. 7–32). American Geophysical Union (AGU).
- Kreidberg, L. (2017). Exoplanet Atmosphere Measurements from Transmission Spectroscopy and Other Planet Star Combined Light Observations. In H. J. Deeg & J. A. Belmonte (Eds.), *Handbook of Exoplanets* (pp. 1–23). Springer International Publishing.
- Kreidberg, L., Bean, J. L., Désert, J.-M., Benneke, B., Deming, D., Stevenson, K. B., Seager, S., Berta-Thompson, Z., Seifahrt, A., & Homeier, D. (2014). Clouds in the atmosphere of the super-Earth exoplanet GJ 1214b. *Nature*, 505(7481), 69–72.
- Kreidberg, L., Hu, R., Kite, E. S., Koll, D., Malik, M., Morley, C., Schaefer, L., & Whittaker, E. (2021). A search for signatures of volcanism and geodynamics on the hot rocky exoplanet LHS 3844b. *JWST Proposal. Cycle 1*, 1846.
- Kreidberg, L., Koll, D. D. B., Morley, C., Hu, R., Schaefer, L., Deming, D., Stevenson, K. B., Dittmann, J., Vanderburg, A., Berardo, D., Guo, X., Stassun, K., Crossfield, I., Charbonneau, D., Latham, D. W., Loeb, A., Ricker, G., Seager, S., & Vanderspek, R. (2019). Absence of a thick atmosphere on the terrestrial exoplanet LHS 3844b. *Nature*, 573(7772), 87–90.
- Kress, V. C., & Carmichael, I. S. E. (1991). The compressibility of silicate liquids containing Fe₂O₃ and the effect of composition, temperature, oxygen fugacity and pressure on their redox states. *Contributions to Mineralogy and Petrology*, 108(1), 82–92.

References

- Kress, V. C., Ghiorso, M. S., & Lastuka, C. (2004). Microsoft EXCEL spreadsheet-based program for calculating equilibrium gas speciation in the C–O–H–S–Cl–F system. *Computers & Geosciences*, 30(3), 211–214.
- Krissansen-Totton, J., Arney, G. N., Catling, D. C., Felton, R., Fortney, J., Garland, R., Irwin, P., Kopparapu, R., Lehmer, O., Lustig-Yaeger, J., Meadows, V., Molaverdikhani, K., Olson, S., Schwieterman, E. W., & Taylor, J. (2019). Atmospheric disequilibrium as an exoplanet biosignature: Opportunities for next generation telescopes. *Bulletin of the American Astronomical Society*, 51, 158.
- Krissansen-Totton, J., Olson, S., & Catling, D. C. (2018). Disequilibrium biosignatures over Earth history and implications for detecting exoplanet life. *Science Advances*, 4(1), eaao5747.
- Kuramoto, K., Umemoto, T., & Ishiwatari, M. (2013). Effective hydrodynamic hydrogen escape from an early Earth atmosphere inferred from high-accuracy numerical simulation. *Earth and Planetary Science Letters*, 375, 312–318.
- Kurokawa, H., Kurosawa, K., & Usui, T. (2018). A lower limit of atmospheric pressure on early Mars inferred from nitrogen and argon isotopic compositions. *Icarus*, 299, 443–459.
- Kuwahara, H., & Sugita, S. (2015). The molecular composition of impact-generated atmospheres on terrestrial planets during the post-accretion stage. *Icarus*, 257, 290–301.
- Lammer, H., Stökl, A., Erkaev, N. V., Dorfi, E. A., Odert, P., Güdel, M., Kulikov, Y. N., Kislyakova, K. G., & Leitzinger, M. (2014). Origin and loss of nebula-captured hydrogen envelopes from ‘sub’- to ‘super-Earths’ in the habitable zone of Sun-like stars. *Monthly Notices of the Royal Astronomical Society*, 439(4), 3225–3238.
- LaTourrette, T., & Holloway, J. R. (1994). Oxygen fugacity of the diamond + C–O fluid assemblage and CO₂ fugacity at 8 GPa. *Earth and Planetary Science Letters*, 128(3), 439–451.
- Le Guern, F., Gerlach, T. M., & Nohl, A. (1982). Field gas chromatograph analyses of gases from a glowing dome at Merapi volcano, Java, Indonesia, 1977, 1978, 1979. *Journal of Volcanology and Geothermal Research*, 14(3), 223–245.
- Le Voyer, M., Kelley, K. A., Cottrell, E., & Hauri, E. H. (2017). Heterogeneity in mantle carbon content from CO₂-undersaturated basalts. *Nature Communications*, 8(1), 14062.
- Leal, A. M. M., Kulik, D. A., Smith, W. R., & Saar, M. O. (2017). An overview of computational methods for chemical equilibrium and kinetic calculations for geochemical and reactive transport modeling. *Pure and Applied Chemistry*, 89(5), 597–643.
- Leconte, J., Forget, F., Charnay, B., Wordsworth, R., & Pottier, A. (2013). Increased insolation threshold for runaway greenhouse processes on Earth-like planets. *Nature*, 504(7479), 268–271.
- Lehmer, O. R., Catling, D. C., & Krissansen-Totton, J. (2020). Carbonate-silicate cycle predictions of Earth-like planetary climates and testing the habitable zone concept. *Nature Communications*, 11(1), 6153.
- Lesher, C. E., & Spera, F. J. (2015). Thermodynamic and Transport Properties of Silicate Melts and Magma. In H. Sigurdsson (Ed.), *The Encyclopedia of Volcanoes (Second Edition)* (pp. 113–141). Academic Press.
- Lesne, P., Scaillet, B., & Pichavant, M. (2015). The solubility of sulfur in hydrous basaltic melts. *Chemical Geology*, 418, 104–116.
- Li, Y., Dasgupta, R., & Tsuno, K. (2017). Carbon contents in reduced basalts at graphite saturation: Implications for the degassing of Mars, Mercury, and the Moon: Carbon in Reduced Planetary Basalts. *Journal of Geophysical Research: Planets*, 122(6), 1300–1320.

References

- Li, Y., Wiedenbeck, M., Shcheka, S., & Keppler, H. (2013). Nitrogen solubility in upper mantle minerals. *Earth and Planetary Science Letters*, 377–378, 311–323.
- Libby-Roberts, J. E., Berta-Thompson, Z. K., Diamond-Lowe, H., Gully-Santiago, M. A., Irwin, J. M., Kempton, E. M.-R., Rackham, B. V., Charbonneau, D., Desert, J.-M., Dittmann, J. A., Hofmann, R., Morley, C. V., & Newton, E. R. (2021). The Featureless HST/WFC3 Transmission Spectrum of the Rocky Exoplanet GJ 1132b: No Evidence For A Cloud-Free Primordial Atmosphere and Constraints on Starspot Contamination. *arXiv:2105.10487 [astro-ph]*.
- Libourel, G., Marty, B., & Humbert, F. (2003). Nitrogen solubility in basaltic melt. Part I. Effect of oxygen fugacity. *Geochimica et Cosmochimica Acta*, 67(21), 4123–4135.
- Lichtenberg, T., Bower, D. J., Hammond, M., Boukrouche, R., Sanan, P., Tsai, S.-M., & Pierrehumbert, R. T. (2021). Vertically Resolved Magma Ocean–Protoatmosphere Evolution: H₂, H₂O, CO₂, CH₄, CO, O₂, and N₂ as Primary Absorbers. *Journal of Geophysical Research: Planets*, 126(2), e2020JE006711.
- Lichtenberg, T., Golabek, G. J., Burn, R., Meyer, M. R., Alibert, Y., Gerya, T. V., & Mordasini, C. (2019). A water budget dichotomy of rocky protoplanets from 26Al-heating. *Nature Astronomy*, 3(4), 307–313.
- Liggins, P. (2022a). *Evo's documentation*. <http://evo-outgas.readthedocs.io/>
- Liggins, P. (2022b). Secondary volcanic atmospheres 1: Model.
- Liggins, P., Jordan, S., Rimmer, P. B., & Shorttle, O. (2022a). Evolution of secondary volcanic atmospheres 1 results.
- Liggins, P., Jordan, S., Rimmer, P. B., & Shorttle, O. (2022b). Evolution of secondary volcanic atmospheres 2 results.
- Liggins, P., Jordan, S., Rimmer, P. B., & Shorttle, O. (2022c). Growth and Evolution of Secondary Volcanic Atmospheres: I. Identifying the Geological Character of Hot Rocky Planets. *Journal of Geophysical Research: Planets*, 127(7), e2021JE007123.
- Liggins, P., Shorttle, O., & Rimmer, P. B. (2020). Can volcanism build hydrogen-rich early atmospheres? *Earth and Planetary Science Letters*, 550, 116546.
- Lillo-Box, J., Figueira, P., Leleu, A., Acuña, L., Faria, J. P., Hara, N., Santos, N. C., Correia, A. C. M., Robutel, P., Deleuil, M., Barrado, D., Sousa, S., Bonfils, X., Mousis, O., Almenara, J. M., Astudillo-Defru, N., Marcq, E., Udry, S., Lovis, C., & Pepe, F. (2020). Planetary system LHS 1140 revisited with ESPRESSO and TESS. *Astronomy & Astrophysics*, 642, A121.
- Line, M. R., Vasisht, G., Chen, P., Angerhausen, D., & Yung, Y. L. (2011). Thermochemical and photochemical kinetics in cooler hydrogen-dominated extrasolar planets: A methane-poor gj436b? *The Astrophysical Journal*, 738(1), Article 32, 32.
- Liu, S.-F., Hori, Y., Lin, D. N. C., & Asphaug, E. (2015). Giant Impact: An Efficient Mechanism for the Devolatilization of Super-Earths. *The Astrophysical Journal*, 812(2), 164.
- Liu, Y., Samaha, N.-T., & Baker, D. R. (2007). Sulfur concentration at sulfide saturation (SCSS) in magmatic silicate melts. *Geochimica et Cosmochimica Acta*, 71(7), 1783–1799.
- Longpré, M.-A., Stix, J., Klügel, A., & Shimizu, N. (2017). Mantle to surface degassing of carbon- and sulphur-rich alkaline magma at El Hierro, Canary Islands. *Earth and Planetary Science Letters*, 460, 268–280.
- Lopez, E. D., Fortney, J. J., & Miller, N. (2012). How Thermal Evolution and Mass-Loss Sculpt Populations of Super-Earths and Sub-Neptunes: Applications to the Kepler-11 System and Beyond. *The Astrophysical Journal*, 761(1), 59.
- Luger, R., & Barnes, R. (2015). Extreme Water Loss and Abiotic O₂ Buildup on Planets Throughout the Habitable Zones of M Dwarfs. *Astrobiology*, 15(2), 119–143.

References

- Lustig-Yaeger, J., Meadows, V. S., & Lincowski, A. P. (2019). The Detectability and Characterization of the TRAPPIST-1 Exoplanet Atmospheres with JWST. *The Astronomical Journal*, 158(1), 27.
- Madhusudhan, N., Piette, A. A. A., & Constantinou, S. (2021). Habitability and Biosignatures of Hycean Worlds. *The Astrophysical Journal*, 918(1), 1.
- Magna, T., Gussone, N., & Mezger, K. (2015). The calcium isotope systematics of Mars. *Earth and Planetary Science Letters*, 430, 86–94.
- Marrero, T. R., & Mason, E. A. (1972). Gaseous Diffusion Coefficients. *Journal of Physical and Chemical Reference Data*, 1(1), 3–118.
- Martin, R. S., Mather, T. A., & Pyle, D. M. (2007). Volcanic emissions and the early Earth atmosphere. *Geochimica et Cosmochimica Acta*, 71(15), 3673–3685.
- Marty, B., & Dauphas, N. (2003). The nitrogen record of crust–mantle interaction and mantle convection from Archean to Present. *Earth and Planetary Science Letters*, 206(3), 397–410.
- Mathez, E. A. (1984). Influence of degassing on oxidation states of basaltic magmas. *Nature*, 310(5976), 371–375.
- Mayor, M., & Queloz, D. (1995). A Jupiter-mass companion to a solar-type star. *Nature*, 378(6555), 355–359.
- McCubbin, F. M., Boyce, J. W., Srinivasan, P., Santos, A. R., Elardo, S. M., Filiberto, J., Steele, A., & Shearer, C. K. (2016). Heterogeneous distribution of H₂O in the Martian interior: Implications for the abundance of H₂O in depleted and enriched mantle sources. *Meteoritics & Planetary Science*, 51(11), 2036–2060.
- McCubbin, F. M., Hauri, E. H., Elardo, S. M., Kaaden, K. E. V., Wang, J., & Shearer, C. K. (2012). Hydrous melting of the martian mantle produced both depleted and enriched shergottites. *Geology*, 40(8), 683–686.
- McSween, H. Y., Grove, T. L., Lentz, R. C., Dann, J. C., Holzheid, A. H., Riciputi, L. R., & Ryan, J. G. (2001). Geochemical evidence for magmatic water within Mars from pyroxenes in the Shergotty meteorite. *Nature*, 409(6819), 487–490.
- Metrich, N., & Clocchiatti, R. (1996). Sulfur abundance and its speciation in oxidized alkaline melts. *Geochimica et Cosmochimica Acta*, 60(21), 4151–4160.
- Métrich, N., Berry, A. J., O'Neill, H. S. C., & Susini, J. (2009). The oxidation state of sulfur in synthetic and natural glasses determined by X-ray absorption spectroscopy. *Geochimica et Cosmochimica Acta*, 73(8), 2382–2399.
- Michael, P. J., & Graham, D. W. (2015). The behavior and concentration of CO₂ in the suboceanic mantle: Inferences from undegassed ocean ridge and ocean island basalts. *Lithos*, 236–237, 338–351.
- Miller, S. L., & Urey, H. C. (1959). Organic Compound Synthesis on the Primitive Earth. *Science*, 130(3370), 245–251.
- Miller-Ricci, E., Seager, S., & Sasselov, D. (2008). The Atmospheric Signatures of Super-Earths: How to Distinguish Between Hydrogen-Rich and Hydrogen-Poor Atmospheres. *The Astrophysical Journal*, 690(2), 1056–1067.
- Moretti, R., Papale, P., & Ottonello, G. (2003). A model for the saturation of C-O-H-S fluids in silicate melts. *Geological Society, London, Special Publications*, 213(1), 81–101.
- Moretti, R. (2021). Ionic Syntax and Equilibrium Approach to Redox Exchanges in Melts. In *Magma Redox Geochemistry* (pp. 115–138). American Geophysical Union (AGU).
- Moretti, R., & Papale, P. (2004). On the oxidation state and volatile behavior in multicomponent gas–melt equilibria. *Chemical Geology*, 213(1), 265–280.

References

- Moretti, R., & Stefánsson, A. (2020). Volcanic and Geothermal Redox Engines. *Elements*, 16(3), 179–184.
- Mori, T., & Notsu, K. (1997). Remote co, cos, co₂, so₂, hcl detection and temperature estimation of volcanic gas. *Geophysical Research Letters*, 24(16), 2047–2050.
- Morley, C. V., Kreidberg, L., Rustamkulov, Z., Robinson, T., & Fortney, J. J. (2017). Observing the Atmospheres of Known Temperate Earth-sized Planets with JWST. *The Astrophysical Journal*, 850(2), 121.
- Moses, J. I., Visscher, C., Fortney, J. J., Showman, A. P., Lewis, N. K., Griffith, C. A., Klippenstein, S. J., Shabram, M., Friedson, A. J., Marley, M. S., & Freedman, R. S. (2011). Disequilibrium carbon, oxygen, and nitrogen chemistry in the atmospheres of hd 189733b and hd 209458b. *The Astrophysical Journal*, 737(1), 15.
- Moses, J. I., Visscher, C., Keane, T. C., & Sperier, A. (2010). On the abundance of non-cometary hcn on jupiter. *Faraday Discussions*, 147, 103.
- Moussallam, Y., Edmonds, M., Scaillet, B., Peters, N., Gennaro, E., Sides, I., & Oppenheimer, C. (2016). The impact of degassing on the oxidation state of basaltic magmas: A case study of Kīlauea volcano. *Earth and Planetary Science Letters*, 450, 317–325.
- Moussallam, Y., Oppenheimer, C., & Scaillet, B. (2019). On the relationship between oxidation state and temperature of volcanic gas emissions. *Earth and Planetary Science Letters*, 520, 260–267.
- Moussallam, Y., Oppenheimer, C., Scaillet, B., Gaillard, F., Kyle, P., Peters, N., Hartley, M., Berlo, K., & Donovan, A. (2014). Tracking the changing oxidation state of Erebus magmas, from mantle to surface, driven by magma ascent and degassing. *Earth and Planetary Science Letters*, 393, 200–209.
- Mugnai, L. V., Modirrousta-Galian, D., Edwards, B., Changeat, Q., Bouwman, J., Morello, G., Al-Refaie, A., Baeyens, R., Bieger, M. F., Blain, D., Gressier, A., Guilluy, G., Jaziri, Y., Kiefer, F., Morvan, M., Pluriel, W., Poveda, M., Skaf, N., Whiteford, N., ... Beaulieu, J.-P. (2021). ARES\ast V. No Evidence For Molecular Absorption in the HST WFC3 Spectrum of GJ 1132 b. *The Astronomical Journal*, 161(6), 284.
- NASA. (2019). *Exoplanet Exploration: Planets Beyond our Solar System*.
- Nash, W. M., Smythe, D. J., & Wood, B. J. (2019). Compositional and temperature effects on sulfur speciation and solubility in silicate melts. *Earth and Planetary Science Letters*, 507, 187–198.
- Newman, S., & Lowenstein, J. B. (2002). VolatileCalc: A silicate melt–H₂O–CO₂ solution model written in Visual Basic for excel. *Computers & Geosciences*, 28(5), 597–604.
- Nicklas, R. W., Puchtel, I. S., Ash, R. D., Piccoli, P. M., Hanski, E., Nisbet, E. G., Waterton, P., Pearson, D. G., & Anbar, A. D. (2019). Secular mantle oxidation across the Archean-Proterozoic boundary: Evidence from V partitioning in komatiites and picrites. *Geochimica et Cosmochimica Acta*, 250, 49–75.
- Nikolaou, A., Katyal, N., Tosi, N., Godolt, M., Grenfell, J. L., & Rauer, H. (2019). What Factors Affect the Duration and Outgassing of the Terrestrial Magma Ocean? *The Astrophysical Journal*, 875(1), 11.
- Nilsson, K., & Peach, C. L. (1993). Sulfur speciation, oxidation state, and sulfur concentration in backarc magmas. *Geochimica et Cosmochimica Acta*, 57(15), 3807–3813.
- Noack, L., Godolt, M., von Paris, P., Plesa, A. .-, Stracke, B., Breuer, D., & Rauer, H. (2014). Can the interior structure influence the habitability of a rocky planet? *Planetary and Space Science*, 98, 14–29.

References

- Noack, L., Rivoldini, A., & Van Hoolst, T. (2017). Volcanism and outgassing of stagnant-lid planets: Implications for the habitable zone. *Physics of the Earth and Planetary Interiors*, 269, 40–57.
- Nyquist, L. E., Bogard, D. D., Shih, C. .-, Park, J., Reese, Y. D., & Irving, A. J. (2009). Concordant Rb–Sr, Sm–Nd, and Ar–Ar ages for Northwest Africa 1460: A 346Ma old basaltic shergottite related to “lherzolitic” shergottites. *Geochimica et Cosmochimica Acta*, 73(14), 4288–4309.
- Ohmoto, H., & Kerrick, D. M. (1977). Devolatilization equilibria in graphitic systems. *American Journal of Science*, 277(8), 1013–1044.
- O’Neill, H., & Mavrogenes, J. A. (2019). The sulfate capacity of silicate melts at atmospheric pressure. *Goldschmidt*.
- O’Neill, H. S. C., Berry, A. J., & Mallmann, G. (2018). The oxidation state of iron in Mid-Ocean Ridge Basaltic (MORB) glasses: Implications for their petrogenesis and oxygen fugacities. *Earth and Planetary Science Letters*, 504, 152–162.
- O’Neill, H. S. C., & Mavrogenes, J. A. (2002). The Sulfide Capacity and the Sulfur Content at Sulfide Saturation of Silicate Melts at 1400°C and 1 bar. *Journal of Petrology*, 43(6), 1049–1087.
- O’Neill, H. S. (2021). The Thermodynamic Controls on Sulfide Saturation in Silicate Melts with Application to Ocean Floor Basalts. In *Magma Redox Geochemistry* (pp. 177–213). American Geophysical Union (AGU).
- Oppenheimer, C., & Kyle, P. R. (2008). Probing the magma plumbing of Erebus volcano, Antarctica, by open-path FTIR spectroscopy of gas emissions. *Journal of Volcanology and Geothermal Research*, 177(3), 743–754.
- Oppenheimer, C., Moretti, R., Kyle, P. R., Eschenbacher, A., Lowenstein, J. B., Hervig, R. L., & Dunbar, N. W. (2011). Mantle to surface degassing of alkalic magmas at Erebus volcano, Antarctica. *Earth and Planetary Science Letters*, 306(3), 261–271.
- Oppenheimer, C., Scaillet, B., Woods, A., Sutton, A. J., Elias, T., & Moussallam, Y. (2018). Influence of eruptive style on volcanic gas emission chemistry and temperature. *Nature Geoscience*, 11(9), 678–681.
- Ortenzi, G., Noack, L., Sohl, F., Guimond, C. M., Grenfell, J. L., Dorn, C., Schmidt, J. M., Vulpius, S., Katyal, N., Kitzmann, D., & Rauer, H. (2020). Mantle redox state drives outgassing chemistry and atmospheric composition of rocky planets. *Scientific Reports*, 10(1), 10907.
- Owen, J. E., Shaikhislamov, I. F., Lammer, H., Fossati, L., & Khodachenko, M. L. (2020). Hydrogen Dominated Atmospheres on Terrestrial Mass Planets: Evidence, Origin and Evolution. *Space Science Reviews*, 216(8), 129.
- Owen, J. E., & Alvarez, M. A. (2015). UV Driven Evaporation of Close-in Planets: Energy-limited, Recombination-limited, and Photon-limited Flows. *The Astrophysical Journal*, 816(1), 34.
- Paris, E., Giuli, G., Carroll, M. R., & Davoli, I. (2001). The Valence and Speciation of Sulfur in Glasses by X-Ray Absorption Spectroscopy. *The Canadian Mineralogist*, 39(2), 331–339.
- Pichavant, M., Di Carlo, I., Rotolo, S. G., Scaillet, B., Burgisser, A., Le Gall, N., & Martel, C. (2013). Generation of CO₂-rich melts during basalt magma ascent and degassing. *Contributions to Mineralogy and Petrology*, 166(2), 545–561.
- Pierrehumbert, R., & Gaidos, E. (2011). Hydrogen greenhouse planets beyond the habitable zone. *The Astrophysical Journal*, 734(1), L13.

References

- Pinto, J. P., Gladstone, G. R., & Yung, Y. L. (1980). Photochemical Production of Formaldehyde in Earth's Primitive Atmosphere. *Science*, 210(4466), 183–185.
- Putirka, K. D., & Xu, S. (2021). Polluted white dwarfs reveal exotic mantle rock types on exoplanets in our solar neighborhood. *Nature Communications*, 12(1), 6168.
- Queloz, D., Bouchy, F., Moutou, C., Hatzes, A., Hébrard, G., Alonso, R., Auvergne, M., Baglin, A., Barbieri, M., Barge, P., Benz, W., Bordé, P., Deeg, H. J., Deleuil, M., Dvorak, R., Erikson, A., Mello, S. F., Fridlund, M., Gandolfi, D., ... Wuchterl, G. (2009). The CoRoT-7 planetary system: Two orbiting super-Earths. *Astronomy & Astrophysics*, 506(1), 303–319.
- Ramirez, R. M., & Kaltenegger, L. (2017). A Volcanic Hydrogen Habitable Zone. *The Astrophysical Journal*, 837(1), L4.
- Ramirez, R. M., Kopparapu, R., Zugger, M. E., Robinson, T. D., Freedman, R., & Kasting, J. F. (2014). Warming early Mars with CO₂ and H₂. *Nature Geoscience*, 7(1), 59–63.
- Ranjan, S., Todd, Z. R., Rimmer, P. B., Sasselov, D. D., & Babbin, A. R. (2019). Nitrogen Oxide Concentrations in Natural Waters on Early Earth. *Geochemistry, Geophysics, Geosystems*, 20(4), 2021–2039.
- Ribas, I., Guinan, E. F., Güdel, M., & Audard, M. (2005). Evolution of the Solar Activity over Time and Effects on Planetary Atmospheres. I. High-Energy Irradiances (1–1700 Å). *The Astrophysical Journal*, 622(1), 680.
- Righter, K., Danielson, L. R., Pando, K., Morris, R. V., Graff, T. G., Agresti, D. G., Martin, A. M., Sutton, S. R., Newville, M., & Lanzirotti, A. (2013). Redox systematics of martian magmas with implications for magnetite stability. *American Mineralogist*, 98(4), 616–628.
- Rimmer, P. B., Ferus, M., Waldmann, I. P., Knížek, A., Kalvaitis, D., Ivanek, O., Kubelík, P., Yurchenko, S. N., Burian, T., Dostál, J., Juha, L., Dudžák, R., Kruš, M., Tennyson, J., Civiš, S., Archibald, A. T., & Granville-Willett, A. (2019). Identifiable Acetylene Features Predicted for Young Earth-like Exoplanets with Reducing Atmospheres Undergoing Heavy Bombardment. *The Astrophysical Journal*, 888(1), 21.
- Rimmer, P. B., & Helling, C. (2016). A Chemical Kinetics Network for Lightning and Life in Planetary Atmospheres. *The Astrophysical Journal Supplement Series*, 224(1), 9.
- Rimmer, P. B., & Helling, C. (2019). Erratum: “A Chemical Kinetics Network for Lightning and Life in Planetary Atmospheres” (2019, ApJS, 224, 9). *The Astrophysical Journal Supplement Series*, 245(1), 20.
- Rimmer, P. B., Jordan, S., Constantinou, T., Woitke, P., Shorttle, O., Hobbs, R., & Paschodimas, A. (2021). Hydroxide Salts in the Clouds of Venus: Their Effect on the Sulfur Cycle and Cloud Droplet pH. *The Planetary Science Journal*, 2(4), 133.
- Rimmer, P., Shorttle, O., & Rugheimer, S. (2019). Oxidised micrometeorites as evidence for low atmospheric pressure on the early Earth. *Geochemical Perspectives Letters*, 38–42.
- Rosenthal, A., Hauri, E. H., & Hirschmann, M. M. (2015). Experimental determination of C, F, and H partitioning between mantle minerals and carbonated basalt, CO₂/Ba and CO₂/Nb systematics of partial melting, and the CO₂ contents of basaltic source regions. *Earth and Planetary Science Letters*, 412, 77–87.
- Rumble, J. R. (2022). *Handbook of Chemistry and Physics (Internet Version 2022)* (103rd ed.).
- Sagan, C. (1977). Reducing greenhouses and the temperature history of Earth and Mars. *Nature*, 269(5625), 224–226.
- Sakuraba, H., Kurokawa, H., Genda, H., & Ohta, K. (2021). Numerous chondritic impactors and oxidized magma ocean set Earth's volatile depletion. *Scientific Reports*, 11(1), 20894.

References

- Sasselov, D. D., Grotzinger, J. P., & Sutherland, J. D. (2020). The origin of life as a planetary phenomenon. *Science Advances*, 6(6), eaax3419.
- Sawyer, G. M., Carn, S. A., Tsanev, V. I., Oppenheimer, C., & Burton, M. (2008). Investigation into magma degassing at nyiragongo volcano, democratic republic of the congo. *Geochemistry, Geophysics, Geosystems*, 9(2).
- Schaefer, L., & Fegley, B. (2007). Outgassing of ordinary chondritic material and some of its implications for the chemistry of asteroids, planets, and satellites. *Icarus*, 186(2), 462–483.
- Schaefer, L., & Fegley, B. (2010). Chemistry of atmospheres formed during accretion of the Earth and other terrestrial planets. *Icarus*, 208(1), 438–448.
- Schaefer, L., & Fegley, B. (2017). Redox States of Initial Atmospheres Outgassed on Rocky Planets and Planetesimals. *The Astrophysical Journal*, 843(2), 120.
- Schaefer, L., Lodders, K., & Fegley, B. (2012). Vaporization of the Earth: Application to Exoplanet atmospheres. *The Astrophysical Journal*, 755(1), 41.
- Schaefer, L., Wordsworth, R. D., Berta-Thompson, Z., & Sasselov, D. (2016). Predictions of the Atmospheric Composition of GJ 1132b. *The Astrophysical Journal*, 829(2), 63.
- Schllichting, H. E., Sari, R., & Yalinewich, A. (2015). Atmospheric mass loss during planet formation: The importance of planetesimal impacts. *Icarus*, 247, 81–94.
- Schmidt, M. E., Schrader, C. M., & McCoy, T. J. (2013a). The primary fO₂ of basalts examined by the Spirit rover in Gusev Crater, Mars: Evidence for multiple redox states in the martian interior. *Earth and Planetary Science Letters*, 384, 198–208.
- Schmidt, M. E., Schrader, C. M., & McCoy, T. J. (2013b). The primary fO₂ of basalts examined by the spirit rover in gusev crater, mars: Evidence for multiple redox states in the martian interior. *Earth and Planetary Science Letters*, 384, 198–208.
- Seager, S., Bains, W., & Hu, R. (2013). Biosignature Gases in H₂-Dominanted Atmospheres on Rocky Exoplanets. *The Astrophysical Journal*, 777(2), 95.
- Seager, S., Kuchner, M., Hier-Majumder, C. A., & Militzer, B. (2007). Mass-Radius Relationships for Solid Exoplanets. *The Astrophysical Journal*, 669(2), 1279–1297.
- Seager, S., & Deming, D. (2010). Exoplanet Atmospheres. *Annual Review of Astronomy and Astrophysics*, 48(1), 631–672.
- Shaw, H. R., & Wones, D. R. (1964). Fugacity coefficients for hydrogen gas between 0 degrees and 1000 degrees C, for pressures to 3000 atm. *American Journal of Science*, 262(7), 918–929.
- Shi, P., & Saxena, S. K. (1992). Thermodynamic modeling of the C-H-O-S fluid system. *American Mineralogist*, 77(9-10), 1038–1049.
- Shinohara, H. (2008). Excess degassing from volcanoes and its role on eruptive and intrusive activity. *Reviews of Geophysics*, 46(4).
- Silver, L., & Stolper, E. (1989). Water in Albitic Glasses. *Journal of Petrology*, 30(3), 667–709.
- Sinclair, C. A., Wyatt, M. C., Morbidelli, A., & Nesvorný, D. (2020). Evolution of the Earth's atmosphere during Late Veneer accretion. *Monthly Notices of the Royal Astronomical Society*, 499(4), 5334–5362.
- Sleep, N. H., & Zahnle, K. (2001). Carbon dioxide cycling and implications for climate on ancient Earth. *Journal of Geophysical Research: Planets*, 106(E1), 1373–1399.
- Smythe, D. J., Wood, B. J., & Kisseeva, E. S. (2017). The s content of silicate melts at sulfide saturation: New experiments and a model incorporating the effects of sulfide composition. *American Mineralogist*, 102(4), 795–803.
- Snellen, I. A. G., Désert, J.-M., Waters, L. B. F. M., Robinson, T., Meadows, V., van Dishoeck, E. F., Brandl, B. R., Henning, T., Bouwman, J., Lahuis, F., Min, M., Lovis, C., Dominik,

References

- C., Eylen, V. V., Sing, D., Anglada-Escudé, G., Birkby, J. L., & Brogi, M. (2017). Detecting Proxima b's Atmosphere with *JWST* Targeting CO₂ at 15 μm Using a High-pass Spectral Filtering Technique. *The Astronomical Journal*, 154(2), 77.
- Som, S. M., Buick, R., Hagadorn, J. W., Blake, T. S., Perreault, J. M., Harnmeijer, J. P., & Catling, D. C. (2016). Earth's air pressure 2.7 billion years ago constrained to less than half of modern levels. *Nature Geoscience*, 9(6), 448–451.
- Sossi, P. A., Burnham, A. D., Badro, J., Lanzirotti, A., Newville, M., & O'Neill, H. S. C. (2020). Redox state of Earth's magma ocean and its Venus-like early atmosphere. *Science Advances*, 6(48), eabd1387.
- Spaargaren, R. J., Ballmer, M. D., Bower, D. J., Dorn, C., & Tackley, P. J. (2020). The influence of bulk composition on the long-term interior-atmosphere evolution of terrestrial exoplanets. *Astronomy & Astrophysics*, 643, A44.
- Stanley, B. D., Hirschmann, M. M., & Withers, A. C. (2014). Solubility of COH volatiles in graphite-saturated martian basalts. *Geochimica et Cosmochimica Acta*, 129, 54–76.
- Stern, R. J., Gerya, T., & Tackley, P. J. (2018). Stagnant lid tectonics: Perspectives from silicate planets, dwarf planets, large moons, and large asteroids. *Geoscience Frontiers*, 9(1), 103–119.
- Stevenson, D. J. (1999). Life-sustaining planets in interstellar space? *Nature*, 400(6739), 32.
- Stock, J. W., & Kitzmann, D. (2021). FastChem 2.0. <https://github.com/exoclime/FastChem>
- Stock, J. W., Kitzmann, D., Patzer, A. B. C., & Sedlmayr, E. (2018). FastChem: A computer program for efficient complex chemical equilibrium calculations in the neutral/ionized gas phase with applications to stellar and planetary atmospheres. *Monthly Notices of the Royal Astronomical Society*, 479(1), 865–874.
- Stolper, E. M., Shortle, O., Antoshechkina, P. M., & Asimow, P. D. (2020). The effects of solid-solid phase equilibria on the oxygen fugacity of the upper mantle. *American Mineralogist*, 105(10), 1445–1471.
- STScI. (2022). *JWST approved programmes*. STScI.edu. Retrieved May 13, 2022, from <http://www.stsci.edu/home/jwst/science-execution/approved-programs>
- Swain, M. R., Estrela, R., Roudier, G. M., Sotin, C., Rimmer, P. B., Valio, A., West, R., Pearson, K., Huber-Feely, N., & Zellem, R. T. (2021). Detection of an Atmosphere on a Rocky Exoplanet. *The Astronomical Journal*, 161(5), 213.
- Swain, M. R., Vasisht, G., & Tinetti, G. (2008). The presence of methane in the atmosphere of an extrasolar planet. *Nature*, 452(7185), 329–331.
- Tagawa, S., Sakamoto, N., Hirose, K., Yokoo, S., Hernlund, J., Ohishi, Y., & Yurimoto, H. (2021). Experimental evidence for hydrogen incorporation into Earth's core. *Nature Communications*, 12(1), 2588.
- Thiemann, E. M. B., Chamberlin, P. C., Eparvier, F. G., Templeman, B., Woods, T. N., Bougher, S. W., & Jakosky, B. M. (2017). The MAVEN EUVM model of solar spectral irradiance variability at Mars: Algorithms and results. *Journal of Geophysical Research: Space Physics*, 122(3), 2748–2767.
- Tian, F. (2015a). Atmospheric Escape from Solar System Terrestrial Planets and Exoplanets. *Annual Review of Earth and Planetary Sciences*, 43(1), 459–476.
- Tian, F. (2015b). History of water loss and atmospheric O₂ buildup on rocky exoplanets near M dwarfs. *Earth and Planetary Science Letters*, 432, 126–132.
- Tian, F., Kasting, J. F., & Solomon, S. C. (2009). Thermal escape of carbon from the early Martian atmosphere. *Geophysical Research Letters*, 36(2).
- Tian, F., Toon, O. B., Pavlov, A. A., & Sterck, H. D. (2005). A Hydrogen-Rich Early Earth Atmosphere. *Science*, 308(5724), 1014–1017.

References

- Todd, Z. R., & Öberg, K. I. (2020). Cometary Delivery of Hydrogen Cyanide to the Early Earth. *Astrobiology*, 20(9), 1109–1120.
- Tomeczek, J., & Gradoń, B. (2003). The role of n₂O and nnH in the formation of NO via HCN in hydrocarbon flames. *Combustion and Flame*, 133(3), 311–322.
- Tosca, N. J., Ahmed, I. A. M., Tutolo, B. M., Ashpitel, A., & Hurowitz, J. A. (2018). Magnetite authigenesis and the warming of early Mars. *Nature Geoscience*, 11(9), 635–639.
- Tosi, N., Godolt, M., Stracke, B., Ruedas, T., Grenfell, J. L., Höning, D., Nikolaou, A., Plesa, A.-C., Breuer, D., & Spohn, T. (2017). The habitability of a stagnant-lid Earth. *Astronomy & Astrophysics*, 605, A71.
- Tsai, S.-M., Kitzmann, D., Lyons, J. R., Mendonça, J., Grimm, S. L., & Heng, K. (2018). Toward Consistent Modeling of Atmospheric Chemistry and Dynamics in Exoplanets: Validation and Generalization of the Chemical Relaxation Method. *The Astrophysical Journal*, 862(1), 31.
- Tsai, S.-M., Lyons, J. R., Grosheintz, L., Rimmer, P. B., Kitzmann, D., & Heng, K. (2017). VULCAN: An Open-source, Validated Chemical Kinetics Python Code for Exoplanetary Atmospheres. *The Astrophysical Journal*, 228(2), Article 20, 20.
- Tsai, S.-M., Malik, M., Kitzmann, D., Lyons, J. R., Fateev, A., Lee, E., & Heng, K. (2021). A Comparative Study of Atmospheric Chemistry with VULCAN. *The Astrophysical Journal*, 923(2), Article 264, 264.
- Tsang, W., & Hampson, R. (1986). Chemical kinetic data base for combustion chemistry. part i. methane and related compounds. *Journal of Physical and Chemical Reference Data*, 15(3), 1087–1279.
- Tu, L., Johnstone, C. P., Güdel, M., & Lammer, H. (2015). The extreme ultraviolet and X-ray Sun in Time: High-energy evolutionary tracks of a solar-like star. *Astronomy & Astrophysics*, 577, L3.
- Turbet, M., Bolmont, E., Bourrier, V., Demory, B.-O., Leconte, J., Owen, J., & Wolf, E. T. (2020). A Review of Possible Planetary Atmospheres in the TRAPPIST-1 System. *Space Science Reviews*, 216(5), 100.
- Usui, T., Alexander, C. M. O., Wang, J., Simon, J. I., & Jones, J. H. (2012). Origin of water and mantle–crust interactions on Mars inferred from hydrogen isotopes and volatile element abundances of olivine-hosted melt inclusions of primitive shergottites. *Earth and Planetary Science Letters*, 357–358, 119–129.
- Virtanen, P., Gommers, R., Oliphant, T. E., Haberland, M., Reddy, T., Cournapeau, D., Burovski, E., Peterson, P., Weckesser, W., Bright, J., van der Walt, S. J., Brett, M., Wilson, J., Millman, K. J., Mayorov, N., Nelson, A. R. J., Jones, E., Kern, R., Larson, E., ... van Mulbregt, P. (2020). SciPy 1.0: Fundamental algorithms for scientific computing in Python. *Nature Methods*, 17(3), 261–272.
- Visscher, C., & Moses, J. I. (2011). Quenching of carbon monoxide and methane in the atmospheres of cool brown dwarfs and hot jupiters. *The Astrophysical Journal*, 738(1), Article 72, 72.
- Visscher, C., Moses, J. I., & Saslow, S. A. (2010). The deep water abundance on Jupiter: New constraints from thermochemical kinetics and diffusion modeling. *Icarus*, 209(2), 602–615.
- Wade, J., & Wood, B. J. (2005). Core formation and the oxidation state of the Earth. *Earth and Planetary Science Letters*, 236(1), 78–95.
- Wadhwa, M. (2008). Redox Conditions on Small Bodies, the Moon and Mars. *Reviews in Mineralogy and Geochemistry*, 68(1), 493–510.

References

- Walker, J. C. G., Hays, P. B., & Kasting, J. F. (1981). A negative feedback mechanism for the long-term stabilization of Earth's surface temperature. *Journal of Geophysical Research*, 86(C10), 9776.
- Walker, J. C. G. (1977). *Evolution of the Atmosphere*. Maxwell Macmillan Canada, Incorporated.
- Wallace, P. J., Plank, T., Edmonds, M., & Hauri, E. H. (2015). Chapter 7 - Volatiles in Magmas. In H. Sigurdsson (Ed.), *The Encyclopedia of Volcanoes (Second Edition)* (pp. 163–183). Academic Press.
- Warren, A. O., Kite, E. S., Williams, J.-P., & Horgan, B. (2019). Through the Thick and Thin: New Constraints on Mars Paleopressure History 3.8 – 4 Ga from Small Exhumed Craters. *Journal of Geophysical Research: Planets*, n/a(n/a).
- Wieser, P. E., Iacovino, K., Matthews, S., Moore, G., & Allison, C. M. (2022). VESIcal: 2. A Critical Approach to Volatile Solubility Modeling Using an Open-Source Python3 Engine. *Earth and Space Science*, 9(2), e2021EA001932.
- Williams, H. M., Matthews, S., Rizo, H., & Shorttle, O. (2021). Iron isotopes trace primordial magma ocean cumulates melting in Earth's upper mantle. *Science Advances*, 7(11), eabc7394.
- Winters, J. G., Medina, A. A., Irwin, J. M., Charbonneau, D., Astudillo-Defru, N., Horch, E. P., Eastman, J. D., Vrijmoet, E. H., Henry, T. J., Diamond-Lowe, H., Winston, E., Barclay, T., Bonfils, X., Ricker, G. R., Vanderspek, R., Latham, D. W., Seager, S., Winn, J. N., Jenkins, J. M., ... Almenara, J.-M. (2019). Three Red Suns in the Sky: A Transiting, Terrestrial Planet in a Triple M-dwarf System at 6.9 pc. *The Astronomical Journal*, 158(4), 152.
- Witham, F., Blundy, J., Kohn, S. C., Lesne, P., Dixon, J., Churakov, S. V., & Botcharnikov, R. (2012). SolEx: A model for mixed COHSCL-volatile solubilities and exsolved gas compositions in basalt. *Computers & Geosciences*, 45, 87–97.
- Wogan, N., Krissansen-Totton, J., & Catling, D. C. (2020). Abundant Atmospheric Methane from Volcanism on Terrestrial Planets Is Unlikely and Strengthens the Case for Methane as a Biosignature. *The Planetary Science Journal*, 1(3), 58.
- Wogan, N. F., & Catling, D. C. (2020). When is Chemical Disequilibrium in Earth-like Planetary Atmospheres a Biosignature versus an Anti-biosignature? disequilibria from Dead to Living Worlds. *The Astrophysical Journal*, 892(2), 127.
- Woitke, P., Herbort, O., Helling, C., Stüeken, E., Dominik, M., Barth, P., & Samra, D. (2021). Coexistence of CH₄, CO₂, and H₂O in exoplanet atmospheres. *Astronomy & Astrophysics*, 646, A43.
- Wordsworth, R. (2012). Transient conditions for biogenesis on low-mass exoplanets with escaping hydrogen atmospheres. *Icarus*, 219(1), 267–273.
- Wordsworth, R., Kalugina, Y., Lokshtanov, S., Vigasin, A., Ehlmann, B., Head, J., Sanders, C., & Wang, H. (2017). Transient reducing greenhouse warming on early Mars. *Geophysical Research Letters*, 44(2), 665–671.
- Wordsworth, R. D., & Pierrehumbert, R. T. (2013a). Water loss from terrestrial planets with co₂-rich atmospheres. *The Astrophysical Journal*, 778(2), 154.
- Wordsworth, R., & Pierrehumbert, R. (2013b). Hydrogen-Nitrogen Greenhouse Warming in Earth's Early Atmosphere. *Science*, 339(6115), 64–67.
- Wordsworth, R., & Pierrehumbert, R. (2014). Abiotic Oxygen-Dominated Atmospheres on Terrestrial Habitable Zone Planets. *The Astrophysical Journal*, 785(2), L20.

References

- Wykes, J. L., O'Neill, H. S. C., & Mavrogenes, J. A. (2015). The effect of feo on the sulfur content at sulfide saturation (scss) and the selenium content at selenide saturation of silicate melts. *Journal of Petrology*, 56(7), 1407–1424.
- Yu, X., Moses, J. I., Fortney, J. J., & Zhang, X. (2021). How to identify exoplanet surfaces using atmospheric trace species in hydrogen-dominated atmospheres. *The Astrophysical Journal*, 914(1), 38.
- Yung, Y. L., Drew, W. A., Pinto, J. P., & Friedl, R. R. (1988). Estimation of the reaction rate for the formation of ch₃O from H + H₂CO: Implications for chemistry in the solar system. *Icarus*, 73(3), 516–526.
- Zahnle, K., Schaefer, L., & Fegley, B. (2010). Earth's Earliest Atmospheres. *Cold Spring Harbor Perspectives in Biology*, 2(10), a004895.
- Zahnle, K. J., Catling, D. C., & Claire, M. W. (2013). The rise of oxygen and the hydrogen hourglass. *Chemical Geology*, 362, 26–34.
- Zahnle, K. J., Gacesa, M., & Catling, D. C. (2019). Strange messenger: A new history of hydrogen on Earth, as told by Xenon. *Geochimica et Cosmochimica Acta*, 244, 56–85.
- Zahnle, K. J., Lupu, R., Catling, D. C., & Wogan, N. (2020). Creation and Evolution of Impact-generated Reduced Atmospheres of Early Earth. *The Planetary Science Journal*, 1(1), 11.
- Zahnle, K. J., & Marley, M. S. (2014). Methane, carbon monoxide, and ammonia in brown dwarfs and self-luminous giant planets. *The Astrophysical Journal*, 797(1), Article 41, 41.
- Zeng, L., Jacobsen, S. B., Sasselov, D. D., Petaev, M. I., Vanderburg, A., Lopez-Morales, M., Perez-Mercader, J., Mattsson, T. R., Li, G., Heising, M. Z., Bonomo, A. S., Damasso, M., Berger, T. A., Cao, H., Levi, A., & Wordsworth, R. D. (2019). Growth model interpretation of planet size distribution. *Proceedings of the National Academy of Sciences*, 116(20), 9723–9728.
- Zeng, L., & Sasselov, D. (2013). A Detailed Model Grid for Solid Planets from 0.1 through 100 Earth Masses. *Publications of the Astronomical Society of the Pacific*, 125(925), 227–239.
- Zolotov, M. Y., Sprague, A. L., Hauck, S. A., Nittler, L. R., Solomon, S. C., & Weider, S. Z. (2013). The redox state, FeO content, and origin of sulfur-rich magmas on Mercury. *Journal of Geophysical Research: Planets*, 118(1), 138–146.

A

Solubility laws as implemented in EVo

Except where explicitly noted, all equations return the weight fraction of a volatile dissolved in silicate melt, pressures/fugacities are in bar, and temperatures are in Kelvin.

A.1 Laws taken from Burgisser et al. (2015)

Each of the solubility laws taken from Burgisser et al. (2015) take the form

$$w_i^m = a_i(\gamma_i X_i P)^{b_i}, \quad (\text{A.1})$$

where a and b are compositionally dependent parameters listed in Table A.1, γ_i is a fugacity coefficient, X_i is the mole fraction of species i in the gas phase and P is the current total pressure of the system. As the gas phase fugacity of i is simply given as

$$f_i = \gamma_i X_i P, \quad (\text{A.2})$$

calculating the fugacity of a species from the melt concentration can be found by simple re-arrangement. See Section A.7 for a note on the H₂ implementation; note that the equation and values given here are identical to the implementation in EVo.

Solubility laws as implemented in EVO

Table A.1 Parameters used in solubility laws taken from Burgisser et al. (2015). T is in Kelvin, where relevant.

Species	a_i	b_i
Basalt		
H_2O	6.576×10^{-4}	0.5698
H_2	3.4×10^{-7}	1.28
CO_2	1.729×10^{-6}	0.854
Phonolite		
H_2O	$-3.166 \times 10^{-9} T^2 + 7.48 \times 10^{-6} T - 3.853 \times 10^{-3}$	$2.555 \times 10^{-6} T^2 - 5.827 \times 10^{-3} T + 3.918$
H_2	3.4×10^{-7}	1.28
CO_2	4.339×10^{-7}	0.8006
Rhyolite		
H_2O	$2.5973 \times 10^{-8} T^2 - 4.8473 \times 10^{-5} T + 2.298 \times 10^{-2}$	$-5.148 \times 10^{-6} T^2 + 9.4853 \times 10^{-3} T - 3.7085$
H_2	3.4×10^{-7}	1.28
CO_2	$2.8895 \times 10^{-9} T - 1.9625 \times 10^{-6}$	$-1.0764 \times 10^{-3} T + 1.9639$

A.2 CH₄: Ardia et al. (2013)

Both pressure and fugacity are taken in GPa (bar $\times 1 \times 10^{-4}$),

$$w_{CH_4}^m (\text{ppm}) = f_{CH_4} e^{4.93 - 0.000193P}. \quad (\text{A.3})$$

A.3 CO: Armstrong et al. (2015)

This solubility law is described as for "non-carbonate C", based on experiments with a low hydrogen content in the melt. Armstrong et al. (2015) assume the mean stoichiometry is C≡O in

$$\log_{10}(w_C^m) (\text{ppm}) = -0.738 + 0.876 \log_{10}(f_{CO}) - 5.44 \times 10^{-5} P, \quad (\text{A.4})$$

so this law is used for CO solubility.

A.4 CO₂: Dixon et al. (1997)

CO₂ solubility is parametrised as

$$X_{CO_3^{2-}}^m = X_{CO_3^{2-}}^m(P_0 T_0) f_{CO_2} e^{(-23(P-1)/(R 1473.15))}, \quad (\text{A.5})$$

where $X_{CO_3^{2-}}^m$ is the mole fraction of carbonate dissolved in the melt, P is the current pressure in bar, R is the gas constant ($83.145 \text{ cm}^3 \text{ bar mol}^{-1} \text{ K}^{-1}$) and $X_{CO_3^{2-}}^m(P_0 T_0)$ is the mole fraction of CO₂ dissolved as carbonate in the melt under standard pressure and temperature

conditions (1 bar, 1473.15 K), calculated as

$$X_{\text{CO}_3^{2-}}^m(P_0 T_0) = 7.94 \times 10^{-7} (\Pi + 0.762), \quad (\text{A.6})$$

and

$$\Pi = -6.5(X_{\text{Si}^{4+}} + X_{\text{Al}^{3+}}) + 20.17(X_{\text{Ca}^{2+}} + 0.8X_{\text{K}^+} + 0.7X_{\text{Na}^+} + 0.4X_{\text{Mg}^{2+}} + 0.4X_{\text{Fe}^{2+}}), \quad (\text{A.7})$$

where X_i are cation mole fractions.

The concentration of CO₂ (weight fraction) is calculated from the mole fraction of carbonate in the melt using (Dixon, 1997)

$$w_{\text{CO}_2}^m = 0.01 \left[\frac{4400 X_{\text{CO}_3^{2-}}^m}{36.6 - 44 X_{\text{CO}_3^{2-}}^m} \right]. \quad (\text{A.8})$$

A.5 CO₂: Dixon et al. (1997) (VC)

This is the simplified form of the Dixon (1997) law expressed above, as implemented in VolatileCalc by Newman and Lowenstern (2002). This form expresses the $X_{\text{CO}_3^{2-}}^m(P_0 T_0)$ term of Eq. (A.5) purely in terms of SiO₂ rather than in terms of cation fractions,

$$X_{\text{CO}_3^{2-}}^m(P_0 T_0) = 8.70 \times 10^{-6} - 1.70 \times 10^{-7} [\text{SiO}_2]^{\text{wt}\%}. \quad (\text{A.9})$$

$X_{\text{CO}_3^{2-}}^m(P_0 T_0)$, the mole fraction of CO₂ dissolved as carbonate in the melt under standard pressure and temperature conditions (1 bar, 1473.15 K), is then used in the formulation of Section A.4 and Eq. (A.5) (Dixon, 1997) above.

A.6 CO₂: Eguchi and Dasgupta, (2018)

This solubility law can be used under both graphite and gas saturated conditions. As this is the only law implemented where graphite saturation can be dealt with while the system is also at volatile saturation, use of this law is enforced while the system is graphite saturated (see Chapter 2 for further discussion). It also calculates the split between CO₂ dissolved as molecular CO₂, and carbonate.

The mole fraction of both molecular CO₂ ($X_{\text{CO}_2, \text{mol}}^m$) and carbonate ($X_{\text{CO}_3^{2-}}^m$) are calculated (note that this is different to the equation published by Eguchi and Dasgupta (2018), this

Solubility laws as implemented in EVO

Table A.2 Coefficients for the CO₂ solubility model of Eguchi and Dasgupta, (2018), Eq. (A.10)

Term	Value	
	CO ₃ ²⁻	CO _{2,mol}
ΔH [J/mol]	-1.6448 × 10 ⁵	-9.0212 × 10 ⁴
ΔV [m ³ /mol]	2.384 × 10 ⁻⁵	1.9244 × 10 ⁻⁵
ΔS [J/K]	-43.6385	-43.0815
B	1.4732 × 10 ³	1.1149 × 10 ³
γ _{NBO}	3.291	-7.0937
A _{Ca²⁺}	1.68 × 10 ⁵	0
A _{Na⁺}	1.759 × 10 ⁵	0
A _{K⁺}	2.1085 × 10 ⁵	0

implementation matches the paper results and the version implemented in their provided excel spreadsheet) through

$$\ln X_i^m = -\frac{\Delta V P}{RT} + \frac{\Delta H}{RT} + \frac{\ln(f_{CO_2})B}{T} + \frac{\Delta S}{R} + \gamma_{NBO} NBO + \frac{\sum_{i=1}^n A_i X_i}{RT}, \quad (\text{A.10})$$

where P (Pa) is the current pressure, T (K) is the magmatic temperature, R (J mol⁻¹ K⁻¹) is the gas constant, f_{CO_2} (bar) is the CO₂ fugacity (either from the gas phase or as enforced by graphite saturation according to Eq. (2.34a)) and X_i are cation mole fractions for Ca²⁺, Na⁺ and K⁺. Other parameters vary with species (molecular CO₂ vs CO₃²⁻), and are given in Table A.2.

The *NBO* (non-bridging oxygen) term of Eq. (A.10) is calculated according to Appendix A of Eguchi and Dasgupta (2018), and accounts for the effect of the major element chemistry of the melt on CO₂ solubility.

The mole fractions of dissolved molecular CO₂ and CO₃²⁻, i , are then converted to weight fractions using

$$w_i^m = \frac{44.01X_i^m}{44.01X_i^m + (1 - (X_{CO_2}^m + X_{CO_3^{2-}}^m))FW_{one}}, \quad (\text{A.11})$$

where FW_{one} is the one-oxygen formula weight of one mole of the volatile-free melt. $w_{CO_2}^m$ is then simply the sum of $w_{CO_2,\text{mol}}^m + w_{CO_3^{2-}}^m$.

A.7 H₂: Gaillard et al. (2003)

This solubility law is cited as the source of the Burgisser et al. (2015) H₂ law for DCompress; however, there is an error in the DCompress implementation so the law in Section A.1 returns

the hydrogen content of the melt as g m⁻³ rather than as a weight fractions. Equation (A.12), offered in EVo specifically as the Gaillard et al. (2003) solubility law, correctly converts the units to return the H₂ content as a weight fraction. ρ is the silicate melt density in g cm⁻³

$$w_{\text{H}_2}^m = \frac{3.4 \times 10^{-7} (\gamma_{\text{H}_2} X_{\text{H}_2} P)^{1.28}}{\rho}. \quad (\text{A.12})$$

A.8 H₂O: Dixon et al. (1997)

This solubility law describes water dissolved as both OH⁻ ions and H₂O molecules, before being converted into a total mass of water that is dissolved in the melt. Currently only the basaltic parametrisation is implemented in EVo, and therefore only the equations suitable for a basaltic melt are described here.

$$X_{\text{H}_2\text{O,mol}}^m = X_{\text{H}_2\text{O,mol}}^m(P_0 T_0) f_{\text{H}_2\text{O}} \cdot \exp\left(\frac{-12(P-1)}{1473.15 R}\right), \quad (\text{A.13})$$

where $X_{\text{H}_2\text{O,mol}}^m$ is the mole fraction of molecular H₂O dissolved in the melt, P is the current pressure in bar, R is the gas constant (83.145 cm³ bar mol⁻¹ K⁻¹) and $X_{\text{H}_2\text{O,mol}}^m(P_0 T_0)$ is the the mole fraction of molecular H₂O dissolved in the melt under standard pressure and temperature conditions (1 bar, 1473.15 K), dependent on the SiO₂ content of the melt, calculated as

$$X_{\text{H}_2\text{O,mol}}^m(P_0 T_0) = -3.04 \times 10^{-5} + 1.29 \times 10^{-6} [\text{SiO}_2]^{\text{wt\%}}. \quad (\text{A.14})$$

To convert from the mole fraction of dissolved molecular H₂O, to the total weight fraction of water, first the mole fraction of hydroxyl groups ($X_{\text{OH}^-}^m$) is calculated by solving to find the root of the regular solution model of Silver and Stolper (1989)

$$-\ln\left(\frac{X_{\text{OH}^-}^{m^2}}{X_{\text{H}_2\text{O,mol}}^m(1 - X_{\text{OH}^-}^m - X_{\text{H}_2\text{O,mol}}^m)}\right) = 0.403 + 15.333 X_{\text{OH}^-}^m + 10.894 X_{\text{H}_2\text{O,mol}}^m, \quad (\text{A.15})$$

achieved using the SciPy fsolve function.

The total mole fraction of water (molecular H₂O + OH⁻, $X_{\text{H}_2\text{O,tot}}^m$) is then calculated as

$$X_{\text{H}_2\text{O,tot}}^m = X_{\text{H}_2\text{O,mol}}^m + X_{\text{OH}^-}^m / 2, \quad (\text{A.16})$$

Solubility laws as implemented in EVo

and converted into a weight fraction of total water through

$$w_{\text{H}_2\text{O,tot}}^m = 0.01 \left[\frac{1801.5X_{\text{H}_2\text{O,tot}}^m}{36.594 - 18.579X_{\text{H}_2\text{O,tot}}^m} \right]. \quad (\text{A.17})$$

A.9 N₂: Libourel, (2003)

P in atmospheres; $P_{atm} = 0.986923 P_{bar}$

$$w_{\text{N}_2}^m = 0.0611 \times 10^{-6} P X_{\text{N}_2} + 5.97 \times 10^{-16} f_{\text{O}_2}^{-0.75} (P X_{\text{N}_2})^{0.5}. \quad (\text{A.18})$$

A.10 Sulfide capacity laws

In all cases the weight fraction of sulfur (speciated as S²⁻) dissolved in the melt, $w_{\text{S}^{2-}}^m$, is calculated as

$$w_{\text{S}^{2-}}^m = C_{\text{S}^{2-}} \frac{f_{\text{S}_2}}{f_{\text{O}_2}}^{0.5}, \quad (\text{A.19})$$

where $C_{\text{S}^{2-}}$ is the sulfide capacity calculated using one of the below methods.

A.10.1 O'Neill and Mavrogenes, (2002)

$$C_{\text{S}^{2-}} = \frac{0.0003(100 - w_{\text{FeO}}^m) e^{0.21 w_{\text{FeO}}^m}}{1 \times 10^{-6}}, \quad (\text{A.20})$$

where w_{FeO}^m is the weight percent of FeO in the melt, according to the current oxygen fugacity.

A.10.2 O'Neill, (2020)

$$\begin{aligned} \ln(C_{\text{S}^{2-}}) = & \frac{-23590}{T} + 8.77 + \frac{1673}{T} [6.7(X_{\text{Na}} + X_{\text{K}}) + 1.8X_{\text{Al}} + 4.9X_{\text{Mg}} + 8.1X_{\text{Ca}} \\ & + 5.0X_{\text{Ti}} + 8.9(X_{\text{Fe}} + X_{\text{Mn}}) - 22.2X_{\text{Ti}}(X_{\text{Fe}} + X_{\text{Mn}}) + 7.2X_{\text{Si}}(X_{\text{Fe}} + X_{\text{Mn}})] \\ & - 2.06erf(-7.2(X_{\text{Fe}} + X_{\text{Mn}})), \end{aligned} \quad (\text{A.21})$$

where X_{Na} etc. are silicate melt mole fractions, defined and renormalised on a single-cation basis so e.g., Al₂O₃ → 2 AlO₁ · 5, SiO₂, MgO etc. The "single_cat" function in the conversions.py file of EVo will perform this conversion from the standard melt oxide composition.

A.11 S⁶⁺: Nash et al. (2019)

The weight fraction of sulfur ($w_{\text{S}^{6+}}^m$), speciated as S⁶⁺, is calculated as

$$w_{\text{S}^{6+}}^m = w_{\text{S}^{2-}}^m \cdot \frac{\text{S}^{6+}}{\text{S}^{2-}}, \quad (\text{A.22})$$

where

$$\log_{10} \left(\frac{\text{S}^{6+}}{\text{S}^{2-}} \right) = \log_{10} \left(8 \log_{10}(2F) + \frac{8.7436 \times 10^6}{T^2} - \frac{27703}{T} + 20.273 \right), \quad (\text{A.23})$$

and F is the molar ratio of Fe₂O₃/FeO.

B

Appendices for Chapter 3

B.1 Effect of pressure and $f\text{O}_2$ on volcanic gases and $f_T^V(\text{H}_2)$

The amount of gas released from a melt and its speciation varies with pressure (Fig. B.1(a, b)). As the pressure reduces, so does volatile solubility therefore increasing the volume of the gas phase. The volume of gas phase also increases according to the ideal gas law, so that Fig. B.1c shows both the increasing amount of volatile in the gas phase, and the expansion of the gas phase according to $PV = nRT$ as the pressure decreases. Figure B.1a shows how the speciation of a gas phase changes with depth, but it should be noted that this is for a fixed $f\text{O}_2$ at all pressures, to isolate the pressure effect on speciation. If left to decompress naturally, a melt (particularly a sulphur rich one) will evolve through a slight $f\text{O}_2$ change and the resulting speciation plot would be a combination of effects from Figs. B.1 and B.2.

The exsolved fraction also varies with constant pressure and variable $f\text{O}_2$ (Fig. B.2). As the $f\text{O}_2$ decreases at low pressure, the weight fraction of gas exsolved decreases, while the gas volume remains almost constant. The decreasing weight fraction reflects oxygen in the gas phase reducing with $f\text{O}_2$. As oxygen is the second heaviest volatile element, reducing the system $f\text{O}_2$ results in a gas phase which is dominated by lighter molecules and therefore has a much lower mean molecular mass. The decreasing weight fraction from oxygen loss is modulated by the presence of sulphur, which initially partitions slightly more into the melt, before increasing in the gas phase as it speciates into less soluble, reducing species (S_2 and H_2S) rather than SO_2 .

However at high pressures (Fig. B.2b), the amount of volatile in the gas phase clearly increases from very low fractions with decreasing $f\text{O}_2$ due to the solubility of a species being linked to its fugacity in the gas phase (Section 2.1.1). As the $f\text{O}_2$ decreases and water in

Appendices for Chapter 3

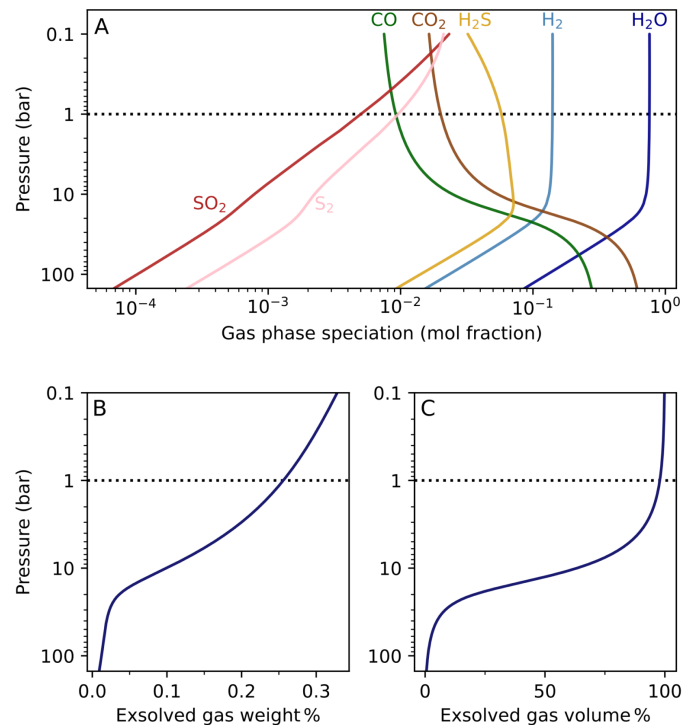


Fig. B.1 A: Speciation of the gas phase from a melt at FMQ-2, with an initial volatile content of 350 ppm H, 50 ppm C and 1000 ppm S, at a range of final pressures. B: Weight % of the same system made up of the gas phase according to pressure. C: Volume % of the system taken up by the gas phase according to pressure. Dotted lines correspond to the same transect on Fig. B.2a.

B.1 Effect of pressure and fO_2 on volcanic gases and $f_T^V(H_2)$

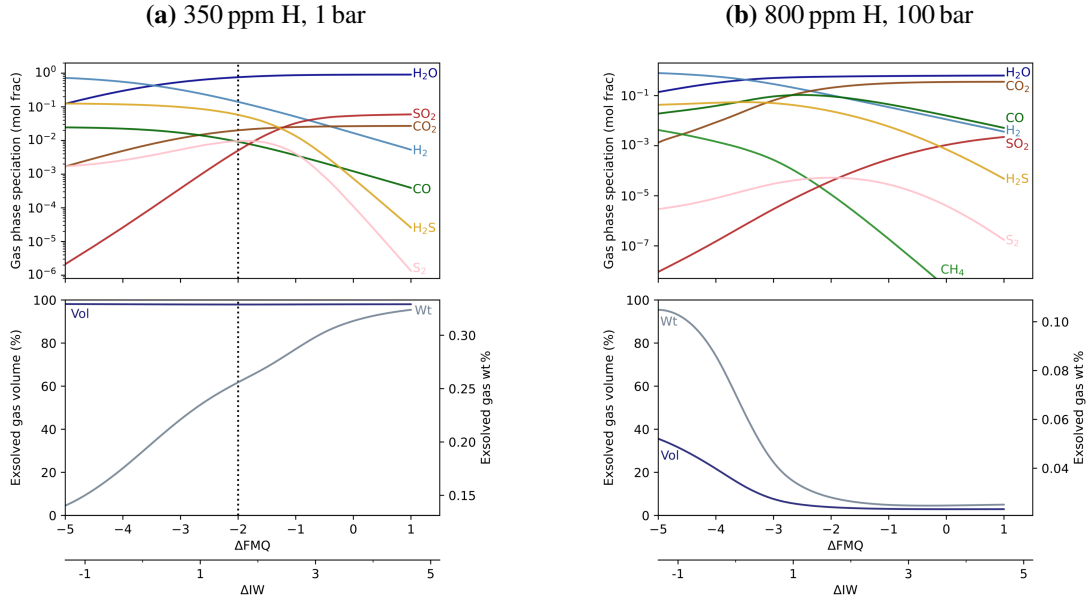


Fig. B.2 Top: Speciation of the gas phase at 1 bar from a melt at a given fO_2 , with an initial volatile content of 50 ppm C, 1000 ppm S and a specified H content. Bottom: Changing gas weight percent and volume percentage of the system taken up by the gas phase. Dotted lines match a corresponding transect point on Fig. B.1.

the gas phase dissociates into H₂ (or is taken up as H₂S in H-poor systems), more water is drawn out of the melt to maintain the $H_2O_{melt} \rightleftharpoons H_2O_{gas}$ equilibrium. The resulting hydrogen does not dissolve back into the melt, as H₂ and H₂S have a much lower solubility than water. Similarly, CO₂ is converted to insoluble CO and CH₄ in the gas phase. The increase in the volatile fraction with decreasing fO_2 is less obvious at low pressures (Fig. B.2a), as almost all the volatile elements are already in the gas phase, so the absolute change in volume with fO_2 is much smaller. With a H-rich magma such as in Fig. B.2b, the lower mean molecular mass of the gas phase is insignificant compared to the amount of volatile exsolving from the melt, so the trend for the weight fraction of gas to decrease is overridden.

There are therefore two factors (pressure and fO_2) which can modulate the amount of volatile released from a magmatic system, independent of the initial volatile load. These two factors interact, so for any melt with a fixed H, C and S content and the same rate of magma flux (mantle heat flow) to the surface, its position in fO_2 and pressure space once it erupts will control the volcanic gas flux (in mol s⁻¹).

The mixing fraction of total hydrogen in a volcanic gas ($f_T^V(H_2)$) emitted at 1 bar surface pressure can be seen to vary with the melts initial volatile content, along with the fO_2 of the erupting melt with reference to the FMQ and IW buffers (Fig. B.3).

Appendices for Chapter 3

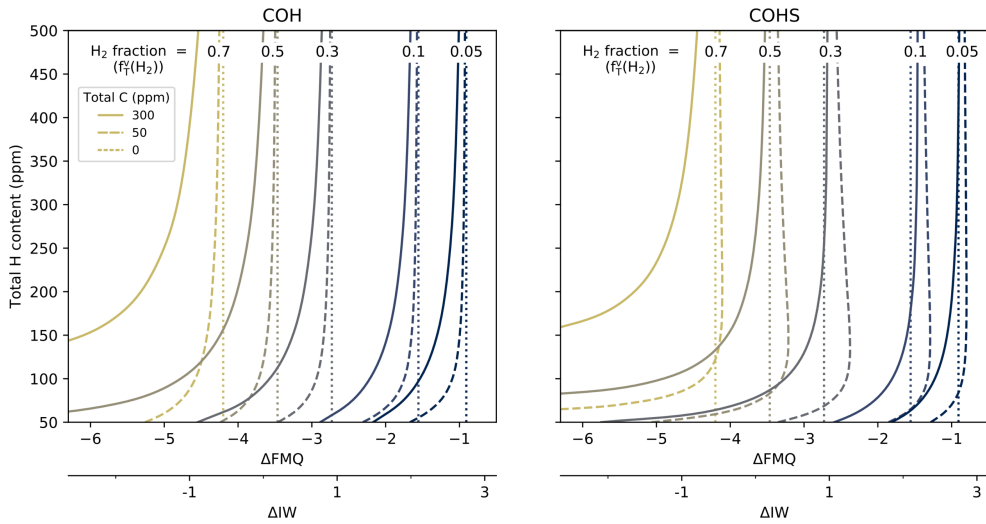


Fig. B.3 Mole fraction of the gas phase occurring as total H_2 at 1 bar, according to the fO_2 of the melt at the surface, and the amount atomic hydrogen and carbon dissolved in the melt at depth.

As the total carbon content of the melt increases, a progressively more reduced system is required to achieve the same $f_T^v(H_2)$. In these melts, a greater fraction of the gas volume is made up of carbon bearing species, mostly CO_2 and/or CO , which both have low to no solubility in magma at low pressures. Therefore, almost all of the volatile carbon in the system is in the gas phase at 1 bar (see Fig. B.1) and a greater C content means a larger absolute amount of reduced, H-bearing species are required to achieve the same $f_T^v(H_2)$.

In a H-rich COH system, the gas phase is predominantly H_2O (H_2 at very low fO_2), whereas in H-poor systems with the same fO_2 , CO_2 and CO are much more dominant. Therefore, to achieve the same $f_T^v(H_2)$, a greater proportion of the water in the system has to be dissociated. With a large volume of water, this dissociation happens easily, but as the available water fraction decreases, a greater reduction in fO_2 is required to drive the dissociation in Eq. (2.1), resulting in the curve towards a lower fO_2 as the H fraction decreases. A reduced H content also means there is a lower volatile fraction in the system as a whole, and therefore the C-bearing species make up a greater proportion of the total gas phase. In H-poor magmas, the $f_T^v(H_2)$ contours asymptote to the fraction of the gas phase made up of H-free, carbon bearing species; the gas phase is then almost entirely composed of H_2 , CO and at higher fO_2 , CO_2 . With higher C contents, this H-free fraction is larger and so the maximum achievable $f_T^v(H_2)$ occurs at a correspondingly greater H content.

Adding sulphur to the system has the effect of shifting the contours to a slightly higher fO_2 , and increasing the H-free gas fraction again to shift the point of maximum achievable $f_T^v(H_2)$

B.2 Outgassing parameterisation

to a higher H content. Whereas in the COH system the only species in the $f_T^V(H_2)$ fraction are H₂ and CH₄, which are both present in low to very low fractions at high to moderate fO_2 , in the COHS system the $f_T^V(H_2)$ fraction includes H₂S. As H₂S can be present in significant fractions at all fO_2 values discussed here, adding S to the system makes achieving a specific $f_T^V(H_2)$ easier than in both the COH and OH systems. The effect of adding S to a system is greatest at around FMQ-3, where the fraction of H₂S approaches its maximum value before much of the H₂O has strongly dissociated into H₂ (Fig. B.2). This effect is particularly strong in H-poor systems, where H₂S becomes the dominant $f_T^V(H_2)$ species (as opposed to H₂) at low fO_2 .

B.2 Outgassing parameterisation

Depending on how the volcanic hydrogen input $f_T^V(H_2)$ is defined, the same volcanic conditions can generate a different atmospheric $f_T(H_2)$ (Fig. B.4).

At the lower bound of $f_T^V(H_2)$, only hydrogen emitted as molecular H₂ is counted. This ignores any input from other hydrogen bearing species, and assumes they are all removed from the atmosphere via mechanisms which do not release H₂. This could be a result of either very efficient H₂S deposition, or a sufficiently oxidising atmosphere such that



preserving atmospheric redox. However, the Archean atmosphere pre-GOE is very unlikely to have been oxidising enough to make this plausible.

On the other end of the scale, the upper bound for $f_T^V(H_2)$ is where all the CH₄ and H₂S is included, weighted according to how much hydrogen will be emitted by an oxidation reaction with each molecule. I.e., one mol of volcanic CH₄ is equal to 4 mols of H₂ in the atmosphere as it reacts according to



and H₂S produces 3 mols of H₂ according to



This would suggest inefficient H₂S deposition and a neutral atmosphere so that H₂S and CH₄ react sufficiently quickly in the troposphere and lower stratosphere such that

Appendices for Chapter 3

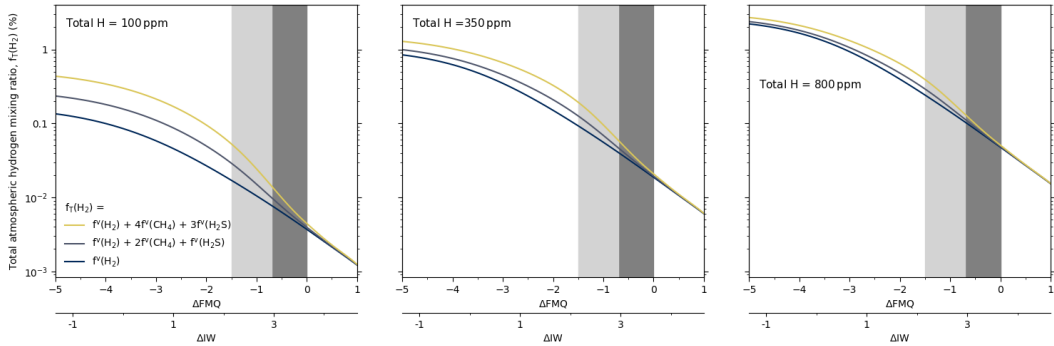


Fig. B.4 The atmospheric $f_T(H_2)$ variation with fO_2 in a one bar atmosphere, 550 ppm C, according to the volatile content and $f_T^V(H_2)$ stoichiometry. Light and dark grey bars represent the possible Archean range and modern MORB range of fO_2 .

$$f_T^V(H_2) = f(H_2) + 4f(CH_4) + 3f(H_2S). \quad (\text{B.4})$$

As seen in Fig. B.4, the middle ground can be represented by

$$f_T^V(H_2) \approx f^V(H_2) + 2f^V(CH_4) + f^V(H_2S). \quad (\text{B.5})$$

This is the same stoichiometry as is used to define $f_T(H_2)$ above the tropopause weighting CH₄ and H₂S according to the number of H atoms they contain, and approximates the idea that a proportion of CH₄ and H₂S will react to H₂, with the rest being lost through alternative mechanisms such as an environment where H₂S and CH₄ deposition may be inefficient, but they are also less reactive in the atmosphere either because the atmosphere is neutral and there is insufficient stellar UV to convert to SO₂/CO₂ before reaching the homopause. Alternatively, species are photochemically restored as soon as they are reacted away in a reducing atmosphere. Changing the stoichiometry of $f_T^V(H_2)$ has the greatest effect at low water contents, where there is a higher ratio of H₂S:H₂, where the greatest difference between the upper and lower bound is 3.5× at 100 ppm, to 1.3× at 800 ppm H₂.

To illustrate the effect of different photochemical regimes on our results for the Archean Earth and early Mars, plots B.5a to B.5c for Earth and B.6a to B.6c for Mars show the effect of using the three different photochemical regimes.

On Earth, a change in the photochemical regime makes very little difference for oxidised systems above FMQ=0. The most frequent set of results for achieving 1 % $f_T(H_2)$ fall in different areas according to the definition of $f_T^V(H_2)$, from low $f_T^V(H_2)$ (Fig. B.5a, early fO_2 range) to high $f_T^V(H_2)$ (Fig. B.5c, modern fO_2 range). However, the range in $f_T(H_2)$ at FMQ-

B.2 Outgassing parameterisation

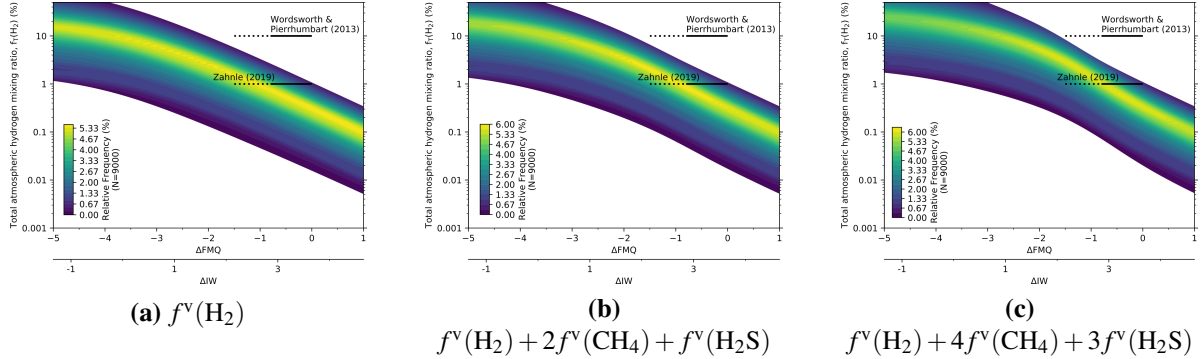


Fig. B.5 The relative frequency of hydrogen mixing ratios in the atmosphere of an Earth-like planet, as a function of the magma fO_2 , represented as a 2D density surface. $\alpha = 0.2\text{-}0.6$, $\beta = 1\text{-}10$ and surface pressures of 0.1 - 10 bar as in the main text, so (b) is equal to Fig. 6. Labelled according to the definition of $f_T(H_2)$ used, and hence the photochemical regime.

1.5 is significantly affected, so where in Fig. B.5a at FMQ-1.5 the most frequent result is 1-3 % $f_T(H_2)$, in Fig. B.5c this range is 2-6 %.

For a Mars-like planet with a hydrous melt scenario, a much larger variation is seen over the relevant fO_2 range. At IW+1, the low $f_T^v(H_2)$ regime (Fig. B.6a) has the most frequent results falling into the range 2 - 3 % $f_T(H_2)$; at the same fO_2 with a high $f_T^v(H_2)$ regime, this range is 8 - 12 % $f_T(H_2)$ (Fig. B.6c). At IW-1, these ranges are 3 - 5 % and 10 - 18 % $f_T(H_2)$, for low and high $f_T^v(H_2)$ regimes respectively.

Under anhydrous conditions, the $f_T(H_2)$ ranges for Mars drop so at IW+1, the low $f_T^v(H_2)$ regime (Fig. B.7a) has the most frequent results falling into the range 0.1 - 0.2 % $f_T(H_2)$; at the same fO_2 with a high $f_T^v(H_2)$ regime, this range is 1 - 2 % $f_T(H_2)$ (Fig. B.6c). At IW-1, these ranges are 0.2 - 0.35 % and 2 - 3 % $f_T(H_2)$, for low and high $f_T^v(H_2)$ regimes respectively.

Appendices for Chapter 3

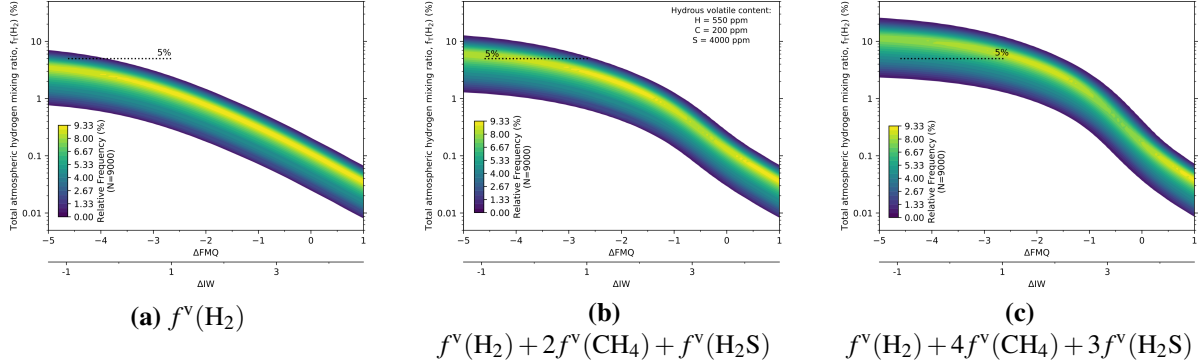


Fig. B.6 The relative frequency of hydrogen mixing ratios in the atmosphere of a Mars-like planet, as a function of the hydrous magma $f\text{O}_2$, represented as a 2D density surface. $\alpha = 0.6 - 1$, $\beta = 0.5 - 2$ and surface pressures of 0.5 - 2 bar as in the main text, so (b) is equal to Fig. 8(a). Labelled according to the definition of $f_T(\text{H}_2)$ used, and hence the photochemical regime.

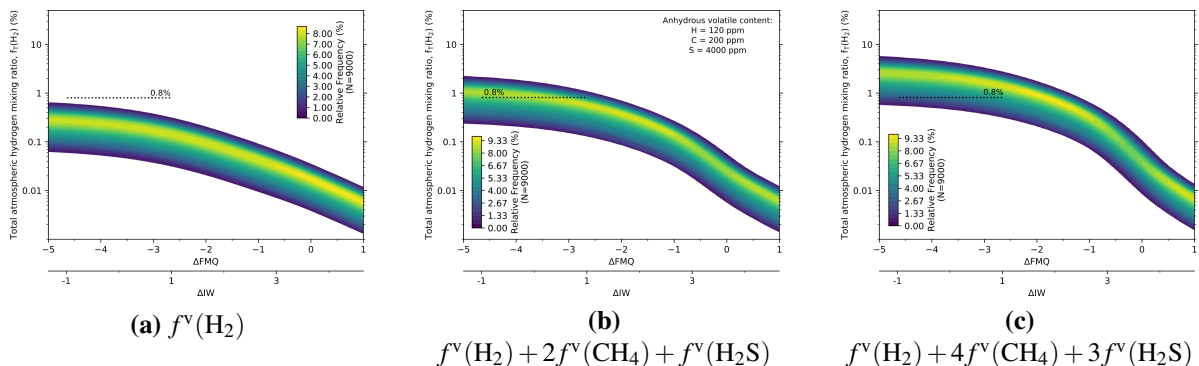


Fig. B.7 The relative frequency of hydrogen mixing ratios in the atmosphere of a Mars-like planet, as a function of the anhydrous magma $f\text{O}_2$, represented as a 2D density surface. $\alpha = 0.6 - 1$, $\beta = 0.5 - 2$ and surface pressures of 0.5 - 2 bar as in the main text, so (b) is equal to Fig. 8(c). Labelled according to the definition of $f_T(\text{H}_2)$ used, and hence the photochemical regime.

C

Full description of the identified rate-limiting reactions

C.1 Atmospheric evolution

Figure C.1 demonstrates how the atmospheric composition evolves for three atmospheric temperatures: 2000 K (Fig. C.1 left), 1000 K (Fig. C.1 middle) and 500 K (Fig. C.1 right).

At 2000 K, the volcanic gas composition relaxes to the atmospheric equilibrium composition on short timescales. In this case we can integrate the atmospheric chemistry at the new temperature until the 2000 K equilibrium is reached.

At 1000 K, the volcanic gas composition relaxes to the atmospheric equilibrium composition on intermediate timescales that are longer than in the 2000 K atmosphere, but are shorter than geological timescales. For CO and CH₄ the time-series demonstrates that these species will reach equilibrium within the integration time, however for NH₃ the timescales to equilibrium are longer than for CO and CH₄ and the solver stalls before NH₃ reaches its true equilibrium. The timescale to the true equilibrium for NH₃ must instead be calculated based on the rate of change of the NH₃ number density and the difference between the final NH₃ number density compared to its equilibrium number density at 1000 K. This is calculated with Eq. (5.1) at the latest time-step before stalling. In Fig. C.1 we also show the timescale estimate that would be obtained for CO and CH₄ if the solver would have stalled at the quasi-steady state before they reached their true equilibrium. We find that the timescale estimates are consistent with the time that was actually taken for these two species to approach equilibrium.

At 500 K, the volcanic gas composition relaxes to the atmospheric equilibrium composition on timescales that are longer than geological timescales. In this case the solver stalls at a

Full description of the identified rate-limiting reactions

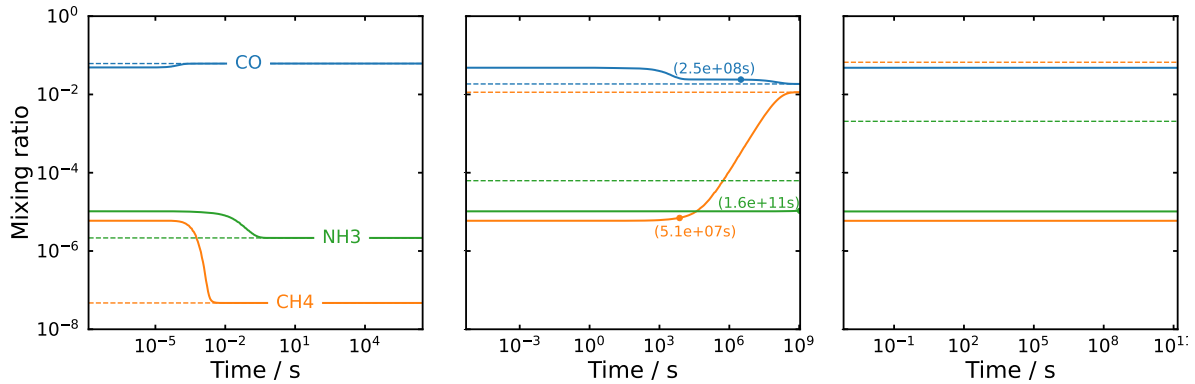


Fig. C.1 Time-series of the volcanic atmosphere composition produced on a planet with a mantle $f\text{O}_2$ equal to IW as it relaxes to ambient atmospheric temperatures for three different cases: (left) 2000 K, (middle) 1000 K, and (right) 500 K. The dashed lines show the equilibrium abundances of each species at the atmospheric temperature calculated by FastChem 2.0 (Stock and Kitzmann, 2021). In the 1000 K case we show, as numbers above filled circles along the lines, the estimated timescales to equilibrium that are computed before the mixing ratio approaches equilibrium. The filled circles have been placed along the lines at the point where the species begins moving towards its final equilibrium abundance, or, in the case of NH₃, at the point where the calculation stalls. The timescale estimates for CH₄ and CO provide an accurate order of magnitude estimate of the final time to equilibrium.

quasi-steady state before any chemical species reaches its equilibrium. The time to the true equilibrium for CO, CH₄, and NH₃ is calculated to be longer than geological timescales (see Section 5.3.1). The species are thus said to be ‘quenched’ at their hotter volcanic gas composition and will not reflect the atmospheric-temperature equilibrium composition unless there is significant catalysis due to other physical processes. In the absence of additional catalysis, the atmospheric composition of the 500 K secondary atmospheres will unintuitively resemble the equilibrium composition of much hotter atmospheres (i.e., at the magmatic temperature ~ 1500 K). The 1000 K atmospheres, not the cooler 500 K atmospheres, end up deviating the most from the hot equilibrium composition of a volcanic gas.

C.2 $\text{CO} \rightleftharpoons \text{CH}_4$ system

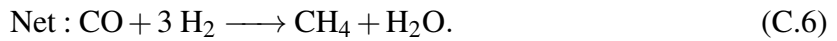
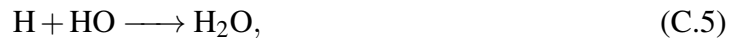
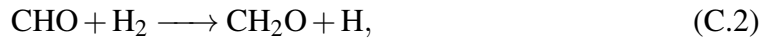
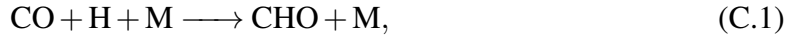
In order to identify the dominant pathways and their rate-limiting steps for relevant species interconversions, we use an algorithm that finds all significant routes from one molecule to another in our reaction network. This is done using the rates of reaction calculated in the chemical-kinetics simulation. Once all significant pathways are found, the rate-limiting step of each pathway is identified as the slowest reaction rate in the sequence of reactions. We do this

C.2 CO \rightleftharpoons CH₄ system

for the pairs of start/end molecules CO \longrightarrow CH₄ and N₂ \longrightarrow NH₃, as a function of *fO*₂ and temperature.

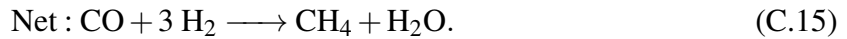
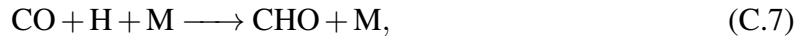
For the CO \longrightarrow CH₄ system, we identify four pathways that each dominate at different atmospheric temperatures.

Pathway A:



Pathway A dominates the conversion at 2000 K over all the *fO*₂ values investigated. The pathway is limited by reaction (C.3).

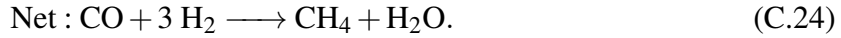
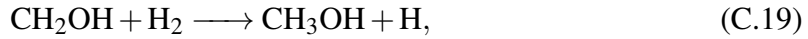
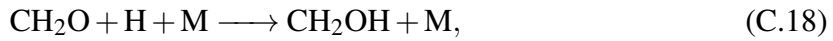
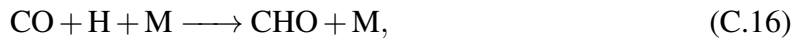
Pathway B:



Pathway B dominates the conversion at 1500 K over all the *fO*₂ values investigated. The pathway is limited by reaction (C.10) at 2000 K and by reaction (C.11) at lower temperatures.

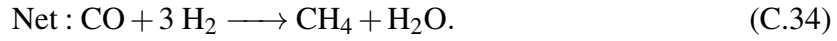
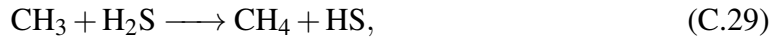
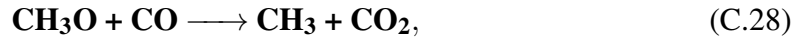
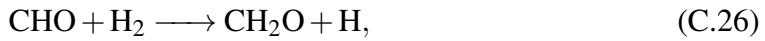
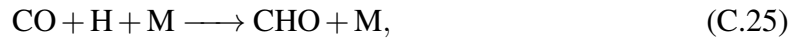
Full description of the identified rate-limiting reactions

Pathway C:



Pathway C dominates the conversion at 1000 K and 800 K over all the $f\text{O}_2$ values investigated. The pathway is limited by reaction (C.20).

Pathway D:



Pathway D dominates the conversion at 500 K over all the $f\text{O}_2$ values investigated. The pathway is limited by reaction (C.28).

The rates of the limiting reactions of each of the pathways A-D are shown in Fig. C.2 as a function of mantle $f\text{O}_2$ for atmospheric temperatures 2000 K, 1500 K, 1000 K, 800 K, and 500 K. Where one pathway's limiting reaction is the fastest, that is the pathway that dominates the conversion. Annotated chemical pathways are shown highlighted in the reaction network alongside the reaction rate figures.

In each case the rate-determining step of the overall conversion is associated with breaking the C–O single bond. This is in agreement with the conclusion of Moses et al. (2011), although

C.2 $\text{CO} \rightleftharpoons \text{CH}_4$ system

they identify a different reaction as the rate-limiting step. Zahnle and Marley (2014), who perform a similar analysis to that of Moses et al. (2011) for the atmospheres of self-luminous giants and brown dwarfs, find results that partially agree with the analysis of Moses et al. (2011), but only under the condition that $\text{CH}_4 \gg \text{CO}$ in the atmosphere. The secondary rate limiting step found by Zahnle and Marley (2014) matches our dominant rate-limiting reaction at 1000 K and 800 K (Eq. (5.3)). Since the volcanic atmospheres that we are focusing on in this study are not initially methane-rich, our rate-limiting step is consistent with the result of Zahnle and Marley (2014).

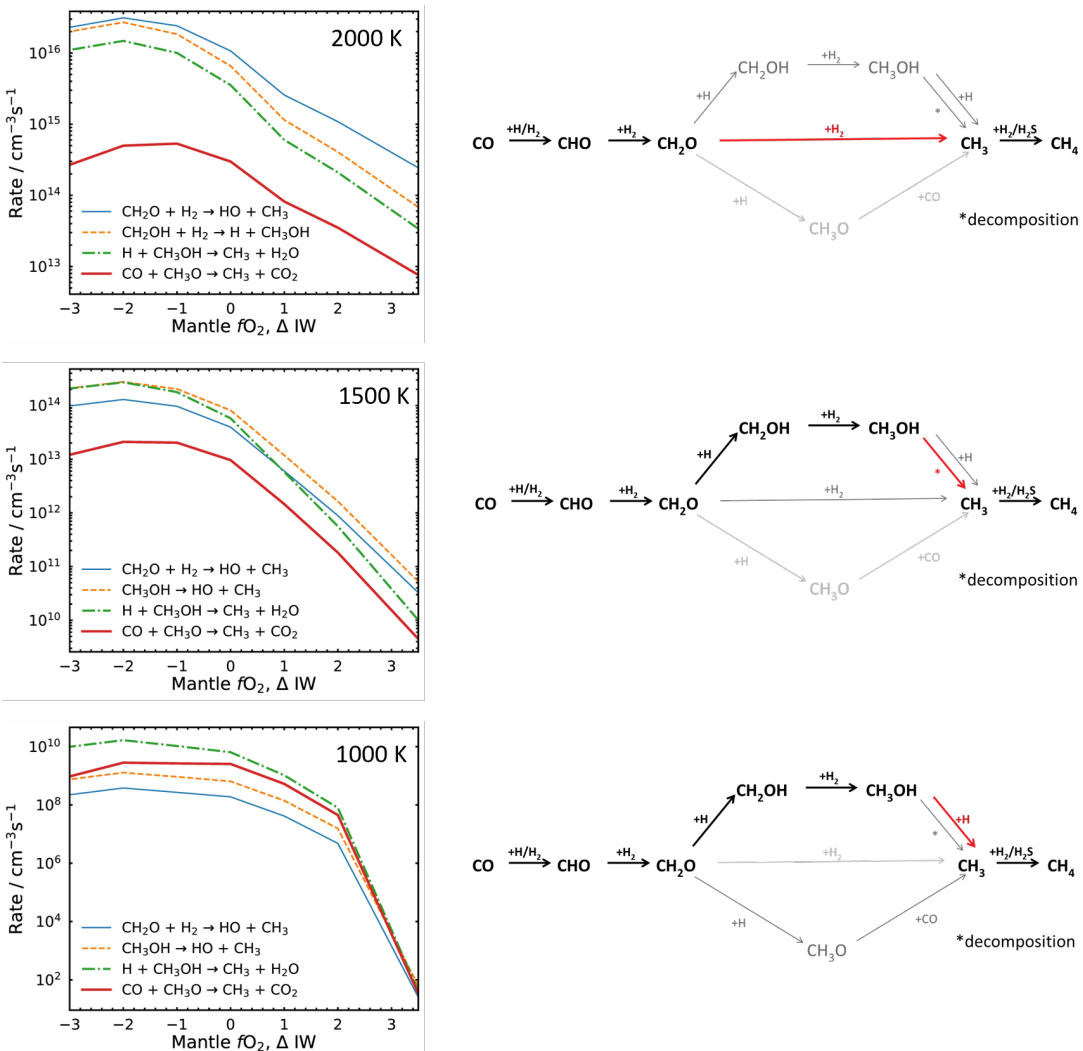


Fig. C.2 Reaction rates as a function of $f\text{O}_2$ of the limiting reactions for pathways that dominate at one or more of the temperatures investigated. Alongside we show the dominant pathway highlighted in the reaction network in bold, and its limiting reaction highlighted in red.

Full description of the identified rate-limiting reactions

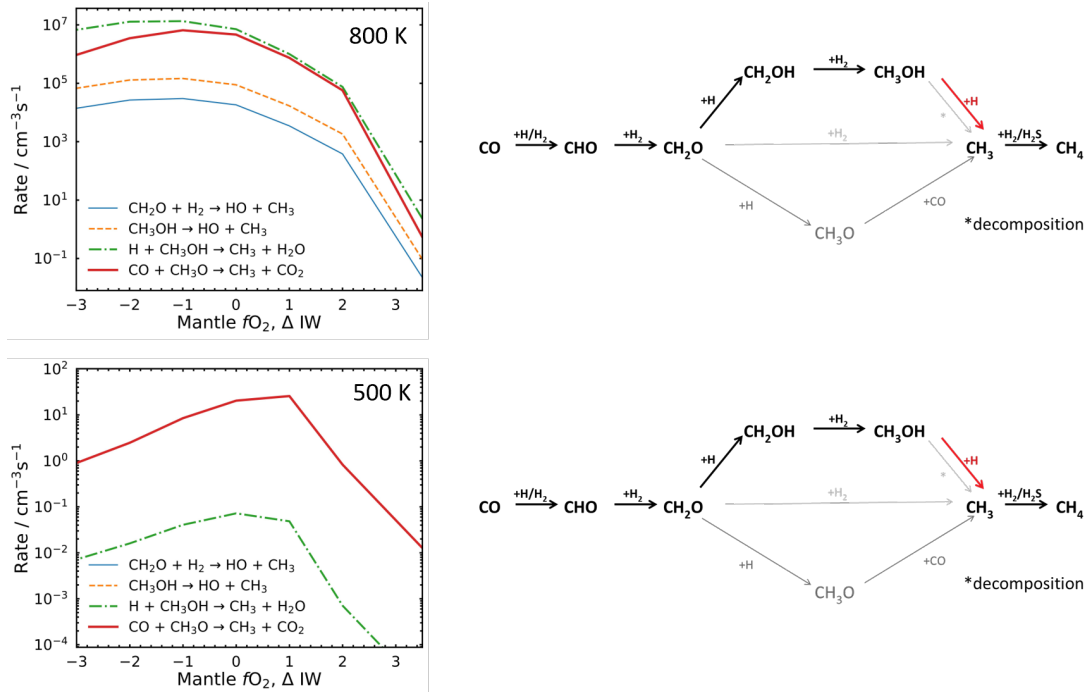
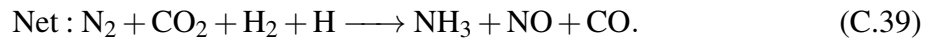
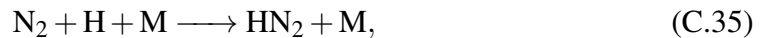


Fig. C.2 Reaction rates as a function of $f\text{O}_2$ of the limiting reactions for pathways that dominate at one or more of the temperatures investigated. Alongside we show the dominant pathway highlighted in the reaction network in bold, and its limiting reaction highlighted in red. (cont.)

C.3 $\text{N}_2 \rightleftharpoons \text{NH}_3$ system

For the $\text{N}_2 \rightarrow \text{NH}_3$ system, we identify one pathway that dominates the conversion over all temperatures and $f\text{O}_2$ values, another pathway (with three variants) that dominates alongside the first only at high temperatures, and two further pathways that are subdominant at different temperatures.

Pathway A:

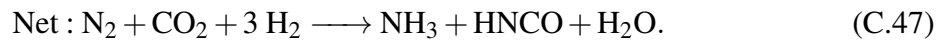
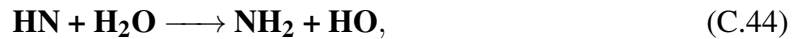


Pathway A is limited by reaction (C.36). Reaction (C.36) produces two N-containing products: HNCO and NO. This reaction splits the network into two branches. Pathway A follows the branch with HNCO. Another pathway, B, with multiple variations depending on the intermediate reagents, follows the branch with NO. At 2000 K and 1500 K both pathways A

C.3 $\text{N}_2 \rightleftharpoons \text{NH}_3$ system

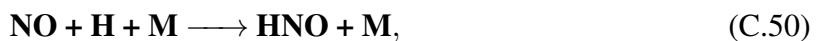
and B are limited by reaction (C.36) and therefore both dominate the conversion at equal rates. At lower atmospheric temperatures, bottlenecks along the NO branch emerge and the different pathways become secondary to pathway A. We show the variants of pathway B and further secondary reaction pathways below.

Pathway B₁:



Pathway B₁ is limited by reaction (C.41) at temperatures of 1500 K and hotter, and limited by reaction (C.44) at temperatures of 1000 K and below.

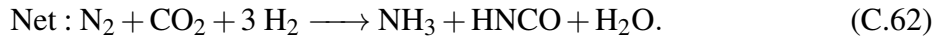
Pathway B₂:



Pathway B₂ is limited by reaction (C.49) at 2000 K, and at 1500 K for $f\text{O}_2 = \text{IW}+2$ and lower. The pathway is limited by reaction (C.52) at 1500K for $f\text{O}_2 = \text{IW}+3.5$. At 1000 K the pathway is limited by reaction (C.50) for $f\text{O}_2 = \text{IW}+1$ and below, and limited by reaction (C.52) for $f\text{O}_2 = \text{IW}+2$ and above. At 800 K the pathway is limited by (C.50) for $f\text{O}_2 = \text{IW}$ and below, and limited by reaction (C.52) for $f\text{O}_2 = \text{IW}+1$ and above.

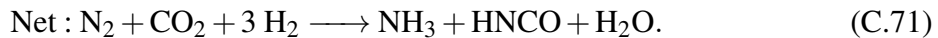
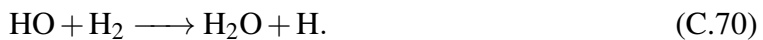
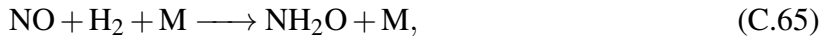
Full description of the identified rate-limiting reactions

Pathway B₃:



Pathway B₃ is limited by reaction (C.56) at 2000 K, and limited by reaction (C.57) at 1500 K and below.

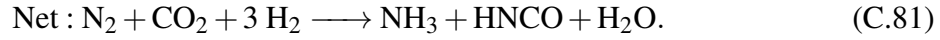
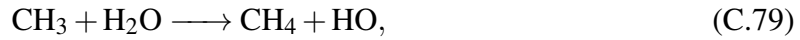
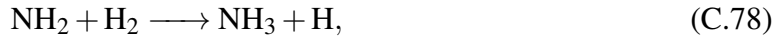
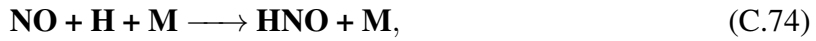
Pathway C:



Pathway C is limited by reaction (C.64) at 2000 K for $f\text{O}_2 = \text{IW-3}$, and limited by reaction (C.66) for $f\text{O}_2 = \text{IW-2}$ and above. The pathway is limited by (C.66) at lower temperatures.

C.3 N₂ ⇌ NH₃ system

Pathway D:



Pathway D is limited by reaction (C.76) at 1500 K and above. At 1500 K the pathway is limited by reaction (C.76) at $fO_2=IW+2$ and above, and is limited by reaction (C.74) and $fO_2=IW+1$ and below. At 800 K the pathway is limited by (C.74) at $fO_2=IW+2$ and below, and is limited by reaction (C.77) at $fO_2=IW+3.5$. This pathway is only significant in the conversion at 1000 K, where it is subdominant and comparative with pathways B and D, because of the increased CH₄ abundance at 1000 K. This reflects how only the warm atmospheres are capable of producing significant abundances of CH₄, but not the cool atmospheres due to kinetic limitations to achieving equilibrium.

Full description of the identified rate-limiting reactions

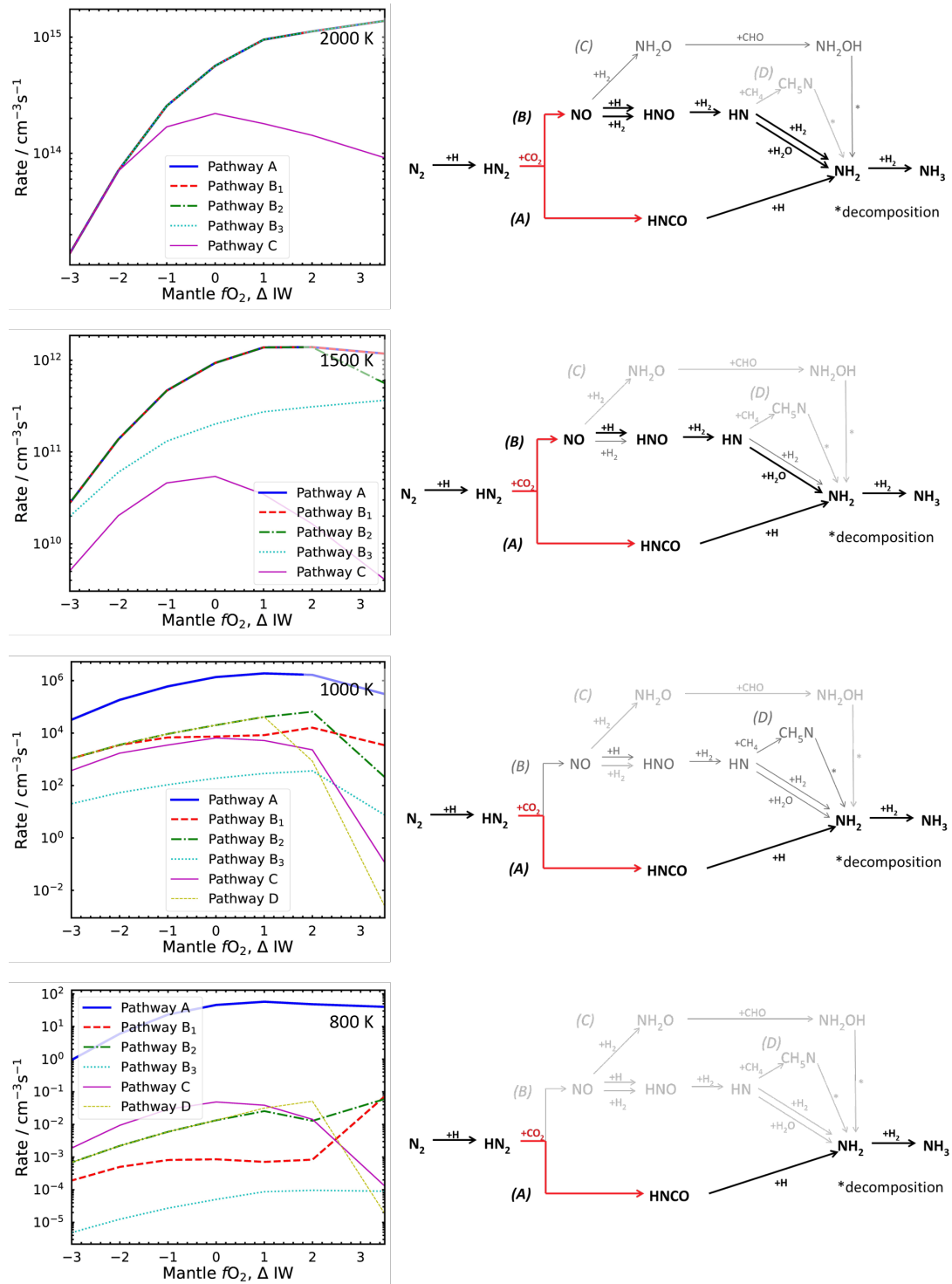


Fig. C.3 Reaction rates as a function of $f\text{O}_2$ of the pathways that are dominant or subdominant at one or more of the temperatures investigated. Alongside we show the dominant pathway highlighted in the reaction network in bold, and its limiting reaction highlighted in red. From top to bottom, the figures correspond to atmospheric temperatures of 2000 K, 1500 K, 1000 K, and 800 K.

C.3 $\text{N}_2 \rightleftharpoons \text{NH}_3$ system

At high temperature the branches via pathways A and B both dominate in the conversion of $\text{N}_2 \longrightarrow \text{NH}_3$ thus a combined reaction pathway and net reaction are as follows:



Compared to previously identified reaction schemes for the $\text{N}_2 \longrightarrow \text{NH}_3$ conversion at high temperatures, the net reaction is the same however the mechanism of conversion is different. Previously identified reaction schemes for H_2 -atmospheres have followed sequential reactions of N_2 with H and H_2 that lead to a single bonded $\text{H}_x\text{N} - \text{NH}_y$ species and the single bond is then broken leading to two $\text{NH}_{x/y}$ species that can then quickly form NH_3 (Line et al., 2011; Moses et al., 2011). The dominant scheme here instead features the reaction $\text{HN}_2 + \text{CO}_2 \longrightarrow \text{HNCO} + \text{NO}$ which breaks the $\text{N} = \text{N}$ double bond, and is responsible for both splitting the scheme into different branches and limiting the overall conversion to NH_3 , with rate coefficient: $k = 3.32 \times 10^{-11} \exp(-12630 \text{ K}/T)$ (Tomeczek and Gradoń, 2003). The reaction is endothermic, with the numerator of the exponent determined by the Gibbs free energy which varies with temperature. The chemical-kinetics simulation uses the temperature dependent value. As quoted here, it is evaluated at 900 K, the approximate quench temperature that was found for NH_3 in our analysis.